Phonon Magnonics

Tsz Cheong Fung

Hertford College

A thesis submitted for the degree of Doctor of Philosophy

Michaelmas Term 2015

Phonon Magnonics

Submitted for the degree of Doctor of Philosophy

Tsz Cheong Fung, Hertford College, University of Oxford

Michaelmas Term 2015

Abstract

This thesis reports on some recent results in the field of acoustics and magnonics.

Chapter 1 reviews the literature on magnonics and GHz frequency transducers, and highlights the lack of understanding of the growth mechanism of magnetron sputtered ZnO thin films. A novel configuration for exciting magnetostatic spin-waves using ZnO transducers is proposed.

Chapter 2 is an introduction to piezoelectricity and how it can be used to generate GHz acoustic waves. A detailed formulation of the Mason model is presented in chapter 3 for predicting the performance of ZnO transducers.

In chapter 4, the fabrication protocol of ZnO transducers in the custom-built sputtering plant is discussed and the transducer characterisation techniques including X-ray and pulse echo measurement are described.

In chapter 5, the characterised properties of the film are compared with modelling prediction. It is found that the piezoelectric and structural properties of the fabricated ZnO films are strongly correlated and are critically dependent on the sputtering conditions and thicknesses.

Chapter 6 is dedicated to plasma characterisation of the sputtering conditions using Langmuir probe diagnostics. The making of the Langmuir probe system and its development are discussed.

Chapter 7 examines the various possible growth mechanisms of the ZnO films with a view to understanding how the c-axis texture forms during sputtering. The results from the Langmuir probe diagnostics and X-ray characterization indicate the detrimental influence of ion bombardment on the film qualities. It is deduced that the c-axis self texturing of ZnO films is driven dominantly by the 'survival of the fastest' mechanism.

Chapter 8 describes the theoretical formulation of magnetostatic spin-wave modes and the mechanism for which the laterally propagating magnetostatic modes are coupled to local elastic standing waves. The experimental evidence (using time resolved spectroscopy) of the acoustic excitation of magnetostatic spin-waves in a YIG film waveguide is then presented in chapter 9; the excitation efficiencies at various magnetic field configurations and carrier frequencies are investigated.

Finally, chapter 10 ends the thesis with the summary of results and outlooks.

Acknowledgements

First and foremost, I would like to express my sincere gratitude to my supervisor Prof. John Gregg for his kindness, support and encouragement. His novel approach and deep understanding of physics have truely inspired me, and I have learnt a great deal from him during the course of this DPhil programme.

I would like to thank Dr. Alexy Karenowska, Prof. Dr. Burkard Hillebrands, Prof. Werner Wolf, Dr. Peter Leek and Dr. Anthony Dyson for stimulating and insightful discussions about the work.

Special thanks goes to my lab mates and colleagues in room 174 - Calvin Tock, Richard Morris, Alistair Inglis, Maciej Malinowski and Jacob Leaver - for their help and the fun for the past 4 years.

I wish to thank all of my friends, especially Ken, Kim, Ben, Sum, Chun Sing for making life in Oxford wonderful, and giving me the emotional support and encouragement to get through difficult times.

Last but not least, I would like to take this opportunity to express my most wholehearted gratitude to my parents for their unconditional support, love and belief in me. To them I dedicate this thesis.

Tsz Cheong Fung, January 2016

Contents

List of Figures

List of Tables

Abbreviations

BAW	**B**ulk **A**coustic **W**ave
SAW	**S**urface **A**coustic **W**ave
std	**S**ubstrate **T**arget **D**istance
FWHM	**F**ull **W**idth **H**alf **M**aximum
OML	**O**rbital **M**otion **L**imited
MSW	**M**agnetostatic **S**pin **W**ave
FWMSW	**F**orward **V**olume **M**agnetostatic **S**pin **W**ave
BVMSW	**B**ackward **V**olume **M**agnetostatic **S**pin **W**ave
FMR	**F**erro**m**agnetic **R**esonance
DUT	**D**evice **U**nder **T**est
YIG	**Y**ttrium **I**ron **G**arnet
GGG	**G**adolinium **G**allium **G**arnet

Dedicated to my parents
for their endless love, care and support.

Chapter 1

Introduction

1.1 Background

In recent years, there has been a growing interest in the study of magnonic systems. Magnonics, being the magnetic analogue of photonics, is the interdisciplinary branch of science which intersects magnetism, spintronics and electronics. In contrast to the use of charge currents for signal processing in semiconductors, magnonics is predicated on the use of spin-waves to transmit, store and process information. Spin-waves were first proposed theoretically in 1930 by F. Bloch [1] and first observed experimentally by J. Griffiths [2]. They correspond to phase-coherent precession of magnetic spins which are dynamic eigenmodes of magnetically ordered materials (illustrated in figure 1.1). From the quantum mechanical point of view, they can be considered as a collective excitation of harmonic oscillators. The term magnon refers to the quasiparticle that represents these excitations.

Magnonic systems have promising prospects as the basis for the next generation of electronics. Compared to conventional electronics, these wave-based systems

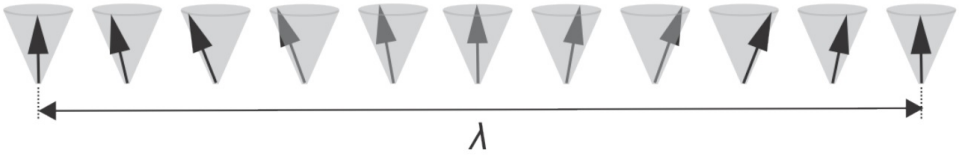

Figure 1.1: This diagram illustrates the precession of spins of a spin-wave in a 1-D chain. The spins are precessing coherently and angular momentum is transferred in spin-wave propagation.The graphic is adopted from [3]

offer numerous advantages. Firstly, they operate in the GHz regime which is conducive to rapid computing power and speed. Furthermore, the miniaturization of magnonic devices is less of a challenge due to the absence of Joule heating and the much smaller spin-wave wavelength (of order microns) relative to electromagnetic waves. Magnonic systems are also highly versatile and suitable for a variety of applications. For instance, the dispersion relations of the spin-wave is easily tunable using small changes in magnetic field and it is also easy to get access to non-linear effects at low threshold powers ($<$1 W) such as solitons [4], bullets [5], fractals [6], chaos [7].

Recent research and development in magnonics has led to numerous discoveries and advancement in technological applications. One such breakthrough is the invention of magnonic crystals. These are artificially made magnetic materials that have periodic spatial modulation of their magnetic parameters [8]. The control of these parameters can be used to tailor band structure of diverse types and thereby allows effective control for manipulating magnon currents [9].

Much research has been carried out at the interface between magnonics and spintronics driven by the prize of ultimately integrating the two technologies. Spintronics is the new science that exploits the electron spin for information processing in additional to the the charge degree of freedom. Perhaps the most well known and influential phenomenon discovered in spintronics is the giant magnetoresistance (GMR) effect [10]. This technology has already been applied worldwide in hard drives read head industrially. Despite this huge commercial success, further

progress is handicapped by the short diffusion length of most practical spintronics materials and the power dissipation issues that bedevil attempts to miniaturize all electron devices. The capability of transmitting angular momentum at room temperature for large distances makes magnonic systems the ideal candidate for spintronic purposes. The investigation of the interplay between charge, spin current and spin-waves has led to the discoveries of many interesting effects including the Spin Hall Effect [11], the Inverse Spin Hall Effect [12], spin torque transfer [13] and spin pumping [14]. Besides spin or angular momentum transport, magnons can also carry heat. The existence of the coupling between thermal phonons and magnons, first realised by K. Uchida's group [15], has provoked a new branch of research known as spincaloritronics, which is very promising for potential applications in future thermoelectric devices.

In this thesis, motivated by technical considerations that we will discuss later, we are preoccupied with phonons in a lower frequency domain than the thermal excitations and we study the 'direct process' coupling of coherent phonons to magnetostatic spin-waves (MSW) at GHz frequencies.

1.2 Magnetostatic spin-waves

Magnetostatic spin-waves (MSW) are large wavelength magnetic excitations that are driven by dipole-dipole interaction. For such long wavelength limit, the exchange interaction between adjacent spins diminishes and becomes negligible. In ferromagnetic thin film, the coupling of the MSWs with the boundary conditions gives rise to diversified dispersion relations. These MSWs are readily observed in epitaxially grown monocrystalline Yttrium Iron Garnet (YIG) thin film on Gadolinium Gallium Garnet (GGG) substrates - YIG is a ferrimagnetic insulator which has the lowest known spin-wave damping at the time of writing. Figure 1.2

shows the typical dispersion relations of the MSWs in a YIG thin film for three different magnetization configurations. A particularly interesting case is when the B-field is parallel to the spin-wave propagation direction; in this configuration, the slope of the dispersion curve is negative which means that the group velocity and the phase velocity are in opposite directions.

1.3 Interaction of magnetostatic spin-waves with acoustic waves

Bulk magnetoelastic coupling is a prerequisite for phonon-magnon coupling. It has been studied extensively since the 1950s in such materials as the ferromagnetic metals cobalt [16] and nickel [17] and in magnetic insulators such as Dysprosium Aluminium Garnet (DAG) -$Dy_3Al_5O_{12}$ [18]; and also in Yttrium Iron Garnet (YIG)- $Y_3Fe_5O_{12}$ [19], the material with which this thesis is concerned. However, this literature mainly focuses on the acoustic interaction with exchange spin-waves [19–22]: little study has been made of the lower frequency domain where acoustic waves couple to magnetostatic spinwaves. Moreover, the bulk magnetoelastic effects that have been studied are necessarily narrowly confined to the situation where magnons and phonons have matched frequencies and wavevectors and thus constitute hybridized magnetoelastic waves: outside of this regime - including for example the GHz MSW regime that interests us - the coupling is negligible. In this thesis we propose and implement a novel magnetoelastic coupling mechanism that works by combining bulk magnetoelastic interaction with local symmetry breaking and is thus capable of broadband phonon-magnon coupling with high efficiency. We are interested in this possibility not only because of the interesting new physics that it deploys, but also because it offers two spectacular advantages over current technology in the quest to integrate magnonics with existing spintronics: it opens

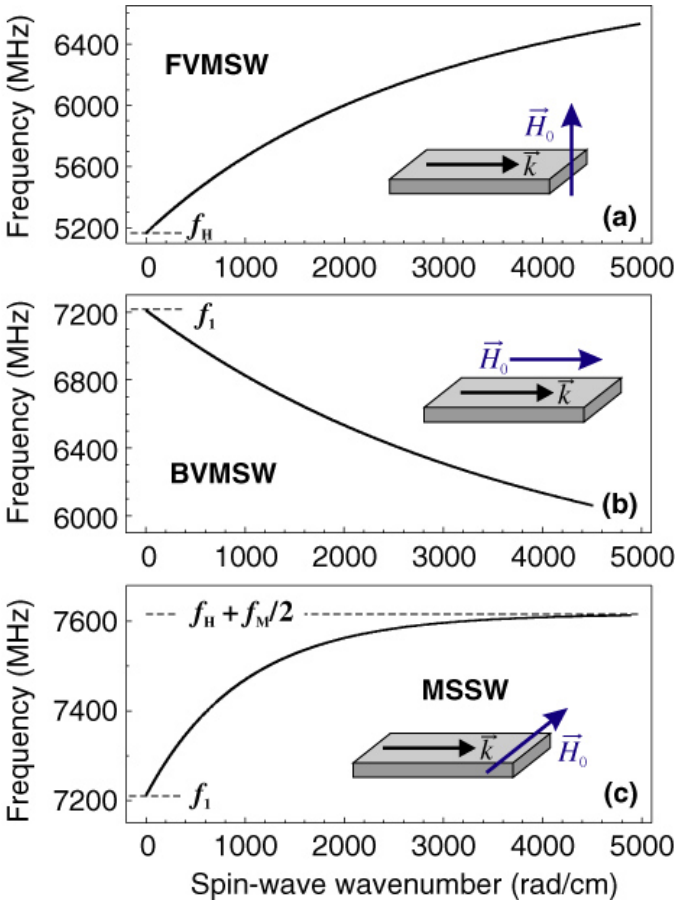

Figure 1.2: The diagram shows the dispersion relations of: (a) Forward volume magnetostatic spin-wave, (b) Backward volume magnetostatic spin-wave (c) Magnetostatic surface spin-wave for a 5 μm thick YIG film. The external bias H_0 used is 1845 Oe and the saturation magnetization is $4\pi M$=1750 G. This diagram is adopted from [23].

up the possibility of magnon generation with high spatial precision and it performs this with minimal heat dissipation. Conventional magnon generation using electromagnetic antennae fails on both of these counts.

Novelty involves generating a longitudinal elastic standing wave across the YIG waveguide for which the localized oscillating Oersted field thereby created is mode coupled to laterally propagating MSWs. This can be achieved by directly launching a longitudinal ultrasonic wave perpendicular to the YIG waveguide as shown in figure 1.3. The size of the transducer electrode can be made very small, thus enabling punctual MSW generation.

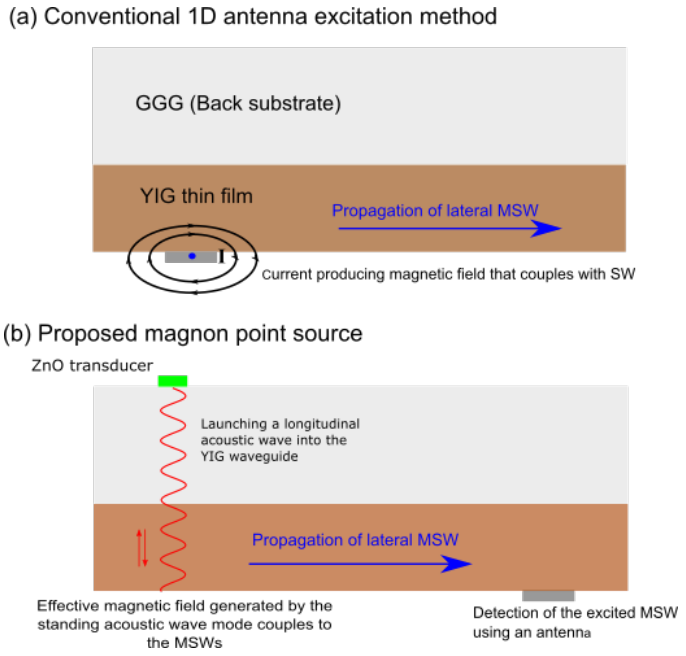

Figure 1.3: Schematics showing the comparison between (a) a linear, 'line' shaped antenna, and (b) the point like, acoustically driven magnon launcher. In a normal linear antenna, the MSW is excited by the oscillating Oersted field produced by the current through a thin wire or a metallic strip; whereas in the case of the acoustic magnon driver, the oscillating Oersted field is caused by the formation of an elastic standing wave across the magnon waveguide.

1.4 Development of ZnO ultrasonic transducers

In order to excite MSW using acoustics, the phonons and magnons involved have to be 'on speaking terms' [1], so we need a high efficiency acoustic transducer that operates at the GHz regime. Such high frequency acoustic transducers are uncommon; commercially available discrete transducers cannot offer the necessary bandwidth. The thickness of the piezoelectric material has to be of order microns to make GHz excitation possible and such devices cannot be self-supporting. GHz ultrasonics therefore requires piezoelectric films with small grain size deposited on a suitable substrate. The various piezoelectric materials capable of producing GHz acoustic waves include cadmium sulphide [24], aluminium nitride [25] and zinc oxide (ZnO). Of these the latter is the most appealing candidate due to its

[1] 'On speaking terms' is a phrase coined by A. Abragam to describe the cross-coupling that obtains between systems of magnetic spins when their precession frequencies match.

high electromechanical coupling and its tendency to form textured and polarized crystals by magnetron sputtering.

Sputtering high quality ZnO transducers is, however, known to be notoriously challenging and dependent strongly on the plasma and growing conditions [26–29]. The existing literature merely reports the engineering parameters (such as power, pressure or substrate target distance) during growth for which their transducers work optimally, but this information is only useful to operators that who possess the same equipment. Moreover, although many authors have succeeded in growing high quality transducers, the underlying growth mechanism for self texturing is still unclear in the literature. In order to understand in detail the mechanism of texture formation and the conditions required for optimal growth, we have conducted an extensive study of the ZnO transducers that are grown in different sputtering conditions. In our study, the ZnO film qualities are characterised using X-ray diffraction and the transducer performance is characterised and compared to the predictions of Mason's model. These results are then correlated with the physical properties of the plasma which were measured using a Langmuir probe. Our study indicates that excessive ion bombardment has an adverse effect on the film growth and that the growth mechanism is predominantly governed by the 'survival of the fastest'. These results may have application not only in the field of ultrasonics, but also in other technologies such as fabrication of ZnO transparent conductive coating [30], ZnO solar cells [31], etc., where high quality c-textured ZnO thin films are required.

Chapter 2

Using piezoelectricity to generate ultrasonic waves (ZnO transducers)

In this chapter, we first introduce the concept of piezoelectricity and the mathematical framework for describing it. We then discuss how piezoelectricity can be applied to excite ultrasonic waves using piezoelectric transducers. Attention will be focussed on studying GHz bulk acoustic wave (BAW) transducers based on piezoelectric ZnO thin films. The crystal structure of ZnO and the electromechanical conversion efficiency of ZnO transducers will be discussed.

2.1 Introduction to piezoelectricity

Piezoelectric effect refers to the ability of certain materials to generate a voltage in response to an applied mechanical stress.

The coupling between the electrical and the mechanical behaviour of a piezoelectric crystal can be described using the linearized, coupled strain-charge equation:

$$T_{ij} = c_{ijnm} S_{nm} - e_{lij} E_l, \tag{2.1}$$

$$D_k = e^T_{knm} S_{nm} + \epsilon_{kl} E_l \tag{2.2}$$

where we have used the Einstein Summation Convention and the symbols represent: the elements of the stress tensor $\tilde{\mathbf{T}}$, electric field $\mathbf{E}$, electric displacement $\mathbf{D}$, strain tensor $\tilde{\mathbf{S}}$, elasticity tensor $\tilde{\mathbf{c}}$, piezoelectric stress tensor $\tilde{\mathbf{e}}$ and dielectric matrix $\tilde{\boldsymbol{\epsilon}}$. The indices i, j, k denote the principal crystallographic axes of the piezoelectric crystal. Equation (2.1) is a modified version of Hooke's law where the piezoelectric stress tensor $\tilde{\mathbf{e}}$ that describes the coupling of the stress $\tilde{\mathbf{T}}$ to the electric field $\mathbf{E}$ has been introduced to take into account the piezoelectric action. Likewise, equation (2.2) describes the coupling of the linear electric displacement $\mathbf{D}$ to the strain $\tilde{\mathbf{S}}$ via the transposed piezoelectric stress tensor $\tilde{\mathbf{e}^{\mathbf{T}}}$.

In order to cast equations (2.1) and (2.2) as a set of matrix equations, we make use of the fact that the strain, stress and the piezoelectric stress tensor are all symmetric tensors; the subscript (ij) can be re-labelled as (α) such that:

$$\alpha = \frac{1}{2}(i+j)\delta_{ij} + [9 - (i+j)](1 - \delta_{ij}) \tag{2.3}$$

This is known as the Voigt notation. Under such notation, the subscripts are transformed as follows: $11 \rightarrow 1$, $22 \rightarrow 2$, $33 \rightarrow 3$, $23 \rightarrow 4$, $13 \rightarrow 5$, $12 \rightarrow 6$. This transforms the stress tensor and the strain tensor in 6×1 vectors, while the elasticity tensor and the piezoelectric stress tensor can be transformed into 6×6 and 6×3 matrices respectively. Equations (2.1) and (2.2) can therefore be rewritten

as:

$$\begin{pmatrix} T_1 \\ T_2 \\ T_3 \\ T_4 \\ T_5 \\ T_6 \end{pmatrix} = \begin{pmatrix} c_{11} & c_{12} & c_{13} & c_{14} & c_{15} & c_{16} \\ c_{21} & c_{22} & c_{23} & c_{24} & c_{25} & c_{26} \\ c_{31} & c_{32} & c_{33} & c_{34} & c_{35} & c_{36} \\ c_{41} & c_{42} & c_{43} & c_{44} & c_{45} & c_{46} \\ c_{51} & c_{52} & c_{53} & c_{54} & c_{55} & c_{56} \\ c_{61} & c_{62} & c_{63} & c_{64} & c_{65} & c_{66} \end{pmatrix} \begin{pmatrix} S_1 \\ S_2 \\ S_3 \\ S_4 \\ S_5 \\ S_6 \end{pmatrix} - \begin{pmatrix} e_{11} & e_{12} & e_{13} \\ e_{21} & e_{22} & e_{23} \\ e_{31} & e_{32} & e_{33} \\ e_{41} & e_{42} & e_{43} \\ e_{51} & e_{52} & e_{53} \\ e_{61} & e_{62} & e_{63} \end{pmatrix} \begin{pmatrix} E_1 \\ E_2 \\ E_3 \end{pmatrix} \quad (2.4)$$

$$\begin{pmatrix} D_1 \\ D_2 \\ D_3 \end{pmatrix} = \begin{pmatrix} e_{11} & e_{21} & e_{31} & e_{41} & e_{51} & e_{61} \\ e_{12} & e_{22} & e_{32} & e_{42} & e_{52} & e_{62} \\ e_{13} & e_{23} & e_{33} & e_{43} & e_{53} & e_{63} \end{pmatrix} \begin{pmatrix} S_1 \\ S_2 \\ S_3 \\ S_4 \\ S_5 \\ S_6 \end{pmatrix} + \begin{pmatrix} \epsilon_{11} & \epsilon_{12} & \epsilon_{13} \\ \epsilon_{21} & \epsilon_{22} & \epsilon_{23} \\ \epsilon_{31} & \epsilon_{32} & \epsilon_{33} \end{pmatrix} \begin{pmatrix} E_1 \\ E_2 \\ E_3 \end{pmatrix}. \quad (2.5)$$

The piezoelectric properties of a crystal are governed by its symmetry. For a crystal to exhibit piezoelectricity, it must lack inversion symmetry: otherwise all elements of the piezoelectric stress tensor would vanish. However, even in a crystal that is not inversion-symmetric, the other symmetries of the structure lead to significant simplification of the tensor with many elements being zero. In section 2.2.2.2, we will show the simplified elasticity, piezoelectric stress and permittivity tensors for crystals with *6mm* symmetry.

2.2 Ultrasonics as an application of piezoelectricity

2.2.1 How to use piezoelectricity to generate or detect acoustic waves

An ultrasonic wave can be excited by applying an oscillating voltage across a piezoelectric material. The application of this voltage induces an oscillating stress due to the piezoelectric effect; this causes the material to vibrate which in turn generates an acoustic wave. During this process, the piezoelectric material converts electric energy into acoustic energy and thus it behaves as a transducer. Likewise, the reverse effect occurs if a piezoelectric material is subjected to an externally driven vibration; in this case the piezoelectric material acts as a sensor which converts acoustic energy back into electric energy.

There are two main types of ultrasonic transducer - bulk acoustic wave (BAW) transducers and surface acoustic wave (SAW) transducers.

BAW transducers produce acoustic waves that propagate in the bulk of the acoustic medium of interest. They can exist in two forms: longitudinal or shear waves. The longitudinal BAW and the shear BAW transducer generate acoustic waves for which the displacements of the acoustic medium are respectively parallel and perpendicular to the direction of propagation of the wave. The most commonly found BAW transducers are piezoelectric plates such as quartz, lithium niobate ($LiNbO_3$), lead zirconate titanate (PZT), etc. (see figure 2.1a). These materials are all very efficient in producing ultrasonic waves, and are mechanically rigid. However, since the resonant frequency of the transducer is inversely proportional to the thickness of the piezoelectric layer, thick piezoelectric plates cannot offer the necessary bandwidth for GHz operation. To generate GHz acoustic waves,

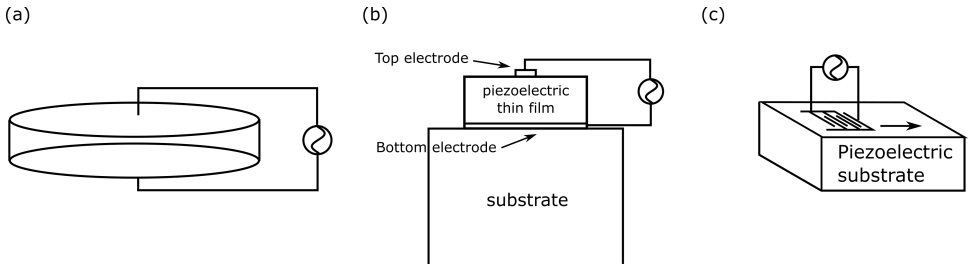

Figure 2.1: A diagram showing the different types of ultrasonic transducer: (a) Rigid BAW piezoelectric plate (e.g. quartz, Lithium niobate ($LiNbO_3$), Lead zirconate titanate (PZT)), (b) Thin film, bulk acoustic wave (BAW) transducers: the transducer comprises a piezoelectric thin film (e.g. Zinc Oxide ZnO, Cadmium sulphide CdS, Aluminium nitride AlN) which is sandwiched between two conducting electrodes; the transducer is attached at the back of a substrate for mechanical support, (c) Surface acoustic wave (SAW) transducers: The structure consists of interdigitated electrodes which are deposited on top of a piezoelectric substrate (e.g. $LiNbO_3$, Lithium tantalate $LiTaO_3$); Surface acoustic waves can be excited by applying an oscillating voltage between the interdigitatated electrodes.

the thickness of the piezoelectric layer has to be of the order of microns. These piezoelectric thin films are mechanically unstable and are usually deposited on a flat substrate. A typical GHz BAW transducer comprises a piezoelectric thin film which is sandwiched between two conducting electrodes; the structure of such transducer is illustrated in figure 2.1b. Among the various materials such as ZnO, CdS or AlN that are suitable for BAW applications, ZnO is the most attractive candidate owing to its high electromechanical coupling coefficient and ZnO devices were thus chosen for the work described in this thesis.

SAW transducers operate differently to BAW transducers: they generate Rayleigh waves that propagate along the surface of an acoustic medium. The amplitude of the surface waves generated typically decay exponentially with depth into the medium. Surface acoustic waves can be generated by applying an oscillating voltage between interdigitated electrodes which are deposited on top of a bulk piezoelectric substrate such as $LiTaO_3$. These SAW devices are now commonly seen in such electronic devices as delay lines, filters, etc.

2.2.2 Bulk acoustic wave (BAW) ZnO transducers

2.2.2.1 The crystal structure of ZnO

ZnO crystallizes into either the cubic zinc blende or the hexagonal wurtzite structure. Both of these structures lack inversion symmetry and exhibit strong piezoelectricity. However, the wurtzite phase is more stable and is predominantly observed. The hexagonal wurtzite structure has point group symmetry *6mm* and space group $P6_3mc$.

Figure 2.2 shows the unit cell of the wurtzite structure which is characterized by two lattice parameters a and c, where a=0.32495 nm and c=0.52069 nm [32] where the [0001] is the c-axis direction. For a crystal structure to have inversion symmetry, it must be possible to map x, y, z onto $-x, -y, -z$. It can easily be seen from figure 2.2 that for ZnO the z to $-z$ mapping does not happen (where we have taken the z direction to coincide with [0001]). This gives rise to an electric dipole moment associated with the c-axis of the crystal which is the piezoelectric axis of the crystal.

Thin films of ZnO can be deposited using various methods such as radio-frequency (RF) sputtering, pulsed laser deposition or molecular beam epitaxy. Of these, RF sputtering is commonly preferred as an economical means of producing highly oriented and uniform ZnO films. ZnO films grown by RF magnetron sputtering are usually polycrystalline and comprise columnar grains with the c- axis parallel to the long dimension of the column. If the ZnO crystallites are randomly oriented, their piezoelectric action globally cancels; so even if the individual grains are piezoelectric in nature, the film will exhibit no overall piezoelectric action. Likewise, if the axes of the grains are perfectly aligned with one another but the number of up-pointing grains is equal to the number of downward pointing grains,

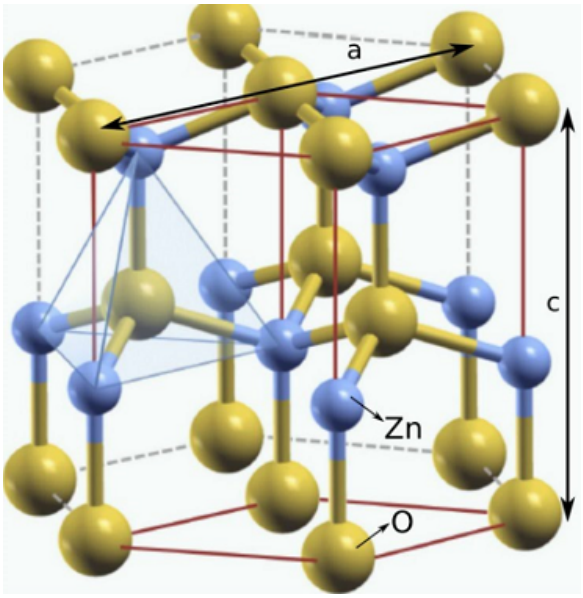

Figure 2.2: The atomic arrangement in the ZnO wurtzite structure is illustrated in the diagram. The yellow and blue spheres represent the O atom and Zn atom respectively. Drawn in the red wireframe is the unit cell with lattice parameters a=0.32495 nm and c=0.52069 nm. The tetragonal configuration formed by the sp^3 coordination between the Zn and O atoms is highlighted in the blue wireframe. The lack of inversion symmetry is evident from the fact that there is no mirror symmetry in a plane perpendicular to the c-axis. This diagram is adopted from [33].

no piezoelectric effect will be observed [1]. Thus, fabricating a high quality transducer requires deposition of a film in which the grains are both strongly oriented and highly polarized.

2.2.2.2 Electromechanical coupling constants for BAW ZnO transducers

In section 2.1, we have mathematically described the piezoelectric effect for a generic piezoelectric crystal. The $6mm$ symmetry of ZnO crystals significantly simplifies the strain charge equations. By convention, the indices '(1,2)' represent the a-axis direction, and the index '3' denotes the c-axis direction. The elasticity tensor $\tilde{\mathbf{c}}$, the piezoelectric stress tensor $\tilde{\mathbf{e}}$ and the permittivity tensor $\tilde{\boldsymbol{\epsilon}}$ then become

[1] This is also referred to as polarization reversal.

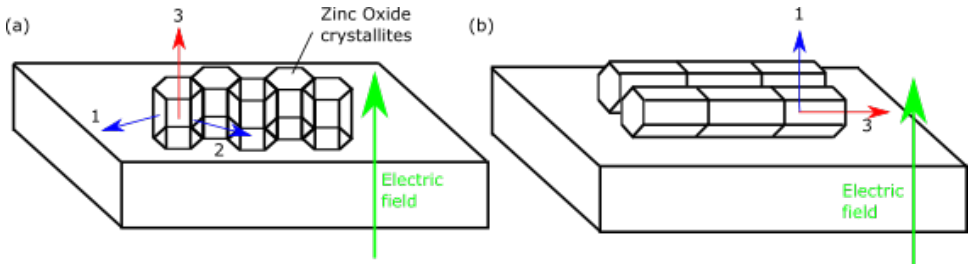

Figure 2.3: (a) The pure longitudinal ZnO BAW transducer: the c-axis aligns with the normal of the substrate and the electric field points in the '3' direction. (b) The pure shear ZnO BAW transducer: c-axis is perpendicular to the normal of the substrate and the electric field points in the '1' direction.

[34]:

$$\mathbf{c} = \begin{pmatrix} c_{11} & c_{12} & c_{13} & 0 & 0 & 0 \\ c_{12} & c_{11} & c_{13} & 0 & 0 & 0 \\ c_{13} & c_{13} & c_{33} & 0 & 0 & 0 \\ 0 & 0 & 0 & c_{44} & 0 & 0 \\ 0 & 0 & 0 & 0 & c_{44} & 0 \\ 0 & 0 & 0 & 0 & 0 & c_{66} \end{pmatrix}, \mathbf{e} = \begin{pmatrix} 0 & 0 & e_{31} \\ 0 & 0 & e_{31} \\ 0 & 0 & e_{33} \\ 0 & e_{15} & 0 \\ e_{15} & 0 & 0 \\ 0 & 0 & 0 \end{pmatrix}, \epsilon = \begin{pmatrix} \epsilon_{11} & 0 & 0 \\ 0 & \epsilon_{11} & 0 \\ 0 & 0 & \epsilon_{33} \end{pmatrix} \tag{2.6}$$

where $c_{66} = \frac{c_{11}-c_{12}}{2}$.

If a BAW ZnO thin film transducer is deposited on a flat substrate surface such as is shown in figure 2.4a, the c-axis orientation of the ZnO grains with respect to the substrate surface determines whether longitudinal or transverse waves can be excited. We now consider the two simplest configurations where the c-axis crystallites are respectively parallel and perpendicular to the substrate normal (see figure 2.3). For the case when the c-axis is parallel to the substrate normal, the electric field is applied along the '3' direction. Assuming an infinite plane transducer with uniform electric excitation, the acoustic propagation direction must be normal to the substrate surface and the strain-charge equations can be simplified to:

$$T_3 = c_{33}S_3 - e_{33}E_3, \tag{2.7}$$

$$D_3 = e_{33}S_3 + \epsilon_{33}E_3. \tag{2.8}$$

This corresponds to the excitation of pure longitudinal acoustic waves that propagate in the '3' direction.

For the case when the c-axis is perpendicular to the substrate normal, the electric field is applied along the '1' direction and the strain-charge equations are now:

$$T_5 = c_{44}S_5 - e_{15}E_1, \tag{2.9}$$

$$D_1 = e_{15}S_5 + \epsilon_{11}E_1, \tag{2.10}$$

and so pure shear waves that propagate in the '1' direction can be excited.

In both of these cases, the strain-charge equations take the simple form of:

$$T = cS - eE, \tag{2.11}$$

$$D = eS + \epsilon E. \tag{2.12}$$

When the c-axis is at an angle θ_c with the substrate normal, the form of the strain-charge equations is complicated. They can be worked out by applying rotational transformations to the tensors involved.

Foster *et al.* [35] has calculated the effective electromechanical coupling constants k_L (longitudinal waves) and k_S (shear waves) of the BAW ZnO transducer for various angles θ_c. The results are illustrated in Figure 2.4b. The electromechanical coupling constant is the measure of how efficiently the piezoelectric material can convert energy between the acoustic and electric domains [2].

[2]The term "efficiency" is usually deployed to describe situations in which mechanical or electrical energy is degraded to heat. In the present context where we are discussing a perfect transducer that exhibits no ohmic heating losses, we follow the literature and (somewhat confusingly) use it as a measure of the amount of mechanical strain obtained per unit of electric field applied.

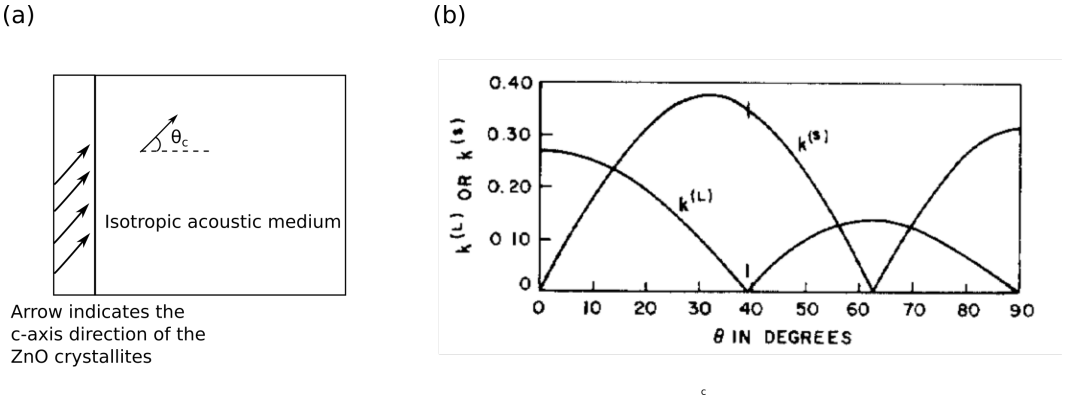

Figure 2.4: (a) Schematics showing the geometry of a ZnO transducer grown on the surface of an acoustically isotropic medium: the angle between the c-axis of the ZnO crystallites and the substrate normal θ_c is highlighted, (b) A plot of the electromechanical coupling constants k_L or k_S with respect to θ_c (plot adopted from [35]). At θ_c=0°, only longitudinal waves can be excited; and at θ_c ≈90°, only shear waves can be excited. An efficient hybrid transducer - a transducer that is capable of generating both longitudinal or shear wave - can be made at θ_c ≈20°.

The constants are different for shear and longitudinal waves and they are defined as:

$$k^2_{(L,S)} = \frac{e_{(L,S)}}{\epsilon_{(33,11)}\rho_{ZnO}v_{(L,S)}} \tag{2.13}$$

where ρ_{ZnO} is the density of the ZnO, $v_{(L,S)}$ is the velocity of acoustic waves, $e_{L,S}$ is the effective piezoelectric stress constant which is a sophisticated function of e_{ij} and the angle θ_c. When θ_c=0°, i.e. when the c-axis is aligned with the substrate normal, only longitudinal waves can be excited. In this case, e_L=e_{33}=1.14 Cm^{-1}, which corresponds to k_L=0.27; meanwhile e_S=0 which leads to k_S=0. This is the particular case that we will study in detail in the rest of this thesis. At θ_c ≈90°, k_L vanishes and only shear waves can be excited. In this configuration, e_S=e_{15}=-0.59 Cm^{-1} and e_L=0 which leads to k_S=0.3 and k_L=0. Interestingly, if one can grow a ZnO film such that the crystallite c-axes make an intermediate angle with the substrate normal, both k_L and k_S are non zero, so one can make a transducer that can excite simultaneously produce longitudinal and shear waves.

Chapter 3

The Mason model and its application to the modelling of bulk acoustic wave (BAW) ZnO transducers

In this chapter, we describe a systematic method for modelling the response of ZnO piezoelectric transducers that have given materials properties and a given geometry. Following Mason's work [36, 37], we use an equivalent transmission line model to describe quantitatively the transduction process and the acoustic transmission. This in turn translates the problem into an exercise in circuit analysis, which can then be solved in a relatively simple manner. However, even with this formalism, the analysis of general ZnO piezoelectric layers that can generate both longitudinal and shear waves is still very complicated. Accordingly, we simplify the analysis by assuming that the transducer can only generate either longitudinal waves or shear waves. In these cases, the strain-charge relations described by equations (2.11), (2.12) can be applied. We will discuss the derivation of the

equivalent circuits and hence the application of Mason's model for simulating the conversion efficiency of the BAW ZnO transducers. We start by investigating the 1D acoustic equation of motion.

3.1 The 1D acoustic equation of motion

The particle displacements u in the presence of an acoustic wave that are propagating in the z-direction are governed by Newton's second law:

$$F = \int T dA = \int \frac{dT}{dz} dV = \int \rho_m \frac{d^2u}{dt^2} dV, \tag{3.1}$$

where F is the net force applied by the acoustic wave; $T{=}\frac{dF}{dA}$ is the stress, which is the force applied to a surface of area A; ρ_m is the density of the acoustic medium and dV denotes an infinitesimal volume element of the acoustic medium. So we have:

$$\frac{dT}{dz} = \rho_m \frac{d^2u}{dt^2}. \tag{3.2}$$

For a non-piezoelectric material, the stress T and the strain $S{=}\frac{du}{dz}$ are related by Hooke's law, such that:

$$T = c_m S, \tag{3.3}$$

where c_m is the elasticity of the acoustic medium. Substituting equation (3.3) into (3.2) yields the acoustic equation of motion:

$$\frac{d^2u}{dz^2} = \frac{\rho_m}{c_m} \frac{d^2u}{dt^2}. \tag{3.4}$$

Putting a trial sinusoidal solution into equation (3.4) gives the phase velocity of the acoustic medium, i.e., $\frac{\omega}{k} = v_m = \sqrt{\frac{c_m}{\rho_m}}$, where ω is the angular frequency and k is the wavenumber. One can also relate F to the particle velocity $v{=}\frac{du}{dt}$ by noticing

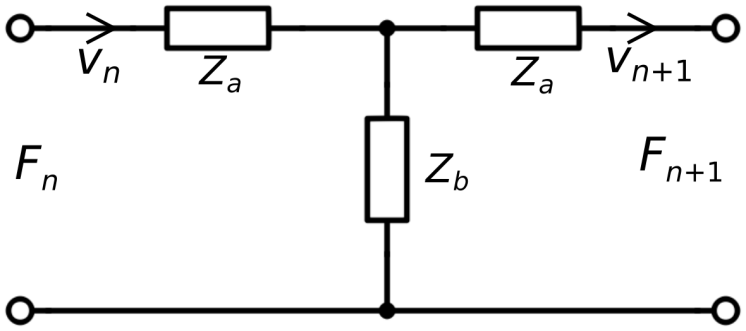

Figure 3.1: The diagram shows the equivalent circuit model for an acoustic transmission line. It is a T network with impedances, $Z_a = jZ_m \tan(\frac{\gamma_m}{2})$ and $Z_b = \frac{-jZ_m}{\sin(\gamma_m)}$, where Z_m is the characteristic impedance of the material m, and $\gamma_m = kt_m$ with t_m being the material thickness. (F_{n+1}, v_{n+1}) is related to (F_n, v_n) by a transfer matrix A_m which is defined in equation (3.15).

that: $\frac{dT}{dz} = \rho_m \frac{dv}{dt} \Rightarrow kT = \rho_m \omega v \Rightarrow \frac{T}{v} = \frac{\omega}{k}\rho_m = \sqrt{\rho_m c_m}$, and so:

$$F = Z_m v = \sqrt{\rho_m c_m} A v = A \rho_m v_m v, \tag{3.5}$$

where $Z_m = A\rho_m v_m$ is the characteristic impedance of the acoustic medium. Here, F and v are analogous to V and I in an electrical circuit, and thus in a long acoustic medium (compared to the wavelength), the acoustic variables F and v may be represented using an equivalent transmission line model.

3.2 Transmission line model for a non-piezoelectric acoustic medium

Consider a slab of acoustic medium of thickness t_m bounded by two planes at $z = z_n$ and $z = z_{n+1}$ with cross sectional area A. The aim of this section is to relate the forces at the boundaries (F_n, F_{n+1}) to the particle velocities at the boundaries (v_n, v_{n+1}) and hence to formulate an equivalent circuit for a non-piezoelectric acoustic medium. We suppose that there exists a superposition of forward and backward travelling waves, so that the spatial dependence of the

particle displacement $u(z)$ can be written as:

$$u(z) = u^+ e^{-jkz} + u^- e^{jkz}, \tag{3.6}$$

where u^+ and u^- are the amplitudes of the forward and backward travelling waves. The particle velocity at z_n is given by:

$$v_n = \frac{du}{dt}(z_n) = j\omega(u^+ e^{-jkz_n} + u^- e^{jkz_n}). \tag{3.7}$$

Similarly, we obtain an expression for v_{n+1},

$$v_{n+1} = \frac{du}{dt}(z_{n+1}) = j\omega(u^+ e^{-jkz_{n+1}} + u^- e^{jkz_{n+1}}). \tag{3.8}$$

Using equation (3.7) and (3.8), we can find u^+ and u^- in terms of v_n and v_{n+1} such that:

$$j\omega u^+ = \frac{v_n e^{jkz_{n+1}} - v_{n+1} e^{jkz_n}}{2j\sin(\gamma_m)}, \tag{3.9}$$

$$j\omega u^- = \frac{v_{n+1} e^{-jkz_n} - v_n e^{-jkz_{n+1}}}{2j\sin(\gamma_m)}, \tag{3.10}$$

where $\gamma_m{=}kt_m$. We now find the relationship of the force F with u^+ and u^-, i.e.,

$$F = AT = Ac_m S = Ac_m \frac{du}{dz} = jkc_m A(u^+ e^{-jkz} - u^- e^{jkz}) = j\omega Z_m(u^+ e^{-jkz} - u^- e^{jkz}). \tag{3.11}$$

Finally, substituting the expressions for u^+ and u^- into equation (3.11) leads to:

$$F_n = \frac{Z_m}{j\sin\gamma_m}(v_n - v_{n+1}) + jZ_m \tan\left(\frac{\gamma_m}{2}\right) v_n, \tag{3.12}$$

$$F_{n+1} = \frac{Z_m}{j\sin\gamma_m}(v_n - v_{n+1}) - jZ_m \tan\left(\frac{\gamma_m}{2}\right) v_{n+1}. \tag{3.13}$$

These equations can be represented by an equivalent circuit as shown in figure 3.1. It is a T-network with impedances $Z_a{=}jZ_m \tan(\frac{\gamma_m}{2})$ and $Z_b = \frac{-jZ_m}{\sin(\gamma_m)}$.

To facilitate the conversion from (F_n, v_n) to (F_{n+1}, v_{n+1}), one can introduce the matrix A_m such that:

$$\begin{pmatrix} F_n \\ v_n \end{pmatrix} = A_m \begin{pmatrix} F_{n+1} \\ v_{n+1} \end{pmatrix}, \tag{3.14}$$

$$A_m = \begin{pmatrix} \cos(\gamma_m) & jZ_m \sin(\gamma_m) \\ j\frac{\sin(\gamma_m)}{Z_m} & \cos(\gamma_m) \end{pmatrix}. \tag{3.15}$$

3.3 Equivalent circuit for ZnO piezoelectric layers (purely longitudinal or purely shear wave)

In this section, we consider a slab ZnO slab of thickness t_p with boundaries at $z = z_n$ and $z = z_{n+1}$ and a cross sectional area A. We begin by relating the acoustic parameters at the boundaries (F_n, v_n), (F_{n+1}, v_{n+1}) to the electrical parameters (V, I). Based on these results, we develop an equivalent circuit that represents the electromechanical coupling and the acoustic transmission of the piezoelectric layer.

In a piezoelectric material, the displacement current density J is related to the electric displacement D by $J=\frac{\partial D}{\partial t}$. If the current I is sinusoidal, $I = JA=\frac{\partial D}{\partial t}A=\mathrm{j}\omega DA$. Hence, we have:

$$D = \frac{I}{j\omega A}. \tag{3.16}$$

Combining equations (2.11) and (2.12), F can be written as:

$$F = TA = cSA - e\big(\frac{D - eS}{\epsilon}\big)A = \big(c + \frac{e^2}{\epsilon}\big)SA - \frac{eDA}{\epsilon} = c'SA - \frac{h}{j\omega}I \tag{3.17}$$

where $h=\frac{e}{\epsilon}$ and $c' = c+\frac{e^2}{\epsilon}$.

The forces at the boundaries of the piezoelectric slab can be obtained by modifying equations (3.12) and (3.13). This is achieved by replacing c_m by c' and adding the

term -$\frac{I}{j\omega}$, i.e.

$$F_n = \frac{Z'}{j\sin(\gamma)}(v_n - v_{n+1}) + jZ'\tan\left(\frac{\gamma}{2}\right)v_n - h\frac{I}{j\omega} \tag{3.18}$$

$$F_{n+1} = \frac{Z'}{j\sin(\gamma)}(v_n - v_{n+1}) - jZ'\tan\left(\frac{\gamma}{2}\right)v_{n+1} - h\frac{I}{j\omega}. \tag{3.19}$$

As e is small, $Z' \approx Z_p{=}A\rho_p v_p$ is the characteristic impedance of the ZnO slab. Here, v_p and ρ_p are defined as the velocity of the acoustic wave and the density of the ZnO piezoelectric layer respectively.

Now, we relate the voltage V to I and the acoustic parameters.

Rearranging equation (2.2), we obtain:

$$E = \frac{D}{\epsilon^s} - \frac{e}{\epsilon^s}\frac{\partial u}{\partial z}. \tag{3.20}$$

Integrating E and using $v{=}\mathrm{j}\omega u$ yields:

$$V = \int_{z_n}^{z_{n+1}} E dz = \frac{Dt_p}{\epsilon} - h\cdot[u(z_{n+1} - u(z_n)] = \frac{It_p}{j\omega A\epsilon} + \frac{h}{j\omega}(v_n - v_{n+1}). \tag{3.21}$$

This equation can be rearranged to give:

$$I = j\omega C_0 V - hC_0(v_n - v_{n+1}) \tag{3.22}$$

where $C_0^{(\mathrm{L,S})} = \frac{\epsilon A}{t_p}$ is the capacitance of the piezoelectric layer. The current therefore comprises a contribution from the capacitance and a contribution from the acoustic power generation due to the piezoelectric effect.

Equation (3.18), (3.19) and (3.22) can then be represented by a 3-port equivalent circuit network as illustrated in figure 3.2. In this circuit, the transformer which has effective turns ratio (1:ϕ where $\phi{=}hC_0{=}k_{(\mathrm{L,S})}\left(\frac{\omega_0 C_0 Z_p}{\pi}\right)^{\frac{1}{2}}$, and $\omega_0 = 2\pi\frac{v_p}{2t_p}$) converts between the electrical parameters (V, I) into acoustical parameters (F, v)

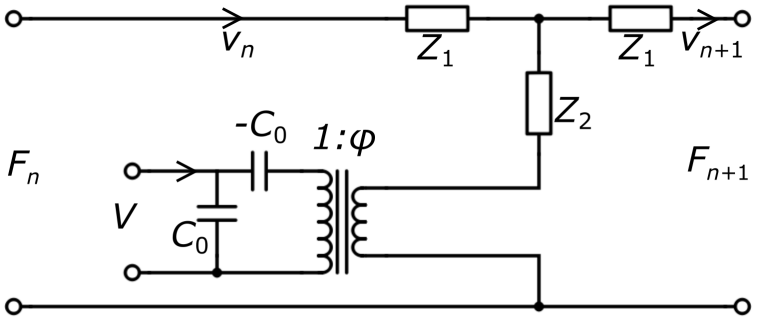

Figure 3.2: An illustration of the Mason equivalent circuit model for a piezoelectric layer. Here, $Z_1 = jZ_0\tan(\frac{\gamma_p}{2})$ and $Z_2 = \frac{-jZ_0}{\sin(\gamma_p)}$, $\gamma_p = kt_p = \frac{\omega t_p}{v_p}$, $Z_0 = A\rho_p v_p$, $\phi = hC_0 = k_{\mathrm{L}}\left(\frac{\omega_0 C_0 Z_0}{\pi}\right)^{\frac{1}{2}}$, $\omega_0 = 2\pi\frac{v_p}{t_p}$, $C_0 = \frac{\epsilon_0\epsilon A}{t_p}$. The transformer network represents the electromechanical coupling while the T network takes into account the acoustic transmission. $\mathrm{C}_0^{(\mathrm{L,S})}$ represents the capacitance of the ZnO piezoelectric layer.

and the T-network takes into account the acoustic generation and transmission in the piezolayer.

If the F_n port is terminated with a back impedance Z_b, then the matrix A relating (V, I) to (F_{n+1}, v_{n+1}) is [38, 39]:

$$\begin{pmatrix} V \\ I \end{pmatrix} = A_p \begin{pmatrix} F_{n+1} \\ v_{n+1} \end{pmatrix} \tag{3.23}$$

$$A_p = \frac{1}{\phi H}\begin{pmatrix} 1 & j\frac{\phi^2}{\omega C_0} \\ j\omega C_0 & 0 \end{pmatrix}\begin{pmatrix} \cos\gamma_p + jz_b\sin\gamma_p & Z_p(z_b\cos\gamma_p + j\sin\gamma_p) \\ j\frac{\sin\gamma_p}{Z_p} & 2(\cos\gamma_p - 1) + jz_b\sin\gamma_p \end{pmatrix}, \tag{3.24}$$

where z_b, ϕ and H are defined as:

$$z_b = \frac{Z_b}{Z_p} \tag{3.25}$$

$$\phi = hC_0 = k_{(\mathrm{L,S})}\left(\frac{\omega_0 C_0 Z_p}{\pi}\right)^{\frac{1}{2}} \tag{3.26}$$

$$\omega_0 = 2\pi\frac{v_p}{2t_p} \tag{3.27}$$

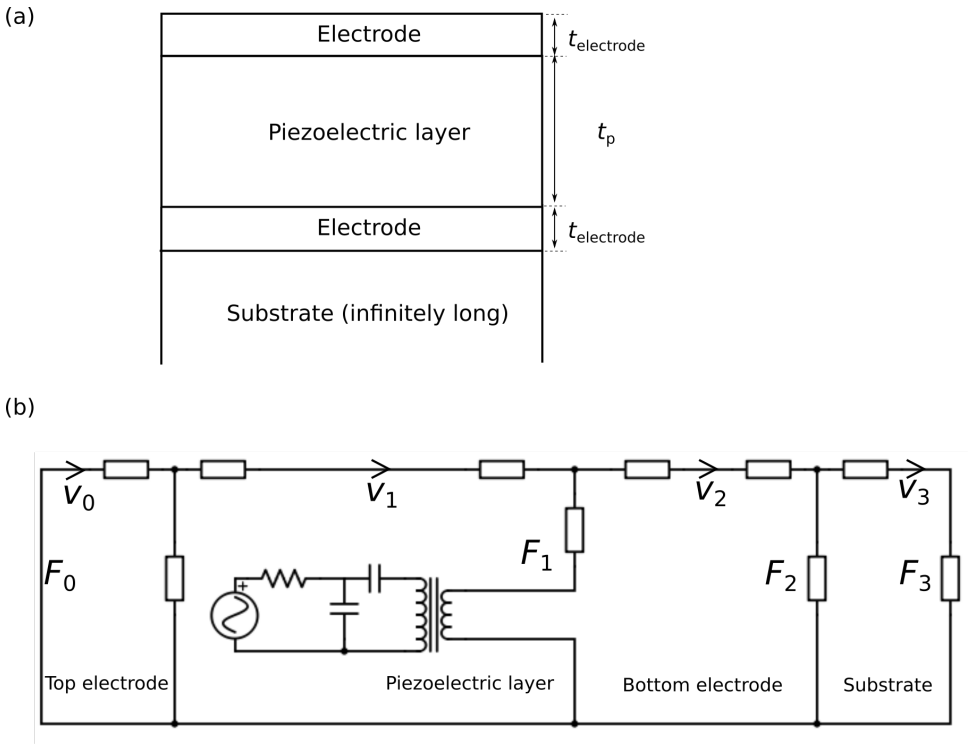

Figure 3.3: The total equivalent circuit model for the transducer is constructed by cascading the circuits for the corresponding piezoelectric and non-piezoelectric layers. A stress-free surface is assumed on the top electrode surface and the acoustic port (F_3, v_3) is terminated by the substrate impedance Z_{sb}, which represents an infinitely thick substrate.

$$H = \cos\gamma_p - 1 + jz_b \sin\gamma_p. \tag{3.28}$$

3.4 Mason's equivalent circuit for ZnO BAW transducers

Combining the equivalent circuits for non-piezoelectric and ZnO piezoelectric layers, one can construct the total circuit for the BAW transducers with the layer structure electrode/ZnO piezoelectric layer/electrode/substrate. The total equivalent circuit is illustrated in figure 3.3. In the model, we have assumed that the substrate is infinitely long. This assumption can be justified by the fact that the acoustic wave is excited by a pulse in the experiment, and the duration of this pulse is much shorter than $\frac{t_{\text{substrate}}}{v_{\text{substrate}}}$ so that no standing wave is formed. We have

assumed that the top electrode surfaces are stress free as they are allowed to move freely in space; this implies we can short circuit the leftmost port. The total impedance of the transducer can be then found by noticing that:

$$\begin{pmatrix} V \\ I \end{pmatrix} = A_p \begin{pmatrix} F_2 \\ v_2 \end{pmatrix} = A_p A_{\text{bottom electrode}} \begin{pmatrix} F_3 \\ v_3 \end{pmatrix} = A_{\text{tot}} \begin{pmatrix} F_3 \\ v_3 \end{pmatrix} \tag{3.29}$$

and the impedance Z_{in} is given by:

$$Z_{\text{in}} = \frac{V}{I} = \frac{A_{\text{tot},11} F_3 + A_{\text{tot},12} v_3}{A_{\text{tot},21} F_3 + A_{\text{tot},22} v_3} = \frac{A_{\text{tot},11} Z_{sb} + A_{\text{tot},12}}{A_{\text{tot},21} Z_{sb} + A_{\text{tot},22}}, \tag{3.30}$$

where in the last step, we have used $\frac{F_3}{v_3} = Z_{sb}$ with Z_{sb} being the characteristic acoustic impedance of the substrate.

The back impedance Z_b that appears in the matrix A_p can be calculated by noticing:

$$\begin{pmatrix} F_0 \\ v_0 \end{pmatrix} = A_{\text{top electrode}} \begin{pmatrix} F_1 \\ v_1 \end{pmatrix}. \tag{3.31}$$

But F_0=0 (short circuit), so we have:

$$Z_{\text{b}} = -\frac{F_1}{v_1} = \frac{A_{\text{top electrode},12}}{A_{\text{top electrode},11}}. \tag{3.32}$$

This equation can be simplified by assuming the ZnO piezo-layer is sandwiched by a back impedance $Z_b = z_b Z_p$ (mentioned previously) and a forward impedance $Z_f = z_f Z_p$ (see figure 3.4), Z_{in} can be found to be [40]:

$$Z_{\text{in}} = \frac{1}{j\omega C_0}\left[1 - \frac{k_{\text{L}}^2}{\gamma_p} \frac{(z_b + z_f)\sin\gamma_p + j2(1-\cos\gamma_p)}{(z_b + z_f)\cos\gamma_p + j(1 + z_b z_f)\sin\gamma_p}\right]. \tag{3.33}$$

We can now calculate the acoustic power that is generated in the transducer for a given input impedance. Using standard transmission line theory, the fraction of

incident electrical power that is converted to acoustic power is:

$$\begin{aligned}\text{Fraction} &= \text{Re}\Big(1-\Big(\frac{Z_{\text{in}}-R_{\text{s}}}{Z_{\text{in}}+R_{\text{s}}}\Big)^2\Big) = \text{Re}\Big(1-\Big(\frac{\frac{1}{R_{\text{s}}}-\frac{1}{Z_{\text{in}}}}{\frac{1}{R_{\text{s}}}+\frac{1}{Z_{\text{in}}}}\Big)^2\Big)\\ &= \text{Re}\Big(1-\Big(\frac{G_{\text{s}}-Y_{\text{in}}}{G_{\text{s}}+Y_{\text{in}}}\Big)^2\Big) = \text{Re}\Big(\frac{4G_{\text{s}}Y_{\text{in}}}{(G_{\text{s}}+Y_{\text{in}})^2}\Big)\\ &= \frac{4G_{\text{s}}G_{\text{in}}}{(G_{\text{s}}+G_{\text{in}})^2+B_{\text{in}}^2}\end{aligned} \tag{3.34}$$

where in the calculation, we have expressed the power transmitted in terms of the admittance $Y_{\text{in}} = \frac{1}{Z_{\text{in}}} = G_{\text{in}} + jB_{\text{in}}$. The conversion 'loss' CL (dB) [1] is therefore given by:

$$\text{CL (dB)} = 10\cdot\log_{10}\Big(\frac{4G_{\text{s}}G_{\text{in}}}{(G_{\text{s}}+G_{\text{in}})^2+B_{\text{in}}^2}\Big). \tag{3.35}$$

3.5 Theoretical predictions of the Mason model

In this thesis, the transducers fabricated can only generate longitudinal acoustic waves and they have the structure Au/Cr/ZnO/Au/Cr/sapphire as shown in figure 3.4. To apply the Mason model developed in section 3.4 in this particular configuration, the transfer matrices can be set as: $A_{\text{top electrode}}$=$A_{\text{Au}}A_{\text{Cr}}$, A_p=$A^{\text{L}}_{\text{ZnO}}$ and Z_{sb}=Z_{sapphire}, and the electromechanical coupling constant is set as k_{L}.

To facilitate the design of a transducer geometry that has maximum conversion efficiency, we now investigate the behaviour of transducers with various ZnO thicknesses t_{ZnO}, electromechanical constants k_{L}, electrode thicknesses and areas.

[1] A term confusingly used in the literature despite there being no real loss in power to heating effects.

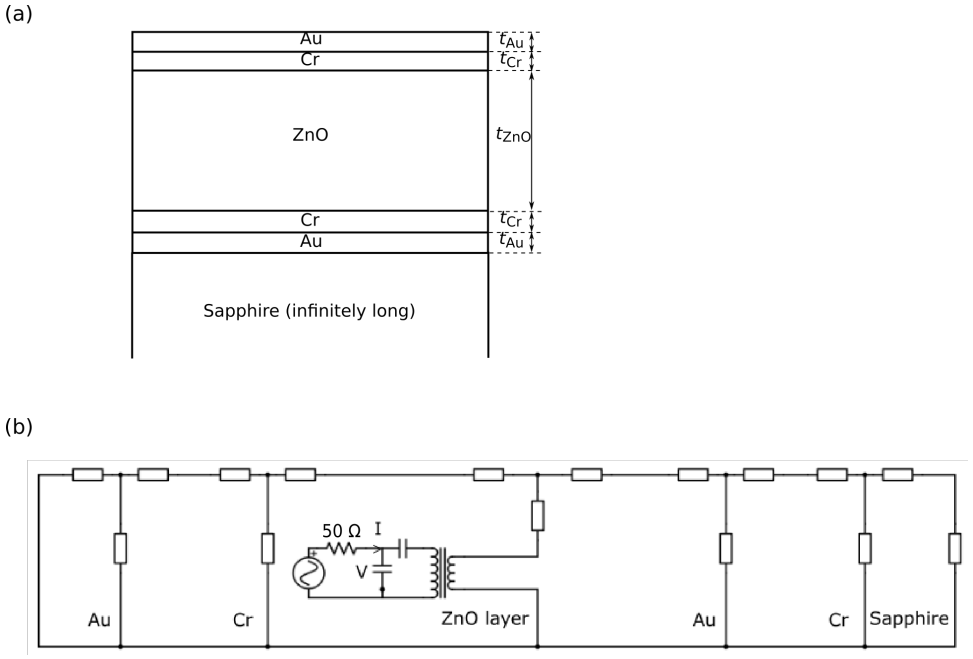

Figure 3.4: (a) The layer structure of the ZnO transducer considered in the Mason model, (b) Applying the Mason model to a transducer structure of Au/Cr/ZnO/Au/Cr/sapphire. In the diagram, t_{Au}, t_{Cr}, t_{ZnO} denote the thicknesses of the gold, chromium and ZnO layers respectively.

3.5.1 Transducer response as a function of ZnO thickness

Figure 3.5 illustrates the possible resonant modes of a BAW ZnO transducer deposited onto a flat substrate. In this configuration, the top electrode of the transducer is free to vibrate in space and so it is an antinode. Conversely, the bottom electrode is attached to a high impedance substrate so the acoustic wave is effectively pinned at this bottom electrode surface causing its amplitude of vibration to minimize. Hence, only odd modes can be excited. If we consider the ideal situation where the electrodes are infinitesimally thin and the acoustic impedance of the substrate is infinitely large, then the ZnO thickness t_{ZnO} is related to the resonant frequency f_0 by:

$$t_{\mathrm{ZnO}} = n\frac{\lambda_0}{2} = n\frac{v^{\mathrm{L}}_{\mathrm{ZnO}}}{2f_0} \tag{3.36}$$

where n is an odd integer greater than 1, i.e., 1, 3, 5, etc.; λ_0 is the wavelength at the resonant frequency and $v^{\mathrm{L}}_{\mathrm{ZnO}}$ is the velocity of the longitudinal acoustic wave in ZnO.

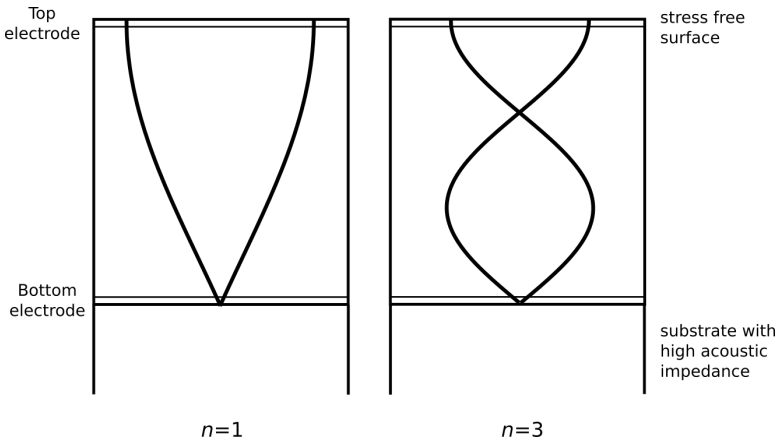

Figure 3.5: Odd modes are excited in a BAW ZnO transducer deposited on a substrate of high acoustic impedance. This is caused by the fact that the top electrode vibrates freely in space while the bottom electrode is pinned by the load imposed by the substrate.

Figure 3.6 demonstrates the frequency dependence of the predicted CL (dB) computed for various t_{ZnO}. The first noticeable result is the progressive increase in the resonant frequency (the point for which the CL is minimal) as the thickness of ZnO reduces. This agrees with the observation that the resonant frequency is inversely proportional to t_{ZnO} in equation (3.36). Moreover, for the same t_{ZnO}, successive peaks in CL are observed (corresponding to the harmonics) with fixed frequency gaps Δf in between. These gaps are closer for thicker ZnO films as predicted by the same equation.

Another interesting feature is the relationship between the minimum CL and t_{ZnO}. The minimum CL is the value of CL at the resonant frequency of the fundamental mode. One might intuitively expect the minimum CL to be the same regardless of the thickness of the ZnO film as long as k_{L} is the same. In fact, this is only true for the case when t_{ZnO} is greater than a threshold value. For t_{ZnO} less than the threshold, the insertion loss increases exponentially, and the CL rises to ∞ as thickness tends to zero. This feature can be seen in figure 3.7 in which the minimum CL is displayed for various t_{ZnO} given the same k_{L}.

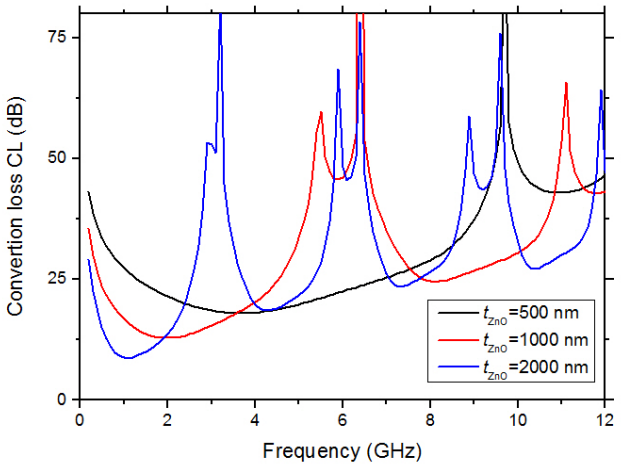

Figure 3.6: The theoretical CL of transducers with t_{ZnO}=500 nm, 1000 nm and 2000 nm. The fitting parameter used are t_{Cr}=4nm, t_{Au}=25 nm, electrode diameter=400 μm and k_L=0.25.

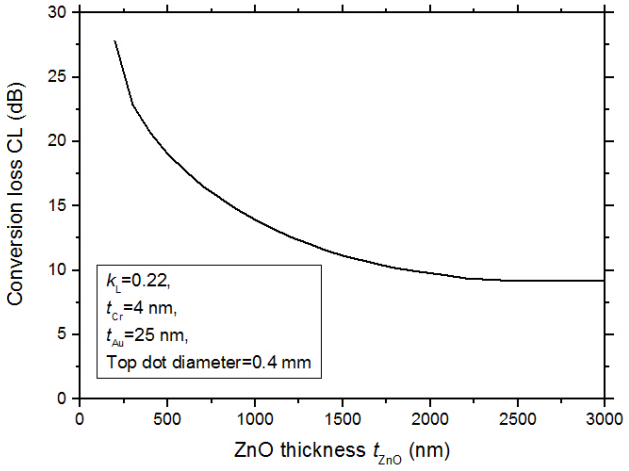

Figure 3.7: Using fixed fitting parameters: t_{Cr}=4 nm, t_{Au}=25 nm, electrode diameter=400 μm and k_L=0.22, the minimum CL is calculated as a function of ZnO thickness. It should be noted that there exists a certain threshold thickness (circa 2000 nm in the case illustrated) below which the CL increases exponentially. Above the threshold thickness, the CL takes its minimum value which is independent of the thickness.

3.5.2 Transducer response as a function of k_L

In section 2.2.2.2, we introduced the parameter k_L as a measure of the efficiency for conversion of electrical power into acoustic power. Figure 3.9 shows the minimum CL for the transducers at various k_L. As one would expect, the minimum

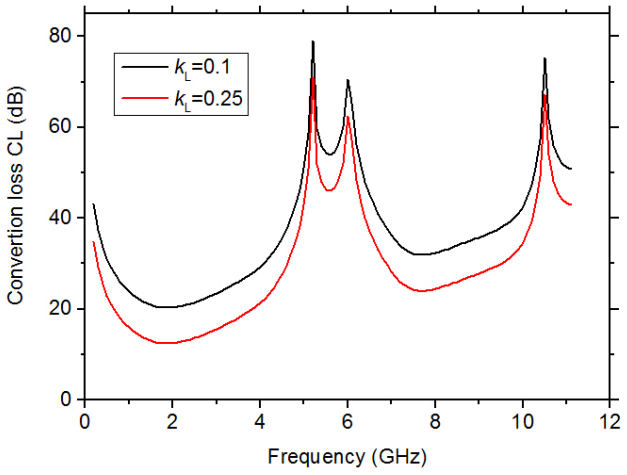

Figure 3.8: The theoretical CL of transducers with k_{L}=0.1, 0.25. The fitting parameter used are t_{Cr}=4 nm, t_{Au}=25 nm, electrode diameter=400 μm and t_{ZnO}=1060 nm.

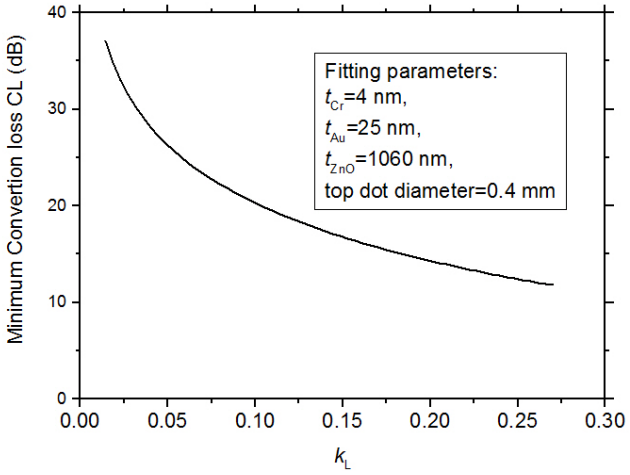

Figure 3.9: The minimum CL of the transducer at various k_{L}.

CL drops monotonically with k_{L}. In figure 3.8 , we have shown the frequency dependence of the CL for k_{L}=0.1 and k_{L}=0.25. It can be seen that k_{L} only influences the amplitude of the CL; the shape of the CL versus frequency curve remains unchanged.

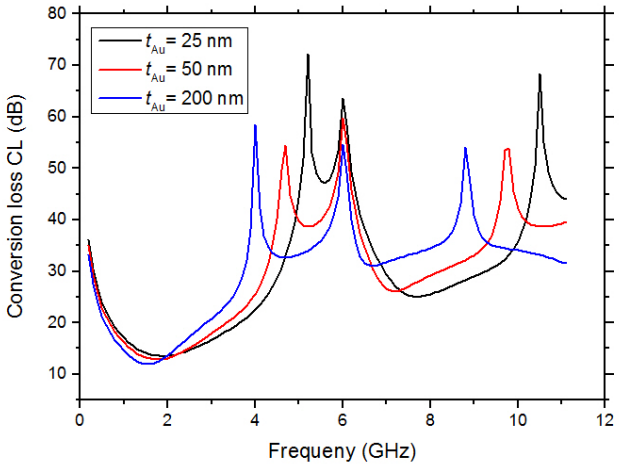

Figure 3.10: The theoretical CL of transducers with various Au electrode thickness t_{Au} of 25 nm, 50 nm and 100 nm. The fitting parameters used are t_{Cr}=4 nm, t_{Au}=25 nm, electrode diameter=400 μm and k_L=0.22.

3.5.3 Transducer response as a function of Au electrode thickness

In the prior analysis of section 3.5.1, we have calculated the resonant frequency in equation 3.36 by assuming that the electrodes are infinitely thin. In reality, electrodes have finite thicknesses, typically around tens of nanometers. Owing to the mass loading effect, the resonant frequency of a real ZnO transducer will be vastly reduced. This feature is predicted by the Mason model, for instance, a 1060 nm thick ZnO without the influence of mass loading should give rise to a resonant frequency of $\frac{6400}{2 \cdot 1060}$ GHz$\approx$ 3 GHz; whereas if the ZnO film is sandwiched by Au electrodes of 25 nm, the resonant frequency drops to around 2 GHz. Figure 3.10 depicts the impact of mass loading on the piezoelectric response of the transducer.

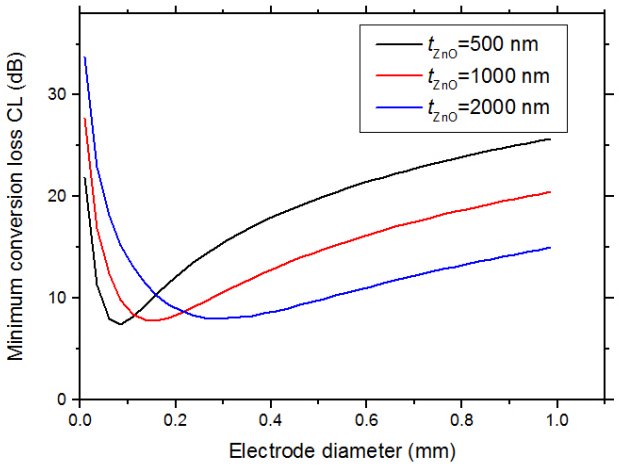

Figure 3.11: The influence of the top dot electrode diameter on the performance of the transducer

3.5.4 Transducer response as a function of the the top signal electrode area

It turns out that the top electrode area has a significant influence on the transducer performance. It is found that the transducer is best matched to the 50 Ω transmission line when the capacitance $C_0 = \frac{\epsilon A}{t_{\mathrm{ZnO}}}$ takes a value such that $Z_c = \frac{1}{j\omega C_0}$=-j50 Ω. This matching as a function of the top electrode area is illustrated in figure 3.11 (circular electrode shape is assumed). Hence, in order to design the most efficient transducer, one has to take the electrode size into consideration.

Chapter 4

Fabrication and characterization of ZnO ultrasonic transducers

In this chapter, we will describe how bulk acoustic wave (BAW) ZnO transducers are fabricated and characterized. We begin by presenting the design and layer structure of the transducers. The techniques required to deposit the electrodes and the ZnO thin films of the transducers will be discussed. We proceed to describe the assembly of the custom-built evaporation/sputtering plant and the fabrication protocols for producing high quality transducers. The transducers fabricated are characterized by two methods - X-ray diffraction and microwave electrical pulse-echo measurement. These measurements enable us to quantify the quality of the ZnO film and the conversion efficiencies of the transducers. We will explain in detail how these characterization methods work and how the various necessary pieces of equipment are set up to obtain accurate, reproducible measurements.

4.1 Design and layer structure of the fabricated transducers

In section 3.4 we described the typical structure of a BAW ZnO thin film transducer which takes the form of a ZnO thin film sandwiched between top and bottom electrodes; and the bottom electrode is in direct contact to the substrate. Now we will describe a slight adjustment to this design which simplifies the fabrication procedure.

In this new structure, there is an extra top ground electrode which has a much larger surface area than the top signal electrode. This top ground electrode couples strongly to the bottom electrode due to their mutual capacitance, so the bottom electrode is effectively grounded. Therefore, the transduction characteristics of these transducer can also be adequately described by the Mason model developed in section 3.4. Having such a top ground electrode avoids the need to use post-deposition lithography to expose the bottom electrode for grounding purposes. This saves time, eliminates cost and avoids the risk of the lithography procedures damaging the quality of the ZnO film.

Each electrode consists of two metallic layers. The first layer is Cr and is present to improve film adhesion and hence to avoid peeling of the film due to their intrinsic stress. The latter is a common problem in magnetron sputtered ZnO films. The second layer is made of Au, this layer provides a highly conductive and uniform layer for the ZnO films to deposit on. Ideally, the electrodes should be made as thin as possible to avoid mass loading. However, in reality, thin electrodes tend to be porous and less conductive. As a compromise between these two constraints, we have used electrodes with a Cr thickness of 4nm and a Au thickness of 25 nm. As previously discussed, the size of the top signal electrode is also important for optimizing the matching of the transducer to the 50 Ω transmission line. For

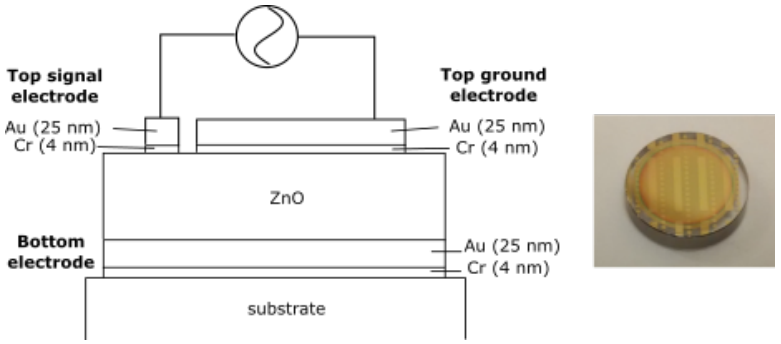

Figure 4.1: A schematic diagram showing the layer structure of the transducers fabricated. The large ground electrode at the top surface is electrically coupled to the bottom electrode via the big capacitance between them, so the bottom electrode is effectively grounded. Each electrode consists of two metal layers: Cr and Au. The Cr layer serves as an adhesive agent so that the film grown does not simply peel off from the substrate due to intrinsic stress while the Au film provides a highly conductive and uniform layer for the ZnO to deposit onto. The structure therefore takes the form of: substrate/Cr/Au/ZnO/Cr/Au.

example, for a transducer that has a ZnO thickness of 1000 nm, the optimum diameter is around 130 μm. However, due to the difficulty of depositing such small dots without the use of lithographic tools, all the transducers we have fabricated have top signal electrode diameters of 400 μm.

4.2 Deposition of ZnO transducers

In this section, we will discuss how a BAW ZnO transducer is fabricated practically. We begin by discussing how the substrate surfaces are prepared before the transducer is deposited. We then present the methods for depositing the metal electrodes and the ZnO thin film. The assembly and design of the custom-built evaporation/sputtering plant is described.

4.2.1 Surface preparation

The substrate needs to be very clean in order to produce high quality transducers. Any oil contaminants such as finger prints militate against good film adhesion.

They may also outgas and impair the chamber vacuum, thus degrading the c-axis texture of the ZnO films. The presence of these hydrocarbon molecules should thus be strenuously avoided. In order to guarantee a clean surface, the substrate is first immersed into a Decon bath (a highly effective surface active cleaning detergent) and is subsequently washed by water rinsing. The substrate is then transferred to a vacuum chamber for sputter-cleaning. This final step is crucial for producing a good quality surface on which to deposit: omitting this step invites the grown films to self-destruct by peeling.

At the microwave frequencies used, the acoustic wavelength is on the order of hundreds of nanometres, so the substrate also needs to be optically flat. This can be achieved by carefully polishing the substrate surface. Any scratch or non-uniformity that has a physical dimension comparable to the wavelength of the acoustic wave can lead to destructive interference of the transduced waves.

4.2.2 Depositing the metal electrodes using thermal evaporation

Both the Cr and Au components of the electrodes of the ZnO transducers are deposited using flash evaporation. The Cr and Au are first loaded into their respective tungsten evaporation boats. A high DC current is passed through the boat so that the metal to be deposited is heated. The boats are held at cherry-red temperature for around 10 seconds to drive off hydrocarbon contamination. The substrate is then unmasked and the boat abruptly raised to flash evaporate the films. The thickness of the deposited metal layer can be controlled by the mass of metals that are loaded into the boats. The top signal electrode and the top ground electrode can be deposited by evaporating the metals through a mask. The mask needs to be thin and should be placed as close to the sample surface as possible in

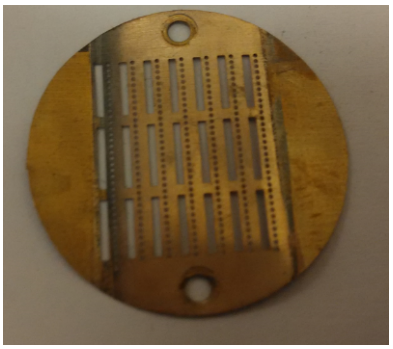

Figure 4.2: The diagram shows the evaporation mask used for depositing top electrodes.

order to avoid misalignment of the Cr and Au layers. Figure 4.2 shows the mask used for the fabricated ZnO transducers.

4.2.3 Depositing the ZnO thin film using magnetron sputtering

Magnetron sputtering can be performed using either a DC or an RF electrical supply. DC sputtering is generally used for target that are conductive whereas RF sputtering can be used for sputtering materials that are either conducting or insulating. ZnO is a semiconductor so our system operates with an RF system at 13.56 MHz which applies an oscillating voltage to the target relative to the metal walls of the chamber. The electric field thus generated acts as a trap for any free electrons[1] in the chamber and imparts an oscillating kinetic energy to them in one dimension. Quasi-elastic collisions with gas atoms feed this energy progressively into the other two dimensions where it accumulates until the electron acquires enough energy to ionise a gas atom, thereby triggering another identical process and hence a chain reaction which then maintain the sputtering plasma. The positive-going excursion of the target suck in burst of highly mobile electrons in the plasma. The target thus set at a negative DC so the positive ions are strongly attracted towards the target surface. They thus bombard the target and transfer

[1] Usually caused by cosmic radiation.

their momentum to the ejected surface atoms. These ejected atoms migrate to the adjacent substrate and a thin film is produced as these atoms reform on the substrate surface.

Sputtering is performed in a vacuum chamber at a working pressure that is typically in the range from 1 mtorr to 50 mtorr. The low pressure allows the sputtered particles to travel directly to the substrate without hitting other gas molecules on the way. During the sputtering process, ions and molecules in the sputtering plasma eventually de-excite emitting photons that give rise to a glow that enables the plasma location and characteristics to be visually monitored. A satisfactory ZnO sputter discharge in an Ar/O_2 gas mixture has an easily recognised lilac glow.

Both the DC and RF sputtering can be used to deposit ZnO film. In the DC mode, Zinc target is used with a pure oxygen working gas. This is known as reactive magnetron sputtering. The control of the stoichiometry of the ZnO films is difficult in this set up and the sputtering rate is significantly lower due to the use of an oxygen plasma. The ZnO film described by this thesis were made by RF sputtering of a ZnO target formed from compressed ZnO powder. It is commonly known that [41] the sputtered particles from a ZnO target contain an excess of Zn atoms over oxygens, so Ar/O_2 is used as a working sputtering gas to oxidize any remnant Zn atoms in order to achieve good film stoichiometry.

A cylindrical magnetron was in-house designed and constructed for ZnO sputter deposition (see figure 4.3 and 4.4). The design has the following features:

1. Magnets of opposite polarities were arranged on a mild steel back plate as illustrated in figure 4.3. At a certain radial distance r from the centre, the B-field produced is parallel to the target surface. Since the electrons drift in the $E \times B$ direction, these electrons are confined in the ring of radius r near the target surface where the plasma is at its densest. This region of the

magnetron is known as the racetrack and it corresponds to maximum target erosion.

2. Strong N42 neodymium iron boron (NdFeB) permanent magnets were used for plasma confinement in order to generate a dense plasma.

3. An unbalanced magnet configuration (i.e. not all B-field flux lines return to the magnetron) was chosen. This is achieved by making the area of the single-ring piece and the central magnet unequal. Magnets of exactly the right dimensions are difficult to find and so we implemented it with a series of button magnets arranged in a ring pattern. The effect of the unbalanced magnetron is that the B-field flux leakage lines guide the plasma to hit the surface of the substrate which is placed directly above the magnetron. This ion and secondary electron bombardment is thought to promote surface diffusion and hence better film growth in sputtering.

4. The ratio of the target diameter to the thickness is kept as high as possible. This geometry tends to enhance the field near the racetrack, and thus giving stronger plasma confinement. It has the disadvantage that the thin targets necessarily employed have a limited lifetime. A large diameter target is therefore desirable to allow a target thickness of at least 5 mm and hence a reasonable working life. The ZnO target that we have used has a diameter of 89 mm and a thickness of 6.6 mm.

5. A thermally and electrically conducting silver-loaded epoxy glue was used to attach the back of a copper disk which was soldered onto a brass annulus. This whole unit can be fitted to the magnetron assembly using two screws, this allows the targets to be conveniently interchangeable.

6. The magnetron is water cooled to avoid overheating of either the target material (causes cracking) or the magnet (residual magnetization degrades

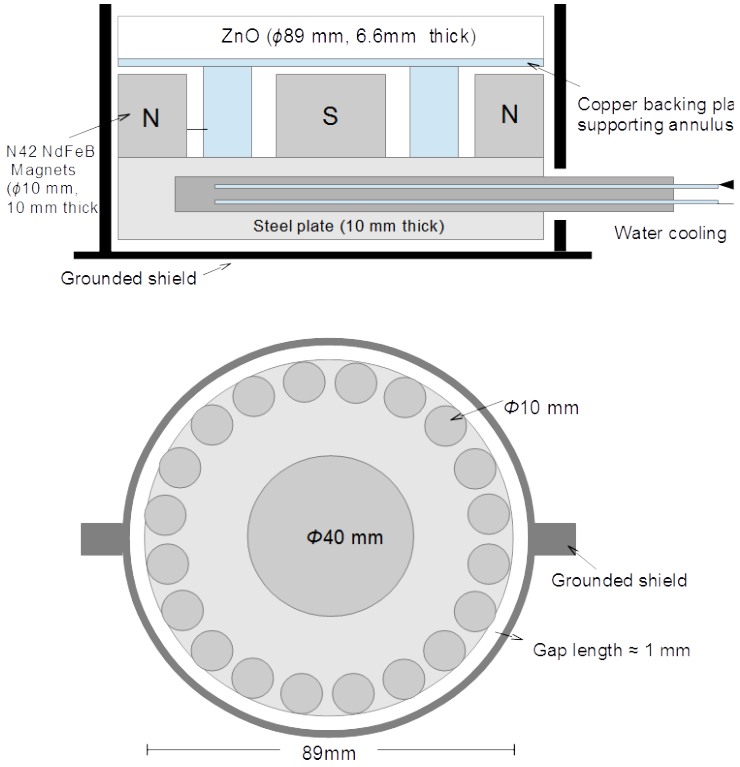

Figure 4.3: The schematic of the magnetron.

at high temperature). A vacuum gap is engineered between the annulus and the NdFeB to avoid heat transfer from the hot target.

7. A grounded shield was put in place close to the target to avoid plasma from striking at the back of the magnetron. This prevents unwanted sputtering and thus minimizes the impurities introduced to the fabricated film.

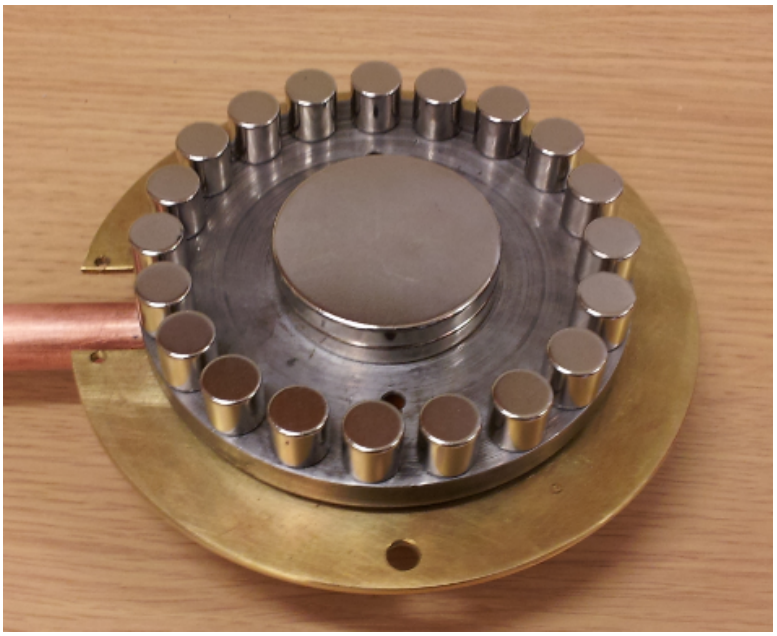

Figure 4.4: The inside of the ZnO magnetron and the spatial arrangement of the NdFeB magnets.

4.2.4 The assembly of a custom built evaporation/sputtering plant

The setup of the custom-built sputtering plant is depicted in figure 4.5. The cylindrical stainless steel vacuum chamber of diameter 8.5" and height 11.5" is supported on an aluminum table. There are multiple $\frac{1}{2}$" feedthroughs on the side of the chamber and a 30 mm thick glass plate is used to seal the top of the chamber allowing good visual monitoring of the deposition processes. The vacuum is provided by a E06 oil diffusion pump which is backed by a rotary pump, and a liquid nitrogen trap is installed to prevent oil backstreaming. Sputtering gas (Ar/O_2 mixture) can be introduced into the chamber via a leak valve. The main chamber and the diffusion pump may be isolated by a butterfly valve, which is used for controlling the gas load of the pump intake. To reduce water contaminant of the gas admitted, the mixture goes through a Peltier cooling device before entering the chamber. A Meissner trap is also installed inside the chamber to selectively pump any residual water vapour: the reducing effect of the hydrogen radials caused by

plasma cracking of water molecules is thought to suppress good thin film growth. The magnetron is mechanically installed via the side feedthrough port and sits near the centre of the chamber. It is connected electrically to the 13.56 MHz RF power generator via a matching network. In addition to magnetron sputtering, the chamber is also capable of thermal evaporation. As shown in figure 4.6, the high current feedthroughs enter via the chamber base plate to power the evaporation boats. The capability of carrying out thermal evaporation and sputtering without the need to break vacuum in between is essential for high quality transducer fabrication. In order to control access of the sputtered or evaporated material to the substrate, the latter may be displaced between two positions where it is respectively exposed and masked. This feature is enabled by an externally operated sliding vacuum feedthrough.

4.2.5 The fabrication protocol

In this section, we present the recipe for fabricating ZnO transducers using our custom-built evaporation/sputtering plant. The protocol (illustrated in figure 4.7) is as follows:

1. Clean the substrate with 5% Decon solution and thoroughly rinse with water.
2. Load the substrate into the chamber, and bake the chamber for at least 6 hours to remove water contamination
3. Meanwhile the chamber is pumped down to below 2×10^{-5} mbar.
4. Allow the chamber to cool down to ambient temperature.
5. Fill the Meissner trap with liquid nitrogen to pump the residual water and oil contaminants.

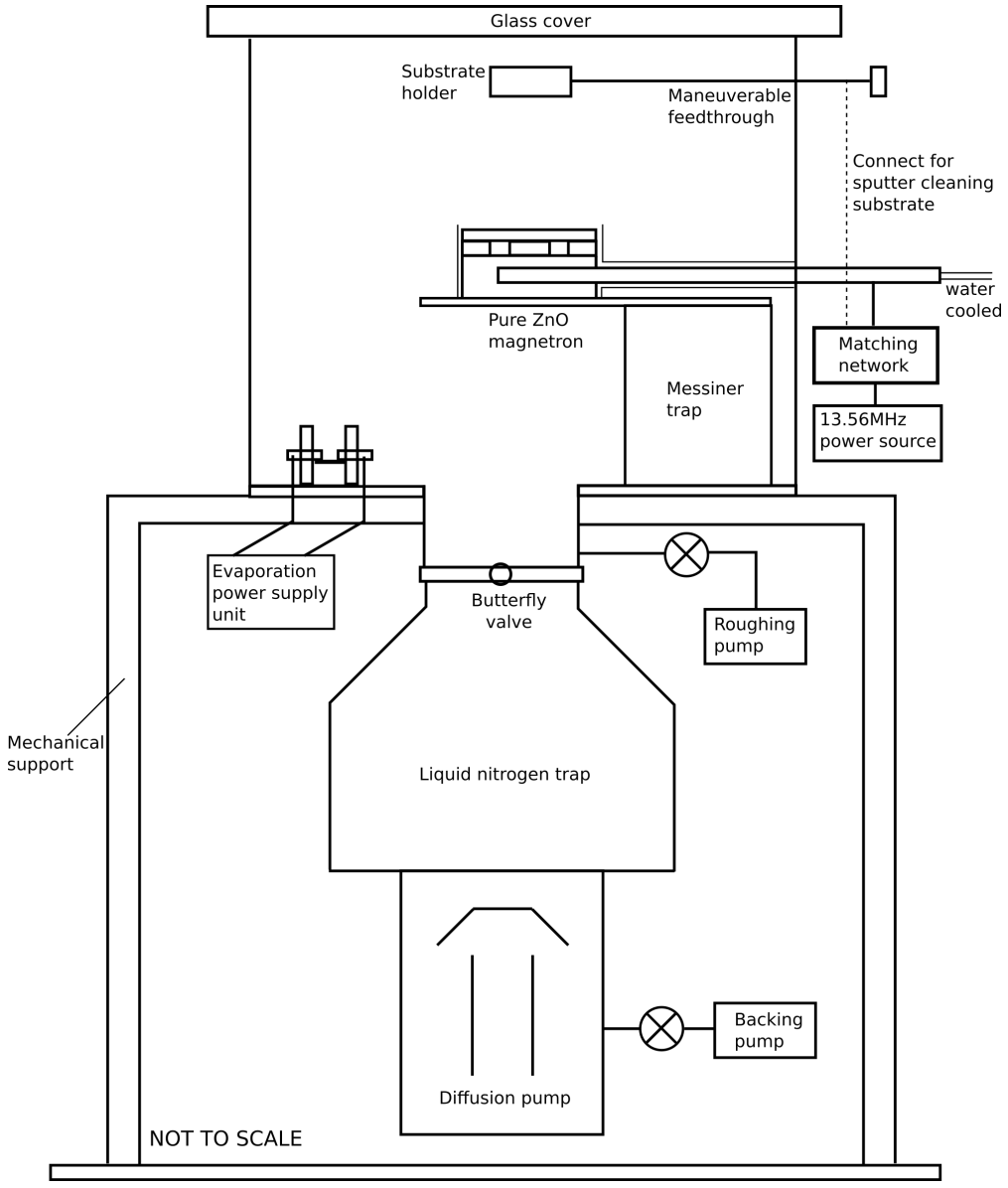

Figure 4.5: A schematic diagram showing the set-up of the sputtering plant.

6. Switch on the Peltier cooler in the gas input line. After it has been cooling for 10 minutes, allow Ar/O_2 gas to enter the chamber via the leak valve. (The Peltier is to condense any the water contaminant in the input gas line.)

7. Connect the electrically floating substrate holder to the RF source, sputter clean the substrate for 7 minutes at 30 W at 4 μbar (having adjusted the matching network for maximum power). This cleans and raises the temperature of the substrate to about 150 °C.

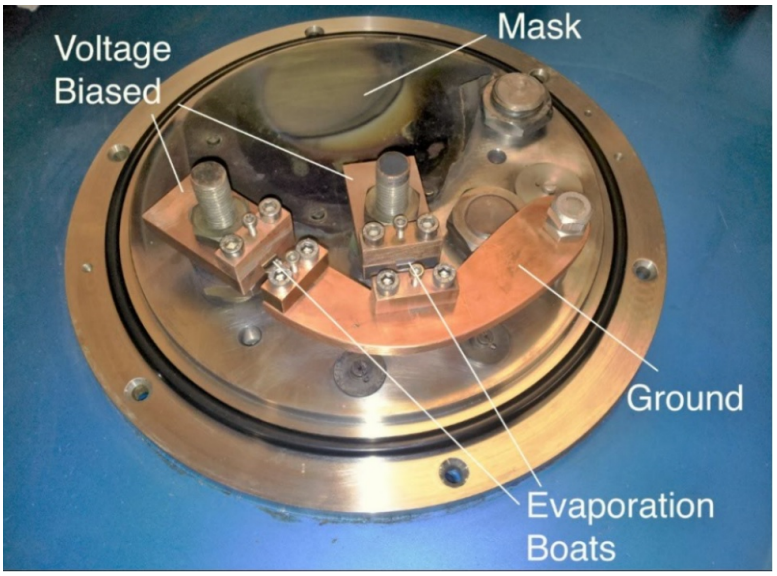

Figure 4.6: The base plate of the sputtering plant, highlighting on the making of the evaporator.

8. Cut off the gas feed leak valve, pre-cook the metal charge to drive off contaminant, then expose the substrate and evaporate 4 nm of Chromium (corresponds to a charge of ≈ 0.0035 g) and then 25 nm of Gold ($\approx$0.05 g) onto the substrate.

9. Reopen the gas feed leak valve, ion clean the Gold film for 15 seconds at 20 W at 4 μbar .

10. Maneuver the substrate so that it faces the centre of the magnetron. Connect RF source to magnetron, excite the plasma at the desired sputtering conditions to sputter ZnO onto the substrate (require re-tuning of the matching network).

11. Depending on the length of the sputtering operation, refill the Meissner trap once every 30 minutes to avoid warmup of the trap and release of the trapped contaminants.

12. After finishing the deposition, wait for at least 3 hours before opening the chamber via a nitrogen line (if humid air accesses the chamber while the trap is cold, water condenses on the trap, so extended pump-down times

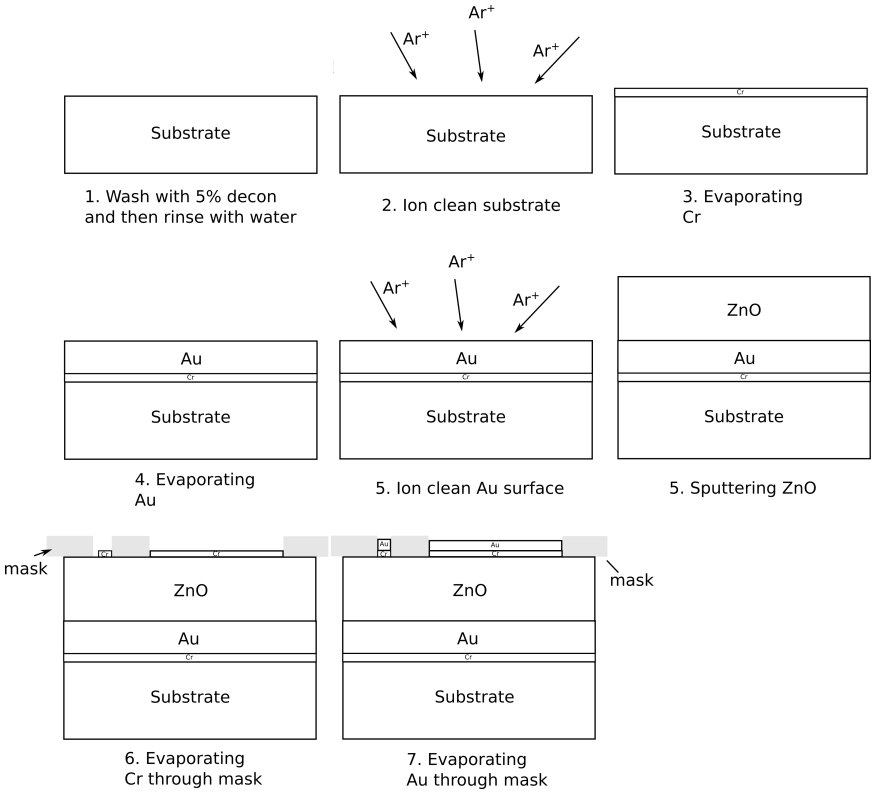

Figure 4.7: An illustration on the fabrication procedures

is required when the plant next operates). As an extra precaution against water adsorption, the plant is vented with dry nitrogen when it is eventually opened.

13. Install the mask onto the substrate holder, and load it onto the chamber again.

14. Pump down the chamber to below 5×10^{-5} mbar.

15. Evaporate 4 nm of Cr (≈ 0.0035 g) and then 25 nm of Au (≈ 0.05 g) onto the substrate.

16. Evacuate chamber and retrieve the sample deposited.

17. The chamber is kept under vacuum when it is not in use. This is to avoid ingress of water vapour and oil contaminants.

4.3 X-ray characterization

4.3.1 Basics of X-ray diffraction

X-ray crystallography is a non-destructive technique for analyzing the structure of crystalline materials. The technique involves irradiating the crystal of interest with a monochromatic X-ray beam and analysing the detected diffraction pattern in which the information about the structural properties of the crystal is encoded.

Consider the diffraction of an incoming X-ray beam by a set of lattice planes of interplanar spacing d. The beam makes an angle θ with the planes as shown in figure 4.16. The path difference between the beams scattered by adjacent planes is then $2d\sin\theta$. At certain angles θ, this path difference is exactly equal to the X-ray wavelength λ (or multiple of the wavelengths) and the diffracted beams constructively interfere giving a strong diffracted signal. This condition can be expressed mathematically by Bragg's law of diffraction.

$$n\lambda = 2d\sin\theta. \tag{4.1}$$

In order to label the lattice planes in a systematic way, the Miller index system is used. The Miller indices describing a family of planes are determined as follows. The crystal lattice is defined by the three lattice vectors $\mathbf{a_1}$, $\mathbf{a_2}$ and $\mathbf{a_3}$. A lattice point is arbitrarily chosen as the origin and the member of the family of planes that passes closest to this origin is determined. This plane intersects the vectors $\mathbf{a_1}$, $\mathbf{a_2}$ and $\mathbf{a_3}$ drawn from the origin at positions $\frac{\mathbf{a_1}}{h}$,$\frac{\mathbf{a_2}}{k}$ and $\frac{\mathbf{a_3}}{l}$. The Miller indices correspond to the family planes is then (hkl). The interplanar spacing between adjacent (hkl) planes is d_{hkl}.

Bragg's approach to diffraction is instructively helpful, but of little use for a deeper understanding of diffraction. A much more powerful and versatile tool involves

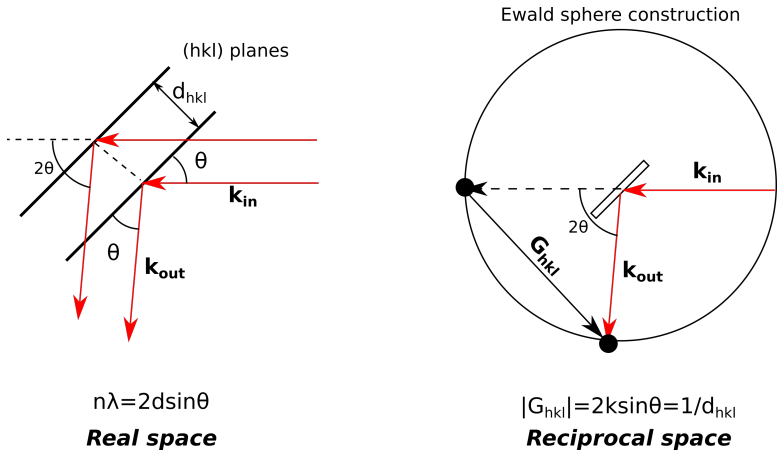

Figure 4.8: The diagram illustrates the Bragg and Laue conditions for X-ray diffraction in the real and reciprocal spaces respectively. In real space, an X-ray beam with wavevector $\mathbf{k_{in}}$ is incident on the (hkl) planes with an angle θ. The incident beam is diffracted by the lattice plane causing the beam to travel away from the crystal with a wavevector $\mathbf{k_{out}}$. Strong diffraction signals are detected when the diffracted beams constructively interfere (i.e. Bragg's condition), and this happens when $n\lambda=2d_{hkl}\sin\theta$. In reciprocal space, the Laue condition is satisfied when the scattering vector $\mathbf{\Delta k} = \mathbf{k_{in}} - \mathbf{k_{out}}$ coincides with the reciprocal lattice vector $\mathbf{G_{hkl}}$. The circle represents an Ewald sphere with radius $k = \frac{2\pi}{\lambda}$ which is drawn to touch the reciprocal lattice point that is chosen as the origin of the reciprocal space. It thus traces out all possible $\mathbf{k_{out}}$ for a given $\mathbf{k_{in}}$. The Laue condition is fulfilled if the surface of the Ewald sphere touches a second reciprocal lattice point (In addition to the reciprocal lattice point at the origin.)

the application of reciprocal space. The reciprocal lattice vectors $\mathbf{G_{hkl}}$ are defined as:

$$\mathbf{G_{hkl}} = h\mathbf{b_1} + k\mathbf{b_2} + l\mathbf{b_3} \tag{4.2}$$

and they are derived from the real space lattice vectors by the relation:

$$\mathbf{b_i} = 2\pi \frac{\mathbf{a_j} \times \mathbf{a_k}}{\mathbf{a_i} \cdot (\mathbf{a_j} \times \mathbf{a_k})}. \tag{4.3}$$

It can be shown that $\mathbf{G}$ is orthogonal to the real space lattice planes (hkl) and the real space interplanar distance d_{hkl} is given by:

$$d_{hkl} = \frac{2\pi}{|\mathbf{G_{hkl}}|}. \tag{4.4}$$

Bragg's law (derived from purely real-space consideration) can therefore be rewritten as:

$$\mathbf{G_{hkl}} = \Delta\mathbf{k} \tag{4.5}$$

and

$$|\mathbf{G_{hkl}}| = 2k_0 \sin\theta \tag{4.6}$$

where $k_0 = \frac{2\pi}{\lambda}$ is the wavenumber of the X-ray and $\mathbf{\Delta k} = \mathbf{k_{out}} - \mathbf{k_{in}}$ is the X-ray scattering vector connecting the incident and diffracted X-ray wavevector. So this means that strong diffraction signals are detected when the scattering vectors coincide with reciprocal lattice vectors; this is known as the Laue condition. All scattering vectors satisfying this condition may be found by the Ewald sphere construction as illustrated in figure 4.8.

In this work, we used X-ray diffraction to analyse our ZnO thin films so as to determine properties such as the crystal structure, preferred orientation of crystallites, crystallite sizes, angular distribution of crystallite orientation and film stress.

4.3.2 Lattice planes and the corresponding reciprocal lattice vectors of c-axis oriented ZnO polycrystalline grains

As noted in the previous section, a family of perfect lattice planes (hkl) is represented by a point whose position vector is the reciprocal lattice vector $\mathbf{G_{hkl}}$. We can now extend this concept to model crystal impurities in reciprocal space.

In the idealised case when all the c-axes of the grains point normal to the substrate, the {002} planes [2] correspond to point in reciprocal space whose position vector

[2]For c-axis oriented ZnO thin films, the lattices planes that are parallel to the substrate are the (00l) planes. The (001) diffraction peak is systematically absent and the first observed (00l) diffraction order is (002).

is $0\mathbf{b_1} + 0\mathbf{b_2} + 2\mathbf{b_3}$ as depicted in figure 4.9a.

Although the ZnO films grown are highly c-axis oriented (as we will demonstrate later in section 5.3.1), inevitably the c-axes of some grains have a slight misorientation relative to the substrate normal direction. The misorientation angle δ is typically normally distributed as shown in figure 4.10. In a real space, one can visualise the misoriented lattice planes as lying perpendicular to cones that make an angle δ with the substrate normal as seen in figure 4.9b(ii). In reciprocal space, the crystallite misorientation is represented by a smearing out of the (0,0,2) reciprocal lattice point to form a section of a spherical surface of radius $|\mathbf{G_{002}}|=2k_0 \sin\theta$ (see figure 4.9b(iii)) that subtends an angle δ at the origin. Of course this model assumes a constant lattice parameter d_{002}. In fact, the lattice parameter also varies very slightly throughout the film, the reciprocal lattice point representing the (002) planes in reciprocal space smeared out into a volume rather than just a surface.

4.3.3 Scanning modes

In a typical X-ray diffraction set-up as shown in figure 4.11, X-rays produced by a fixed source are directed to a sample that is attached on a sample bed and the diffracted beams are collected using a detector. Both the sample bed and the detector can vary in position. Conventionally, the angle between the incident X-ray beam and the sample bed surface is defined as ω and the angle between the incident X-ray beam and the detector is 2θ.

In this section, we will describe various scanning modes including $\theta/2\theta$, $2\theta/\omega$ and ω scans and we will discuss how these scans can provide useful structural information about the c-axis oriented ZnO thin films.

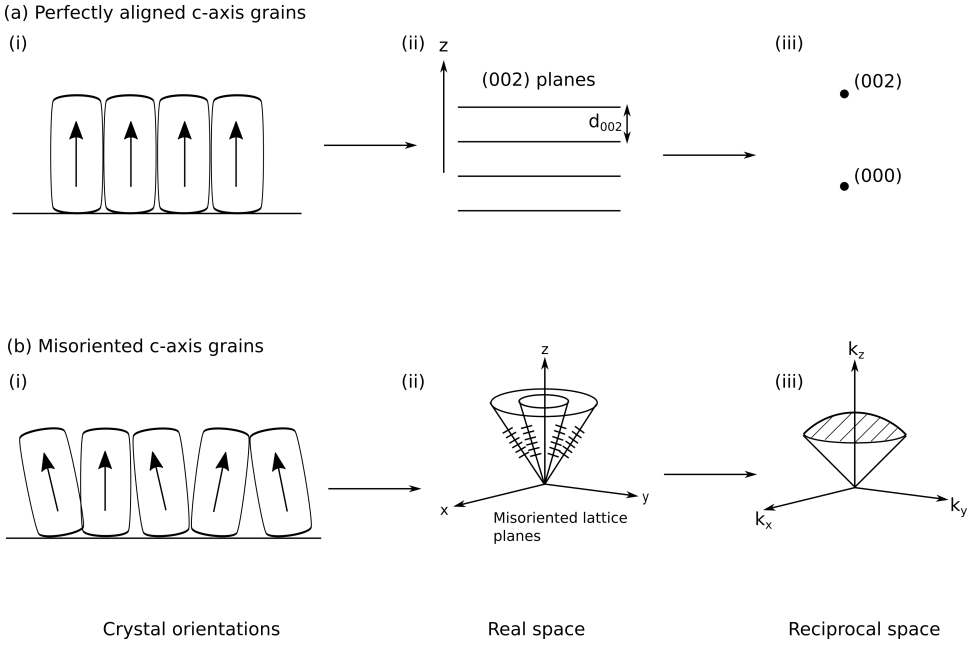

Figure 4.9: (a) Case when all c-axis grains points parallel to the substrate normal: (002) planes in real space are represented by a single vector in reciprocal space. (b) Case when the c-axis grains are slightly misoriented and lie at angle δ to the substrate normal: the misoriented lattice planes lie perpendicular to cones that make an angle δ with the substrate normal; these planes can be represented by a section of spherical surface in reciprocal space.

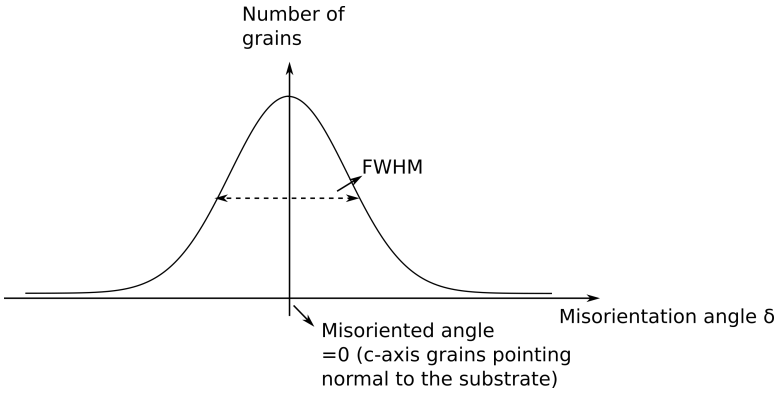

Figure 4.10: The normal distribution of misorientation angle δ. When δ=0, the c-axis of the grains point parallel to the substrate normal.

4.3.3.1 Gonio ($\theta/2\theta$ scan)

The $\theta/2\theta$ scan is a coupled scan in which both sample bed and detector move simultaneously so that ω=θ. When the angle θ satisfies the Bragg condition, a diffraction peak is detected if {002} lattices planes are present in the ZnO thin films grown.

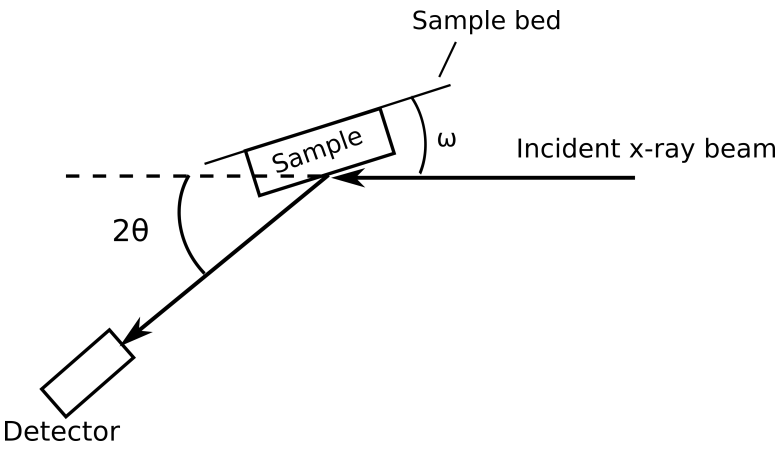

Figure 4.11: A typical X-ray diffraction set up: ω= angle between the incident X-ray beam and the sample bed surface; 2θ= angle between the incident X-ray beam and the detector.

The $\theta/2\theta$ scan can be more conveniently understood in reciprocal space. Figure 4.12 illustrates how the incident $\mathbf{k_{in}}$ and diffracted wavevectors $\mathbf{k_{out}}$ change as θ varies. $\mathbf{k_{in}}$ lies in the dotted circle of radius $k_0=\frac{2\pi}{\lambda}$ centred at the reciprocal lattice point (0,0,0). As θ increases, the angle 2θ between $\mathbf{k_{in}}$ and $\mathbf{k_{out}}$ opens up and the tip of the $\mathbf{k_{out}}$ vector tracks along the dotted line until it coincides with the (0,0,2) reciprocal lattice point, in which case Bragg's condition is satisfied leading to a peak to the detected diffraction pattern. Suppose the sample is misaligned with the sample bed at an angle Δ. The dotted line then misses the (002) reciprocal lattice point and so for a perfect crystal, no diffraction signal is observed.

Now, suppose that the film is imperfect and comprises an ensemble of crystallites whose c-axes have a spread of angles relative to the substrate normal. In figure 4.12, the arc encompassing the (0,0,2) reciprocal lattice point represents the locus of the tips of the reciprocal lattice vectors that correspond to the (002) planes of the misoriented crystallites. If we misalign the sample by an angle Δ relative to the sample bed, the tip of the $\mathbf{k_{out}}$ vector will still track through the arc and a diffraction signal will be observed provided that the angular misorientation represented by the arc exceeds the misalignment angle Δ.

It should be noted that the diffraction peak is never infinitely sharp even for a

perfect crystal structure due to broadening caused by instrument limitations (finite slit sizes) and finite crystallite sizes (the diffracted beam from different crystallites are incoherent with each other). The lower limit of the crystallite size (τ) can be estimated using the Scherrer equation,

$$\tau = \frac{K\lambda}{\beta \cos\theta} \tag{4.7}$$

where β is the full width half maximum (FWHM) of the peak in radian, and K is a shape factor $\approx$0.9.

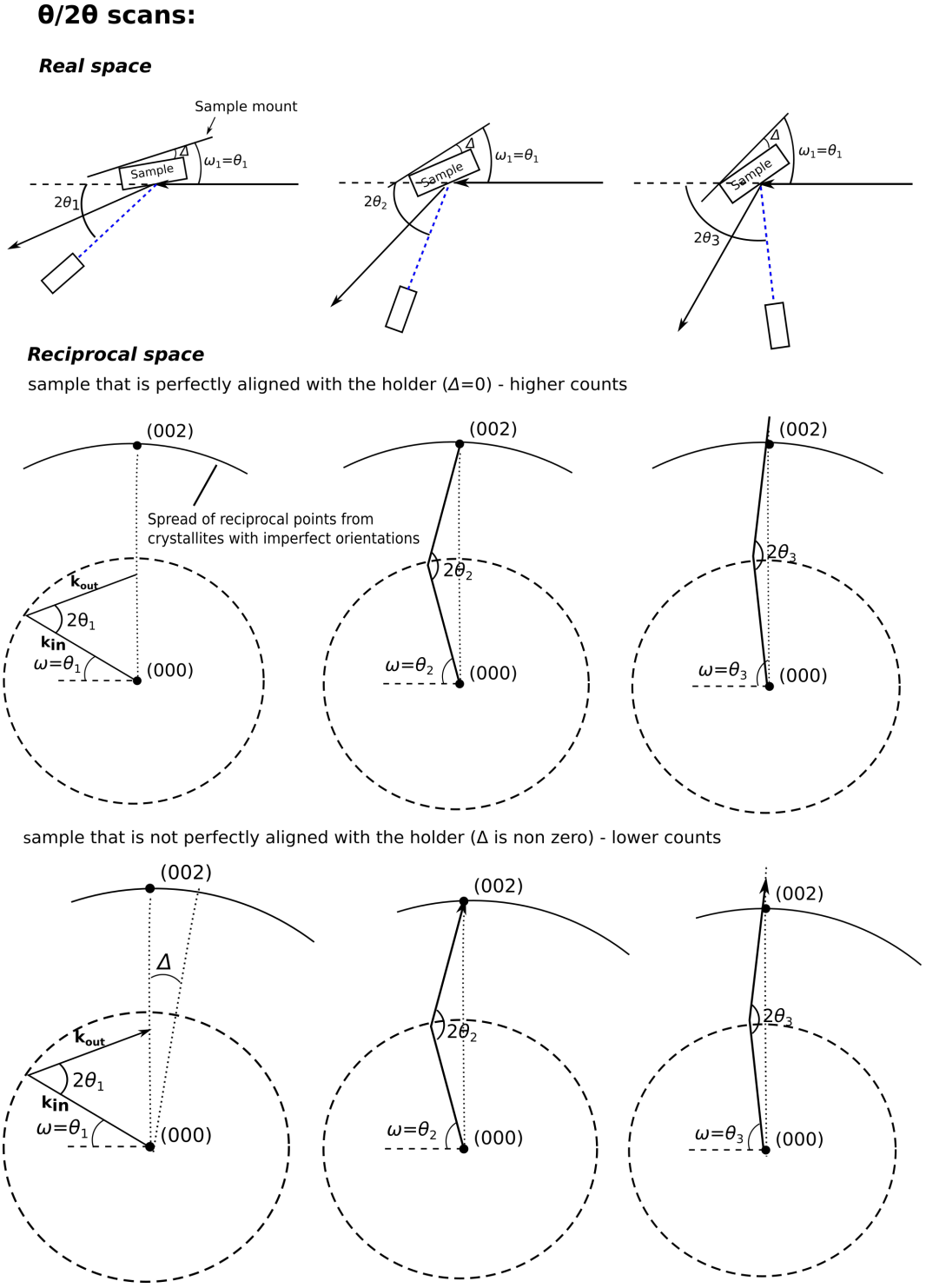

Figure 4.12: This diagram illustrates how the incident $\mathbf{k_{in}}$ and diffracted wavevectors $\mathbf{k_{out}}$ change as θ varies in the $\theta/2\theta$ scan. In this scan mode, $\omega{=}\theta$. In reciprocal space, $\mathbf{k_{in}}$ stays within the dotted circle as θ changes; $\mathbf{k_{out}}$ is at an angle 2θ with respect to $\mathbf{k_{in}}$ and the tip of the $\mathbf{k_{out}}$ vector tracks along the dotted line during the scan. Bragg's condition is satisfied when the tip of $\mathbf{k_{out}}$ coincides with the (0,0,2) point in the reciprocal space. It can be seen clearly in the real space that if there is a misalignment between the sample and the sample bed, the detector will be mispositioned with respect to the diffracted beam and the tip of $\mathbf{k_{out}}$ will miss the (002) point. However, if the crystallites being analysed have a spread of misalignment angles relative to the substrate normal, a diminished diffraction peak will still be observed as long as the angular spread of the misorientation is larger than the misalignment angle Δ.

4.3.3.2 $2\theta/\omega$ scan

The $\omega/2\theta$ scan is essentially the same as the $\theta/2\theta$ scan, the only subtle difference is that there is an offset in ω to compensate for the alignment error of the sample, i.e., $\omega = \theta + \Delta$. Doing this aligns the diffracted beam with the detector position 2θ when Bragg's condition is satisfied, and the maximum peak signal is again detected. In reciprocal space, the addition of Δ to ω in the $\omega/2\theta$ scan moves the track of the tip of the $\mathbf{k_{out}}$ vector by exactly the angle Δ that is necessary if it is to find the misaligned (0,0,2) reciprocal lattice point. For an imperfect crystal comprising an ensemble of grains with a range of c-axis misalignments, $\mathbf{k_{out}}$ again hits the centre of the arc and delivers maximum X-ray signal.

In order to carry out this scan mode, the sample stage must be designed such that it can offset any given random misalignment. Often it can be achieved by allowing the sample stage to rotate with respect to ω and ψ, where ω is as defined previously, and ψ is the angle of rotation with respect to the axial direction. The angle ϕ, defined as the angle of rotation with respect to the azimuthal direction, does not need to be corrected if the thin film sample of interest is uniform. The angles ω, ψ, ϕ are illustrated in figure 4.15.

If the alignment error is satisfactorily compensated, the height of the diffraction peak can be used as a measure for quantifying the strength of c-axis orientation for ZnO films.

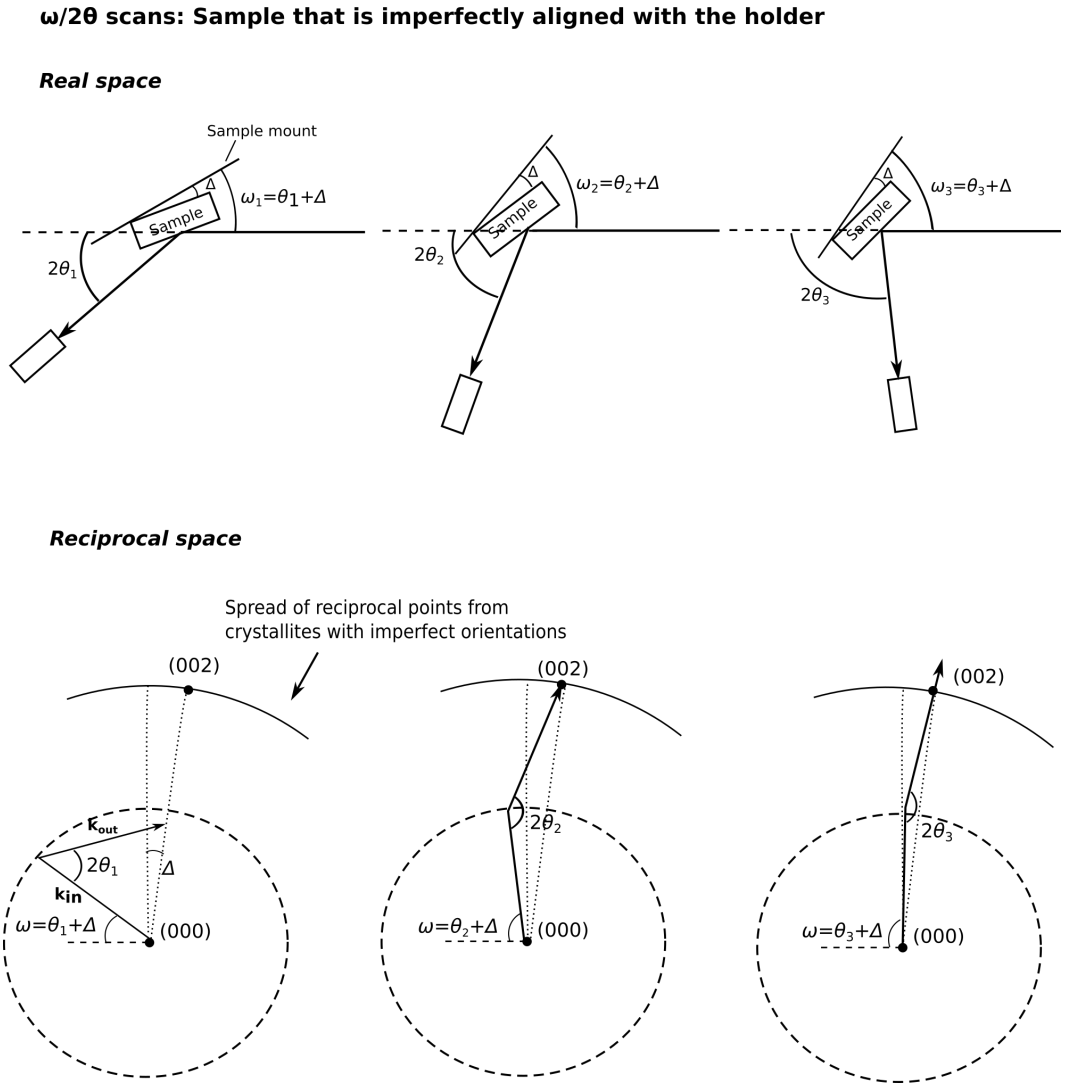

Figure 4.13: This diagram illustrates how the incident $\mathbf{k_{in}}$ and diffracted wavevectors $\mathbf{k_{out}}$ changes as θ varies in the $\omega/2\theta$ scan. The mechanics for which $\mathbf{k_{in}}$ and $\mathbf{k_{out}}$ changes is essentially the same as that of the $\theta/2\theta$ scan except the fact that an offset is artificially introduced to ω such that $\omega = \theta + \Delta$. This compensates the alignment error of the sample so that maximum diffraction signal can be obtained.

4.3.3.3 ω scan (Rocking curve)

In the ω scan, the sample bed rotates (ω is varied) while the detector position (2θ) is held fixed. The value of 2θ is set to satisfy Bragg's condition for the specific lattice planes of interest. So, for example to study the {002} planes in c-axis oriented ZnO thin films, 2θ is set to 2θ=2arcsin$\frac{\lambda}{2d_{002}}$.

Referring to figure 4.14, in a rocking curve scan, $\mathbf{k_{in}}$ and $\mathbf{k_{out}}$ respectively trace out the red circle and black dotted circle in the reciprocal space. Diffraction signals are detected when the tip of $\mathbf{k_{out}}$ coincides with the black arc (which represents the reciprocal vectors for misoriented lattice planes as discussed previously). The signal will peak when the tip of $\mathbf{k_{out}}$ hits the centre of the arc. From figure 4.14, it is clear that if the sample is misaligned by an angle Δ, the diffraction peak will also be shifted by Δ.

The full width half maximum (FWHM) of the ω scan therefore provides us with information about the angular distribution of c-axis planes. The offset of the peak from ω=θ = arcsin$\frac{\lambda}{2d_{002}}$ indicates the misalignment angle. Assuming that the peak measured is Gaussian, the total volume of c-axis crystallite is proportional to the product (FWHM×peak height).

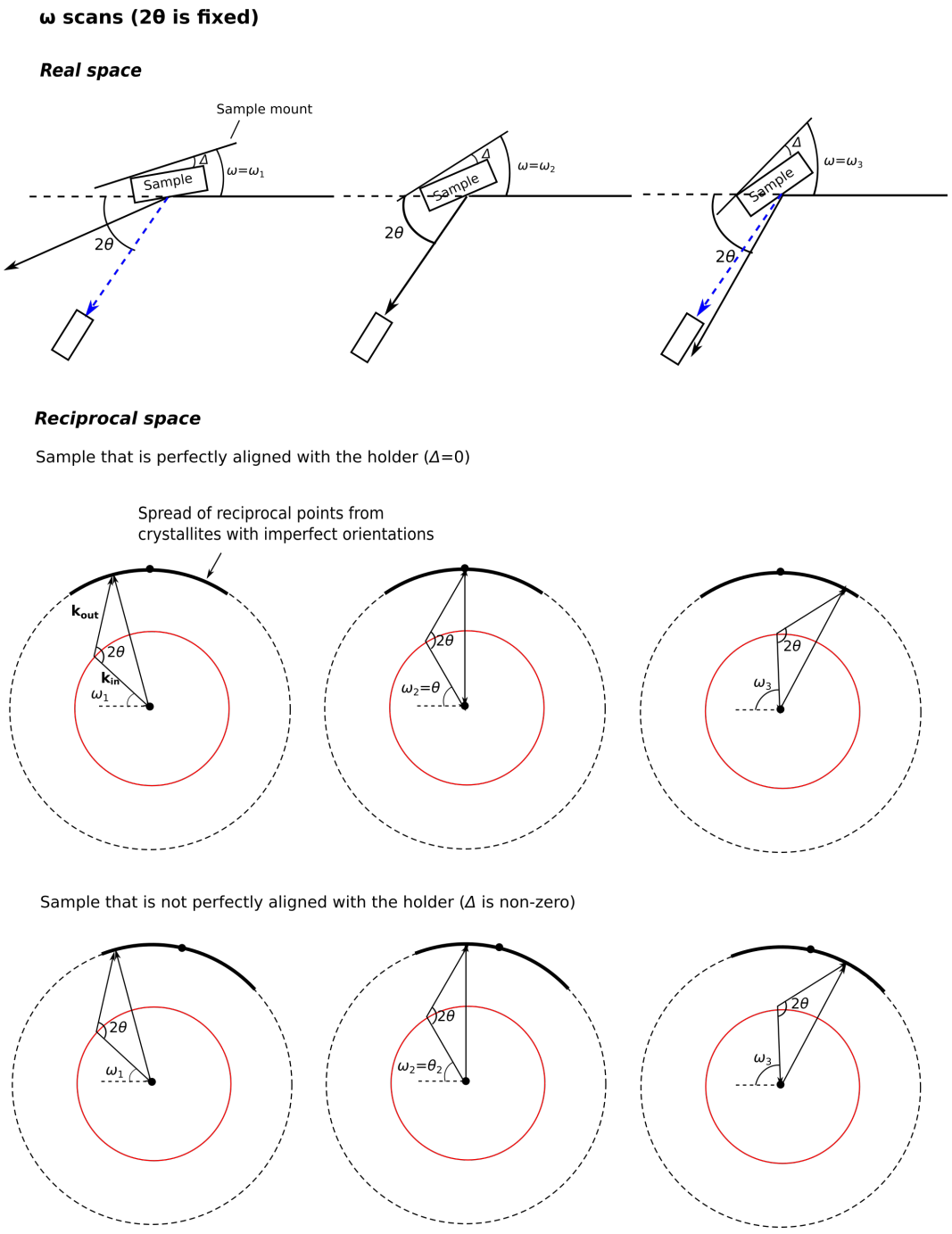

Figure 4.14: In the ω scan, the detector position is fixed while the angle between the incident beam and the sample stage varies. In the reciprocal space, $\mathbf{k_{in}}$ and $\mathbf{k_{out}}$ rotates on the red circle and the dotted black circle respectively. The diffraction signal reaches its maximum when $\mathbf{k_{out}}$ lies at the centre of the black arc.

4.3.4 The practicalities of taking X-ray data

Two Philips PANanalytical XRD systems (X' Pert Powder diffractometer and X' Pert Pro diffractometer- MRD) were used to analyse the ZnO thin films that we fabricated. Rapid $\theta/2\theta$ scans were taken using the powder diffractometer without any sample alignment. More accurate $2\theta/\omega$ and ω scans were performed using the MRD system. Our discussion will focus on the setup of the MRD system and the protocols for making a diffraction measurements and compensating alignment errors.

4.3.4.1 The Philips PANanalytical X'Pert MRD Pro system

Figure 4.16 shows the setup as used for the $2\theta/\omega$ and ω scans. The X-rays produced first pass through a $\frac{1}{2}^{\circ}$ divergence slit. The resulting beam is then monochromated by reflection of a X-ray mirror and directed to a soller slit. The soller slit consists of a set of fine parallel foils which suppress angular divergence of the beam. The outgoing beam then goes into the Ge[220]-4-crystal monochromator which preferentially selects the Cu Kα radiation with λ=0.154056 nm. A beam mask is installed at the end of the monochromator to restrict the beam size. The size of the beam is set to be 5 mm$\times$10 mm. The sample stage is then manipulated so that the X-ray impinges directly onto the sample and finally the diffracted beam is measured with a detector.

The sample sets on a triple-axis goniometer which is capable of moving in the X, Y and Z direction and can vary all of the ω, ψ and ϕ. This allows the alignment of beam and sample as well as accurate compensation of the sample misalignment.

To make a diffraction measurement, we need to align the X-ray beam so that it directly hits the sample. A preliminary alignment can be made by placing the sample at the centre of the sample stage and optimizing the sample height z. After

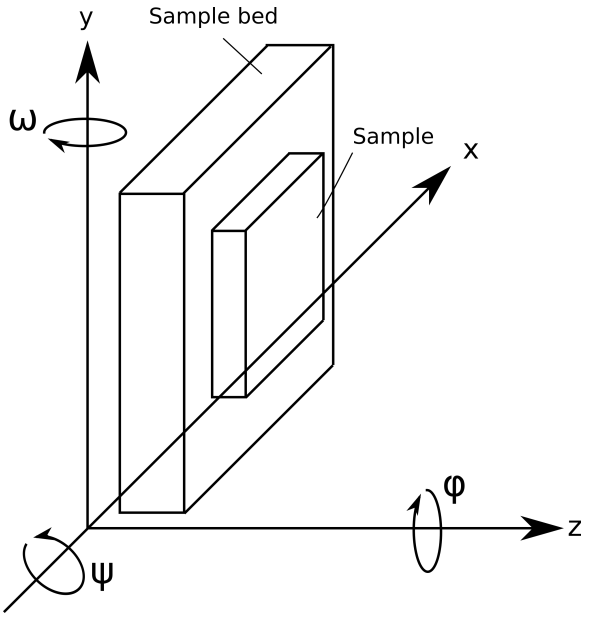

Figure 4.15: Visualisation of the angles ω, ψ and ϕ with respect to the sample stage.

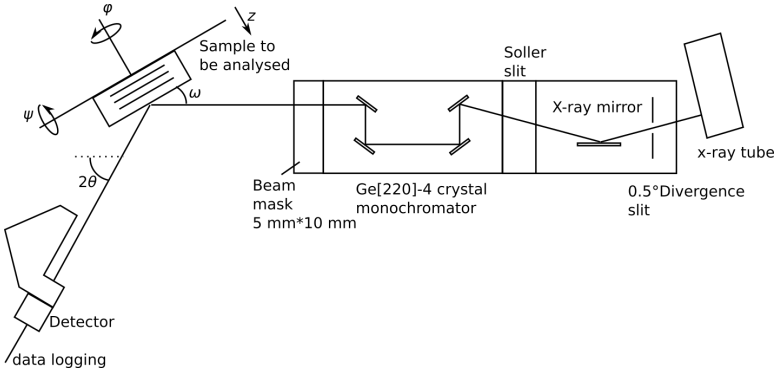

Figure 4.16: This diagram shows the experimental set up in the Philips PANanalytical X'Pert XRD system.

optimizing z, the misalignment of ω and ψ is compensated. Then X and Y are optimized. The detailed protocol is as follows:

A. Preliminary alignment of the sample position:

1. Place the sample as close to the centre of the sample stage as possible.

2. Set 2θ=0°.

3. Optimize the z position by scanning z until the X-ray counts have fallen to 50% thus indicating that the sample assembly is blocking 50% of the beam and hence that the sample is in the beam centre.

4. Align the sample surface parallel to the beam by scanning ω to find the value that maximises the X-ray counts for each iteration.

5. Repeat step 3-4 until the change in z is less than 0.2 mm.

B. Finding the offset required to compensate the sample misalignment:

1. Set ω=θ, and the detector position 2θ to the values where the diffraction peak is expected in the absence of misalignment.

2. Perform a ω scan and set ω to the value that gives maximum counts.

3. Perform a ψ scan and set ψ to the value that gives maximum counts.

4. Repeat steps 2-3.

5. Optimize the 2θ position by scanning the detector and setting to the value that gives maximum counts.

6. Repeat steps 2-5 until the changes in the ω, ψ offsets are less than 0.2° and the change in 2θ is less than 0.05°.

C. Further alignment of the sample position

1. Perform an X-scan, align X on peak counts.

2. Perform a Y-scan, align Y on peak counts.

3. Repeat steps 1-2 until the changes in X, Y are less than 0.2 mm.

D. Optimizing all variables

1. Repeat B and C until the changes in ω, ψ offsets are less than 0.2° , the changes in X and Y are less than 0.2 mm, and the change in 2θ is less than 0.05°.

4.4 Pulse echo characterization

4.4.1 The concept of pulse echoes

The piezoelectric action of a transducer can be tested directly using acoustic pulse echo measurements. In these measurements, a microwave pulse is first applied to the transducer. This launches an acoustic pulse into the transducer substrate. The wave propagates until it reaches the opposite substrate-air boundary where most of the acoustic power is reflected. When the wave returns to the transducer, the latter acts as a detector that converts acoustic energy into electrical signal via the piezoelectric effect thereby delivering a first electrical echo signal. Meanwhile, the wave reflects at the transducer/substrate interface and sets off again towards the opposite interface. This cycle repeats until the acoustic waves die away mainly due to dissipation in the substrate. The measured electrical signal is thus a series of successively attenuated echoes. From this acquired electrical signal, the conversion loss (CL) of the transducer can be found from the relation:

$$\text{CL (dB)} = \frac{1}{2}\Big(\text{IL (dB)} - \text{2-way acoustic attenuation (dB)}\Big) \tag{4.8}$$

where the insertion loss IL (dB) is defined as the relative magnitudes of the incident electrical power and the detected power of the first echo.

4.4.2 Experimental set-up

Figure 4.17(b) shows the experimental set-up used for pulse echo measurements. The HMC-T2220 signal generator is used to supply a microwave carrier of known power to the custom-built single pole double throw (SPDT) switches. The first SPDT switch is used as a single pole single throw (SPST) switch (terminal 2 is unconnected) in order to provide additional isolation between the source and transducer. The second SPDT switch connects the transducer to the microwave source when it is at position 1 and to the amplifier circuits when it is at position 2. The switches are controlled such that (refer to figure 4.17) the transducer is connected to the source for a brief period to excite the acoustic pulse; and then for the rest of time time, it is connected to the amplifier circuits for echo measurement. The resulting echoes are then amplified by the ZVA-213-S+ amplifier, rectified using the HP33330B diode and finally measured using the 104-MXs-B LeCroy oscilloscope with a 50 Ω termination. The two SPDT switches and the oscilloscope are synchronized via the internal trigger from SPDT switch B. All the apparatus is kept at 50 Ω in order to avoid power reflection between components. Labview programs were used to control the signal generator and the digital scope for frequency sweeps and data acquisition respectively.

The specifications of the experimental apparatus are:

1. Digital oscilloscope:

   A LeCroy 104-MX-B (2 GHz) oscilloscope was used to capture the echo waveforms measured by the transducer. The scope communicates with the computer via an ethernet connection. The waveform acquired is averaged over 5 captures. To measure the frequency response of the transducer, echo waveforms were recorded at successive frequencies. This was achieved by repeating the algorithm: increment the frequency by 100 MHz, wait for 200 ms, then make 10 measurements on the waveform to flush out of oscilloscope

memory of the 5 waveforms captured and stored at the previous frequency; then acquire the data. The scope is triggered at 10 kHz using the custom built combined pulse generator and SPDT switch unit B.

2. The signal generator:

   A Hittite synthesized signal generator HMC-T2220 with GPIB control is used. Its output has a wide frequency range from 10 MHz to 20 GHz with a resolution of 1Hz and a versatile power output from -60 dBm to 30 dBm with 0.1 dBm resolution.

3. Pulse generator and single pole double throw (SPDT) switch combined unit:

   This unit is custom built in the lab. The SPDT switch is driven by a switch driver. When logic '0' is applied to the driver, switch contacts 1 and 3 are connected; whereas when logic '1' is applied, contacts 2 and 3 are connected. Fast switching can be achieved by feeding a short pulse (15-30 ns) into the switch driver. This pulse can be generated by AND gating two wide square pulses that are separated in time by a variable delay (15-30 ns). The initial wide square pulses can be produced by using a simple Schmitt trigger oscillator, whilst the variable delay between the two pulses can be controlled using an adjustable RC time constant.

4. The amplifier:

   The echo signals are amplified by a Mini-circuit ZVA-213-S+ amplifer. This is a wide band amplifier that works from 800 MHz to 21 GHz with +26 dB of gain.

5. Detector diode:

   The echo signal is rectified using the HP33330B when the diode is 50 Ω terminated, the signal power P_{in} and the output voltage V_{out} are related by:

$$V_{\text{out}}(\text{mV}) = \exp\big(2.495 + 0.203 \times P_{\text{in}}(\text{dBm}) - 0.026 \times (P_{\text{in}}(\text{dBm}))^2\big) \quad (4.9)$$

6. Electrical contact to the ZnO transducer:

   The picoprobe model 10 (the ground-signal option) is used to make electrical contact to the transducer. The probe operates from DC to 7 GHz with a 50 Ω input impedance and has a 6 dB 2-way insertion loss. The probe is integrated with a Thorlab DT12 3-axis translation stage to enable different regions of the transducers to be easily accessed. To form a connection to the transducer, the probe is carefully lowered using the translation stage until the signal pin contacts the top dot, and the ground pin contacts the capacitive grounding layer. The pins need to be bent at a certain angle to ensure better physical contact between the probe and the electrodes. This may change the characteristic impedance of the probe (might introduce more self inductance), but it does not seem to have a detrimental effect on its performance. We have chosen to use probe tips that are made of palladium rather than the tungsten to avoid damage to the thin films.

4.4.3 Examples of pulse echoes measured

Using the method as described in section 4.4, we measured the pulse echo response of the fabricated transducers. Figure 4.18 shows a typical trace of successively attenuated acoustic echoes at 1.9GHz. As expected, the echoes decay exponentially due to heat dissipation in the substrate. The sharp peak at the beginning of the traces is not an echo, it is caused by microwave leakage from the switch. Figure 4.19 shows a similar measurement at a much higher frequency (9.148 GHz) and a larger amplification (+56 dB). The characteristic increase in acoustic attenuation at higher frequency can be clearly seen. To the author's knowledge, this echo signal is at a higher frequency than anything so far reported in the literature. This reinforces our belief that we have succeeded in developing ZnO transducers of very high quality.

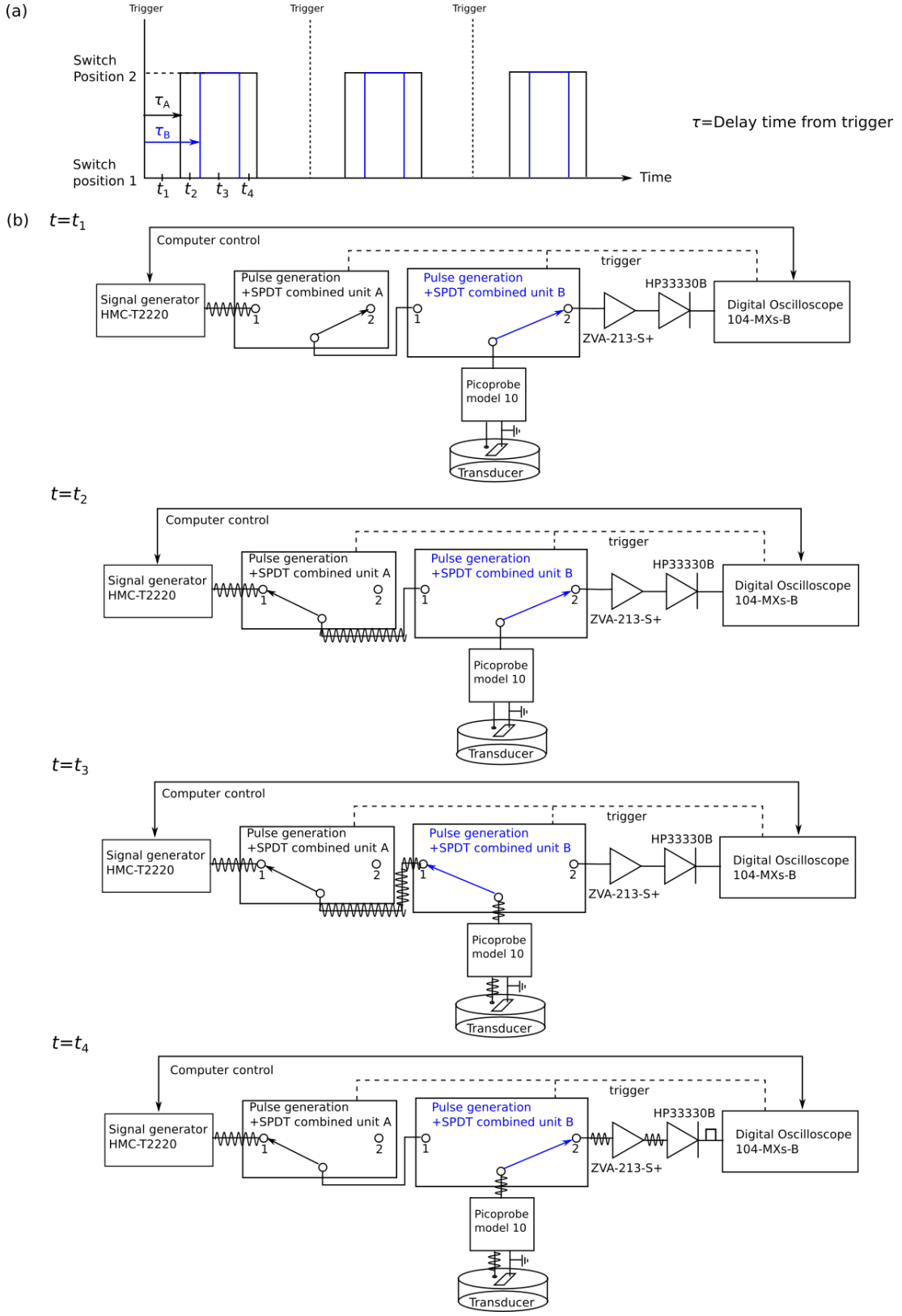

Figure 4.17: (a) The switch positions relative to the trigger as a function of time, (b) At $t = t_1$, both SPDT switches are on position 2, no microwave carrier is transmitted to the transducer. At $t = t_2$, SPDT switch A is on position 1 while SPDT switch B is on position 2; again no microwave carrier is transmitted to the transducer. At $t = t_2$, both SPDT switches are on position 2, the microwave carrier is connected to the transducer, so an acoustic wave is excited. At $t = t_4$, SPDT switch A is on position 1 while SPDT switch B is on position 2, so the transducer is connected to the amplifier circuit for echo measurement.

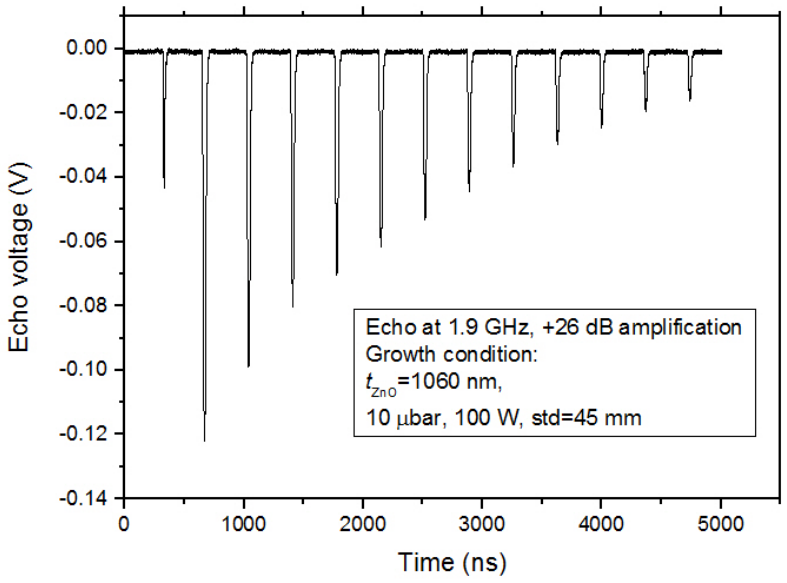

Figure 4.18: The echo voltage measured at 1900 MHz with +26 dB amplification for a ZnO transducer grown at a sputtering gas pressure of 10 μbar, substrate-target-distance=45 mm, 100 W of power and film thickness t_{ZnO}=1060 nm.

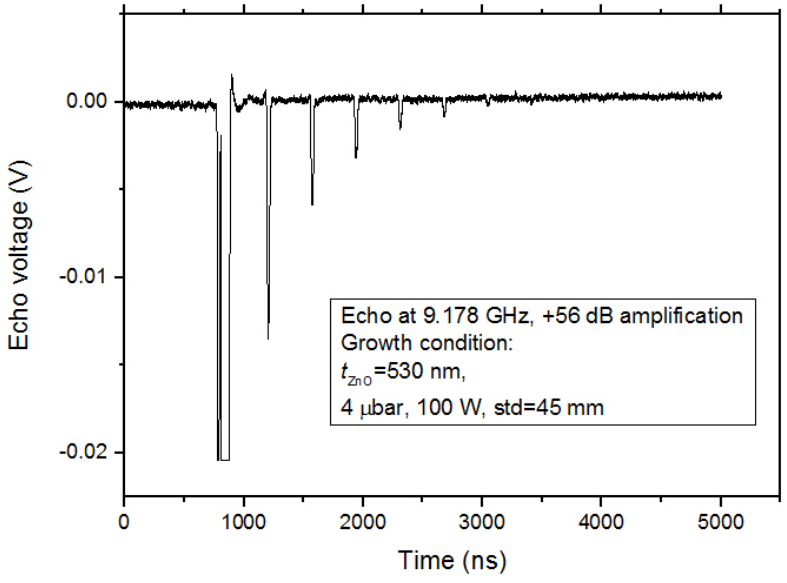

Figure 4.19: The echo voltage measured at 9148 MHz with +56 dB amplification, for a ZnO transducer grown at a sputtering gas pressure of 4 μbar, substrate-target-distance=45 mm, 100 W of power and film thickness t_{ZnO}=530 nm.

Chapter 5

The structural and piezoelectric properties of ZnO transducers

In this chapter, the properties of the ZnO transducers that were fabricated under various sputtering conditions are discussed. We describe the experimental procedures for characterising the transducers and show how the Mason model is applied to predict transducer performances. The experimental and simulated results will then be compared in section 5.2. From this comparison, we deduce some interesting properties of the transducers including the structural properties of the ZnO thin films and the relationship between these structural characteristics and transducers performance.

5.1 Experiments

All the transducers were fabricated with the layer structure described in section 4.1. They are grown on 10 mm diameter and 2 mm thickness c-axis oriented sapphire single crystals. Sapphire is used as the substrate because it has very low acoustic attenuation at high frequency. The thicknesses of the Cr and Au layers

were kept constant at 4 nm and 25 nm (measured by quartz monitor) respectively for all transducers. The diameter of all the signal top electrodes is 400 μm.

Using the fabrication protocol described in section 4.2.5, ZnO transducers were grown under various sputtering conditions as shown in table 5.2. The variables include different substrate target distances- std (25/45 mm), sputtering gas pressure (4/10/20 μbar) and power (60/100 W). A number of ZnO transducers, all having the same sputtering condition (45 mm std, 10 μbar, 100 W) but different thicknesses of 265 nm, 530 nm, 800 nm, 1060 nm were also fabricated. The gas mixture ratio of Ar-O_2 is fixed at 1:1 in all cases. Although the temperature of the substrate is not controlled in the sputtering process, a spot measurement using a thermistor indicates that the substrate temperature only varies between about 135-185°C. In view of the effective temperature of the growing surface under ion bombardment, this temperature variation is considered to be insignificant. The substrate is heated up to around 150°C in the ion cleaning process before the deposition of ZnO, so the temperature stays fairly constant throughout the whole sputtering process.

After the transducers are fabricated, they are first characterized by the $\theta/2\theta$ scan in the X-ray powder diffractometer. The 2θ position and the FWHM of the peaks are extracted from the diffraction patterns. More accurate X-ray measurements are then made in the X'pert Pro MRD where the $2\theta/\omega$ and ω scan are performed with precision alignments. The protocol for these X-ray measurements can be found in section 4.3.4.1. From the 2θ value, the FWHM of the ω scan and the (002) peak value are extracted.

The transducers were then subsequently tested by the pulse echoes measurement as described in 4.4.2. Acoustic pulses are excited with an input electrical power of +25 dBm. Six different top electrodes on the same sample were tested. The voltages of their first echo peaks were measured and averaged and the measurement

error is calculated from the standard deviation of the six echo voltages. The echo voltages were then used to calculate the conversion losses of the transducers using the known gains and losses of the switch/amplifier circuitry.

Using Mason's model that we adapted to our purposes in section 3.4, the conversion efficiencies of the transducers were predicted and compared to the measurement values.

5.2 Experimental results

5.2.1 X-ray diffraction patterns

The preliminary $\theta/2\theta$ scan shown in figure 5.1 of a 265nm thick ZnO transducer grown at power=100 W, pressure=4 μbar, std=45 mm shows the main X-ray features of our device. The ZnO(002) peak around 34.4° can be clearly identified. There are also two large and sharp peaks at 41.7° and 90.8° corresponding to the sapphire (006) and (0012) peaks respectively. One can identify a small Au(111) peak at 38.2° and the ZnO(004) peak at 72.7°. The ZnO(004) peak arises from the 2^{nd} order Bragg diffraction from the {002} planes. We cannot identify any (100) a-axis peak at 31.8°. All the other transducers that we have grown were found to exhibit similar $\theta/2\theta$ scans and no a-axis diffraction peak was found in any transducer. The crystalline sizes of all the fabricated films were found to be around 50 nm by inputting the FWHM of the (002) peaks into the Scherrer equation.

Figure 5.2 shows the $2\theta/\omega$ scans (a) and the ω scans (b) for ZnO transducers grown under identical sputtering conditions but of different thicknesses. From powder diffractometry we know that all of our ZnO thin films are c-axis oriented, so we have focussed on investigating the (002) diffraction peak near 2θ=34.4°. To get an acceptable X-ray detector count rate, we used a large receiving slit (1 mm) in the

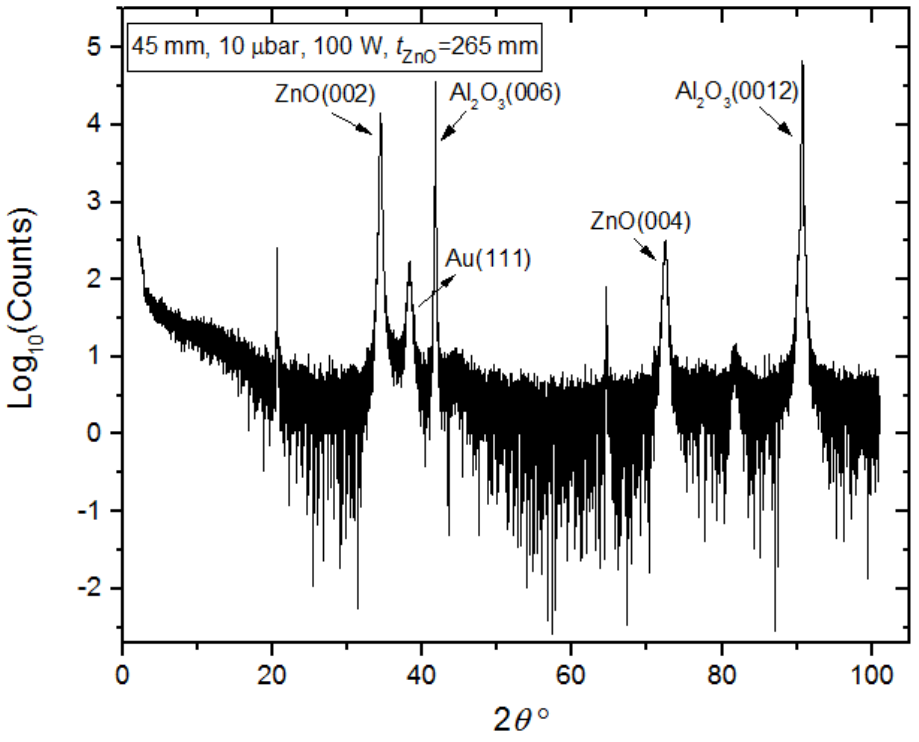

Figure 5.1: The diagram shows a $\theta/2\theta$ scan of a 265 nm thick ZnO transducer grown at power=100W, pressure=4 μbar, std=45 mm.

X-ray measurements and this leads to the broadened peaks obtained in the $2\theta/\omega$ scans. Hence, we cannot estimate the size of the crystalline grains from these scans because most of the broadening comes from instrumental effects. Nevertheless, the height of the peak should still be a good indicator for quantifying the degree of c-axis orientation in ZnO films of the same thickness so long as the alignment of the beam with the sample is correctly set and the misalignment offsets are satisfactorily compensated.

The rocking curves in figure 5.2b indicates that the misorientation angles of the c-axis grains do indeed show a Gaussian distribution about the substrate normal. The total volume of c-axis crystallites is thus proportional to the area under the rocking curve which in turn is proportional to the product FWHM×peak height

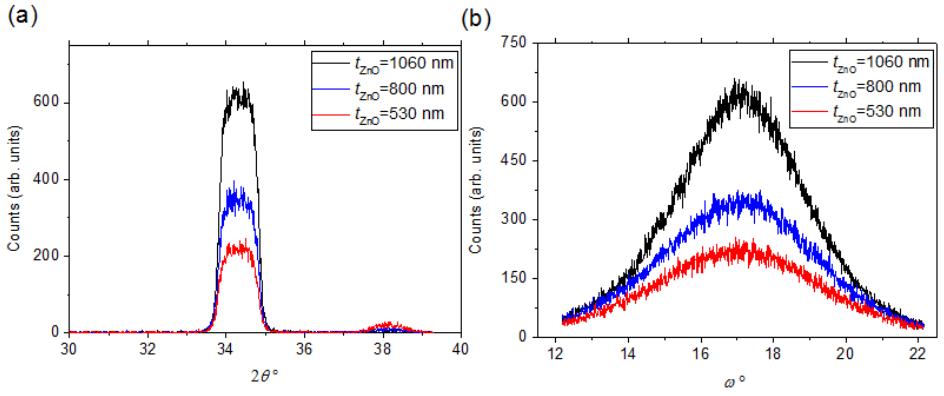

Figure 5.2: This diagram illustrates the results from the $2\theta/\omega$ scan (a) and the ω scan (b) for ZnO transducers with t_{ZnO}=265 nm, 530 nm and 1060 nm. The three transducers are grown at the same sputtering condition at power=100 W, pressure=10 μbar, std=45 mm.

[1].

The FWHM, (002) peak height and the 2θ positions for transducers grown in other sputtering conditions are displayed in table 5.2.

5.2.2 Pulse echoes

Figure 5.3 shows examples of pulse echo traces taken from transducers that were grown under different sputtering conditions. The initial peak originates from microwave leakage and should be ignored. The difference in echo voltages observed suggests that the transducer performance is highly dependent on the sputtering conditions. It was also found that the amplitude of the echoes observed from

[1]To be more accurate, the total volume of the c-axis crystallites is proportional to the total occupied volume of reciprocal space. So in fact, the broadening of the θ value caused by finite crystallite sizes should be taken into account when calculating the total volume. Nevertheless, since we have chosen a slit size that is big enough to capture all the diffracted beams with the corresponding angular spread in θ, the volume integration along θ is effectively performed by the detector.

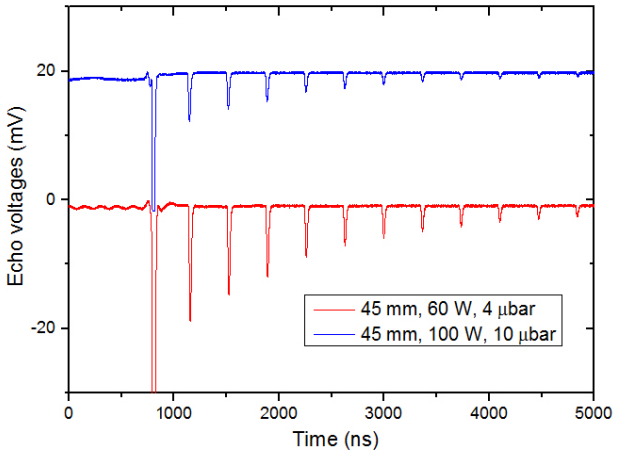

Figure 5.3: Examples of pulse echoes traces from transducers that were grown under different sputtering conditions.

different transducers that were made in the same transducer batch do not vary to any considerable extent. This indicates that the sputtered ZnO film is fairly uniform. The echo voltages for the different transducers can be found in table 5.2.

5.2.3 Measured and simulated frequency response of the transducers

Using the fitting parameters as shown in table 5.1, the insertion losses of the transducers with t_{ZnO}=530 nm, 800 nm and 1060 nm are computed using the Mason model and compared to the data that was measured on samples of these various thicknesses that were grown under the same sputtering condition (Figure 5.4). For the sample with t_{ZnO}=1060 nm, an excellent fit was obtained whereas for samples with t_{ZnO}=800 nm and 530 nm, the fit is noticeably worse especially towards the low frequency end, and the predicted bandwidth tends to be marginally less than the measured bandwidth. One can also see that the measured insertion loss appears to level off at the high frequency end. This is an artifact caused by the fact

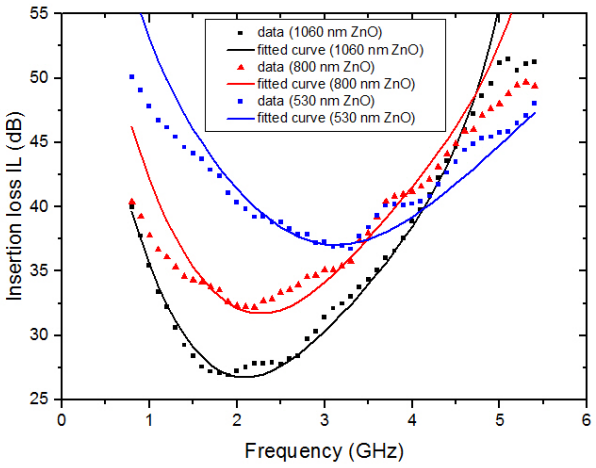

Figure 5.4: The graph shows the predicted and measured frequency responses of ZnO transducers with t_{ZnO}=530 nm, 800 nm and 1060 nm. The three transducers are grown under the same sputtering conditions (power=100 W, pressure=10 μbar, std=45 mm).

Data	t_{Au} (nm)	t_{ZnO} (nm)	Expected t_{ZnO} (nm)	k_t
Black	18	960	1060	0.25
Red	25	860	800	0.2
Blue	25	600	530	0.2

Table 5.1: The table shows the fitting parameters used in the Mason model for calculating the frequency response of various ZnO transducers as shown in figure 5.4. The electrode diameter and the thickness of Cr are fixed at 400 μm and 4 nm respectively.

that at 50 dB insertion loss, the signals are so small such that they are no longer resolvable against the background noise.

We have also plotted the predicted and the measured resonant frequency against t_{ZnO} in figure 5.5. Reasonably good agreement is found between the predicted and experimental curves but once again, the model is less accurate as t_{ZnO} becomes smaller.

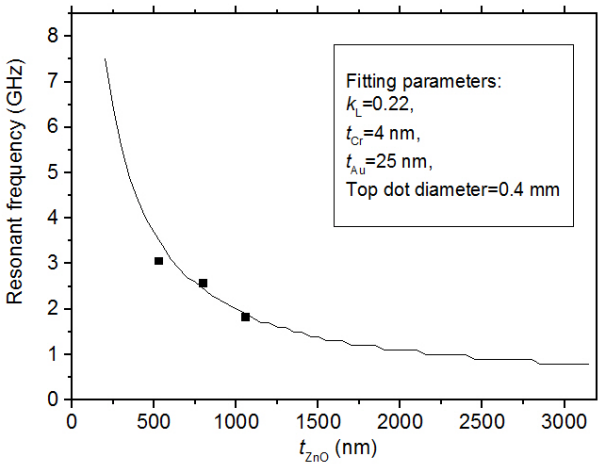

Figure 5.5: The graph shows the predicted and the measured resonant frequency of the transducers against t_{ZnO}

5.3 The properties of ZnO transducers

In this section, we analyse the measurements made on transducers of different sputtering conditions and thicknesses to deduce their piezoelectric and structural properties, in particular, residual stress of the film, crystal orientation, total number of crystallites and polarization. We will also examine the dependence of the relationship between the piezoelectric activity and the crystal quality of the ZnO grains. These analyses lead us to an overall picture as to how the piezoelectric and structural properties are inter-related. This is presented in the conclusion section.

5.3.1 Self texturing with c-axis orientation perpendicular to the substrate surface

For devices made under all sputtering conditions, ZnO(002) peaks were observed. No a-axis peaks were found in the $\theta/2\theta$ scan. This confirms that the ZnO thin films of all transducers are c-axis oriented and agrees with the observation that the transducers made all exhibit longitudinal piezoelectric activity as deduced from the velocity measurements of the pulse echoes.

5.3.2 Compressive stress is developed in ZnO thin films grown on Au layers

By comparing the 2θ position in the $2\theta-\omega$ scan with the bulk value, i.e., $2\theta_{\text{bulk}}$=34.443°, the residual stress of the ZnO film may be deduced. The residual stress σ_{film} of the ZnO films can be calculated using the relation [42]:

$$\sigma_{\text{film}} = \frac{2c_{13}^2 - c_{33}(c_{11}+c_{12})}{2c_{13}} \times \frac{d_{\text{film}} - d_{\text{bulk}}}{d_{\text{bulk}}} \tag{5.1}$$

where d_{film} and d_{bulk} are the (002) plane spacings for the ZnO film and bulk ZnO respectively. Using c_{11}=208.8 GPa, c_{12}=119.7 GPa, c_{13}=104.2 GPa, c_{33}=213.8 GPa, we have:

$$\sigma_{\text{film}} = -232.81\,\text{GPa} \times \frac{d_{\text{film}} - d_{\text{bulk}}}{d_{\text{bulk}}}. \tag{5.2}$$

In all of our grown samples, θ_{film}-θ_{bulk} are measured to be negative, so $d_{\text{film}} - d_{\text{bulk}}$ is positive. This implies the existence of a compressive residual stress. This residual stress arises from two main contributions:

Firstly, the difference in thermal expansion coefficient α of the substrate and the film causes the film to deform as both substrate and film are cooled to room temperature from the higher sputtering temperature. Since α for Au ($14.2\times10^{-6}\,\text{K}^{-1}$) is higher than that for the ZnO ($4.75\times10^{-6}\,\text{K}^{-1}$), we expect the film to develop a planar compressive stress as illustrated in figure 5.6. The thermal stress is given by:

$$\sigma_{\text{thermal}} = \frac{E_f}{1-\nu_f}(\alpha_s - \alpha_f)(T - T_d) \approx 2.025 \times 10^{-3}\,\text{K}^{-1}(T - T_d)\,\text{GPa} \tag{5.3}$$

where $E_f = 150\,\text{GPa}$ and $\nu_f = 0.3$ are the Young modulus and the Poisson's ratio of the ZnO film respectively, α_s and α_f are the thermal expansion coefficients of the substrate and film respectively, T-T_d is the difference between room temperature

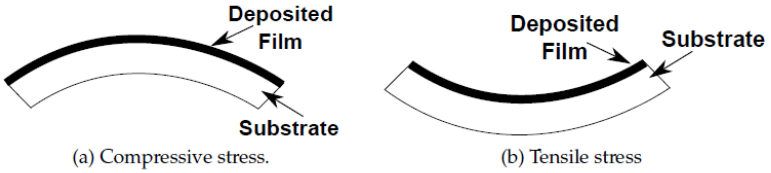

Figure 5.6: An illustration of the effect of compressive stress (a) and tensile stress (b) in sputtered thin films. Consider the case when the thermal expansion coefficient of the substrate is higher than that of the film. As the sample cools down from the deposition temperature to room temperature, the substrate will contract more than the film. This difference in contraction causes the sample to deform. So a compressive stress is developed in the film. The opposite will happen when the thermal expansion coefficient of the film is higher than that of the substrate, in which case the film will exhibit tensile stress.

and the temperature during deposition. Using the information that $T - T_d \approx -120\,\mathrm{K}$, the thermal stress is around -0.243 GPa. This value accounts for 16-83% of the stresses in all of our samples.

Another contribution to the observed compressive strain is the stress caused by the ion peening. In magnetron sputtering, the energetic ions can penetrate through the surface layer of the film, thereby increasing both the density of the film and the unit cell dimension. The films produced therefore tend to buckle under their own internal stresses.

5.3.3 The existence of a dead layer

Figure 5.7 compares the total X-ray area under the rocking curve (which is proportional to the total volume of c-axis crystallites) with the thicknesses of various ZnO films grown under the same sputtering condition. A clear linear trend is seen but with a non-zero $x$axis intercept. Simplistically, one would expect this intercept to be zero since zero X-ray area should correspond to the case where there is no film. The volume of c-axis crystallites must therefore increase non-linearly before a threshold thickness (as shown in the dotted line) after which the crystallite number rises uniformly as thickness increases. The initial slow increase in

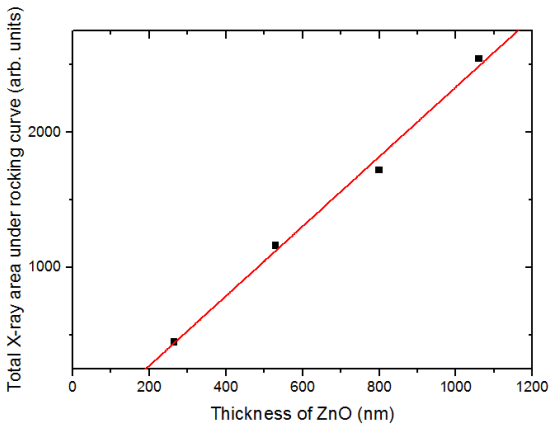

Figure 5.7: This figure plots the relationship between the total X-ray area under rocking curve and the thickness of the ZnO layer in the transducer

the X-ray area indicates that the ZnO crystal begins to grow with an amorphous structure at the Au/ZnO interface. The structure then gradually self-textures into c-axis columnar grains. Hence, there exists a dead layer for which the structure of the film is amorphous and the thickness of this dead layer can be roughly estimated by the x-intercept of the total X-ray area versus thickness curve. For the sputtering conditions: at substrate-target distance=45 mm, pressure=10 μbar and power=100 W, the thickness of the dead layer is around 190 nm.

5.3.4 Orientation improves with thickness

FWHMs of transducers grown under the same sputtering conditions but with different thicknesses ranging from 265 to 1060 nm are found to reduce from 7.48° to 4.12°. This indicates an improvement of orientation with increasing thickness.

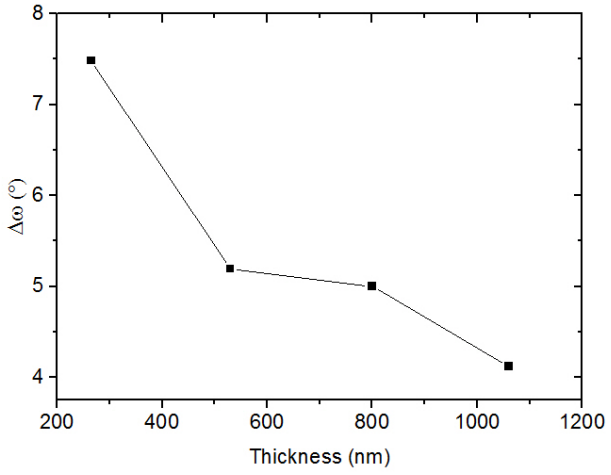

Figure 5.8: The data shows that the FWHM of the rocking curve $\Delta\omega$ reduces as the thickness increases, implying that the texture and c-axis orientation of the ZnO film improves with thickness.

5.3.5 Polarization does not significantly vary with the thickness of the ZnO film

Good c-axis orientation does not guarantee good transducer action; for instance, it might be possible to have a perfectly oriented c-axis crystal but if the ratio of upward and downward pointing c-axis grains happens to be the same then no piezoelectric action would be observable.

To find out how the polarization varies with the ZnO film thickness, we compare the measured and simulated (with the Mason model) of a set of transducers of varying thicknesses grown under the same sputtering conditions. Figure 5.9 compares the simulated insertion loss for fixed value of k_{L}=0.22 with the measured insertion loss. The good agreement between the experimental data and the computed result indicates that k_{L} stays fairly constant as the thickness increases, and thus the polarization does not significantly vary with the thickness of the ZnO film for $t_{\mathrm{ZnO}} > t_{\mathrm{dead\ layer}}$.

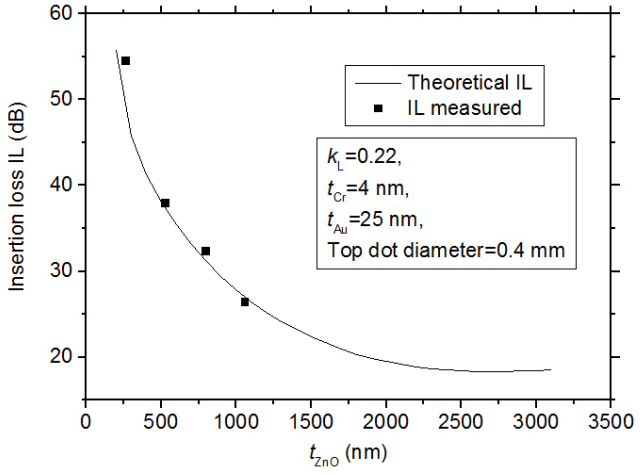

Figure 5.9: Using fixed fitting parameters: t_{Cr}=4 nm, t_{Au}=25 nm, $\phi_{\text{top dot}}$=400 μm and k_{L}=0.22, the minimum insertion losses are calculated as a function of ZnO thicknesses. The simulated insertion losses agrees well with the measured data. This indicates that the polarization does not significantly vary with the thickness of the ZnO film.

5.3.6 Polarization reversal is insignificant

Figure 5.10 shows a plot of the total integrated X-ray area against echo voltage for transducers all of the same thickness that are grown under different sputtering conditions. The linear relationship between the piezoelectric response and the volume of c-axis oriented crystallite suggests that the polarization ratio of the c-axis crystallites is fixed, and thus the degradation of acoustic transduction as the sputtering conditions are changed is caused by poor crystalline quality. Although the c-axis peak height is a reasonably good indicator of the piezoelectric action, in odd cases (e.g. the sample that was grown with sputtering conditions 45 mm substrate target distance, 20 μbar, 100 W), it is possible to observe good piezoelectric action from a transducer that has a low c-axis peak provided that its FWHM in the rocking curve is large so that the total X-ray area is high. The best transducer, however, was found to have a high c-axis peak and low FWHM. Hence, a transducer that has a high c-axis peak and hence highly oriented crystallite is guaranteed to show good piezoelectric action, but a transducer with a low c-axis

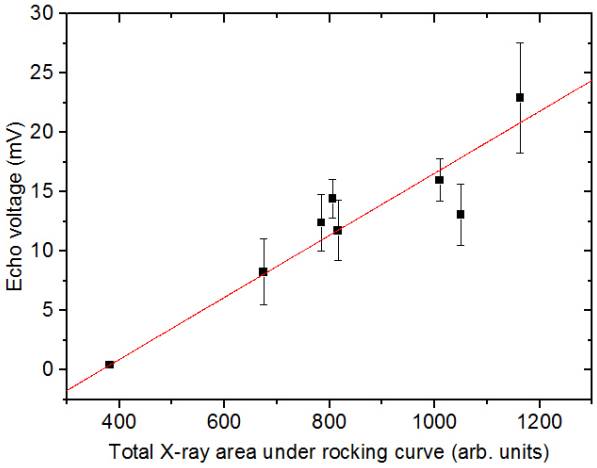

Figure 5.10: This figure shows the linear relationship between the echo voltages and the total integrated X-ray area for transducers that have the same thickness but are grown in different sputtering conditions. This suggests that polarization reversal is insignificant.

peak (i.e. the crystallite orientates relative to the film normal are spread) can also show good action owing to the fact that the cosine of a small angle is still close to unity.

The best transducer we made was found to have a k_{L} value of around 0.22, which is about 81% of the bulk value as quoted by Foster *et al.* [35]. This suggests that polarization reversal is insignificant in magnetron sputtered ZnO films.

5.3.7 Conclusion

In this short section, we summarize the properties of the ZnO transducers based on the results obtained. The first three bullet points are illustrated in figure 5.11a and the fourth is seen in figure 5.11b.

- The k_{L}s of the sputtered ZnO films stay fairly constant as the thickness of the ZnO layer is varied but are strongly dependent on the sputtering conditions.

- The polarization ratio of the c-axis crystallites is fixed, and for a given transducer thickness, the total number of properly oriented crystallites is smaller for ZnO films that have smaller k_{L}.

- In any ZnO film, there exists an initial layer that is piezoelectrically dead for which the ZnO layer structure is highly disordered.

- The transducer conversion loss is fairly constant at large film thickness but shoots up as the thickness is reduced below a certain threshold value. This is because thin piezoelectric layers are ineffective in driving the heavy mechanical load imposed by the electrodes and substrates. As the ZnO thickness increases, the conversion loss levels off at a certain threshold value. This behaviour is predicted by our Mason model simulations (see section 3.5.1).

- We can also explain why the Mason model is less accurate in predicting transducer performance for thinner ZnO samples as discussed in section 5.2.3. The inaccuracy arises from the fact that the Mason model only assumes a homogenous piezoelectric layer, so its modelling ability decreases with sample thickness as the corresponding fraction of $t_{\mathrm{dead\ layer}}$ to the actual thickness is higher.

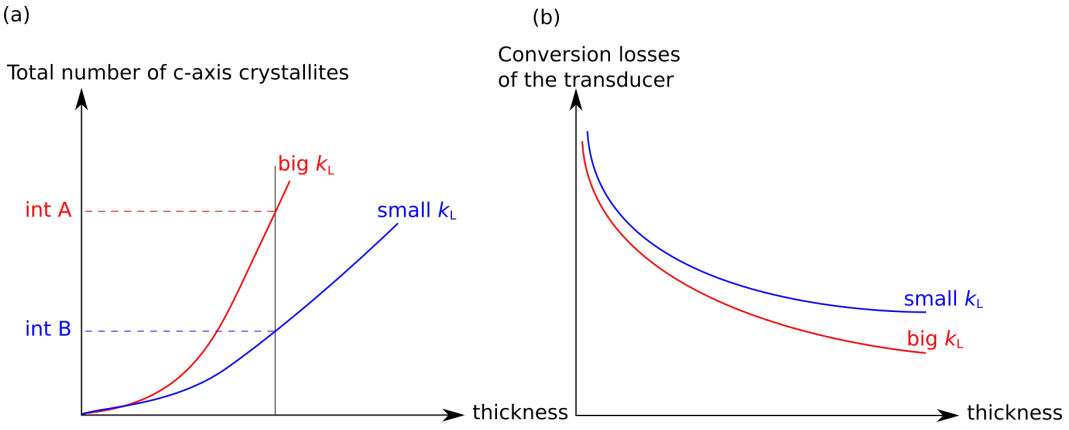

Figure 5.11: (a) An illustration of the expected total X-ray area vs thickness for samples of different k_L. The rate of increase of X-ray area with thickness is expected to be lower in small k_L samples as a larger fraction of the ZnO grown would have a disordered structure. (b) Transducers with smaller k_L have less piezoelectric activity. The conversion loss should plateau at a certain threshold thickness as predicted in the Mason model.

Power (W)	Pressure (μbar)	Std (mm)	Thickness (nm)	f_0 (MHz)	IL (dB)	$C_{\max}$ (arb.units)	$\Delta\omega$ (°)	$2\theta_{\text{MRD}}$ (°)	$2\theta_{\text{powder}}$ (°)
60	4	45	530	3050	-41.4	139	5.87	34.22	34.29
100	4	45	530	3050	-40.8	209	5.02367	34.28	34.29
100	10	45	265	5000	-54.5	60	7.48	34.32	34.41
100	10	45	530	3050	-37.9	224	5.19	34.3	34.30
100	10	45	800	2561	-32.3	345	5.00	34.33	34.41
100	10	45	1060	1820	-26.4	618	4.12	34.33	34.40
100	20	45	530	3050	-40.3	98	8.22	34.40	34.30
60	10	45	530	3050	-41.1	110	7.13	34.35	34.41
100	4	25	530	3050	-43.0	143	4.72	34.35	34.42
60	4	25	530	3040	-55.1	43	8.87	34.37	34.41
100	10	25	530	3050	-39.8	223	4.53	34.37	34.41

Table 5.2: The table shows the characterization of various transducers grown at different sputtering conditions (Power (W), Pressure (μbar) and substrate-target distance std (mm)) at a fixed 1:1 Ar-O_2 gas mixture ratio. Here, f_0 is the resonant frequency of the transducer, IL stands for the insertion loss at f_0, $C_{\max}$ and $2\theta_{\text{MRD}}$ are the strength of the c-axis peak and 2θ values in the $2\theta/\omega$ scan/ω scan respectively, $\Delta\omega$ is the FWHM of the rocking curve, $2\theta_{\text{powder}}$ is the 2θ value measured in the $\theta/2\theta$ scan using the powder diffractometer.

Chapter 6

Langmuir probe diagnosis of RF ZnO plasma in magnetron

As discussed in previous chapters, we have succeeded in manufacturing excellent ZnO piezoelectric thin films that have electromechanical coupling constants up to 80% of the bulk value. Sputtering is a process that requires optimisation in a multidimensional parameter space and thus requires in the worse case very extensive fine-tuning of the sputtering plant and countless hours of trial and errors. Any additional insight or information that can shorten this very time inefficient optimization is extremely valuable. Although the very substantial background literature [26–28, 43, 44] on ZnO fabrication gives guidelines as to sputtering conditions for producing high quality ZnO films, these conditions are usually described in terms of the 'engineering parameters' such as power, target-substrate distance, pressure etc. These convey little useful information to readers other than those who happen to possess exactly the same fabrication equipment as the contributing author, since only in this circumstance do they translate directly to the essential 'physics parameters' local to the film growth process that actually determine the quality of the growing film.

The purpose of this chapter is therefore to describe an approach to successful piezoelectric transducer growth that is of more general application and we do this by focussing on measuring, interpreting and reporting these more universally relevant 'physics parameters' that need to be implemented at the growing film in order to guarantee satisfactory film fabrication. Having access to these physics parameters can also allow us to understand the growth mechanisms behind the formation of self textured, c-axis oriented ZnO thin films. These mechanisms will be discussed later in chapter 7.

The relevant physics parameters involved here include the growth rate of the thin film, the effective substrate temperature as well as the plasma conditions. The first parameter can be measured easily using the quartz thickness monitor and will not be discussed in detail. Instead, we will focus on investigating the plasma conditions such as sheath width, wall potential, interface electric field, plasma density, ion bombardment flux, ion energy, and electron temperature, which can be inferred via the use of a Langmuir probe. Plasma conditions including electron temperature, ion flux and energy are important parameters for determining the effective surface temperature of the substrate in sputtering.

Langmuir probe diagnostics essentially involve measuring the current induced in a DC biased conducting probe that is inserted into a plasma (see figure 6.1). The information about the nature of the plasma is encoded on the resulting I-V curve, which is subsequently analysed theoretically to deduce the relevant physical conditions. By designing and building a special miniaturized Langmuir probe and positioning it carefully in the magnetron plasma, quite accurate localised plasma conditions can be extracted.

This chapter is organised as follows. We will begin by understanding the electrical properties of the RF plasma in a sputtering plant. The application of Langmuir probe diagnostics on the RF plasma will then be studied and the expected ideal

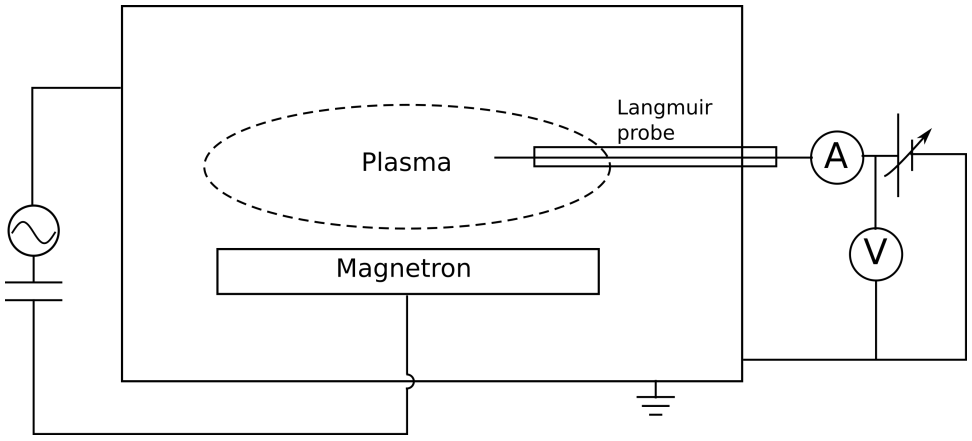

Figure 6.1: A sketch of Langmuir probe diagnostics in a RF sputtering environment

I-V curves will be derived. We will then discuss how a realistic *I-V* curve differs from the ideal case and how the acquired data can be analysed using various models. We then investigate the *I-V* curve distortion due to both insufficient RF compensation and to the presence of magnetic field and discuss how various techniques and configurations can be used to avoid them. A suitable design of a miniaturized Langmuir probe plus accompanying circuitry is then proposed together with a recipe for measuring and analysing the plasma parameters of the magnetron discharge. Finally, results obtained under various sputtering conditions are presented and compared.

6.1 Electrical properties of RF plasma

In this section, we discuss the dynamics of the electric potential of a RF plasma formed between two asymmetric electrodes (e.g. a sputtering chamber). We begin by explaining some of the physics facts that is genuine to the plasma systems.

One implementation of a plasma is a quasi-neutral ionised gas with freely moving electrons and ions. Their velocity probability densities typically follow Maxwellian distributions.

Consider the case when an electrically isolated wall introduced into the plasma. The electrons and ions in the plasma move freely in space and occasionally these charge carriers will collide with the wall. Since the mass of the electron is smaller, the electron mobility is higher than that of the ions. So the wall will charge negatively relative to the plasma potential V_s until the electron flux is suppressed by the opposing electric field produced by the negative charge on the wall. Close to the wall, a plasma sheath is formed. This is a volume that has a positive space charge (of ions) and across which the electric field from the negatively charged wall is amortised. Consequently, outside the sheath, the electric field in the sheath has no influence so ion current or electron current depends on thermal diffusion of charge carriers into the sheath. The potential of such a 'floating' wall is defined as the floating potential or 'wall potential' V_f. When sitting at V_f, the wall will collect no net current, i.e. the ion current drawn is equal to the electron current drawn.

Now consider the case when the wall is electrically connected to a voltage source and we thereby arrange that the potential V of the wall is less than V_f, then the electron flux will be even more suppressed so a net ion current can be collected. Inversely, if $V > V_f$, then a net electron current will be drawn to the wall. Again in these cases, the currents collected are caused by thermal diffusion of charge carriers into the sheath. Thus, the current drawn for a given potential of the wall should look like as shown in figure 6.3a, where the non-linearity of the curve, i.e. low ion current at $V < V_f$ and a high electron current $V > V_f$ arises from the difference in thermal flux between the electrons and the ions.

In an RF sputtering system, the 'walls' mentioned previously are the two electrodes: the target and the ground electrodes. When the plasma is excited by an external RF source (see figure 6.1), there is an RF current flowing across the 'target→plasma→ground' circuit. The total current flow must be continuous which means that the current taken by each electrode must be equal and

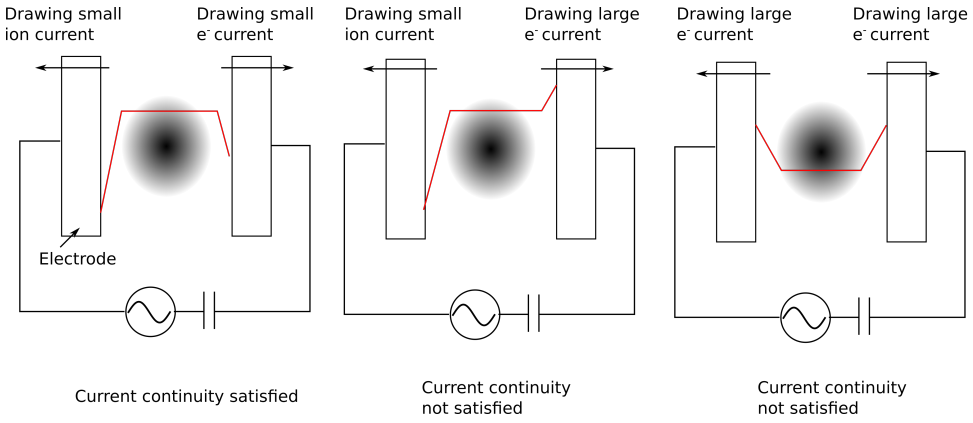

Figure 6.2: This diagram illustrates the various currents drawn into the electrodes with a given electrode potential and plasma potential. Current continuity is only satisfied in the case when both electrodes are negative with respect to the plasma. The red lines indicate the spatial distributions of the electric potential.

opposite (i.e., if an ion current is taken in one electrode, an electron current must be drawn on the other electrode and vice versa). This condition, together with the non-linearity of the voltage-current characteristics, forces the potential of the contacting electrodes to be negative relative to the plasma. This is illustrated in figure 6.2 and can be understood as follows. If the potentials of both electrodes are higher than the plasma potential, then both electrodes will draw a net electron current and current continuity cannot be satisfied. Likewise in the case where one electrode has a potential lower than the plasma potential and the other electrode has a potential higher than the plasma potential, the small ion current drawn in one electrode cannot compensate the high electron current drawn in the other electrode so once again current continuity cannot be satisfied again.

It is also worth noting that the electrodes are asymmetric in the sputtering system, with the surface area of the ground bias much larger than that of the target. The large surface area of the ground implies that its voltage swing should be smaller than that of the target potential in order to maintain current continuity.

In an RF plasma in a properly earthed apparatus, the plasma potential and the floating potential both oscillate and the ground potential stays fixed relative to the laboratory's ground. However, in order to understand the dynamics of electric

potentials in the plasma system, it is much more convenient to redefine the plasma potential as the zero of potential. Under such a transformation, the potential of the ground electrode now oscillates.

We therefore expect the potentials of the electrodes to vary as shown in figure 6.3b which plots the target potential (blue line) and ground potential (red line) with respect to the plasma potential. As discussed, these potentials are always lower than the plasma potential V_s. The voltage variation for $V > V_f$ should be very small (drawing electron current) compared to that for $V < V_f$ (drawing ion current) due to current continuity requirement and the non-linearity of the I-V characteristics.

To find the target potential relative to ground, one can simply subtract the blue curve from the red curve and the result is a sine-like curve with a negative DC offset as shown in figure 6.4 where we have transformed back to the frame of reference with V_{ground}=0 V.

We illustrate the spatial variation of the electric potential in figure 6.4. In the bulk of the plasma, the plasma potential stays relatively constant [1]; whereas near the electrode surface, the potential plummets severely once the plasma sheath is entered.

The behaviour of the electric potentials of the plasma system can be modelled using an equivalent circuit model as shown in figure 6.5. In the plasma sheath region, the positive space charges can be modelled primarily as capacitive; meanwhile an additional parallel resistor represents the collisional power dissipation in the sheath. A diode is also incorporated in the sheath equivalent circuit to model the non-linearity introduced by the relative suppression of ion currents compared to electron currents. The capacitance connecting the RF source includes the total

[1] actually there are significant variations of the plasma potential across the chamber due the plasma confinement, this will be discussed later in later section of this chapter

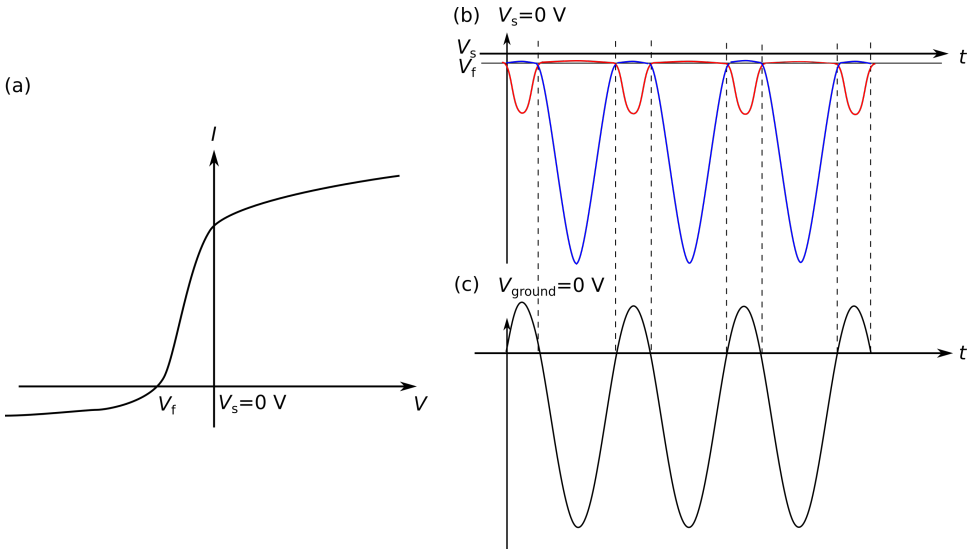

Figure 6.3: (a) A sketch showing the expected current drawn I when there exists a voltage V between the electrode and the plasma. (b) The red line shows the oscillation of the ground potential relative to the plasma potential V_s=0 V; while the blue line shows the variation of the target potential with respect to V_s. Combining the graphs in (b) and (c), one would expect the target potential-to- ground to take a form similar to that of the black line. In this curve, we have transformed back to V_{ground}=0 V.

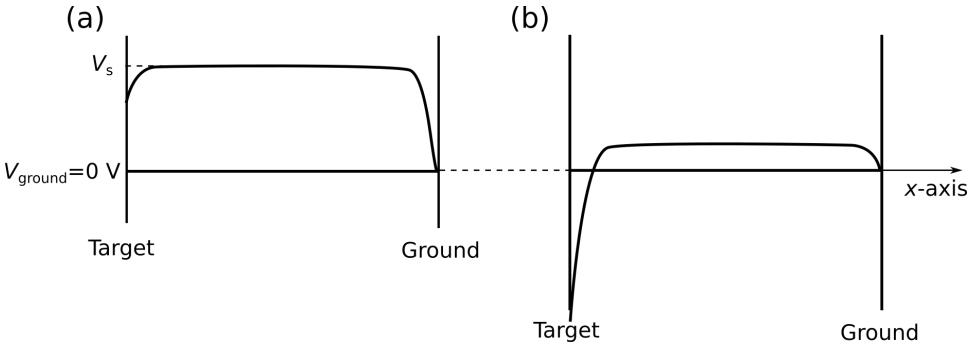

Figure 6.4: A sketch illustrating the 'simplified' spatial variation of the electric potential of an asymmetric magnetron discharge for two instants in time that are half an RF cycle apart.

capacitance arising from the target insulator and the matching network. The charge storage ability of this capacitance allows the target to acquire and store a constant negative DC bias which is fueled once a cycle by the positive RF excursions that collect bursts of electron current. Away from the electrode, the bulk plasma is simply represented using a resistor to take into account the bulk power dissipation due to collisions.

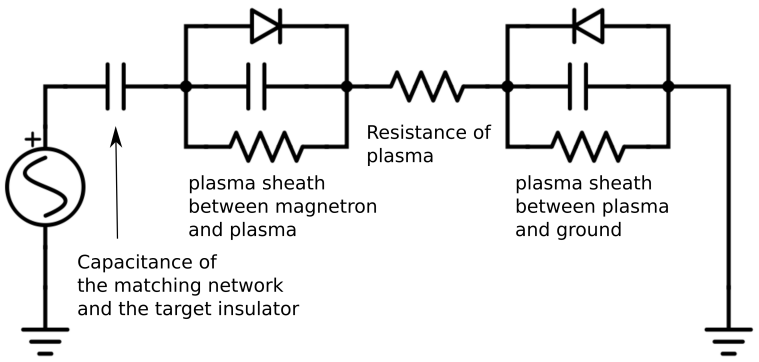

Figure 6.5: An equivalent circuit of a capacitive magnetron discharge

6.2 Langmuir probe diagnostics of a RF plasma

In order to investigate the plasma conditions of the RF magnetron plasma, a single Langmuir probe comprising a cylindrical metallic wire is inserted into the magnetron plasma and subsequently DC biased to collect either an ion or an electron current.

Consider the situation when the probe is DC biased with respect to ground at a voltage V_{DC}. If the probe is perfectly compensated (this will be discussed later in section 6.4), then the voltage of the probe $V_p(t)$ is given by (see figure 6.6):

$$V_p(t) = V_{\mathrm{DC}} + (V_s(t) - V_{s,\mathrm{DC}}). \tag{6.1}$$

where $V_{s,DC}$ is the DC voltage applied relative to ground to make the probe voltage equal to the plasma potential and V_s(t) is the plasma potential relative to ground at time t. The difference between the probe potential with respect to the plasma potential therefore transforms as:

$$V_p(t) - V_s(t) = V_{\mathrm{DC}} - V_{s,\mathrm{DC}}. \tag{6.2}$$

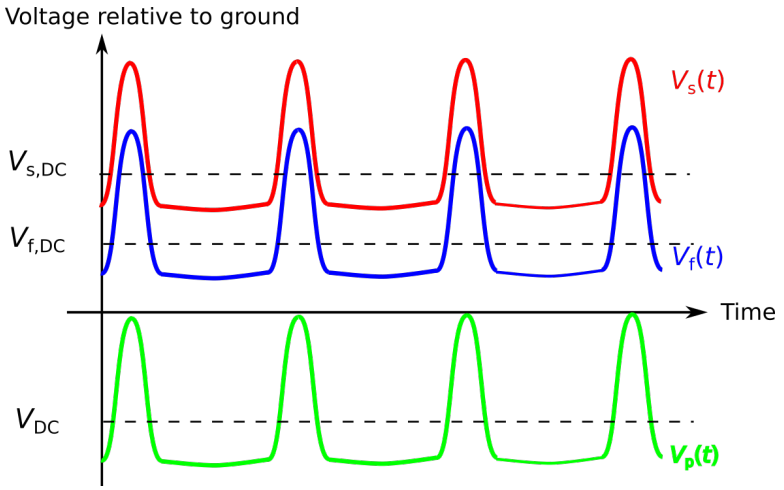

Figure 6.6: A diagram showing the relationship between the plasma potential $V_s(t)$, the probe potential $V_s(t)$ and the floating potential V_f when the probe is biased with V_{DC} relative to ground.

Under this condition, DC Langmuir probe theories can be applied. In what follows, we will derive the expected I-V characteristics of such a compensated Langmuir probe. The plasma is considered to be collisionless, i.e., it is a low pressure plasma with a large particle mean free path.

When $V_{p,\mathrm{DC}}$<$V_{s,\mathrm{DC}}$, the probe is negatively biased; positive charges accumulate around the probe forming a positive space charge sheath. It acts to shield surrounding plasma from the effect of the probe so that charge carriers outside the sheath experience no electric field due to the probe's presence. The characteristic length scale for this electrical screening is referred as the Debye length λ_D. One would then expect to collect a current that corresponds to ions diffusing thermally into the sheath. However, it can be shown that, under the assumption that the ions are moving much slower than the electrons, the ion current is instead determined by the 'Bohm criterion'. The criterion stated that in order for a sheath to form, the ion must enter the sheath with a speed exceeding the Bohm velocity $u_0 = \sqrt{\frac{k_B T_e}{m_i}}$ where T_e is the electron temperature and m_i is the ion mass. This condition can be derived based on the fact that the ion density ought to be greater than the electron density in the positive space charge region. Consequently, there

exists a pre-sheath region where the ions are being accelerated to the Bohm velocity. Detailed calculation showed that that the density of ions falls to $1/e$ of the bulk value in the pre-sheath region [45]. Since the flux of ions coming into the sheath is $e^{-1}nu_0$, the ion current I_i collected is:

$$I_{is} = 0.61neu_0A_p \tag{6.3}$$

where I_{is} is the saturation ion current, A_p is the area of the probe and n is the density of ions. Although electrons are being repelled in the negatively biased regime, some electron current is still be collected since electrons are light and mobile. Assuming that the electron thermal energy is governed by the Maxwellian distribution with an electron temperature T_e, the electron current I_e is given by:

$$I_e = I_{es}e^{\frac{-e(V_{s,\mathrm{DC}}-V_{p,\mathrm{DC}})}{k_BT_e}}, \tag{6.4}$$

where I_{es} is the electron saturation current.

When $V_{p,\mathrm{DC}}$ is larger than $V_{s,\mathrm{DC}}$, the probe is positively biased and there is a negative space charge sheath. The thermal flux of electrons falling into the sheath is given by $\frac{1}{4}nv_{th}$, with $v_{th} = \sqrt{\frac{8k_BT}{\pi m_e}}$ being the thermal velocity of the electron and $\mathrm{m_e}$ is the mass of the electron. The saturation electron current I_{es} is therefore:

$$I_{es} = \frac{1}{4}nev_{th}A_p. \tag{6.5}$$

The ion current in the positively biased regime is negligible compared to the electron current. Hence, the total current collected I is:

$$I = \begin{cases} -0.61neu_0A_p + \frac{1}{4}nev_{th}A_pe^{\frac{-e(V_{s,\mathrm{DC}}-V_{p,\mathrm{DC}})}{k_BT_e}} & \text{for } V_{p,\mathrm{DC}} < V_{s,\mathrm{DC}} \\ \frac{1}{4}nev_{th}A_p & \text{for } V_{p,\mathrm{DC}} > V_{s,\mathrm{DC}} \end{cases} \tag{6.6}$$

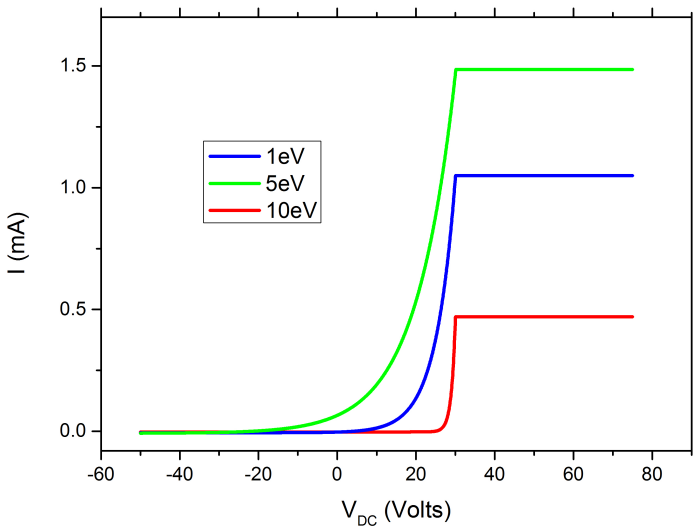

Figure 6.7: The ideal I-V characteristics of a Ar plasma with physical parameters $V_{s,\mathrm{DC}}$=40 V, n=10^{16} m^{-3} and A= 1.75 mm^2 for different electron temperatures at T=1 eV, 5 eV and 10 eV. The x axis represents the DC bias relative to ground V_{DC}.

The voltage for which the current collected is zero is known as the floating potential $V_{f,\mathrm{DC}}$. This corresponds to the voltage that the probe would develop if it were electrically insulated. Since the electrons are more mobile, the rate of electrons hitting the probe is larger than that of the ions, so the probe needs to acquire a more negative voltage with respect to the plasma in order to equalise the ion and electron currents. By setting I=0 in equation 6.6 , a relationship between $V_{f,\mathrm{DC}}$ and $V_{s,\mathrm{DC}}$ is found:

$$V_{f,\mathrm{DC}} = V_{s,\mathrm{DC}} + \frac{k_B T_e}{e} \ln\left(0.61\sqrt{\frac{2\pi m_e}{m_i}}\right) \tag{6.7}$$

Figure 6.7 shows the ideal I-V characteristics of a Ar plasma simulated with parameters $V_{s,\mathrm{DC}}$=40 V, n=10^{16} m^{-3} and A_p= 1.75 mm^2 for different electron temperatures at T_e=1 eV, 5 eV and 10 eV.

The voltage for which there is a sharp gradient discontinuity is the plasma potential. Keeping $V_{s,\mathrm{DC}}$ and n constant and raising the electron temperature means more electron current is collected and $V_{f,\mathrm{DC}}$ sits at a more negative potential. This is because the high T_e electrons tend to have larger kinetic energy leading to a higher thermal flux, so more electron charge accumulation on a floating probe is required to repel the incoming electron flux in order to maintain zero net current.

6.3 Realistic I-V characteristics of a Langmuir probe in RF plasma

Unfortunately, in the real world, the actual experimental I-V curves measured are often found to be different from those that are predicted by the idealised theoretical model above. A typical I-V characteristic is shown in figure 6.8. There are two main features that distinguish it from the ideal curve. Firstly, the sharp kink at the plasma potential is rounded such that the slope of the I-V curve becomes continuous. This is caused by the presence of plasma potential oscillations by imperfect probe compensation (as discussed in section 6.4). Secondly, the ion and electron currents do not saturate at the positive and negative extremes of probe bias, but instead continue to rise owing to the enlargement of the probe collection area.

Depending on the geometry of the probe and the size of the sheath, numerous theories were developed to explain and predict how the collection area increases with bias. They include the Child-Langmuir (C-L) [46], the Allen-Boyd-Reynolds (ABR) [47], the orbital motion limited (OML) [48] and the Laframboise theories [49].

Both C-L and ABR theories are based on solving Poisson's equation which governs the relationship between the charge density and the electric potential of the

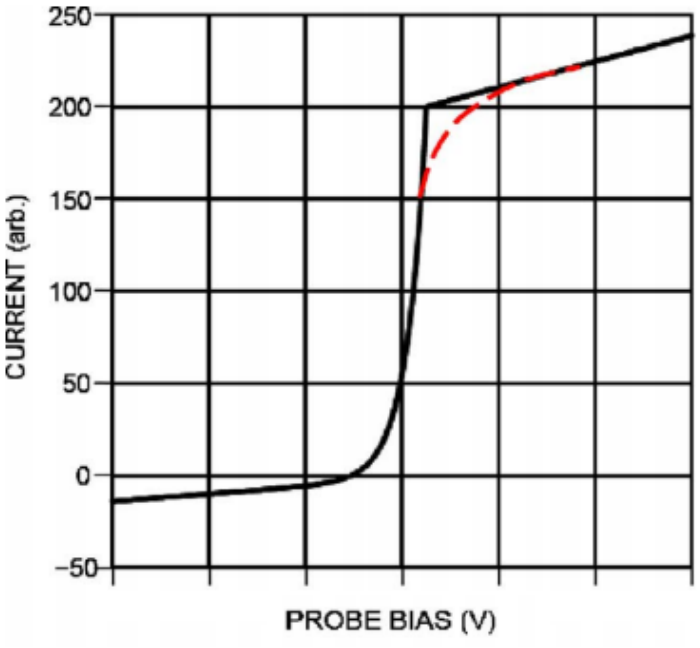

Figure 6.8: A diagram showing the difference between a realistic I-V curve acquired by a Langmuir probe and the ideal I-V curve.

sheath as derived in Appendix A. Disappointingly, Poisson's equation cannot be solved analytically for this case. The C-L theory makes the approximation that the dimensionless parameter $\eta = \frac{|V_{s,\mathrm{DC}} - V_{p,\mathrm{DC}}|}{k_B T_e}$ is much greater than unity; and this condition, the Poisson's equation simplifies to a simple second order linear differential equation which can be integrated straightforwardly to yield:

$$d^2 = \frac{4}{9}\frac{\epsilon_0}{J_0}\left(\frac{2e}{m}\right)^{\frac{1}{2}} |V_p - V_s|^{\frac{3}{2}}, \tag{6.8}$$

where J_0 is the space charge limited current density, m is the mass of the charge carrier, ϵ_0 is the permittivity of free space and d is the sheath thickness. This result is derived assuming a planar geometry; however, it can be shown that for $\frac{r_p}{\lambda_D} < 3$, with r_p being the radius of the probe, equation (6.8) also applies for cylindrical probes. The ABR theory takes the different route of solving the Poisson's equation numerically, and then approximating the numerical solution by fitting an appropriate analytical function.

For cylindrical probes, both C-L and ABR theories break down if the sheath size

is large compared with the probe radius, i.e., $\lambda_D \gg r_p$. Under this condition, the orbital motion of the charge carriers around the probe can no longer be neglected. The OML theory uses simple calculations that involve analysing the trajectory of a charged carrier under the central electrostatic force of the biased probe (see appendix B). The effective collection radius r_{eff} of the probe is found to be:

$$r_{\text{eff}} = \frac{2}{\sqrt{\pi}}\Big(e\eta\Big)^{\frac{1}{2}} r_p \tag{6.9}$$

for $\eta \gg 1$. The Laframboise theory is the most accurate theory available, as it takes into account of the effect of both sheath expansion and orbital motion of the charges. Numerical results are presented in Laframboise's thesis [49] and analytical fitting to the results are available in Ref. [50].

6.4 RF compensation

In order to carry out I-V measurements so that the DC Langmuir probe theories described in section 6.2 can be applied and analysed, one has to find a way to allow the instantaneous AC voltage of the probe to follow the temporal variations in the space potential. If this is not seen too, the measurements are distorted and the electron temperature deduced is therefore severely overestimated (see figure 6.10).

The equalisation of the AC voltage of the probe and the space potential can be achieved using compensation techniques. There are two types of compensation: active and passive.

In active compensation, AC signals are directly fed into the probe to cancel out any difference in AC voltage between the probe and the plasma. This method

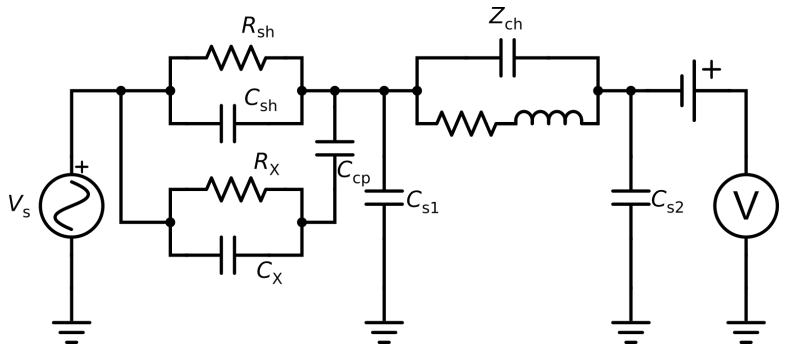

Figure 6.9: An equivalent circuit model highlighting the interplay between the impedances of the sheath Z_{sh}, the compensating electrode, the RF chokes Z_{ch} and the stray capacitances C_{s1}, C_{s2}. In order to compensate adequately, the impedance of the sheath has to be smaller than the rest of the compensating circuits.

requires advanced electronics and very involved tuning, and hence takes a long time to set up.

The passive compensation mode is comparatively easier to implement. The idea is to reduce the impedance path between the plasma and the probe, and at the same time, increase the impedance between the probe and the ground. This effectively forms a potential divider between the sheath and the probe-to-ground impedance so that the voltage across the sheath is minimized. Practically, the plasma-to-probe impedance can be minimized by exposing the plasma to a large compensation electrode which couples to the probe via a capacitor. In this way, only the AC part of the signals are affected. The probe-to-ground impedance can be increased by introducing resonant series LC circuits comprising of chokes with parallel-connected capacitance. These RF blockers should be located as close to the probe as possible to avoid stray capacitance. The passive compensation scheme can be understood more clearly using an equivalent circuit diagram as shown in figure 6.9. Here, Z_{sh}, Z_x and Z_{ck} represent the sheath impedance of the probe, the compensation electrode and the RF chokes respectively; C_{cp} and C_s indicate the capacitance of the coupling capacitor and the stray capacitance.

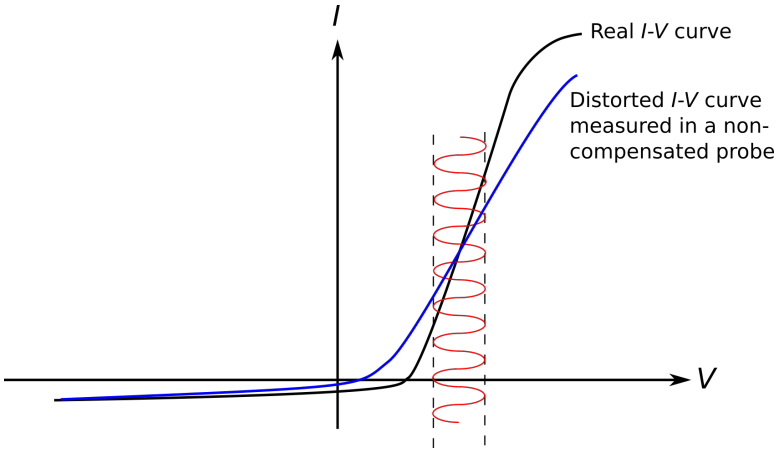

Figure 6.10: The black line shows the real I-V curve. As the relative probe voltage $V_p - V_s$ oscillates due to voltage drop in the sheath, the acquired I-V curve from an uncompensated Langmuir probe is distorted.

6.5 Langmuir probe analysis in magnetic field

In a magnetron configuration, the strong NdFeB magnets provide the magnetic field required both to increase sputter ratio and to allow the discharge to run at a low gas pressure. The magnetic field, however, can be detrimental to the Langmuir probe analysis. It is well known that the presence of magnetic field suppresses the current collected by the probe: this can lead to distortion of the knee region of the I-V characteristics and underestimation of the plasma density [51].

Charged particles follow a helical path with Larmor radius r_L in the presence of magnetic field B. The Larmor radius is given by:

$$r_L = \frac{mv_\perp}{qB} \tag{6.10}$$

where q, m are the charge and mass of the charge particle respectively and $v_\perp$ is the component of the velocity perpendicular to the direction of the magnetic field. The distortion effect is dependent on the ratio of the probe radius to the Larmor radius, β=$\mathrm{r}_p/\mathrm{r}_L$. When β<<1, the Larmor radius is so large that the trajectory of the particle can be approximated as a straight line. Under this circumstance, the particle trajectory is largely unaffected and the collection area is unchanged.

In contrast, conditions of large β result in more severe distortion of the I-V curve. Since the mass of the ion is much larger than that of the electron, the Larmor radius for the ion is relatively large, and hence β is small. Therefore, unless the magnetic field is very large, the ion collection part of the I-V curve is unaffected.

The effect of magnetic field on the I-V curve is also related to the angle of the field with respect to the probe. Under strong field condition, the particles are effectively confined and therefore move in the direction of the magnetic field. This means that the current collected is reduced when the field is parallel to the probe. This effect can be minimized by placing the field perpendicular to the probe so that the effective diffusion coefficient of the particles across the sheath is unchanged.

The optimum Langmuir probe measurement configuration is to use a probe that is as small as possible and to align the probe perpendicular to the magnetic field. In this study, the radius of the probe used is 0.028 mm, and the magnetic field present is less than 50 mT. This means that for a 1 eV electron, $\beta < 0.5$. According to [51], at β=0.5, the modification to the I-V curve is less than 20%, which is comparable to the experimental error. Thus, the effect of magnetic field is ignored in our Langmuir probe analysis.

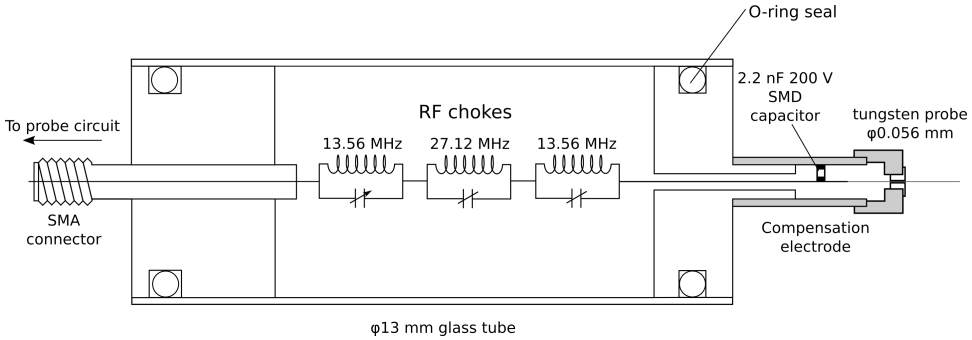

Figure 6.11: The schematics of the in-house designed and constructed Langmuir probe used for measuring the ZnO magnetron plasma

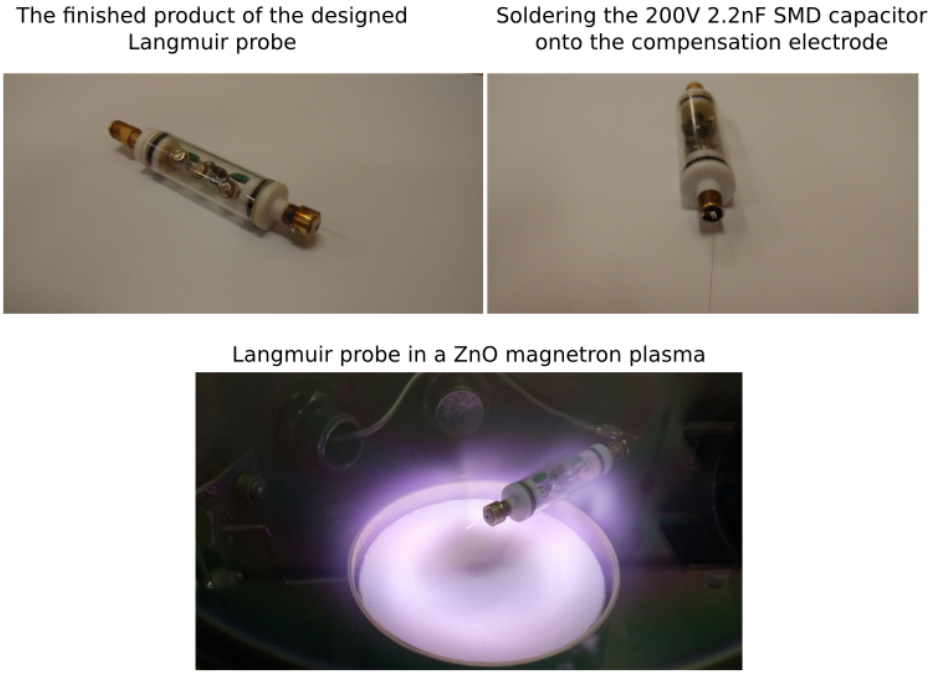

Figure 6.12: Showing the orientation of the Langmuir probe with respect to the magnetron in the vacuum chamber; a red hot, glowing tip was observed at high positive voltage (the regime which large electron current was being drawn.)

6.6 Design of the Langmuir probe and circuitry

The Langmuir probe needs to be configured both mechanically and electrically in order to obtain reliable quantitative results. This section serves to provide a guide to construct a simple Langmuir probe that is usable in diagnosing the plasma conditions of RF magnetrons.

We first discuss the mechanical construction of the probe, which is shown in figure

6.12. To begin with, the material for constructing the probe must be able to withstand the high temperature of the plasma. In this respect, glass tube and PTFE were chosen as working materials for making the insulated casing of the probe which shields the internal conducting parts. The whole body of the Langmuir probe should also be made as small as possible to minimize the perturbative effect of its presence on the properties of the adjacent plasmas. The dimensions of our Langmuir probe used were 70 mm long and 13 mm in diameter.

The diameter of the current collecting tip has to be made as small as possible to avoid error due to distortion from magnetic field (see section 6.5). Due to the small diameter, a very rigid material is needed to provide the physical integrity (otherwise the tip would not remain straight). Tungsten wire of diameter 0.028 mm was used in our Langmuir probe. In order to integrate such a small tungsten wire into the rest of the electrical circuit, a small hole is first drilled into a ϕ1.6 mm solderable wire, and the tungsten wire is crimped into the bigger wire using a pair of pliers.

The RF blockers, each consisting of parallelly connected capacitor and inductor are installed as close to the tip as possible to minimise the stray capacitance. For this reason, the chokes are put inside the glass casing, only 20 mm away from the tip. These RF chokes were tuned to resonance at the first and second harmonics of the applied RF field, i.e., at 13.56 MHz and 27.12 MHz. This is to minimise the voltage drop in the sheath at these two frequencies so that the voltage oscillation of the probe tip faithfully follows that of the space potential. An S_{21} measurement was made on the tuned RF chokes as shown in figure 6.13. The signal attenuation is about 75 dB at 13.56 MHz and 55 dB at 27.12 MHz. It should be noted that capacitors with lossy plastic dielectric should be avoided as they heat and melt when subjected to large RF voltages; this issue can be resolved by using mica ceramic capacitors instead.

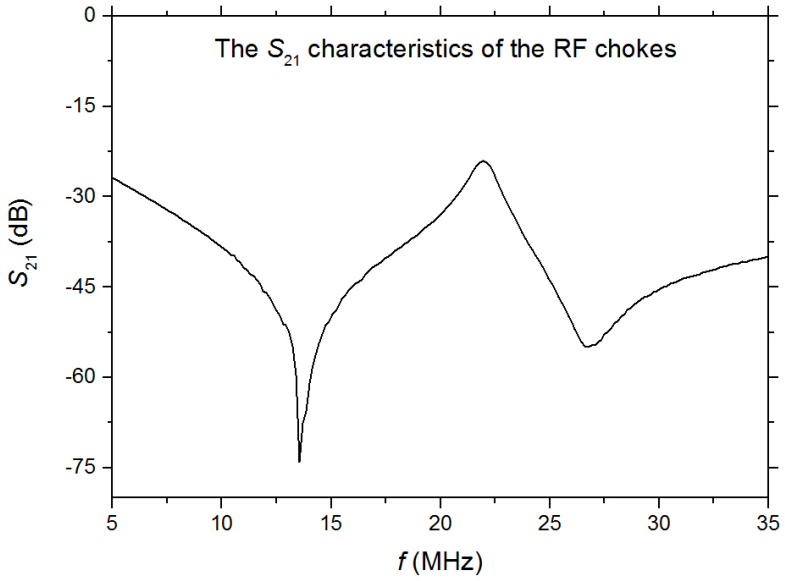

Figure 6.13: This figure shows the S_{21} measured for the tuned RF chokes. One can identify a large drop in S_{21} at 13.56 MHz and 27.12 MHz.

The RF compensation can be improved further by having a compensation electrode. This electrode should be put as close to the probe tip as possible and cannot be made too large, otherwise the compensation electrode will sense and relay a different variation of space potential owing to the position dependence of the plasma properties near the a magnetron. The compensation electrode in the probe that we constructed had of diameter 7.5 mm and length 8 mm. The compensation electrode is connected to the probe circuit via a 2.2 nF high voltage (200 V) SMD capacitor which is soldered on the inside of the metal electrode (see figure 6.12).

The Langmuir probe is connected to a bendable semi-rigid coaxial cable which allows easy manipulation of the probe position and orientation with respect to the magnetron. The probe is positioned above the centre of the magnetron in the position where the films grow. In this position, the magnetic field is normal to the magnetron; so as discussed in section 6.5, it is best to orient the probe parallel to the magnetron as illustrated in figure 6.12 in order to minimize the effect of the magnetic field.

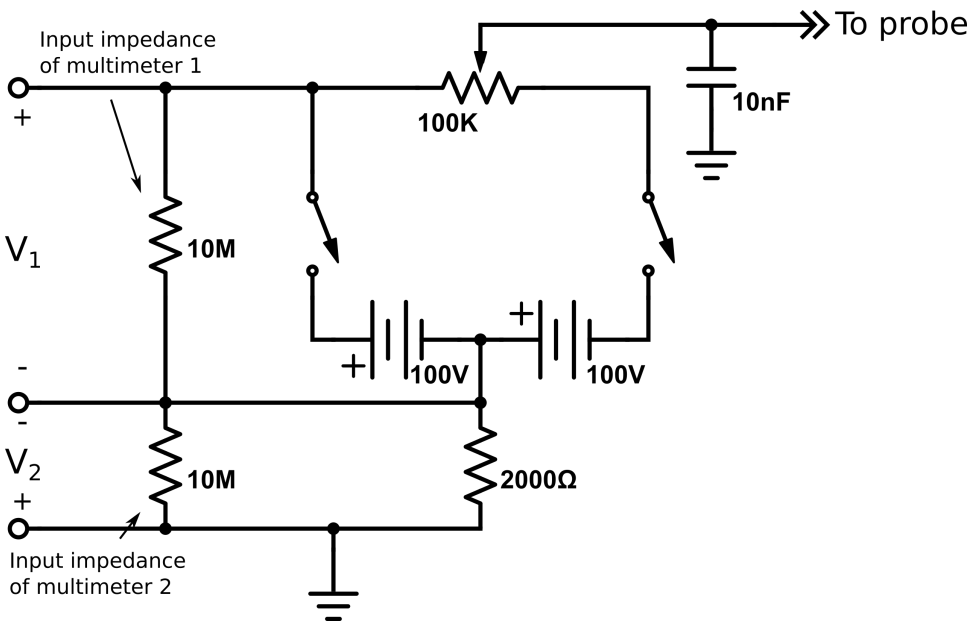

Figure 6.14: The circuit diagram of the probe circuit for Langmuir probe data acquisition

In order to acquire the *I-V* characteristics, a voltage sweep unit and a current measuring device are needed. The voltage sweep can be produced, for example, by a programmed DC signal generator, or even by stepping down the mains voltage. However, one has be careful with the sweep rate; fast voltage sweep would introduce a large capacitive current which would severely distort the *I-V* curve acquired. In our probe circuit, we use 100 Volt banks, each comprises twelve 9 volt batteries. The voltage sweep is obtained by manually varying the 100 KΩ potentiometer from -100 V to 100 V at a rate of about 2 minutes per full sweep. While the voltage is sweeping, ion or electron currents are being drawn from the plasma, and they pass through a current shunt resistor (2000 Ω) which connects the current to a voltage reading. Illustrated in figure 6.14 is the probe circuitry. In this particular set up, the current I is given by $I = \frac{V_2 \text{Volts}}{2000\,\Omega}$ and the voltage applied to the probe with respect to ground is $V = V_1 - V_2$. Both V_1 and V_2 are measured using a high impedance (10 MΩ) digital multimeter and the results are logged by a computer using a Labview interface. To further reduce the noise due to the stray RF breakthrough (inevitably the RF choke does not block all the RF), a 10 nF

capacitor is inserted between the probe circuit and the Langmuir probe to short the 13.56 MHz breakthrough to ground. The capacitance value chosen is such that its impedance at 13.56 MHz signal is small, but the capacitive current due to the voltage sweep is still significantly less than the ion current being collected.

6.7 Analysis of Langmuir probe measurement for a ZnO plasma

If the configuration of the Langmuir probe I-V measurement is set up correctly, one should obtain an analysable curve. In order to extract a reliable the physical properties of the plasma from this data, one needs to apply the appropriate theories that correspond to the specific plasma operations regime. There exists a large volume of literature on the subject of analysing the I-V characteristics, and the level of complexity of each analytical model varies. This section aims to outline the simplest model that works well with our magnetron plasmas.

The procedures for analysing the I-V data are as follows:

1. Smoothing of the I-V data

    - We need to smooth the data in order to get an accurate measure of $\frac{dI}{dV_{\mathrm{DC}}}$ for locating the plasma potential. However, the smoothing process needs to preserve the shape of the I-V curve, so it is immediately obvious that the moving average technique is not appropriate. Instead, for this purpose, the Savitzky-Golay (S-G) filter is used. This filter first divides the whole data set into multiple data subsets. The subsets will then be individually fitted to polynomials of order n. Figure 6.15a and b compare the noisy raw data with the smoothed data using a S-G filter of polynomial order 2 at a window of 400 data points.

2. Finding the floating potential $V_{f,\mathrm{DC}}$

   - $V_{f,\mathrm{DC}}$ is found by locating the voltage for which the current is zero, this is when the ion current is equal to that of the electron current.

3. Locating the plasma potential $V_{s,\mathrm{DC}}$

   - Because the electron current saturates at the plasma potential, a kink is observed in the I-V curve as illustrated in figure 6.15f, g. An accurate value of $V_{s,\mathrm{DC}}$ can be found by locating the voltage for which $-\frac{dI}{dV_{\mathrm{DC}}}$ is maximum.

4. Finding the electron temperature T_e

   - The logarithm of the total current versus voltage is linearly fitted between the range of $V_{f,\mathrm{DC}}$ and $V_{s,\mathrm{DC}}$. An initial estimate of the electron temperature can be found by setting $\frac{1}{k_{\mathrm{B}}T_e}$=slope of linear fit.
   - Using this initial temperature estimate T_e, the ion current is fitted by the function $I_i = I_{i0}(1+\eta)^{\kappa}$ (figure 6.15e) in accordance with the Laframboise parametrization [52]. This takes into account the sheath expansion at large voltage deviation from the plasma potential. The electron current I_e is then given by $I_e = I_{tot} - I_i$.
   - Now by linearly fitting ln T_e versus V_{DC}, one obtains a better estimation of the electron temperature.
   - The last two steps are repeated to get an increasingly accurate value of T_e. The good linear fit of ln I_e versus V_{DC} confirms the reliability of our data.

5. Finding the ion/electron density n

   - Due to the uncertainty of the ion mass (the ratio of ion species that is present in the plasma is unknown for a mixed $\mathrm{Ar/O_2}$ sputter-gas but

could probably be discovered using optical spectroscopy), it is difficult to estimate the ion density using the ion current. Instead, as long as $r_p/r_L<1$ (as discussed in section 6.5), we can rely on using the characteristics of electron current to find n. In the regime of thick sheath (due to the small mass of the electron), OML theory is applicable and the electron density is given by:

$$n^2 = -\frac{\pi^2 m_e}{2A_p e^3}\frac{dI^2}{dV_{\mathrm{DC}}}, \tag{6.11}$$

and the term $\frac{dI^2}{dV_{\mathrm{DC}}}$ can be determined by the slope of the linear curve given by I^2 versus V_{DC} for $V_{\mathrm{DC}}>V_{s,\mathrm{DC}}$ (see figure 6.15g). Because of plasma neutrality, the ion density should be the same as the electron density.

6. Estimating the sheath thickness x_{pf} at $V_{f,\mathrm{DC}}$ and the electric field E at the surface of a planar substrate with dimensions much larger than λ_D

   - In order to find an analytical solution for the sheath thickness and the electric field of the cylindrical Langmuir probe, one has to solve Poisson's equation. However, as described in section 6.2, since this equation is practically insoluble, numerous tactics and tricks have been used to yield approximate solutions; they usually involve heavy computational analysis. Fortunately, what interests us in this particular Langmuir probe analysis is to find how the substrate behaves during magnetron sputtering. The problem falls into the 'thin sheath' regime, where the substrate dimension is much larger than λ_D and the Child-Langmuir law applies. The sheath thickness at the floating potential x_{pf} is given by:

$$x_{pf} = 1.018\Big(\frac{e(V_{s,\mathrm{DC}} - V_{f,\mathrm{DC}})}{k_B T_e}\Big)^{\frac{3}{4}}\lambda_D \tag{6.12}$$

where the Debye length is:

$$\lambda_D = \sqrt{\frac{\epsilon_0 k_B T_e}{e^2 n}} \tag{6.13}$$

and the largest electric field near the surface is given by the Mackeown equation:

$$E = \left(\frac{2.88 n^2 e k_B T_e (V_{s,\mathrm{DC}} - V_{f,\mathrm{DC}})}{\epsilon_0}\right)^{\frac{1}{4}}. \tag{6.14}$$

The full derivation of these equations is described in Appendix A. It should be noticed that the sheath thickness actually oscillates at 13.56 MHz with the applied RF voltage; the value we obtain here is the mean values of these oscillations.

7. Estimating the ion flux J to a planar substrate

   - At the plasma potential, the sheath thickness of the cylindrical probe is zero, so the effective collection area is equal to the probe area. Hence, the ion flux J incident on a planar substrate can be estimated from the ion current drawn to a cylindrical probe held at the plasma potential, i.e.,

$$J = \frac{I_{i0}}{A_p e} \tag{6.15}$$

6.8 Results and Discussion

Using the analytical methods as described in the previous section, the I-V curves for the ZnO magnetron at various powers (40-120 W), pressures (2 μbar-20 μbar) and substrate-target distances (25 mm or 45 mm centrally above the magnetron) are investigated. The results are summarised in figure 6.16. Here, the red and blue lines indicate measurements at 25 mm and 45 mm respectively, while the circle, square, triangle and diamond symbols represent data points at pressures of 2, 4,

10 and 20 μbar respectively. In the following, we will discuss how the plasma's 'physical parameters' vary with the 'engineering parameters' and how they relate to the substrate environment of the substrates during a sputter deposition process.

1. Electron temperature T_e

   - The electron temperature characterises the kinetic energy of the electrons and hence the ionising capability of electrons in a plasma. The electron gains energy by electrostatic repulsion from the target, so we expect the electron energy to be higher when the target potential is more negative. In a region that is close to the target surface, the ejected secondary electrons have less chance to collide with other atoms or ions, so they maintain a relative high energy. As we move away from the target, these electrons lose their energy via collisions with other particles in the system, and therefore we expect T_e to reduce at higher target-substrate distances. In our particular magnetron configuration, T_e decreases from around 3 eV to 2 eV [2] as the substrate-target distance increases from 25 mm to 45 mm. It is also found that T_e reduces with increasing pressure. This can be explained by the fact that, at a lower pressure, there are fewer atoms to participate in ion- forming collisions; thus in order to sustain the plasma, the system will have to compensate by having higher electron energies. The reduction of T_e as pressure increases is also accompanied by a reduction of the target potential. Although one might expect that the increase in power should raise T_e, T_e actually stays fairly constant with increasing power. This might be due to the increase in ion density which leads to more electron-atom/ electron-ion collisions causing electron energy relaxation and reduction of T_e.

[2] Note that the conventional units for describing electron temperature is in eV rather than K.

As a rule of thumb, a pure Ar plasma usually has a T_e of around 1 eV. In much of the literature as well as in our studies, it is found that the introduction of O_2 into the plasma has a tendency to raise T_e. The reason for this is still under debate, but it is generally believed that this comes from the electronegativity of the oxygen plasma, due to the presence of O^- ions. It follows that because of plasma neutrality and the negative charge of the O^-, there are more ions than electrons, and so the electrons need to have higher energy (and thus a higher T_e) to sustain the plasma excitation. It has also been reported that bi-Maxwellian distributions were detected in other magnetron systems; however, this behaviour has not been observed in our measurement.

2. $V_{s,\mathrm{DC}} - V_{f,\mathrm{DC}}$

   - When a floating substrate is immersed in a plasma, the substrate will build up a potential that is equal to the floating potential (potential for which current is zero). This potential is always lower than the plasma potential, and so as soon as the ions wander into the plasma sheath next to the substrate surface, they will be accelerated by the electric field and acquire an energy of $V_{s,\mathrm{DC}} - V_{f,\mathrm{DC}}$. Therefore, $V_{s,\mathrm{DC}} - V_{f,\mathrm{DC}}$ determines the average kinetic energy of the singly charged positive ion bombardment which is of order of around 10 eV. It is found that the dependence of the $V_{s,\mathrm{DC}} - V_{f,\mathrm{DC}}$ is the same as that of T_e which is expected as $V_{s,\mathrm{DC}} - V_{f,\mathrm{DC}}$ should be directly proportional to T_e according to equation (6.7).

3. Ion flux J

   - The ion flux is found to be of order $10^{19}\,\mathrm{m^{-2}s^{-1}}$ and it tends to increase with increasing pressure and power and with decreasing substrate-target distance. At low substrate-target distance and high power, the electrons

travel at faster speeds and thus the rate of ion creation increases leading to a bigger ion flux. At higher pressures, the concentration of the gas molecules is larger, so the probability for an electron to hit an atom and create an ion also increases. Again, this leads to an increase in ion flux. Combining the ion flux with the previously deduced $V_{s,\mathrm{DC}} - V_{f,\mathrm{DC}}$, we can find the power flux $J^*(V_{s,\mathrm{DC}} - V_{f,\mathrm{DC}})$ to the substrate. This provides the activation energy for reconfiguration of surface structure of the film as the ion bombardment enhances adatom mobility. The ion bombardment action therefore gives rise to an effective substrate temperature which is much larger than the actual temperature of the substrate.

4. Electron density/ Ion density n

   - The electron density is measured to be of order $10^{16}\,\mathrm{m}^{-3}$ in our magnetron system. This value is quite high considering a thick ZnO target is used. This indicates that a strong plasma confinement is achieved using the strong neodymium magnets. The dependence of n with pressure, power and substrate-target distance are similar to that of J.

5. Electric-field E in the plasma sheath near the substrate surface

   - The electric field of the plasma sheath near the substrate surface was thought to be an important parameter for determining the growth of a thin film that has a preferred orientation or polarization. The effect of the electric field is to lift the energy degeneracy involved between structures of different orientations or polarizations such that a particular one is favoured. In our magnetron system, the electric field near the surface can be as high as $50{,}000\,\mathrm{Vm}^{-1}$. This is a very large electric field; to put it in perspective, it is 1/20 of the electric field needed to ionize air. It is found that the electric field increases with decreasing substrate-target distance and increasing power. This is caused by the

increase in n and the corresponding reduction in the Debye length. On the other hand, at increasing pressure, due to the decrease in T_e, the sheath thickness increases which means that the electric field reduces.

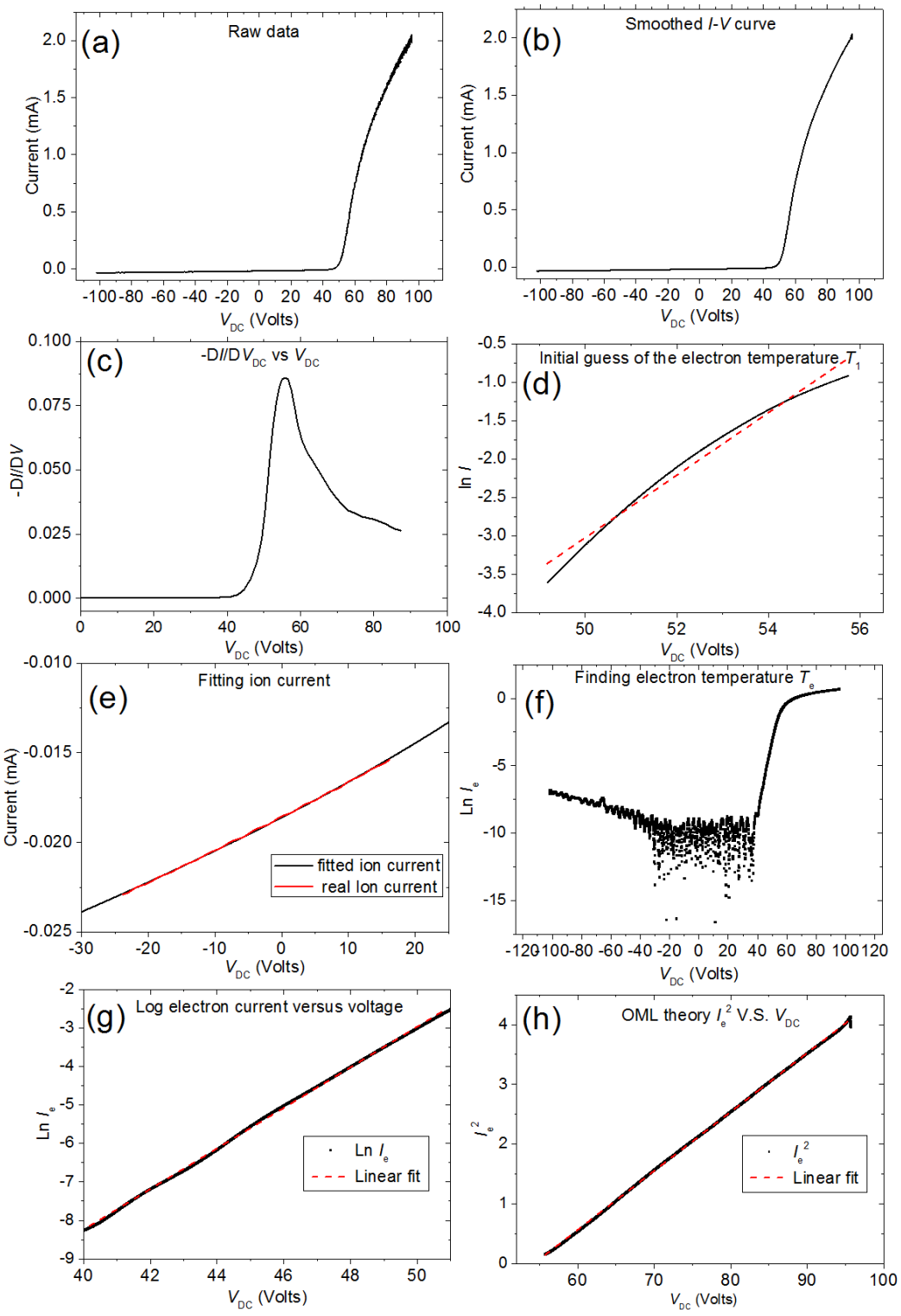

Figure 6.15: (a) raw I-V curve. (b) Smoothed I-V curve using the S-G filter. (c) Smoothed $-\frac{dI}{dV_{\mathrm{DC}}}$ vs voltage. (d) Taking the logarithm of the total current and fitting a linear curve to get an initial guess of the electron temperature. (e) With the evaluated $V_{f,\mathrm{DC}}, V_{s,\mathrm{DC}}$ and the approximated T_e, the ion current is fitted by the function $I_i = I_{i0}(1+\eta)^{\kappa}$ according to the Laframboise parametrization [52]. (f)After calculating $I_e = I_{tot} - I_i$, take the logarithm of I_e and plot it against V_{DC}. The transition from the Maxwellian electron current regime to the saturated current regime marks the turning point at V_{DC}=$V_{s,\mathrm{DC}}$. (g) The linear fit of the logarithm of electron current $\ln I_e$ versus V_{DC}. (h) Linear fit of I_e^2 versus V_{DC} according to the OML theory

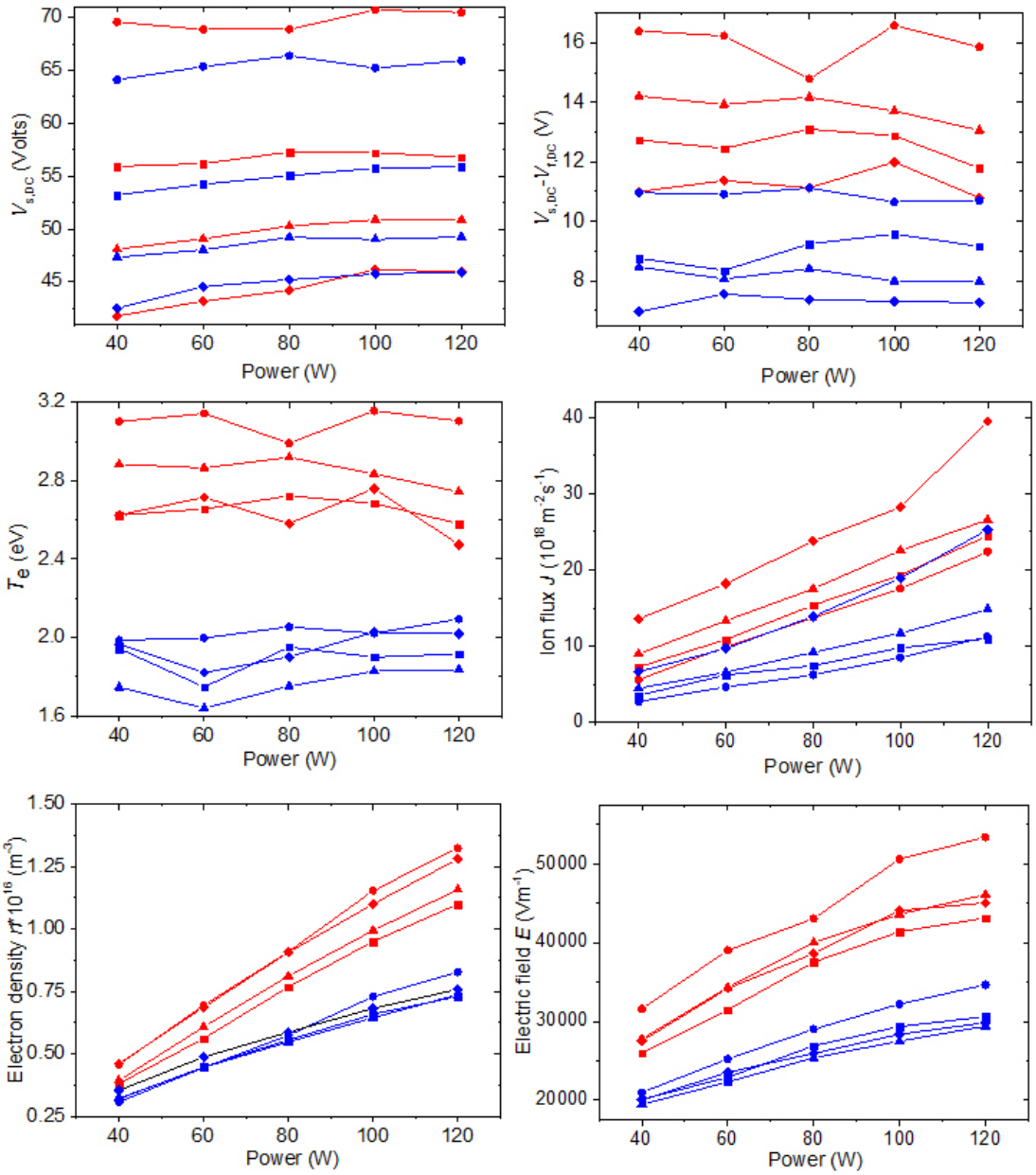

Figure 6.16: Plots of the floating potential V_f, plasma potential V_s, electron temperature T_e, ion flux J, electron density n and electric field E at various powers, pressures and substrate-target distances. Here, the red and blue lines indicate measurements at 25 mm and 45 mm respectively; while the circle, square, triangle and diamond symbols represent data points at different pressures at 2, 4, 10 and 20 μbar respectively.

Chapter 7

Growth mechanisms of c-axis oriented ZnO films and the optimum growth condition

Having used Langmuir probe diagnosis and deposition rate calibration (see table 7.1) to find the physical parameters that characterise the growth conditions, we are in a position to look for correlations between this data and the structural properties of the ZnO thin films made under the various different sputtering conditions. As such, we can gain insight into the deposition process and ultimately reveal the underlying growth mechanism for ZnO thin films with preferred c-axis orientation of the grains.

In this chapter, we will first present the basic micro-evolution processes involved in polycrystalline film growth; this serves as a prerequisite for investigating the growth mechanisms in ZnO thin films. Various aspects of the growth of c-axis oriented ZnO films will be discussed including epitaxial growth, the polarization effect due to the action of the plasma wall potential, the minimization of surface energy and the 'van der Drift' evolutionary selection by 'survival of the fastest'. By

comparing the various models and experimental knowledge about the structural properties of our ZnO films, we deduce that the governing mechanism for growth of c-axis oriented films is the 'survival of the fastest' theory. We further investigate the relationship between ion bombardment and structural properties of the films. It is discovered that the parameter $\Xi = \frac{\text{ion flux} \times \text{ion energy}}{\text{deposition rate}}$ is strongly correlated with the c-axis texture of the film; and that films grown in a high Ξ condition tends to have little c-axis orientation. The adverse effects of having large Ξ can be explained by the tendency of the (0001)-oriented film to renucleate due to the additional cluster dissociation and adatom surface diffusion mobility induced by low energy ion bombardments.

7.1 Microevolution of polycrystalline film growth

The growth of a polycrystalline film typically involves four main processes:
nucleation→impingement/sticking of island→grain growth →coalescence of grains.

1. The film nucleates and begins to grow on a substrate. In this process, the incoming depositing species, also known as the precursors, land on the substrate. The precursors bond to each other due to their mutual attraction, so they cluster into islands of condensed phase. If the substrate possesses a crystal structure, the interaction between the substrate and the precursors can lead to nucleation with a preferred orientation (figure 7.1a). This is known as epitaxial growth. If the substrate is amorphous and the surface mobility is high, it is energetically favourable for the nucleation to present the crystal plane of lowest surface energy plane to the substrate surface which lays the foundation for highly oriented grain growth later on (figure 7.1b). However, when the surface diffusion is insufficient, the nucleation tend to be randomly oriented (figure 7.1c).

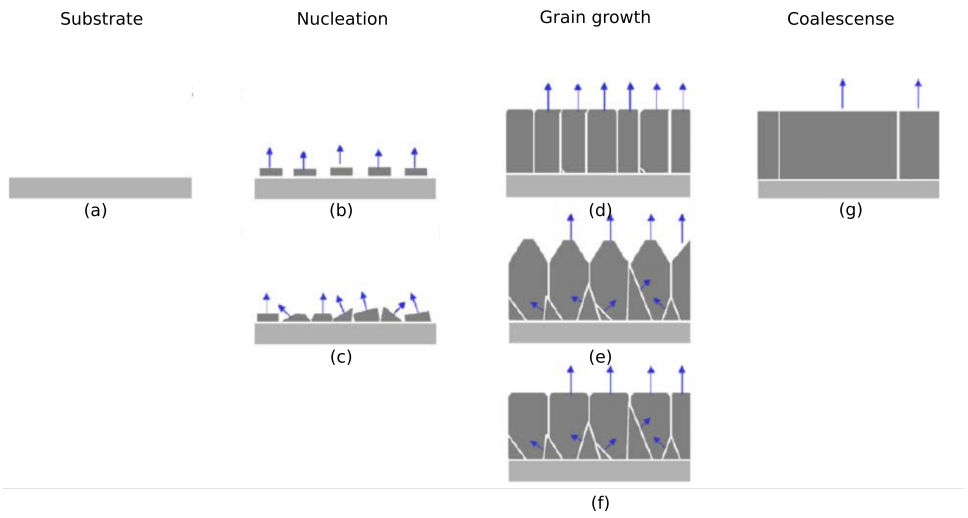

Figure 7.1: (a) Substrate before deposition. (b) Nucleation with preferred orientation. (c) Nucleation without preferred orientation. (d) Grain growth given a preferred nucleation, an equiaxed columnar structure is formed. (e) When the surface diffusion is low, planes with high surface energies are preferred forming non-equiaxed columnar structure with surface texture. (f) When the surface diffusion is high, planes with low surface energies are preferable and non-equiaxed columnar structure without surface texture is formed. (g) Coalescence of grains (diagram adopted from [53]).

2. The islands grow laterally and eventually collide; they will tend to coalesce and lead to the formation of a grain. The grain grows vertically forming a columnar structure.

3. If the nucleation were initially oriented during the nucleation stage, the preferred orientation tends to persist during the grain growth. Films grown under this condition usually have an equiaxed columnar structure (figure 7.1d).

   For randomly oriented nuclei, the preferred orientation of the grain is determined by the surface mobility of the adatoms. The level of surface mobility can affect film orientation in three ways. Firstly, when the surface mobility is extremely low, the structure tends to be randomly oriented as the precursors cannot reorientate themselves to form a coherent structure. Secondly, in situations when surface mobility is low but sufficient such that adatoms only have just enough energy to diffuse within the same grain, then the

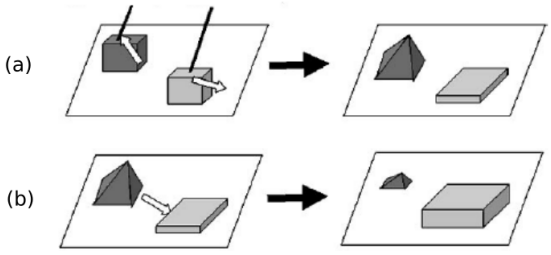

Figure 7.2: (a) When surface diffusion is slow but high enough that adatoms diffuse within the grain, higher surface energy planes will have faster vertical growth speed. They thus dominate the structure of the film due to evolutionary selection. (b) When the surface diffusion is high, i.e., when the adatoms have enough energy to diffuse across the grain, growth of lower surface energy planes is more favourable. This diagram is directly adopted from [54].

planes with high surface energy dominate due to their faster vertical growing speed. This can be understood in terms of the minimization of the total surface energy of the grain which leads to the elongation of grain and thus faster vertical growth (see figure 7.2a) along the high surface energy plane direction. Films grown under this condition usually take the form of non-equiaxed columnar film with surface texture as shown in figure 7.1e. This is also referred to as the van der Drift [55] evolutionary selection model which states that the faster growing species will grow on the expense of the slower growing ones, so the end product consists predominantly of grains with the fast growing orientation. Thirdly, when the surface mobility is high such that the adatoms can migrate to other grains, then the vertical growth rates of the grains will be equalised, so the lowest surface energy plane would dominate the growth due to minimization of overall surface energy (see figure 7.2b). The films fabricated in this case tend to have a non-equiaxed columnar structure without surface texture as shown in figure 7.1f.

4. Finally, the columnar grains coalesce with each other, forming even larger grains as illustrated in figure 7.1g.

7.2 The possible growth mechanisms for preferred orientation in our fabricated ZnO thin films

The mechanism that promotes c-axis orientations ZnO thin film sputter-growth is still unclear in the literature. Four possible growth models have been suggested. In this section, we will offer up each model to the data obtained from our Langmuir probe measurements of the plasma and X-ray measurements of the film and identify the mechanism whose features seem best correlated with the experimental data.

7.2.1 Epitaxial growth

Interaction between the ZnO and the crystal substrate can lead to preferred nucleation. It has been demonstrated that ZnO films can be grown epitaxially in different orientations depending on the substrate; e.g., ZnO thin films grown on c-oriented sapphire [56] or AlN substrates [57] tend to have (002) orientation whereas $(11\bar{2}0)$ oriented ZnO can be produced by epitaxial growth on R-oriented sapphire. In our fabrication, the ZnO thin film is grown on top of a Au electrode layer. According to Wager *et al.*[58], a good crystalline Au(111) substrate layer can improve the quality of ZnO(002) deposited using sputtering. However, as we have demonstrated in section 5.3.3 that there exists an initial dead (disordered) ZnO layer near the Au-ZnO interface, epitaxial growth does not seem to be the driving force for c-axis texture in our samples.

7.2.2 Symmetry breaking under the action of the wall potential

It was proposed that [43] the electric field in the plasma sheath can potentially be significant in the structural formation of ZnO films. As discussed in chapter 5, since the mobility of the electrons is high compared to the ions, an electrically isolated substrate charges to a potential that is negative with respect to the plasma. This leads to the formation of a plasma sheath and an associated electric field that is perpendicular to the substrate surface. It follows that the interaction of the electric field with the polar ZnO structure acts as a symmetry breaker for (0001) and $(000\bar{1})$ planes, and hence contributes to a global asymmetry which promotes a net polarization.

However, it was evident from our Langmuir probe results that the electric field at lower substrate-to-target distance is higher; the fact that even better transducers (more c-axis oriented) can be grown at higher substrate target distance seems to suggest that the electric field does not contribute much to the texture formation.

7.2.3 Minimization of surface energy

Fujimura *et al.* [59] has calculated the surface energy of various planes in ZnO thin films. His calculation is based on counting the number of bonds that the surface lacks, and then multiplying this number by the Zn-O bond energy. Since the (0001)/$(000\bar{1})$ planes are the most densely packed plane (i.e., highest reticular density), the number of bonds in the direction perpendicular to the plane must be smallest. Thus, he deduced that the (0001)/$(000\bar{1})$ planes have the lowest surface energy. However, crystallite surfaces could have different structure to that of the bulk; moreover, this model predicts no surface energy difference between the (0001) and $(000\bar{1})$ surface.

Using more sophisticated models that incorporate surface reconstruction, recent papers [60–62] have predicted the opposite result, i.e., the $(0001)/(000\bar{1})$ planes are the highest surface energy planes and the a-axis planes $(10\bar{1}0)$ and $(11\bar{2}0)$ have lower surface energies. In addition, the calculation shows the $(000\bar{1})$ surface to have a lower surface energy than the (0001) surface. The difference in surface energy between the (0001) and $(000\bar{1})$ surfaces is evident in Hickernel's experimental work [63]. In this paper, it has been demonstrated that the etch rate of the (0001) plane is about 10 times slower than that of the $(000\bar{1})$ plane. He has also reported in another paper [64] that the etch rate for a-axis oriented films is 40-50 times higher than that of the (0001) plane. These results support the finding in the fore-mentioned calculations.

If we now assume the a-axis planes are indeed the lowest energy planes, then minimization of surface energy should give rise to a-axis orientation. The fact that this is not observed in our samples, and that no initial preferred nucleation is found suggests that the mechanism of minimization of surface energy is not relevant.

7.2.4 Survival of the fastest

As discussed in section 7.1, under the condition that surface mobility is low but nonetheless high enough that the adatoms will diffuse within the grain, the planes that have higher surface energy would have a faster vertical growth rate and thus they grow at the expense of the planes that have lower surface energy.

Since we expect the (0001) planes to have the highest surface energy, this is the plane that would dominate according to the 'survival of the fastest mechanism'. This model predicts an initially randomised oriented layer as all possible planes are allowed to grow at the beginning of growth; this seems to agree with our finding about the dead layer at the Au/ZnO interface.

Hence, all the evidences seem to suggest that the 'survival of the fastest' is the growth mechanism which accounts for the formation of c-axis orientations in our fabricated films.

7.3 Why are some films better or worse than the others?

We have discussed in the previous section that surface diffusion plays an important role in determining whether the film grains prefer to orient with the highest energy plane perpendicular to the film normal due to 'survival of the fastest' or with the lower energy planes due to the minimization of surface energy mechanism. In this section, we will assess the effect of ion-bombardment-induced cluster dissociation and surface diffusion enhancement on the structural properties of the ZnO films and how this could militate against (0001) plane formation.

During film growth in an Ar/O_2 sputtering environment, there are two types of ions that bombard the substrate.

The first type is the negative O^-. Typically, even for gas mixtures with a high Ar to O_2 ratio (1:1), only a tiny fraction - of the order of 1% of the ions are of this type (Ref. [65]). Any O^- ions that comes close to the target surface is strongly repelled and some of these eventually hit the substrate with very high kinetic energy ($\approx$ 200 eV). Ions of such high energy can cause severe damage to the film by excessive implantation and sputtering; and films grown under such ion irradiation tend to have large surface roughness which gives them a cloudy or milky like appearance. We cannot extract energy and flux information specific to these negative O^- ions from the Langmuir probe measurements, but judging from the fact that all our films look clear and reflective, the flux of negative O^- ions is likely to be quite small.

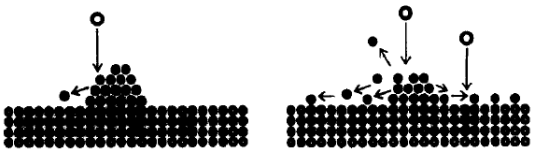

Figure 7.3: An illustration on cluster dissociation and enhancement of adatom mobility caused by low energy ion bombardement.

The other type is the positive ions. These ions diffuse thermally, and some fall by chance into the plasma sheath near the substrate surface and subsequently accelerate towards it under the potential difference $V_{s,\mathrm{DC}} - V_{f,\mathrm{DC}}$ (of order 10 eV). The ion flux J and the energy $V_{s,\mathrm{DC}} - V_{f,\mathrm{DC}}$ are well characterised in the Langmuir probe measurements of chapter 5. Ions of this energy scale can typically induce surface effects such as dissociation of small clusters (see figure 7.3) and also the enhancement of surface adatom mobility depending on the total amount of ion energy transferred to the surface in the time required to condense one layer of atoms. This can be effectively represented by the parameter Ξ such that

$$\Xi = J \cdot \frac{V_{s,\mathrm{DC}} - V_{f,\mathrm{DC}}}{\text{Deposition rate}}. \tag{7.1}$$

In Figure 7.4, we have compared the strength of the c-axis peak with respect to the parameter Ξ under various sputtering conditions. A clear trend can be seen as the c-axis diffraction peak drops as Ξ increases. This can be explained by the fact that the increase in cluster dissociation and surface mobility between grains suppresses the (0001) formation by 'survival of the fastest' and at the same time increases the likelihood of renucleation of planes with lower surface energies. Frequent occurrences of renucleation cause the structure to become more randomly oriented (like those near the Au/ZnO interface) and thus contribute less to the X-ray diffraction signals. When $\Xi = 2.5 \cdot 10^{26}\,\mathrm{Vm}^{-3}s^{-1}$, the formation of (0001) planes becomes strongly suppressed, and the structure is essentially randomly orientated. However, as shown by the red data point in the graph, we found that the c-axis diffraction peak becomes pronounced again at even higher Ξ. We suspect

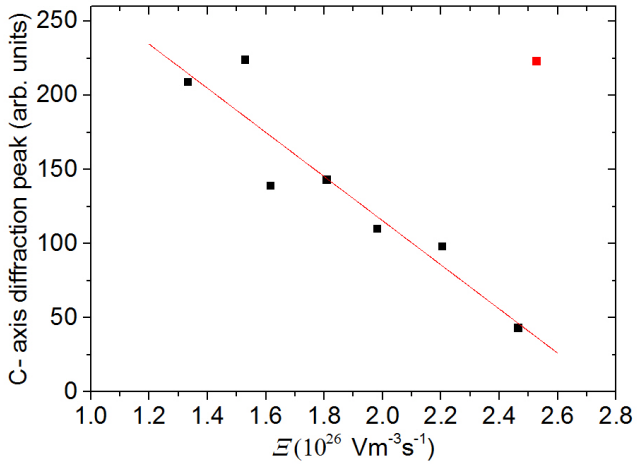

Figure 7.4: The measured c-axis peak versus the parameter $\Xi = \frac{J \cdot (V_s - V_f)}{\text{Deposition rate}}$ for ZnO films that were grown under various sputtering conditions but with the same thickness.

that beyond certain threshold level of Ξ, the suppression of (0001) formation is so high that the ZnO crystallites can save energy by preferentially orienting with the next highest energy plane, (i.e. the $(000\bar{1})$ planes). This finding seems to agree with the study by Ikoma *et al.* [66] which suggests that this unusual orientation can be encouraged by strong ion bombardment conditions. The same argument can be used to predict the formation of a-axis orientations at even stronger ion bombardment conditions, and this has been observed in Refs. [44, 67].

There is also bombardment from particles other than positive and negative ions, such as the secondary electrons. However, these electrons typically have smaller kinetic energies (around 1-3 eV from Langmuir probe measurements). These energies are of the order (or less than) of the binding energy of the atoms in the cluster, and so they are less likely to cause cluster dissociation and hence suppress the fast vertically-growing species. Instead, they serve to facilitate surface mobility within the grain and thus promote better (0001) oriented crystalline quality.

7.4 Optimum growth condition

In conclusion, we have found that the optimum sputtering conditions correspond to minimizing the parameter Ξ. This suggests that good c-axis oriented ZnO films can be produced by decreasing the ion flux or the ion energy directed towards the substrate but without decreasing the deposition rate of the ZnO species. Ultimately, we want to translate this finding into a practical recipe for the growth of good transducers. For any arbitrary magnetron, it is difficult to locate the local minimum of Ξ in terms of engineering parameters (one has to rely on the use of the Langmuir probe measurements); e.g., increasing the pressure would increase J and sputtering rate but lower the energy ($e(V_s - V_f)$) and the mean free path. Hence, the key lies in the design of the ZnO magnetron - one can design a magnetron such that Ξ is intrinsically low and can be minimized at a known sputtering condition.

We have discussed in section 4.2.3 that an unbalanced ZnO magnetron was used in our ZnO deposition. An unbalanced magnetron promotes ion bombardment of the substrate, so in hindsight, our choice of the unbalanced design was not conducive to growing c-axis oriented ZnO films. On the positive side, the unbalanced design was what allowed us to see the effects of ion bombardment and to unlock the growth mechanisms of the c-axis texture formation. In the author's opinion, the best growth conditions for c-axis oriented ZnO films could be more easily achieved by using a balanced magnetron in a sputtering condition with high substrate target distance, high power and low pressure. A balanced magnetron with strong magnetic field confinement prevents charge species from escaping the the target region so that a nearby substrate can simultaneously enjoy the benefit of high growth rate and low bombardment that are the key to making high quality c-axis oriented piezoelectric films.

Power (W)	Pressure (μbar)	Std (mm)	Thickness (nm)	$C_{\max}$ (arb.units)	$\Delta\omega$ (°)	$V_{s,\mathrm{DC}}$-$V_{f,\mathrm{DC}}$ (V)	J ($\mathrm{nm}^{-2}s^{-1}$)	E (Vm^{-1})
60	4	45	530	139	5.87	8.35	6.23	22903
100	4	45	530	209	5.02	9.57	9.80	29347
100	10	45	265	60	7.48	7.99	11.7	27494
100	10	45	530	224	5.19	7.99	11.7	27494
100	10	45	800	345	5.00	7.99	11.7	27494
100	10	45	1060	618	4.12	7.99	11.7	27494
100	20	45	530	98	8.22	7.31	18.9	28369
60	10	45	530	110	7.13	8.06	6.58	22299
100	4	25	530	143	4.72	12.9	19.3	41388
60	4	25	530	43	8.87	12.5	10.9	31469
100	10	25	530	223	4.53	13.7	22.6	43593

Table 7.1: The table shows the data acquired from the Langmuir probe and X-ray characterization of various transducers grown at different sputtering conditions (Power (W), Pressure (μbar) and substrate-target distance std (mm)) at a fixed 1:1 Ar-O_2 gas mixture ratio. Here, C_{max} and $\Delta\omega$ are the c-axis diffraction peak and the FWHM of the rocking curve respectively obtained from the MRD diffractometer, $V_{s,\mathrm{DC}} - V_{f,\mathrm{DC}}$ is the voltage between the bulk plasma and the substrate, J is the ion flux, E is the electric field near the surface of the substrate.

Chapter 8

Background theory of acoustic excitation of magnetostatic spin-waves (MSW) in YIG thin films

Following the successful development of efficient acoustic ZnO transducers, we are in a position to investigate experimentally the viability of the spinmechatronics device proposed in chapter 1 — one that excites laterally propagating spin-waves in a YIG thin film structure by directly injecting a confined longitudinal elastic wave. Before we dive into the experimental details and results, we first develop the necessary theoretical concepts and formulations for understanding each of the key physical processes involved.

We will begin by deriving the equations governing magnetostatic spin-wave (MSW) modes in source-free insulating mediums. These theories will then be applied to predict the behaviour of the uniform precession and propagating MSW modes in a thin film geometry. We will proceed to study the magnetoelastic coupling effects

in YIG, and discuss how an effective oscillating magnetic field can be generated by a longitudinal acoustic wave. Finally, we will discuss how a standing elastic wave can form when a longitudinal acoustic wave is injected perpendicular to the waveguide and how its corresponding effective magnetic field (caused by magnetoelastic coupling) can couple to the laterally propagating MSWs in YIG thin films.

8.1 Governing equations for magnetostatic modes

8.1.1 The Landau Lifshitz equation

Analogous to a spin-top that precesses due to the gravitational force, the dynamics of an individual magnetic moment $\boldsymbol{\mu}$ under the influence of an effective H field $\mathbf{H_{eff}}$ is governed by the torque equation:

$$\boldsymbol{\tau} = \frac{d\boldsymbol{J}}{dt} = \boldsymbol{\mu} \times \mathbf{H_{eff}}, \tag{8.1}$$

where $\boldsymbol{\tau}$ is the torque and $\boldsymbol{J}$ is the angular momentum of the magnetic moment. The magnetic moment is related to its angular momentum by:

$$\boldsymbol{\mu} = -\gamma \boldsymbol{J} \tag{8.2}$$

where γ is the gyromagnetic ratio. Using equations (8.1) and (8.2) and the fact that the magnetization $\mathbf{M}$ is proportional to $\boldsymbol{\mu}$, we can rewrite the torque equation as:

$$\frac{d\mathbf{M}}{dt} = -\gamma\big(\mathbf{M} \times \mathbf{H_{eff}}\big). \tag{8.3}$$

This is known as the Landau Lifshitz equation [68].

The effective local field $\mathbf{H_{eff}}$ that is experienced by the magnetic moments can be expressed as the derivative of the total magnetic free energy density F with

respect to its magnetization $\boldsymbol{M}$:

$$\mathbf{H_{eff}} = -\frac{\partial F}{\partial \mathbf{M}}, \tag{8.4}$$

and this allows us to find $\mathbf{H_{eff}}$ for a given F. The total magnetic free energy density F comprises many contributions. These include those arising from: the external field (F_{ext}), exchange interaction (F_{ex}), demagnetization energy (F_d), anisotropy energy (F_{an}), magnetoelastic interaction (F_{me}), so that

$$F = F_{ext} + F_{ex} + F_d + F_{an} + F_{me} + ... \tag{8.5}$$

The spin precession inevitably decays in time because of various relaxation processes, and this effect can be taken into account by introducing a term (the Gilbert term) that pulls the spin-top inwards so that the angle of precession decreases. Equation (8.3) can be modified accordingly to give:

$$\frac{d\mathbf{M}}{dt} = -\gamma\Big(\mathbf{M} \times \mathbf{H_{eff}} - \eta\mathbf{M} \times \frac{d\mathbf{M}}{dt}\Big), \tag{8.6}$$

which is known as the Landau Lifshitz Gilbert equation [69] with η being the phenomenological damping coefficient.

8.1.2 Polder susceptibility

Now, we will analyse the dynamical interaction between the magnetization and the magnetic field for a magnetic material using the Landau Lifshitz equation. Consider the situation when the magnetic medium is magnetized to saturation in the z direction.

We begin by decomposing $\mathbf{H_{eff}}$ and $\mathbf{M}$ into static and dynamical parts, i.e.,

$$\mathbf{H_{eff}} = \mathbf{H_{in}} + \mathbf{h(t)} \tag{8.7}$$

$$\mathbf{M} = \mathbf{M_s} + \mathbf{m(t)}. \tag{8.8}$$

where $\mathbf{H_{in}}$ is the static internal field of the magnetic material and $\mathbf{M_s}$ is the saturated magnetisation.

By substituting equation (8.8) into the Landau Lifshitz equation (8.3), one obtains:

$$\frac{d\mathbf{M}}{dt} = -\gamma[\mathbf{M_s} \times \mathbf{H_{in}} + \mathbf{m} \times \mathbf{H_{in}} + \mathbf{M_s} \times \mathbf{h} + \mathbf{m} \times \mathbf{h}]. \tag{8.9}$$

$\mathbf{H_{in}}$ and $\mathbf{M_s}$ point in the same direction, the z direction, otherwise the spin would experience a non-zero static torque (we assume no magnetocrystalline anisotropy); thus their vector product becomes zero. We further approximate by considering only the linearised terms, so higher order terms such as $\mathbf{m(t)} \times \mathbf{h(t)}$ are ignored.

The linearised Landau Lifshitz equation becomes:

$$\frac{d\mathbf{M}}{dt} = -\gamma[\mathbf{m} \times \mathbf{H_{in}} + \mathbf{M_s} \times \mathbf{h}]. \tag{8.10}$$

If we assume the solution to this equation is oscillatory, i.e., $\mathbf{m}, \mathbf{h} \propto e^{i\omega t}$ where ω is the angular frequency of the oscillation, then

$$i\omega\mathbf{m} = -\gamma(\mathbf{m} \times \mathbf{H_{in}} + \mathbf{M_s} \times \mathbf{h}). \tag{8.11}$$

Solving this equation, we find that $\mathbf{m(t)}$ and $\mathbf{h(t)}$ are related by a tensor $\hat{\chi}$ such that

$$\mathbf{m} = \hat{\chi}\mathbf{h}, \tag{8.12}$$

$$\hat{\chi} = \begin{pmatrix} \chi & -i\kappa & 0 \\ i\kappa & \chi & 0 \\ 0 & 0 & 1 \end{pmatrix}, \tag{8.13}$$

(8.14)

$$\chi = \frac{\omega_H \omega_M}{\omega_H^2 - \omega^2}, \quad \kappa = \frac{\omega \omega_M}{\omega_H^2 - \omega^2}. \tag{8.15}$$

Here $\omega_H = \gamma H_{in}$, $\omega_M = \gamma M_s$ and $\hat{\chi}$ is also known as the Polder susceptibility tensor [70].

8.1.3 Maxwell's equations

In additional to satisfying the Landau Lifshitz equation, the 'real' magnetic field $\mathbf{H} = \mathbf{H_{ext}} + \mathbf{H_d}$ also has to obey Maxwell's equations. Here, $\mathbf{H_{ext}}$ and $\mathbf{H_d}$ denote the external applied magnetic field and the demagnetising field of the magnetic sample, respectively. Maxwell's equations are:

$$\nabla \cdot \mathbf{D} = \rho_c \tag{8.16}$$

$$\nabla \cdot \mathbf{B} = 0 \tag{8.17}$$

$$\nabla \times \mathbf{E} = -\frac{\partial \mathbf{B}}{\partial t} \tag{8.18}$$

$$\nabla \times \mathbf{H} = \mathbf{J_c} + \frac{\partial \mathbf{D}}{\partial t} \tag{8.19}$$

where $\mathbf{E}$, $\mathbf{D} = \epsilon \mathbf{E}$, ϵ, $\mathbf{J_c}$, ρ_c, $\mathbf{M}$ are respectively the electric field, electric displacement, permittivity, charge density, current density, and magnetization for a linear medium. For a source-free, insulating medium like YIG, $\mathbf{J_c}$ and ρ_c are zero.

Maxwell's equations now become:

$$\nabla \cdot \mathbf{D} = 0 \tag{8.20}$$

$$\nabla \cdot \mathbf{B} = 0 \tag{8.21}$$

$$\nabla \times \mathbf{E} = -\frac{\partial \mathbf{B}}{\partial t} \tag{8.22}$$

$$\nabla \times \mathbf{H} = \frac{\partial \mathbf{D}}{\partial t}. \tag{8.23}$$

According to Refs. [71–73], there exists a branch of solutions to Maxwell's equations for which the speed of the excitation is much slower than that of light, and the wavevector of these waves k is much larger than the wavevector $k_0 = \omega\sqrt{\mu_0\epsilon}$ of plane electromagnetic waves of similar frequency. It has also been shown that the electric field component of these excitations is very small, so the excitation is predominantly magnetic. Under these conditions, the magnetostatic approximation can be made, i.e., $\nabla \times \mathbf{H}$=0. The dynamics of the magnetic excitations (spin-waves) can therefore be described by:

$$\nabla \times \mathbf{H} = 0, \tag{8.24}$$

instead of equation (8.23).

8.1.4 Walker's equation

In the case when the effective internal field $\mathbf{H_{in}}$ is equal to the 'real' magnetic field $\mathbf{H}$, then by combining Maxwell's equations and the Polder susceptibility relation (derived from the Landau Lifshitz equation), we can derive the governing equation for magnetostatic modes. Again, we are assuming that both the magnetization and the internal static field lies along the z direction.

By defining the magnetostatic scalar potential ψ such that:

$$\mathbf{h} = \nabla\psi \tag{8.25}$$

and substituting this into equations (8.22) and (8.12), one obtains:

$$\nabla \cdot \Big[(1+\hat{\chi})\nabla\psi\Big] = 0. \tag{8.26}$$

Expanding in terms of cartesian coordinates (canonical to a planar geometry), we find Walker's equation [74]:

$$(1+\chi)\Big(\frac{\partial^2\psi}{\partial x^2} + \frac{\partial^2\psi}{\partial y^2}\Big) + \frac{\partial^2\psi}{\partial z^2} = 0. \tag{8.27}$$

8.2 Uniform precession modes in magnetic thin films

In this section, we examine the uniform precession mode — the ferromagnetic resonance mode FMR ($\nabla \cdot \mathbf{m}$=0) — in a thin film geometry. The properties of the FMR mode for an arbitrary geometry will first be derived. We will then apply this to the special case of a thin film which is subjected to an oblique magnetic field at an angle θ_{ext} to the normal of the film plane.

In the absence of magnetocrystalline anisotropy, the internal static field of a magnetic material is given by:

$$\mathbf{H_{in}} = \mathbf{H_{ext}} + \mathbf{H_d} \tag{8.28}$$

where $\mathbf{H_{ext}}$ is the external field applied, and $\mathbf{H_d}$ is the demagnetizing field. The demagnetizing field can be expressed as:

$$\mathbf{H_d} = -\widetilde{\mathbf{N}}\mathbf{M}, \tag{8.29}$$

where

$$\widetilde{\mathbf{N}} = \begin{pmatrix} N_{xx} & N_{xy} & N_{xz} \\ N_{yx} & N_{yy} & N_{yz} \\ N_{zx} & N_{zy} & N_{zz} \end{pmatrix} \tag{8.30}$$

is the demagnetization tensor.

Assuming that the internal field $\mathbf{H_{in}} = H_{in}\hat{z}$ and the magnetisation $\mathbf{M} = M_s\hat{z}$ of the magnetic medium are in the z direction; then the linearised Landau Lifshitz equation (equation (8.11)) becomes:

$$i\omega\mathbf{m} = -\gamma\Big[\widetilde{\mathbf{N}}\mathbf{m} \times \mathbf{M_s} + \mathbf{m} \times (\mathbf{H_{ext}} - \widetilde{\mathbf{N}}\mathbf{M_s})\Big]. \tag{8.31}$$

Breaking down this equation into components yields[72]:

$$\begin{pmatrix} i\omega + \gamma N_{xy} M_s & \gamma(H_{ext,z} - N_{zz}M_s + N_{yy}M_s) \\ -\gamma(H_{ext,z} - N_{zz}M_s + N_{xx}M_s) & i\omega + \gamma N_{xy} M_s \end{pmatrix} \begin{pmatrix} m_x \\ m_y \end{pmatrix} = 0. \tag{8.32}$$

A solution exists when the determinant of the 2×2 matrix becomes zero, and this allows us to calculate the FMR frequency ω_{FMR} in the Kittel MacDonald form [75, 76]:

$$\omega_{\mathrm{FMR}} = \Big[(\omega_H + \gamma N_{xx} M_s)(\omega_H + \gamma N_{yy} M_s) - \gamma^2 N_{xy}^2 M_s^2\Big]^{\frac{1}{2}} \tag{8.33}$$

where $\omega_H = \gamma(H_{ext,z} - N_{zz}M_s) = \gamma H_{in}$.

Now we apply the above equations to the case of a thin film geometry with a magnetic field $\mathbf{H_{ext}}$ applied obliquely to the film at an angle θ_{ext} to the normal of

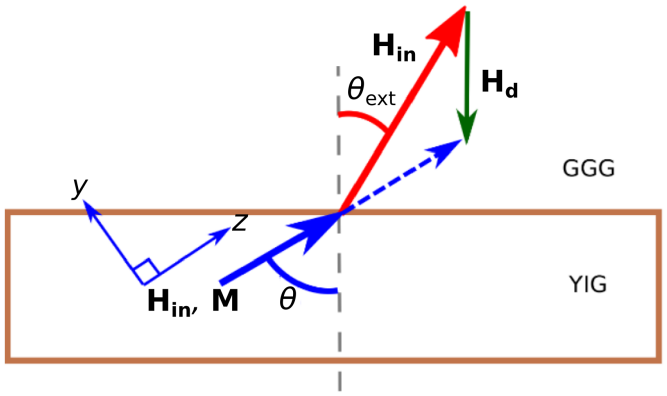

Figure 8.1: An illustration of the relationship between the applied field $\mathbf{H_{ext}}$ and the internal field $\mathbf{H_{in}}$ in a film geometry.

the film plane. In this case, the internal field H_{in} is oriented at an angle θ from the substrate normal as shown in figure 8.1. Again for consistency, we define the z direction to be the direction of the internal field $\mathbf{H_{in}}$ and magnetisation $\mathbf{M}$; the x direction is directed along the substrate plane and the y direction is perpendicular to x and z.

To find $\widetilde{\mathbf{N}}$ for a given θ, we proceed as follows. When the magnetisation is normal to the film, the demagnetising field is -$\mathbf{M}$; whereas if the magnetisation is tangential to the film, no demagnetising field is present. It follows that $\widetilde{\mathbf{N}}$ can be simplified to form:

$$\widetilde{\mathbf{N}} = \begin{pmatrix} 0 & 0 & 0 \\ 0 & N_{yy} & N_{yz} \\ 0 & N_{zy} & N_{zz} \end{pmatrix}. \tag{8.34}$$

When the angle θ of the internal field with respect to the normal is 0° or 90°, $\widetilde{\mathbf{N}}$ is diagonalised and has values:

$$\mathbf{N_{0^\circ}} = \begin{pmatrix} 0 & 0 & 0 \\ 0 & 0 & 0 \\ 0 & 0 & 1 \end{pmatrix}, \mathbf{N_{90^\circ}} = \begin{pmatrix} 0 & 0 & 0 \\ 0 & 1 & 0 \\ 0 & 0 & 0 \end{pmatrix}. \tag{8.35}$$

In the case of an oblique magnetic field, the demagnetisation matrix transforms as $\mathbf{N}_\theta = \mathbf{R}\mathbf{N}_{\mathbf{0}^\circ}\mathbf{R}^T$, with the transformation operator being the rotation matrix:

$$\mathbf{R} = \begin{pmatrix} 0 & 0 & 0 \\ 0 & \cos\theta & \sin\theta \\ 0 & -\sin\theta & \cos\theta \end{pmatrix}. \tag{8.36}$$

Hence, calculation of $\mathbf{N}_\theta$ yields:

$$\mathbf{N}_\theta = \begin{pmatrix} 0 & 0 & 0 \\ 0 & \sin^2\theta & \sin(2\theta)/2 \\ 0 & \sin(2\theta)/2 & \cos^2\theta \end{pmatrix}. \tag{8.37}$$

Substituting the corresponding values of N_{ij} into equation (8.33), one obtains the FMR frequency for the thin film:

$$\omega_{\mathrm{FMR}} = \sqrt{\omega_H(\omega_H + M_s \sin^2\theta)} \tag{8.38}$$

where

$$\omega_H = \gamma H_{in} = \gamma\Big[H_{ext}\cos(\theta_{ext} - \theta) - \cos(2\theta)M_s\Big] \tag{8.39}$$

An extra equation relating H_{ext}, M_s, θ, θ_{ext} can be obtained using the boundary conditions that $B_\perp$ and $H_\parallel$ have to be continuous across the film surface, and this yields:

$$H_{ext}\sin(\theta - \theta_{ext}) = \frac{M_s}{2}\sin(2\theta) \tag{8.40}$$

Using equation (8.38), (8.39) and (8.40), ω_{FMR}, θ, H_{in} can be found for a given H_{ext}, θ_{ext} and M_s.

The relationships between θ and θ_{ext}, θ_{ext} and H_{ext} as well as H_{in} and θ for a YIG thin film that has a FMR frequency of 3 GHz are numerically soluble (using

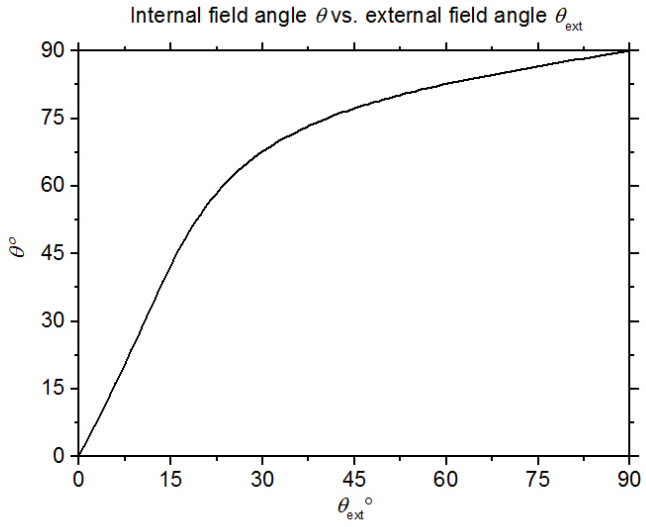

Figure 8.2: The dependence of the internal field angle θ on the angle of the externally applied field angle θ_{ext} (FMR at 3 GHz).

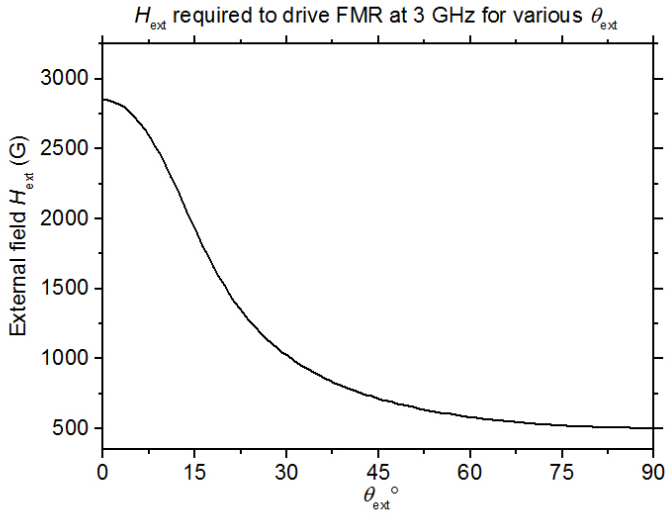

Figure 8.3: The B-field required to drive FMR at 3 GHz as a function of external field angle θ_{ext}.

$4\pi M_s$= 1780 G) and are illustrated in figures 8.2, 8.3, 8.4.

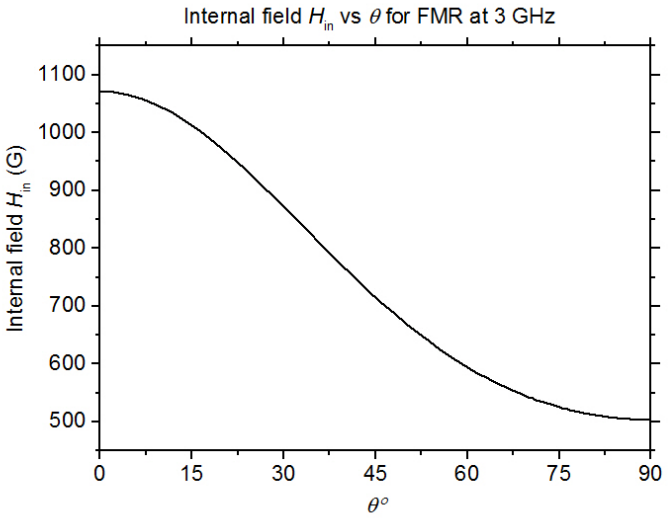

Figure 8.4: The internal field H_{in} required to drive FMR at 3 GHz as a function of internal field angle θ

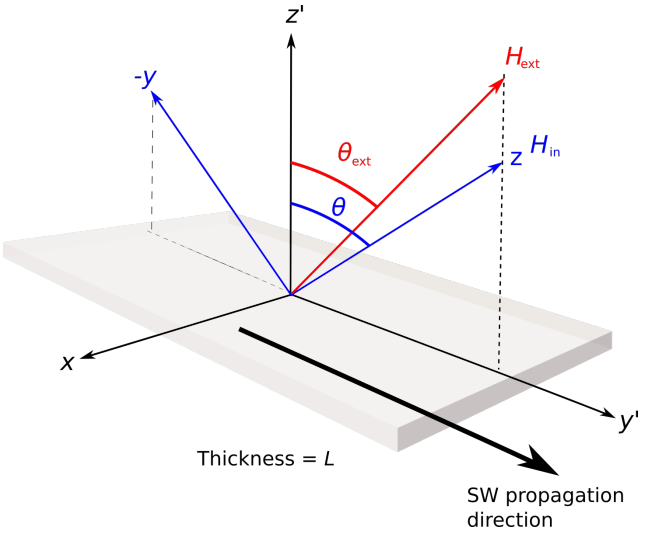

Figure 8.5: Schematics showing the geometry considered when solving for the magnetostatic spin-wave modes. Here θ_{ext} is the angle between the externally applied field and the film normal, and θ is the angle between the internal field and the normal. The magnetic field is applied in the y'-z' plane.

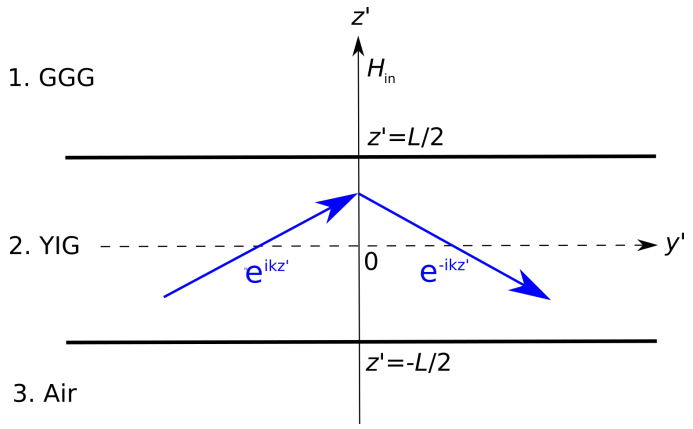

Figure 8.6: Superposition of plane waves in a bounded YIG waveguide.

8.3 Laterally propagating magnetostatic modes in magnetic thin films

The previous section discussed the specific case for which $\nabla \cdot \mathbf{m}$=0. Generally, simultaneous solutions of Maxwell's equations in the magnetostatic limit (equations (8.22), (8.24)) and the Landau Lifshitz equation (equation (8.3)) exist for $\nabla \cdot \mathbf{m} \neq 0$. This means that the spatial profile of the magnetisation $\mathbf{m}$ also contributes to the magnetic field $\mathbf{h}$, and this gives rise to propagating modes with non-zero k. The dispersion relations of these propagating modes can be derived by solving Walker's equations with appropriate boundary conditions.

We look again at the case when the applied magnetic field is long the y'-z' plane. Here, z' is pointing perpendicular to the plane of the thin film and y' is the direction of the wave propagation. The magnetisation is assumed to point along the z axis and the wave propagates along the y' axis. Consider the geometry where the YIG thin film (region 2) is bounded on one side by the GGG (region 1) and on the other side by the air or vacuum (region 3) as shown in figure 8.6.

Let's take the simple case when $\theta_{ext} = \theta = 0°$, i.e. when the applied magnetic field is perpendicular to the film. In this configuration, the y axis and the z axis are aligned with the y' and z' direction respectively. The solution of Walker's

equation can be found by first putting in a trial solution and then forcing it to fulfill the boundary conditions. The trial solution can be guessed in an intuitive way as follows: suppose a plane wave is launched with wavevector $\mathbf{k} = \mathbf{k_t} + k_z\hat{z}$, where $\mathbf{k_t} = k_x\hat{x} + k_y\hat{y}$, this wave would bounce off the interfaces either side of the YIG film, and so the steady state solution is a superposition of two waves with opposite z velocities. Hence, a possible (symmetric) form for the magnetostatic potential in region 2 is:

$$\psi_2(\mathbf{r}) = Ae^{i\mathbf{k_t}\cdot\mathbf{r}}\frac{e^{ik_z z} + e^{-ik_z z}}{2} = Ae^{i\mathbf{k_t}\cdot\mathbf{r}}\cos(k_z z). \tag{8.41}$$

Substituting equation (8.41) into Walker's equation (8.27), we obtain:

$$\frac{k_t}{k_z} = -\frac{1}{\sqrt{-(1+\chi)}}. \tag{8.42}$$

χ=0 for the GGG and the vacuum (see section 8.1.2), and therefore $k_{t,d} = \pm ik_{z,d}$ (d denoting dielectric) according to Walker's equation (8.27). If we choose the potential to be zero at $\pm\infty$, we get exponentially decaying solutions for ψ_1 and ψ_3 such that:

$$\psi_1(\mathbf{r}) = Be^{i\mathbf{k_{t,d}}\cdot\mathbf{r} - k_{z,d}z}, \tag{8.43}$$

$$\psi_3(\mathbf{r}) = Ce^{i\mathbf{k_{t,d}}\cdot\mathbf{r} + k_{z,d}z}. \tag{8.44}$$

We now impose the boundary conditions, i.e., $b_\perp$ continuous (ψ continuous) and $h_\parallel$ continuous (-$\nabla_z\psi$ continuous) [1] at the YIG/GGG and YIG/air boundaries. Since ψ is continuous, we have:

$$Be^{\frac{-k_t L}{2}} = A\cos(\frac{k_z L}{2}) \tag{8.45}$$

$$Ce^{\frac{-k_t L}{2}} = A\cos(\frac{k_z L}{2}), \tag{8.46}$$

[1] The continuity of $b_\perp$ and $h_\parallel$ arise from $\nabla \cdot B = 0$ and $\nabla \times H = 0$ respectively.

so $B = C$. Since -$\nabla_z \psi$ is continuous,

$$k_t B e^{\frac{-k_t L}{2}} = A k_z \sin(\frac{k_z L}{2}) \tag{8.47}$$

$$-k_t C e^{\frac{-k_t L}{2}} = -A k_z \sin(\frac{k_z L}{2}). \tag{8.48}$$

Hence, combining equations (8.46), (8.48) and (8.42), one gets the dispersion relation:

$$\tan\left(\frac{k_t L}{2}\sqrt{-(1+\chi)}\right) = \frac{1}{\sqrt{-(1+\chi)}}. \tag{8.49}$$

This equation has multiple solutions for a given ω and they correspond to the even modes since the modes we chose to examine are symmetric. If an asymmetric trial solution is tried instead of the symmetric choice made in equation (8.41), i.e., $\psi_2 = D e^{i\mathbf{k_t}\cdot\mathbf{r}} \sin(k_z z)$, we obtain:

$$-\cot\left(\frac{k_t L}{2}\sqrt{-(1+\chi)}\right) = \frac{1}{\sqrt{-(1+\chi)}}, \tag{8.50}$$

and the solutions to this equation correspond to the odd modes. The detailed calculations can be found in Stancil's book [71].

This configuration - when the magnetic field is perpendicular to the surface of the sample, is referred to as the **forward volume magnetostatic spin-wave FVMSW**. Here, the term 'forward' means that the group velocity is positive, i.e., it is in the same direction as that of the phase velocity; the term 'volume wave' corresponds to the fact that the wave-mode is active (non-decaying) throughout the whole ferrite region.

A second simple case is when $\theta_{ext} = \theta = 90°$. A similar analysis to the one discussed above gives the result:

$$\tan\left(\frac{k_z L}{2\sqrt{-(1+\chi)}}\right) = \sqrt{-(1+\chi)} \tag{8.51}$$

for even modes, and

$$-\cot\left(\frac{k_z L}{2\sqrt{-(1+\chi)}}\right) = \sqrt{-(1+\chi)} \tag{8.52}$$

for odd modes. These configurations are referred to as the **backward volume magnetostatic spin-wave BVMSW** modes and they are characterized by the peculiar property that the group velocity is always opposite to the phase velocity.

Now when the magnetic field is pointing at an arbitrary angle θ_{ext} to the normal of the plane, both FVMSW and BVMSW types are allowed simultaneously provided that $\gamma H_{in} < \omega < \gamma\sqrt{H_{in}(H_{in}+M_s)}$. Using similar methods to those described above, and with adequate frame transformations, the dispersion relation can be solved analytically as shown by Bajpai [77, 78]. In this case, the dispersion relation can be simplified to a form described in Slavin's paper [79]:

$$kL = \frac{\mid \mu \sin^2\theta + \cos^2\theta \mid}{\sqrt{-\mu}} \times \left[\frac{\pi n}{2} + \tan^{-1}\left(\frac{1+\mu}{2\sqrt{-\mu}}\mathrm{sgn}(\mu\sin^2\theta + \cos^2\theta)\right)\right] \tag{8.53}$$

where n=1, 2, 3.....is the mode number and

$$\mu = 1 + \frac{M_s H_{in}}{H_{in}^2 - (f/\gamma)^2}. \tag{8.54}$$

We calculate these dispersion relations numerically for different external field angles θ_{ext} with f_{FMR} being fixed at 3.0 GHz, γ=2.8 $\times$ 10^6 s^{-1}, $4\pi M_s$=1780 G, L=7.8 μm, n=1. To do this, we first find the corresponding internal field angle θ and H_{in} using equation (8.38), (8.39) and (8.40). We then feed these values into equation (8.54) to find the allowable k value for a given frequency f. Figure 8.7 shows the calculated dispersion relations for various θ_{ext}. Notice that, except for the special case when θ_{ext} =0° or 90° where there is a one-to-one correspondence between f and k, there are always two f's available for each k value, one

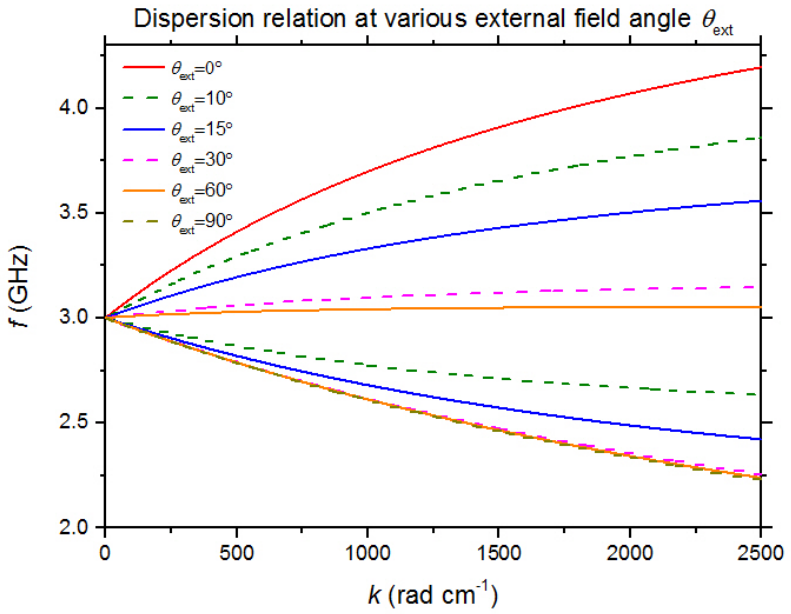

Figure 8.7: The dispersion relations of an obliquely magnetised YIG thin film at various θ_{ext} (n=1 mode).

representing the BVMSW and the other representing the FVMSW.

The group velocities of these magnetostatic modes can be found by simplify differentiating the dispersion relation, i.e., $v_g = 2\pi\frac{df}{dk}$. Using the dispersion relation calculated, we find the group velocities of BVMSW and FVMSW which are shown in figure 8.8. As expected intuitively, the speed of the FVMSW decreases as θ increases while the speed of the BVMSW declines with smaller θ. When θ_{ext} is 45°($\theta \approx 15°$), the speeds of both BVMSW and FVMSW are the same and their dispersion curves are symmetric (blue curve in figure 8.7).

8.4 Magnetoelastic coupling of YIG

8.4.1 Crystal structure of YIG

Yttrium Iron Garnet (YIG), chemical formulae of $Y_3Fe_2{}^{3+}(Fe^{3+}O_4{}^{2-})_3$ is a room temperature ferrimagnetic insulator with very low spin-wave damping [23] and a

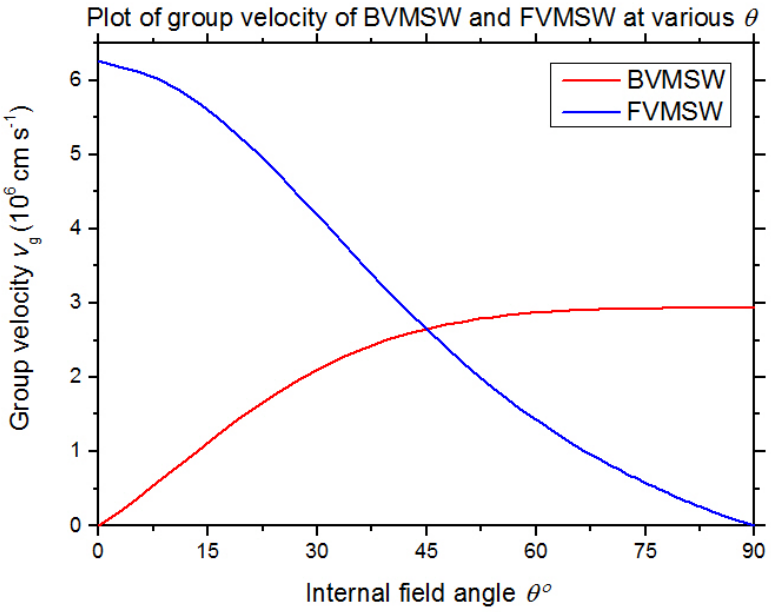

Figure 8.8: Group velocities v_g of FVMSW and BVMSW with f_{FMR}=3 GHz as a function of internal field angle θ (n=1 mode).

narrow ferromagnetic resonance linewidth [80]. The Fe^{3+} ions in YIG are the magnetic species. The electronic configuration of each Fe^{3+} ion is $3d^5$ with quantum numbers S=5/2, L=0 and $J = L + S$=5/2, so the d-orbital shell is half filled and the magnetic moment is 5 μ_B per ion, where μ_B is the Bohr magneton. Since the orbital angular momentum of the Fe^{3+} ions is zero, they are S-state ions which are characterised by symmetrical orbital charge distributions. As explained later, this has profound significance for the magnetoelastic coupling in YIG. The crystal structure of YIG can be described using a conventional cubic unit cell (space group O_h) with lattice constant a_0=12.376Å that consists of four formulae units - a total of 80 atoms. The 20 Fe^{3+} ions in the unit cell are located in two inequivalent positions - 8 of the ions are on the a-sites, and the other 12 ions are on the d-sites, where the a and d sites are surrounded by the octahedral and tetrahedral O^{2-} anion environments respectively (see figure 8.9). These 20 Fe^{3+} ions are all antiferromagnetically coupled to each other by superexchange interaction with J_{ad}=-40 K, J_{dd}=-13.4 K and J_{aa}=-3.8 K (where the exchange interaction is measured in Kelvin) [81]. For practical purpose, the ferrimagnetic nature of YIG

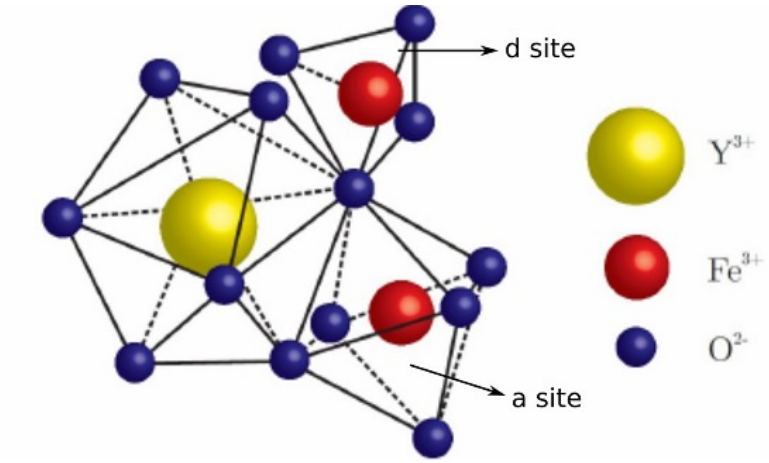

Figure 8.9: The figure shows the YIG crystal structure. The magnetic Fe^{3+} ions located at the center of the octahedral a site and the tetrahedral d site surrounded by O^{2-} anion. Graphics adopted from Ref. [83]

allows it to be thought of as a ferromagnet with a saturated magnetization of $4\pi M_s$= 1780 G and a Curie temperature of T_c=559 K [82].

8.4.2 Micromechanisms of magnetoelastic coupling

Spin-waves are weakly coupled to the elastic waves in YIG. The following sections discuss the possible mechanisms and the quantitative description of magnetoelastic coupling in YIG.

8.4.2.1 Dipole-dipole interaction

Magnetoelastic coupling caused by dipole-dipole interaction can be understood in terms of a linear chain of dipoles that are connected together by springs [84]. An elastic strain modulates the spin separation and hence the dipole-dipole interaction energy, thereby giving rise to magnetoelastic interaction. However, it has been shown by Kittel [85] that classically, this effect averages to zero in a perfect cubic lattice. Nevertheless, because of the lowering of symmetry in the presence of strain, the variation of dipolar energy due to elastic distortions could lead to a

magnetoelastic effect that is of the right order of magnitude to explain what is empirically measured [86] [2].

8.4.2.2 Crystal field strain anisotropy

When the crystal is strained, the crystal field changes causing the crystalline anisotropy energy to be strain dependent [85].

The physical origin of crystal field strain anisotropy can be understood as follows [87]. Suppose we put a non S-state ion (not the case in YIG) in a crystal field: the degenerate m_l states are split and their wavefunctions are mixed in order to minimize the electrostatic repulsion from the surrounding anions. Hence, if the crystal is strained, the crystal field is perturbed and so is the orbital wavefunction. As a result, by virtue of spin orbit interaction, the magnetization is affected. In the case of strong crystal fields and strong spin-orbit interaction, this effect makes a dominant contribution to the magnetoelastic energy of non S-state ions. The mechanism of magnetoelastic coupling for S-state ions is similar, but the effect is much smaller. The difference is that the S-state ion (L=0 state) is non-degenerate and has a symmetric orbital charge distribution, so it cannot mix and form a wavefunction that is compatible with the crystal field. The mixing therefore relies on the excitation of higher $3d$ configuration states (in the upper half shell) for which the probability of occurrence is quite small. Consequently, the magnetoelastic coupling due to crystal field strain anisotropy is expected to be minimal for S-state ions and this is one of the reasons why the spin-wave damping in YIG is very low. Experimentally the magnetoelasticity of YIG is found to be of the same order of magnitude as is predicted by numerical simulation of this effect [88].

[2] The phenomenological magnetoelastic constants of YIG, B_1 and B_2 are measured to be $3.48\times10^6\,\mathrm{erg\,cm^{-3}}$ and $6.96\times10^6\,\mathrm{erg\,cm^{-3}}$ respectively [72]. The formulation of these constants will be discussed later in section 8.4.3.

8.4.2.3 Strain dependence of exchange interaction

A strain will cause the atomic positions to shift and cause modulation of the wavefunction overlap between neighbouring magnetic ions. The modulation of the exchange energy can be expressed as [89]:

$$H_{mod} = \sum_{i,j} [\mathbf{J}(\mathbf{R_i} - \mathbf{R_j} + \mathbf{u_i} - \mathbf{u_j}) - \mathbf{J}(\mathbf{R_i} - \mathbf{R_j})]\mathbf{S_i} \cdot \mathbf{S_j} \tag{8.55}$$

where i, j is the summation over all the magnetic ions and $\mathbf{J}$ is the exchange constant which is a function of $\mathbf{R_i} - \mathbf{R_j}$ (the distance between the ions in position i and j) and $\mathbf{u_i}$ (the displacement vectors of $\mathbf{R_i}$).

8.4.3 Phenomenological description of magnetoelastic coupling

Regardless of the micromechanism for the magnetoelastic coupling, we can describe its effect quantitatively using a phenomenological approach. The magnetoelastic coupling Hamiltonian can be thought of as a perturbation to the total energy of the magnetic system, and so it can be approximated using the Taylor expansion [85]. Since magnetization is odd under time reversal symmetry, while the energy term is even, one looks for terms that are quadratic in magnetization. The magnetoelastic coupling Hamiltonian H_{me} including the second order terms can be written as:

$$H_{me} = \sum_{i,j,k,l} \frac{B_{ijkl}}{M_s^2} M_i M_j \epsilon_{kl} + \sum_{p,q,r,s} \frac{A_{pqrs}}{M_s^2} \frac{\partial M_p}{\partial x_r} \frac{\partial M_q}{\partial x_s} \epsilon_{rs} \tag{8.56}$$

where B_{ijkl} and A_{pqrs} are the magnetoelastic coefficients that are entries of the fourth rank tensors $\mathbf{B}$ and $\mathbf{A}$ respectively, M_s is the saturation magnetization of

the material, M_i and ϵ_{kl} [3] are the components of the magnetization and strain in a chosen reference frame.

It should be noted that H_{me} must be invariant under all the crystal's symmetry operations. In the case of YIG, these symmetry operations are included in the cubic space group O_h. Because of this symmetry restriction, one can reduce the number of possible magnetoelastic coefficients (most of the terms are zero due to symmetry, see Ref. [90] for detailed derivation). Equation (8.56) can simplified to the form [72]:

$$\begin{aligned} H_{me} =& \frac{B_1}{M_0^2}\sum_i M_i''^2\epsilon_{ii}'' + \frac{B_2}{M_0^2}\sum_i\sum_{j\neq i} M_i'' M_j''\epsilon_{ii} \\ &+ \frac{A_1}{M_0^2}\sum_p\sum_q\sum_{r\neq q}\frac{\partial M_p''}{\partial x_q''}\frac{\partial M_p''}{\partial x_r''}\epsilon_{qr}'' + \frac{A_2}{M_0^2}\sum_p\sum_q\left(\frac{\partial M_p''}{\partial x_q''}\right)^2\epsilon_{qq}'' \end{aligned} \tag{8.57}$$

with only 4 independent magnetoelastic coefficients B_1, B_2, A_1 and A_2. The double prime denotes that the coordinate system is defined with respect to the crystallographic axes.

At large k, the terms described by A_1 and A_2 dominate the magnetoelastic energy as $\partial M_p/\partial x_q$ is large; while at small k, these terms are negligible.

Nevertheless, for YIG, in experiments running in the GHz regime, the k involved is low enough that the the terms described by A_1 and A_2 are not important and can be neglected. The magnetoelastic Hamiltonian can be further simplified as [91]:

$$H_{me,\mathrm{YIG}} = \frac{B_1}{M_0^2}\sum_i M_i''^2\epsilon_{ii}'' + \frac{B_2}{M_0^2}\sum_i\sum_{j\neq i} M_i'' M_j''\epsilon_{ii}''. \tag{8.58}$$

This simplification has been justified by numerous experiments. Using a magnetoelastic Hamiltonian of the form described by equation (8.58), magnetoelastic effects in YIG such as the elastic wave Faraday rotation [92], and the change in

[3] In earlier chapters, we have defined the strain tensor as $\tilde{\boldsymbol{S}}$. Here we redefine the strain as $\tilde{\boldsymbol{\epsilon}}$ to make it consistent with most literature.

acoustic velocities with magnetic field [93, 94] can be understood. In the rest of this report, this simplified magnetoelastic Hamiltonian will be employed.

8.5 Excitation and detection of lateral magnetostatic spin-waves at various oblique magnetic field angles in YIG thin films

In our proposed experiment (as discussed in section 1.2), a ZnO transducer is used to send a longitudinal acoustic wave perpendicularly into the YIG thin film. Due to magnetoelastic coupling, we would expect the incoming acoustic wave to generate an effective magnetic field $\mathbf{h_{me}}$ in the YIG. The form of $\mathbf{h_{me}}$ at various applied magnetic field angles θ_{ext} is studied in section 8.5.1. In section 8.5.2, we will then discuss how the reflection of the elastic wave across the YIG/air boundary could lead to standing elastic wave across the YIG thin film waveguide. The formation of the standing waves modifies the field profile $\mathbf{h_{eff}}(\mathbf{r})$ across the waveguide. The coupling of $\mathbf{h_{eff}}(\mathbf{r})$ to the laterally propagating MSWs will then be investigated in section 8.5.3. Finally, we will present a qualitative description of the detection efficiencies expected in section 8.5.4. The overall concept of the various excitation and detection processes is summarized in figure 8.10.

8.5.1 Calculation of the effective field generated by the injected phonons

It is well known (Melkov's book, page 320 [72]) that the magnetoelastic coupling vanishes if the longitudinal elastic wave propagates in the same direction of applied field; however, it has been shown [87] that if the field is applied at an angle to the propagation direction, magnetoelastic coupling is non-zero. Hence, we will

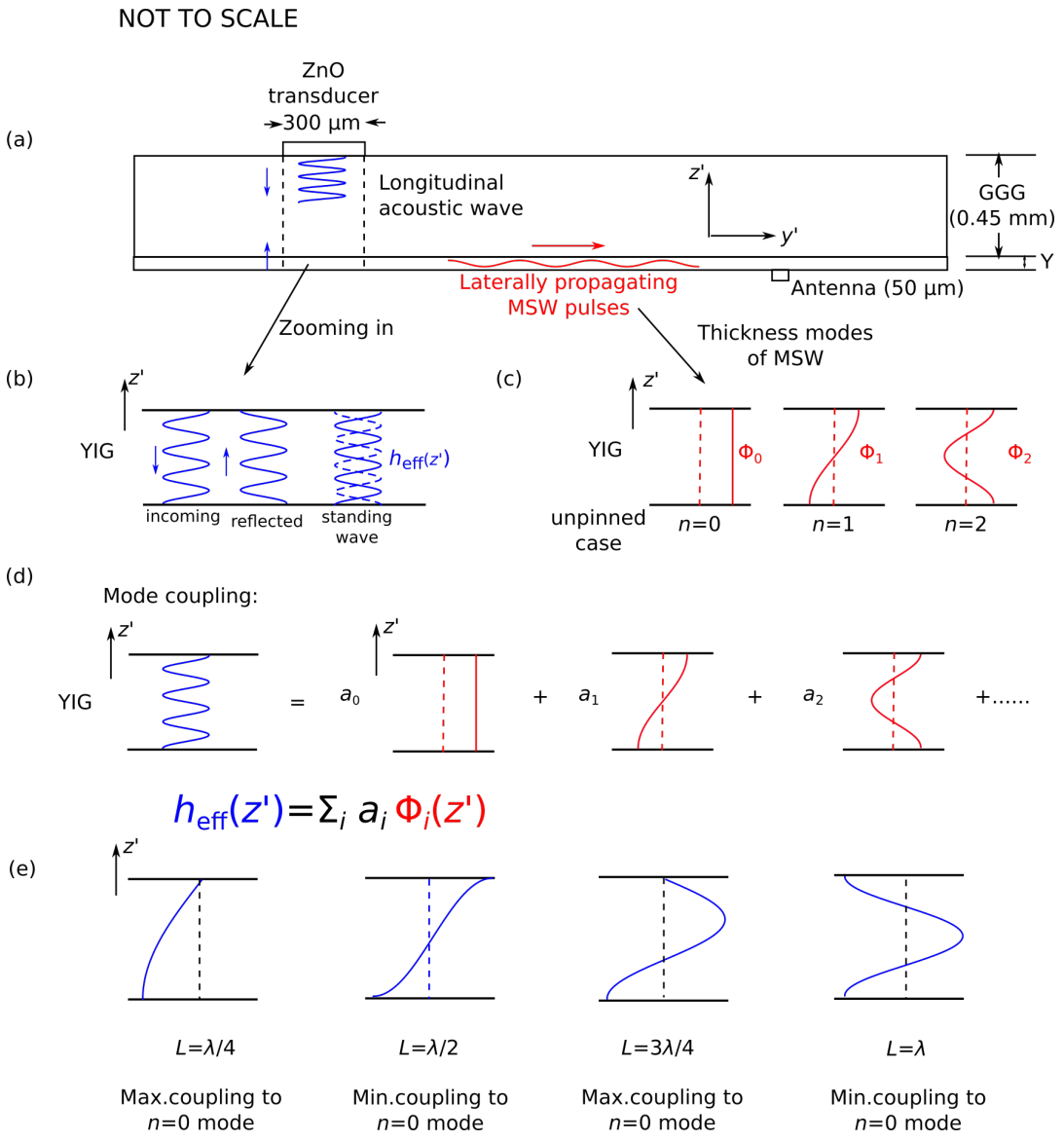

Figure 8.10: (a) A schematic diagram illustrating the configuration and geometry proposed for the excitation of laterally propagating MSW (red line) by injecting a longitudinal acoustic wave (blue line) perpendicular to the YIG thin film. (b) The elastic standing wave formed creates an effective field $\mathbf{h_{eff}}(\mathbf{r})$ across the YIG thin film, (c) MSW modes for the unpinned case, (d) The mode coupling of the MSW to the effective field $\mathbf{h_{eff}}(\mathbf{r})$. (e) Expecting the MSW excitation efficiency to vary depending on the wavelengths of elastic waves fitted inside the YIG film.

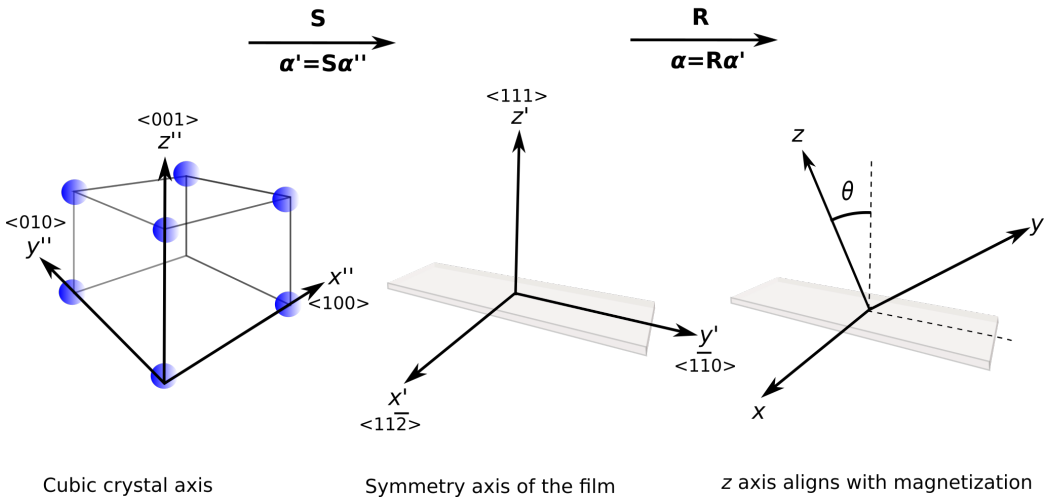

Figure 8.11: The reference axis considered for magnetoelastic coupling calculation

investigate how $\mathbf{h_{me}}$ can be computed for a $\langle 111 \rangle$ YIG thin film when a magnetic field is applied to the film at an angle θ_{ext} to the film normal. We will assume that the internal static field makes an angle θ in accordance with equations (8.38), (8.39) and (8.40).

From equation (8.4), the effective magnetic field should be of form [17]:

$$\mathbf{h_{me}} = -\frac{1}{M_s}\frac{dF_{me}}{d\boldsymbol{\alpha}}, \tag{8.59}$$

where $\boldsymbol{\alpha} = \frac{\mathbf{M}}{M_s}$ is the reduced magnetization vector. We have discussed in section 8.4.3 that the form of the F_{me} for a cubic crystal can be expressed as:

$$F_{me} = B_1 \sum_i \alpha_i''^2 \epsilon_{ii}'' + B_2 \sum_i \sum_{j \neq i} \alpha_i'' \alpha_j'' \epsilon_{ij}'', \tag{8.60}$$

where α_i''s and ϵ_{ij}s denote the components of the reduced magnetization vector and the strain tensor in a coordinate system chosen with respect to the cubic crystallographic axis. In order to calculate α_i''s and ϵ_{ij}''s for a given magnetization and applied strain (in the z' direction), we need to apply some appropriate rotational transformations.

Following the approach in M. Lewis' paper [21], consider a change in reference frame as shown in figure 8.11. First, a transformation **S** takes the crystal axis frame (x'', y'', z'') into a frame that aligns with the symmetry axes of the film (x', y', z'). Since we know that the orientation of the film is $\langle 111 \rangle$ perpendicular to the surface and $\langle 1\bar{1}0 \rangle$ on the long axis of the strip-like waveguide, we can find the third axis by simply taking the cross product of the two and we thereby deduce **S** to be:

$$\mathbf{S} = \begin{pmatrix} \frac{1}{\sqrt{6}} & \frac{1}{\sqrt{6}} & \frac{-2}{\sqrt{6}} \\ \frac{1}{\sqrt{2}} & -\frac{1}{\sqrt{2}} & 0 \\ \frac{1}{\sqrt{3}} & \frac{1}{\sqrt{3}} & \frac{1}{\sqrt{3}} \end{pmatrix}. \tag{8.61}$$

Another transform **R** rotates the z' axis so that it aligns with the internal magnetisation **M** (and the internal field) and we define the coordinates of this frame to be (x, y, z) where the z axis points along **M**. **R** can be represented by a matrix that describes a rotation by an angle θ (the internal field angle with respect to the film normal) about the x' axis, i.e.

$$\mathbf{R} = \begin{pmatrix} 1 & 0 & 0 \\ 0 & \cos\theta & \sin\theta \\ 0 & -\sin\theta & \cos\theta \end{pmatrix}. \tag{8.62}$$

It follows that $\boldsymbol{\alpha''}$ be written in terms of $\boldsymbol{\alpha}$ such that $\boldsymbol{\alpha} = \boldsymbol{RS\alpha''}$, or $\boldsymbol{\alpha''} = \boldsymbol{S^T R^T \alpha}$, i.e.,

$$\boldsymbol{\alpha''} = \begin{pmatrix} \frac{1}{\sqrt{6}} & \frac{1}{\sqrt{2}}\cos\theta + \frac{1}{\sqrt{3}}\sin\theta & -\frac{1}{\sqrt{2}}\sin\theta + \frac{1}{\sqrt{3}}\cos\theta \\ \frac{1}{\sqrt{6}} & -\frac{1}{\sqrt{2}}\cos\theta + \frac{1}{\sqrt{3}}\sin\theta & \frac{1}{\sqrt{2}}\sin\theta + \frac{1}{\sqrt{3}}\cos\theta \\ -\frac{2}{\sqrt{6}} & \frac{1}{\sqrt{3}}\sin\theta & \frac{1}{\sqrt{3}}\cos\theta \end{pmatrix} \boldsymbol{\alpha}. \tag{8.63}$$

We now investigate how the strain tensor $\boldsymbol{\epsilon''}$ transforms. In the experiment, a

longitudinal acoustic wave is applied along the ⟨111⟩ direction, and so straightforwardly we have:

$$\boldsymbol{\epsilon'} = \begin{pmatrix} 0 & 0 & 0 \\ 0 & 0 & 0 \\ 0 & 0 & \epsilon'_{33} \end{pmatrix}. \tag{8.64}$$

Using standard matrices transformation rules, we have:

$$\boldsymbol{\epsilon''} = \mathbf{S^T}\boldsymbol{\epsilon'}\mathbf{S} = \frac{1}{3}\epsilon'_{33}\begin{pmatrix} 1 & 1 & 1 \\ 1 & 1 & 1 \\ 1 & 1 & 1 \end{pmatrix}. \tag{8.65}$$

We are now in a position to calculate the magnetoelastic energy in terms of α_i and ϵ'_{33}. We do so by expanding F_{me} (described in equation (8.60)) using equations (8.63), (8.65), and this leads to:

$$F_{me} = \frac{1}{12}\epsilon'_{33}[4B_1 + (-2\alpha_1^2 + \alpha_2^2 + \alpha_3^2)B_2 - 3(\alpha_2^2 - \alpha_3^2)B_2\cos 2\theta + 6\alpha_2\alpha_3 B_2 \sin 2\theta]. \tag{8.66}$$

By differentiating F_{me} with respect to α_i and then approximating $\alpha_1 = \alpha_2 = 0$ and $\alpha_3 = 1$, we find the effective field

$$\mathbf{h_{me}} = -\frac{1}{6M_s}\epsilon'_{33}B_2(1 + 3\cos(2\theta))\hat{z} - \frac{1}{2M_s}B_2\sin(2\theta)\hat{y}. \tag{8.67}$$

As the oscillating effective magnetic field that is parallel to the internal field (in the z direction) does not contribute in the spin-wave dynamics, the effective field is therefore given by:

$$\mathbf{h_{me,\perp}} = -\frac{1}{2M_s}B_2\sin(2\theta)\epsilon'_{33}\hat{y}. \tag{8.68}$$

This agrees with the result reported in Refs. [91, 95].

8.5.2 Formation of a standing wave across the waveguide

In the previous section, we have investigated how an effective magnetic field $\mathbf{h_{me,\perp}}$ is produced by the presence of a longitudinal elastic wave. We will now investigate how reflection from the GGG/YIG and YIG/air interfaces could modify the effective internal field profile across the YIG film.

The elastic wave is projected by the acoustic transducer across the GGG substrate and impinges on the YIG thin film. The first interface that the elastic wave encounters is the YIG/GGG interface. It is known that the acoustic impedance of the YIG ($3.74\times10^6\,\mathrm{gs^{-1}cm^{-2}}$ [95, 96]) is very similar to that of GGG ($4.58\times10^6\,\mathrm{gs^{-1}cm^{-2}}$[97]), so only a very small fraction (around 1%) is reflected. Reflection at the GGG/YIG interface can thus be neglected. The elastic wave then propagates into the YIG and then encounters the second interface; the YIG/air interface. Since the impedance of air is very low, we can effectively treat the YIG/air plane as a stress free surface. Hence, all the acoustic wave will be reflected and the acoustic amplitude is maximized at the interface. The incoming and reflected wave therefore interfere with each other, so a standing wave is formed (see figure 8.10c).

The field $\mathbf{h}_{\text{eff}}$ in the waveguide is then be modified, so that its spatial profile in the z' direction takes the form $\cos(kz'+\omega t)+\cos(kz'-\omega t)=2\cos(kz')\cos(\omega t)$.

Now, the elastic wave is also confined within the electrode diameter ϕ_{dot} of the transducer, so the effective field can be written as:

$$\mathbf{h_{eff}}(\mathbf{r}') = -\frac{1}{M_s}B_2\sin(2\theta)\epsilon'_{33,s}\cos(k_{z'}z')\Pi\Big(\frac{x'}{\phi_{dot}}\Big)\Pi\Big(\frac{y'}{\phi_{dot}}\Big)\hat{y} \tag{8.69}$$

where $\epsilon'_{33,s}$ is the amplitude of ϵ_{33} and Π denotes the rectangular function.

This analysis is still valid if the applied elastic wave is pulsed so long as the pulse length is long enough. For example, in the actual experiment (presented in chapter 9), the pulse length of the 3GHz elastic wave applied is 15 ns. Given a longitudinal acoustic velocity of about 7.2×10^5 cms^{-1}[95], the 15 ns pulse contains about 45 cycles of oscillations. Each cycle of oscillation occupies roughly 2.3 μm in space at 3 GHz. Comparing this with the thickness of the waveguide (7.8 μm), we conclude that we are in the regime where the above analysis is valid.

8.5.3 Mode coupling to laterally propagating MSW excitation

Given an external driving field $\mathbf{h_{eff}}(\mathbf{r}')$, the energy E_n coupled to a particular excited spin-wave mode $\mathbf{m_n}(\mathbf{r}')$ is:

$$E_n = \int \mathbf{h}_{\text{eff}}(\mathbf{r}') \cdot \mathbf{m_n}(\mathbf{r}')dV = \int \mathbf{h}_{\text{eff}}(\mathbf{r}') \cdot \mathbf{m_n}(\mathbf{r}')dx'dy'dz' \tag{8.70}$$

In order to find the dot product in the above equation, we need to know the mode shape. According to Kalinikov [98], a good approximation for the mode shape $\mathbf{m_n}(\mathbf{r}')$ is given by:

$$\mathbf{m_n}(y', z') = M_s[\Phi_n^x(z')\hat{x} + \Phi_n^y(z')\hat{y}]e^{ik_{y'}y'}, \tag{8.71}$$

where

$$\Phi_n^p(z') \propto \left[\cos\kappa_n^p(z' + \frac{L}{2})\right] + \frac{d_2^p}{\kappa_n^p}\sin\left[\kappa_n^p(z' + \frac{L}{2})\right], \tag{8.72}$$

and p=x or y, d_1^p, d_2^p are the pinning parameter at the GGG/YIG and YIG/air interface respectively, and κ_n^p is the spin wave mode wavenumber which can be determined by:

$$[(\kappa_n^p)^2 - d_1^p d_2^p]\tan(k_p^n L) = \kappa_n^p(d_1^p + d_2^p). \tag{8.73}$$

To visualise the modes more intuitively, consider the case when the pinning parameters $d_1^p = d_2^p = 0$ are zero, i.e., the spins are totally unpinned. In this condition, $\tan(\kappa_n^p L) = 0 \rightarrow \kappa_n^p = \frac{n\pi}{L}$, n=0,1,2, etc.; so $\mathbf{m_n}(z')$ becomes:

$$\mathbf{m_n}(z') \propto M_s \Big[\cos \frac{n\pi}{L}(z' + \frac{L}{2})\hat{x} + \cos \frac{n\pi}{L}(z' + \frac{L}{2})\hat{y} \Big]. \tag{8.74}$$

The first three modes for the totally unpinned case are shown in figure 8.10c.

For a general pinning condition, the energy associated with mode n is given by:

$$\begin{aligned} E_n \propto & \int_{-\frac{L}{2}}^{\frac{L}{2}} B_2 \sin(2\theta)\epsilon'_{33,s} \cos(k_{z'}z') \Big\{ \Big[\cos \kappa_n^p (z' + \frac{L}{2}) \Big] + \frac{d_2^p}{\kappa_n^p} \sin \Big[\kappa_n^p (z' + \frac{L}{2}) \Big] \Big\} dz' \\ & \times \int_{-\infty}^{\infty} \Pi\Big(\frac{x'}{\phi_{dot}}\Big) dx' \times \int_{-\infty}^{\infty} \Pi\Big(\frac{y'}{\phi_{dot}}\Big) e^{ik_{y'}y'} dy' \end{aligned} \tag{8.75}$$

The integral in z' is essentially the Fourier decomposition of the effective field $\mathbf{h_{eff}}(\mathbf{r'})$ into the corresponding spin-wave modes (see figure 8.10d). In the x' direction, the dimension of the top dot is small compared to the width of the waveguide, so the amplitude variation of the lateral spin-wave mode is considered to be constant regardless of the pinning condition. In the y' direction, we expect an oscillatory mode ($\propto e^{ik_{y'}y'}$) as the lateral spin-wave propagates in this direction. Therefore, the integral in the x' direction is a constant and the integral in the y' direction is:

$$\int_{\frac{-\phi_{dot}}{2}}^{\frac{\phi_{dot}}{2}} e^{ik_{y'}y'} dy' \propto \mathrm{sinc}(k_{y'}\phi_{dot}) \tag{8.76}$$

We see that the excitation efficiency decreases as ϕ_{dot} increases because of the spatial decoherence in the y' direction due to destructive interference. Hence, the acoustic transducer is only capable of exciting MSW that have wavelengths larger than ϕ_{dot}.

8.5.4 Detection of the generated MSW

In the same way that the wavelength excited is limited by the size of the electrode diameter, the receiving antenna can only receive MSW that have wavelengths that are larger than its own width.

Moreover, since the wavelength of the electromagnetic wave is large, the antenna detects most efficiently for the n=0 mode (for totally unpinned case) [4]. Hence, as seen in figure 8.10e, acoustic modes for which the thickness L of the YIG film is an even number of quarter wavelengths do not couple to magnons as the above integral sums to zero. The excitation efficiency therefore oscillates if the wavelength of the acoustic wave changes which can be achieved by modifying the carrier frequency.

From the crude calculations described in the previous section, regardless of which mode is being excited, we predict that the excitation efficiency of the spin-wave is roughly proportional to $\sin(2\theta)$ and so we expect the strength of the spin-wave excited to be the strongest when the internal field angle θ=45° or $\theta_{ext} \approx 15°$.

[4] Or n=1 mode when the spins are totally pinned - corresponding to the situation described in section 8.3. In such case the excitation efficiency still oscillates as the wavelength of the acoustic wave changes similar to that in the unpinned case; however, the peaks and troughs would appear at slightly different wavelengths.

Chapter 9

Experiments on acoustic excitation of lateral magnetostatic spin-waves (MSW) in YIG thin films

In this chapter. we will demonstrate experimentally the viability of exciting lateral magnetostatic spin-waves (MSW) in a YIG thin film structure by direct injection of longitudinal acoustic waves. An experiment is designed to fire pulses of acoustic energy at the YIG film and the magnon signals thereby excited are measured in a time-resolved manner using an antenna a distance along the waveguide. The timing information of the measured signal allows us to distinguish signals between electromagnetically generated or acoustically generated magnon signals.

This chapter is organised as follows. We start by describing the procedures involved in sample preparation of the YIG film, then the experimental set-up and the apparatus required for time-resolved spectroscopic measurement are outlined. We then consolidate our understanding of the MSW propagation by studying magnons

that are excited and detected using conventional electromagnetic antennae. In particular, the MSW velocities at various applied magnetic field angles are calibrated. Finally, we report the experimental observation of acoustically excited magnons. The dependence of the magnon signals on power, frequency and magnetic field angle is investigated.

9.1 Sample preparation

9.1.1 The YIG waveguide

A high quality monocrystalline YIG thin film sample that was grown by liquid phase epitaxy is used in our experiments. A strip waveguide of dimensions 18 mm long and 2 mm wide was cut carefully from the wafer and 45° cuts were made at the two ends of the waveguide. The cuts are made to avoid reflection of spin-waves from the end boundaries that might interfere with the desired spin-wave signal. A common YIG thin film waveguide usually has YIG deposited on both sides of the GGG substrate, but the YIG waveguide we used only have YIG deposited on one side. This fact is verified by checking that satisfactory magnon transmission was only obtained when the transmit and receive antenna are placed on one side of the YIG/GGG system; placing them on the other face gave a large insertion loss. The thickness of the sample used is 0.45 mm and the YIG film has a thickness of 7.8 μm. The geometry of the YIG waveguide is shown in figure 9.2c.

9.1.2 Deposition of ZnO transducer

The ZnO transducer was grown on the back side of the GGG substrate, i.e., the side opposite to that bearing the YIG thin film (see figure 9.2c). We followed the recipe that has been developed in section 4.2.5, and the 520 nm thick ZnO thin film

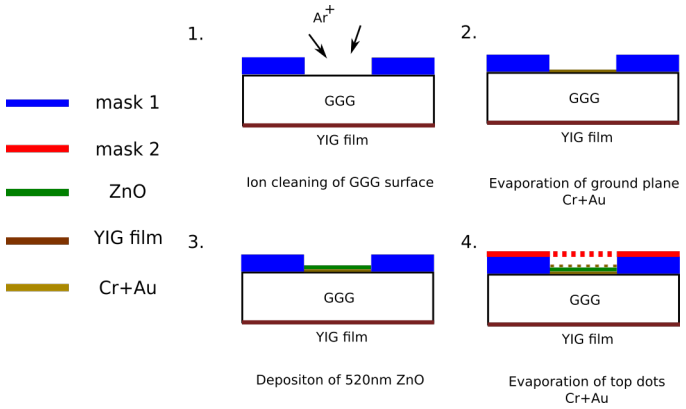

Figure 9.1: Depositon of a ZnO transducer on the back side of the YIG waveguide

was grown at at a power of 100 W and a pressure of 4μbar of 1:1 Ar/O_2 sputter gas mixture for 52minutes. A mask for top dot was designed specifically so that the capacitive ground electrode and an array of top dots with lateral separation 0.5 mm could be deposited onto the ZnO layer (see figure 9.2a).

9.1.3 Sample mount

As shown in figure 9.2d, the YIG waveguide (with the transducer deposited) was mounted using GE varnish onto a 0.5 mm thick duroid chip with the YIG side down. The 50 μm wide antennae which are separated 10.7 mm apart, were printed on the duroid chip and were soldered to the SMA connectors of the sample holder. Notice the shape of the ground side of the antennae. The large rectangular pad acts as a capacitive coupling to the ground plane on the back side of the duroid chip. The grounding of the chip is arranged by silver gluing it to the sample holder.

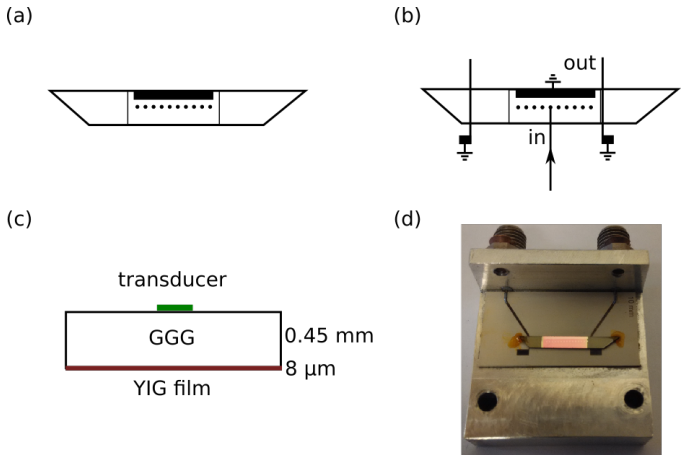

Figure 9.2: (a) Figure showing the deposition of a ZnO transducer onto the reverse side of a YIG waveguide, (b) Figure showing the electrical connections to the transducer and to the antennae underneath the YIG waveguide, (c) Geometry of the YIG waveguide, (d) This picture shows YIG waveguide plus ZnO transducer mounted on a sample holder.

9.2 Time-resolved spectroscopy for MSW detection

9.2.1 The experimental setup

In this section, we describe the experimental setup for measuring the temporal characteristics of the excited and detected spin-wave pulses. The schematic diagram of the set-up is shown in figure 9.3.

Two spin-wave excitation methods are used and compared.

The first method is to drive a current pulse through a conventional antenna which generates a local magnetic field for exciting propagating spin-waves (configuration 1). This is a well known technique for exciting and detecting spin-waves; and the point of this exercise is to calibrate the spin-wave velocity of our YIG sample at various applied field angles. The second method (configuration 2) is the one that we are interested in: the excitation of lateral spin-wave via the injection of

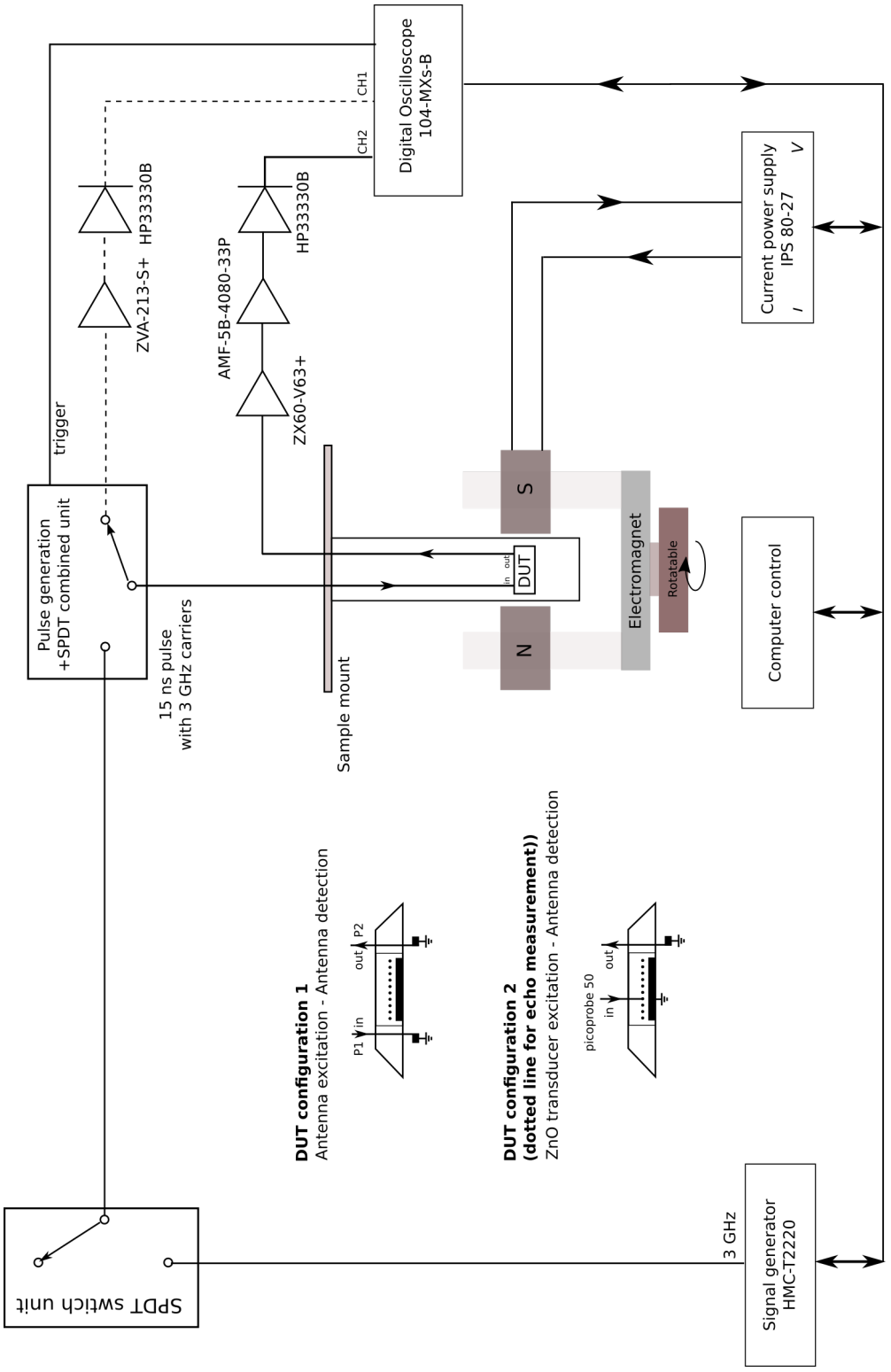

Figure 9.3: Experimental set-up for time resolved spectroscopy of MSW. DUT in this figure stands for device under test.

a pulsed longitudinal acoustic wave. The excited spin-wave packets then propagate through the YIG waveguide and are subsequently detected using an antenna. The signal from the antenna is amplified and rectified, and the signal acquired is measured using a digital oscilloscope that is triggered by the pulse generator. In configuration 2, the echoes of the acoustic wave are monitored at the same time as that of the detected spin-wave, so the timing of both the acoustic and spin-wave pulses can be directly compared.

The magnetic field of the sample is provided by a rotatable electromagnet whose field can be controlled by a variable power supply. This allows the spin-wave signals in both configurations to be monitored at various magnetic fields.

In order to facilitate data acquisition, Labview programs were built to control the digital oscilloscope, the current power supply and the signal generator, so that data can be taken and saved to a computer automatically.

The experimental set-ups are shown in figure 9.2.1.

9.2.2 Experimental apparatus

Most of the equipment including the digital oscilloscope, signal generator, single pole double throw (SPDT) switch units, amplifier and diode used in the time resolved spectroscopy experiments are identical to those used in the pulse echo measurements as described in section 4.4.2, but some additions and changes in procedure are needed as described below.

9.2.2.1 Digital oscilloscope

The waveform acquired is averaged over 5 captures. In experiments involving magnetic field sweep, the protocol is as follows: Increase current by 0.001 A, then

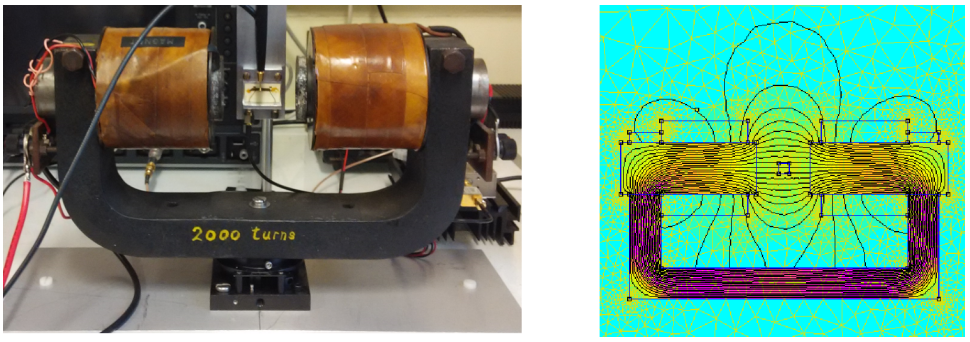

Figure 9.4: A diagram showing the horseshoe electromagnet used in the experiment, and the FEMM simulation of B-field distribution at 5 A.

wait for 200 ms, make 10 measurements on the waveform, then take data. It is worth noting that any microwave devices such as mobile phones or computer WiFi should be removed from the vicinity, as the GHz pickup from these devices seriously contaminates the signal measured.

9.2.2.2 The amplifiers and the diodes

The amplifiers were chosen to perform well at 3 GHz, which is the frequency at which the experiments were performed. The acoustic echo signals are amplified by the Mini-circuits ZVA-213-S+ amplifier as before; the output from the magnon detection antenna requires two cascaded amplifiers. A Mini-circuits ZX60-163+ (20 dB low noise amplification from 0.05 to 6 GHz) followed by a power amplifier (provides a 40 dB gain from 2 to 8 GHz).

9.2.2.3 The electromagnet and the current power supply

A small horseshoe electromagnet as shown in figure 9.4 is used in the experiment. The magnet consists of two coils, each of which surrounds the soft iron core. The poleface separation is adjustable with a maximum value of 60 mm and in our experiment, it was varied from 40 up to 50 mm. In this regime, we find from actual measurement and simulation that the homogeneity of the magnet is roughly

1 mT per 10 mm at the centre between the pole faces at 5 A (5 A is the current flowing in one of the coils, the actual current supply is 10 A). It was also found that under these conditions, the angular distribution of the field is minimal and can be neglected, i.e. the field is effectively perpendicular to the pole). The electromagnet is not water cooled, so it is workable continuously from 0-8 A and temporarily from 8-11 A for several minutes. The current is supplied using an ISO-TECH IPS 80-27 which is capable of supplying current up to 20 A at 60 V with a resolution of 0.001 A. Even though the magnet is heating up when current is applied, the voltage is automatically adjusted so that the current supplied is remarkably stable. Computer control of the power supply via GPIB is also possible. The magnetic field produced as a function of current at different poleface separation was calibrated using a Hall probe (the probe was placed at the center of the poleface gap where the YIG waveguide is positioned). A rotatable stand was constructed and mounted onto the electromagnet such that it can rotate without interfering with the sample.

9.3 Calibration of the MSW velocities at various applied magnetic fields angles

We use the experimental set up (configuration 1) as described in section 9.2.1 to measure the transit time of spin-waves between two parallel antennae separated by a distance of 10.7 mm. In the experiment, a 15 ns pulse with a 3 GHz carrier is sent into P1, and the transmitted spin-wave signal is detected in P2 which is then amplified, rectified and recorded by the oscilloscope. This process is repeated as the bias field is swept in the region of interest. A 3D graph is thus obtained: the magnitude of the signals detected is displayed as a variation in colour while the x and y axes show magnetic field (mT) and time (ns) respectively. This experiment

is repeated for various θ_{ext} and the transit time τ is then compared with the theories as discussed in section 8.3.

Figures 9.5 and 9.6 show the results obtained. The initial vertical line indicates the direct electromagnetic pick-up between the input and output antenna, so this line marks the instant at which the pulse is excited. Some time later, we see a big signal that is strongly dependent on the magnetic field. This signal arises from the transmitted spin-wave that was originally excited by the input antenna. One would expect this signal to be the strongest when the applied field is close to $\omega = \gamma\sqrt{H_{in}(H_{in} + M\sin^2\theta)}$. The transit time of the spin-wave at a particular magnetic field can be measured by finding the time after excitation at which the received magnon signal reaches maximum.

The experimental values for the magnon transit times (at the magnetic field for which the signal is maximized) are found to agree well theoretical values as shown in figure 9.7, with the exception of a slight overestimate at small θ_{ext}. The theoretical curve in the figure is calculated as $k\rightarrow 0$ for the n=1 mode assuming the thickness of the YIG film is 7.8 μm. The main source of error comes from the physical alignment of the sample with respect to the calibrated marker in the rotating stage. It should also be noted that the theoretical curve is not 100% correct because there is an uncertainty in the saturated magnetization used and the ideal boundary condition is not met in real situation (e.g., there exists a grounding layer near to the YIG, which might perturb the dispersion relation).

The efficiency of excitation depends strongly on how well the Oersted field of the antenna couples to the spin-wave mode, so we expect the detected signal to be strongly dependent on the angle of the applied field. Although we can measure the amplitude of these magnon signals, it is hard to calibrate their excitation efficiencies since the spin-wave attenuation across the sample also varies with the field angle.

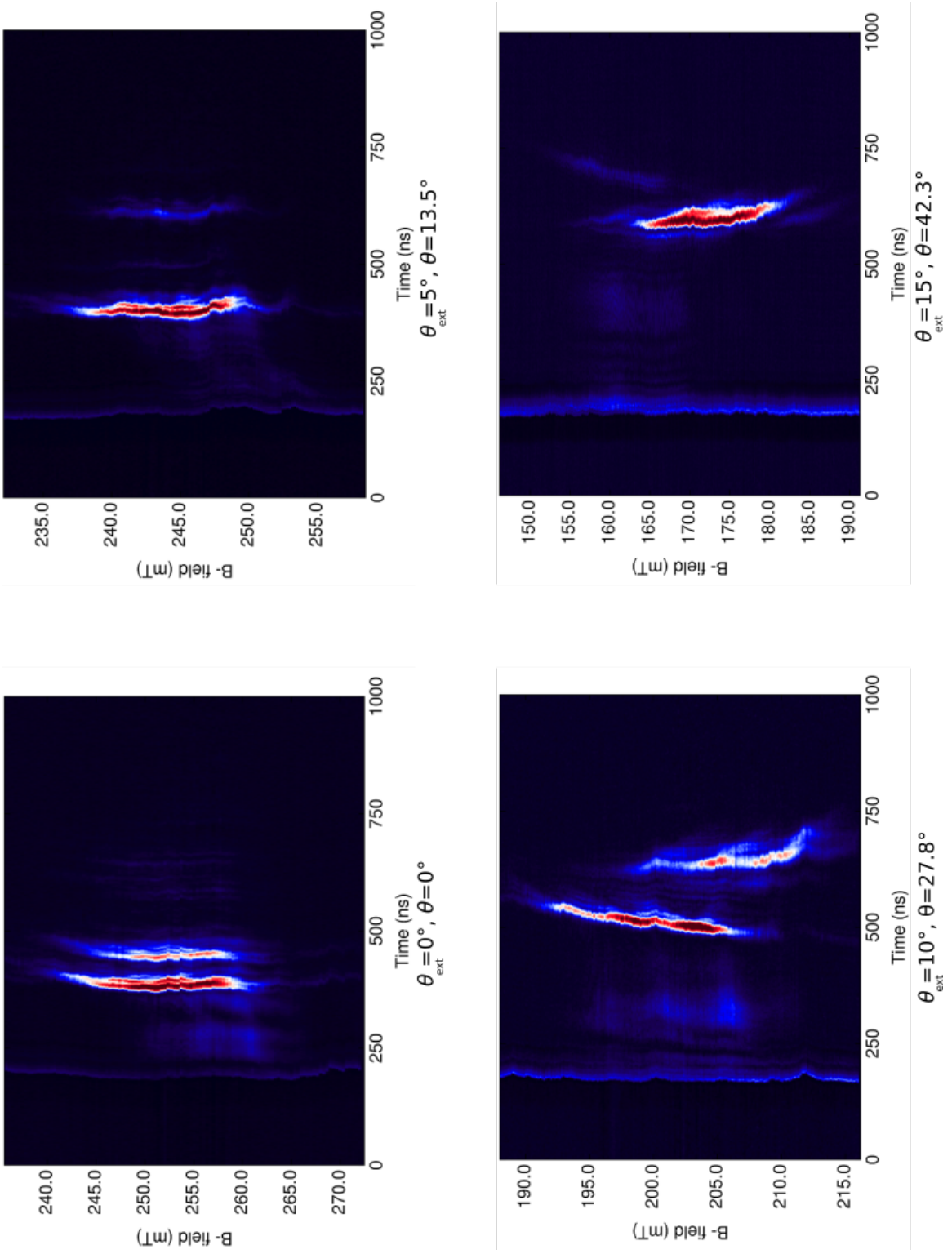

Figure 9.5: Figure showing the spin-wave signal measured by the output antenna for configuration 1 (θ_{ext} ranges from 0-15°).

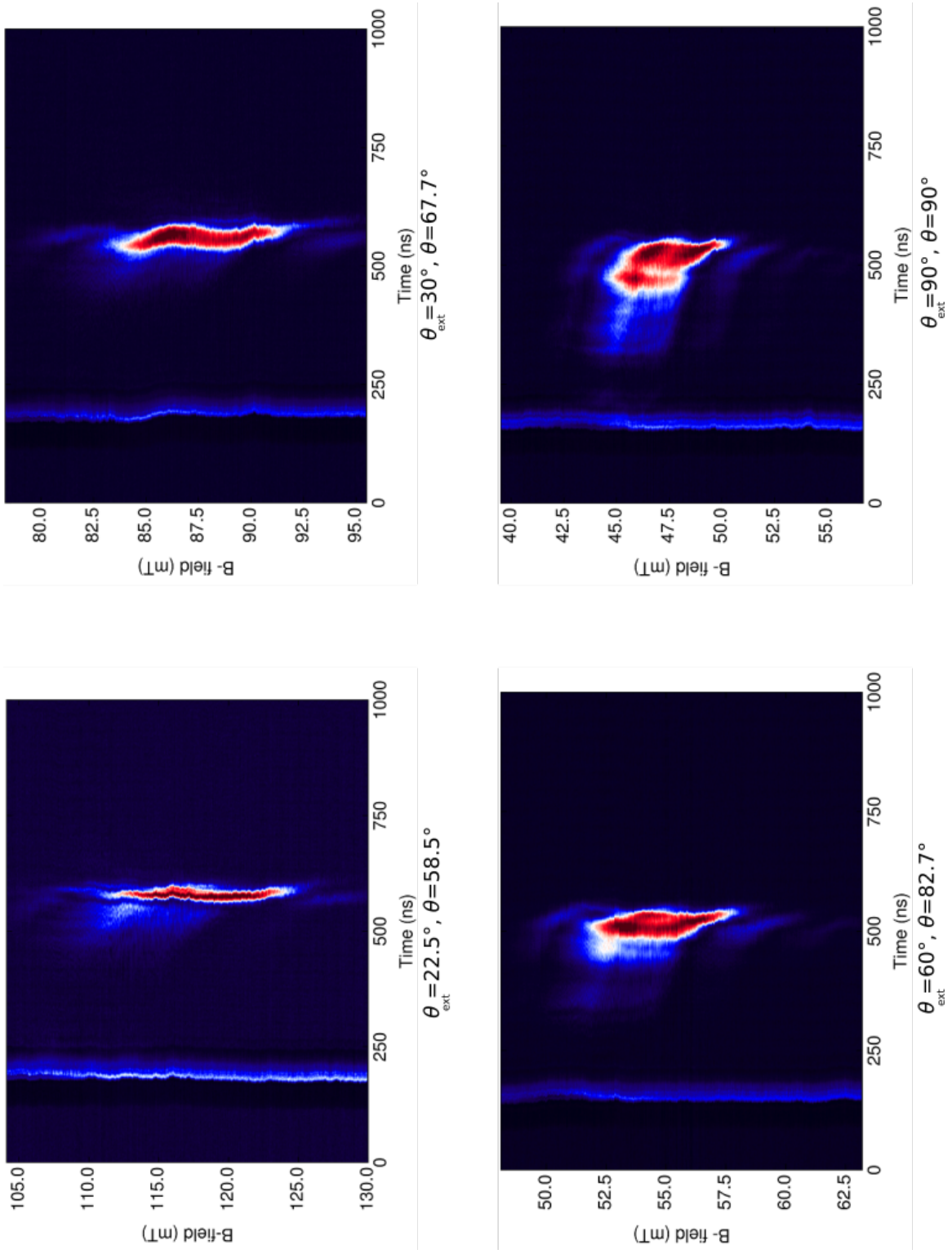

Figure 9.6: Figure showing the spin-wave signal measured by the output antenna for configuration 2 (θ_{ext} ranges from 22.5-90°).

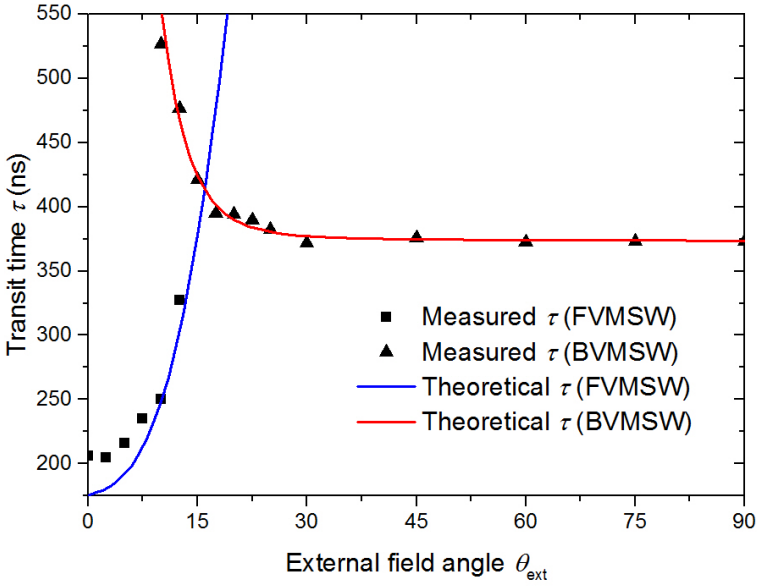

Figure 9.7: The theoretical calculated transit time versus experimental value (L=7.8 μm).

There are also some peculiar features in the results obtained.

1. Although the excitation of both FVMSW and BVMSW are allowed in our experimental setup at all θ_{ext} except for $\theta_{ext} = 0°$ or 90°; we were only able to detect both of these spin-waves at $\theta_{ext} = 10° - 12.5°$. The main reason for this is that when the internal angle θ is not close to 45°, the speed of magnons for the non-dominant type is very slow, meaning that its attenuation is large compared to that of the dominant type.

2. Some signal is detected quite a long time before the main peak arrives. This effect is particularly strong when θ_{ext}=90° and gradually reduces as θ_{ext} decreases. A possible reason for this is that the antenna radiates over a substantial distance so that the resulting spin-wave excitation is not very localised.

3. For θ_{ext}=5°, and θ_{ext}=10°, two signal peaks are observed. From the transit time of the second peak, it is likely that it is the BVMSW pulse that is being simultaneously excited with the first arriving FVMSW pulse.

4. There are also two signal peaks at θ_{ext}=0°. It is clear that the first peak corresponds to the first order n=1 FVMSW mode. However, the second peak is unexpected as a BVMSW is unable to excite in this configuration. This peak does not arise from the excitation of higher modes either, as these modes have a much slower velocity. It is possible that it is excited by the side bands of the applied pulse signal. Since the Fourier transform of a square pulse is a sinc function, a square pulse has side bands either side of the carrier frequency. The upper side band could excite spin-waves at higher k and these waves would have a slightly slower velocity than the one that is excited by the main band; whereas the lower band could not excite any spin-wave as it lies out of the dispersion relation.

9.4 Time resolved measurement of the acoustic excitation of lateral magnetostatic spin-waves

This section presents the data obtained from measuring the output signal of the receive antenna when a longitudinal acoustic wave is launched into the YIG waveguide. This signal is extensively investigated as a function of transducer to antenna distance, power, applied field angle and frequency. Our results - taking account of the timing information - suggest that lateral propagating spin-waves can be excited as the acoustic wave impinges on the YIG waveguide due to magnon-

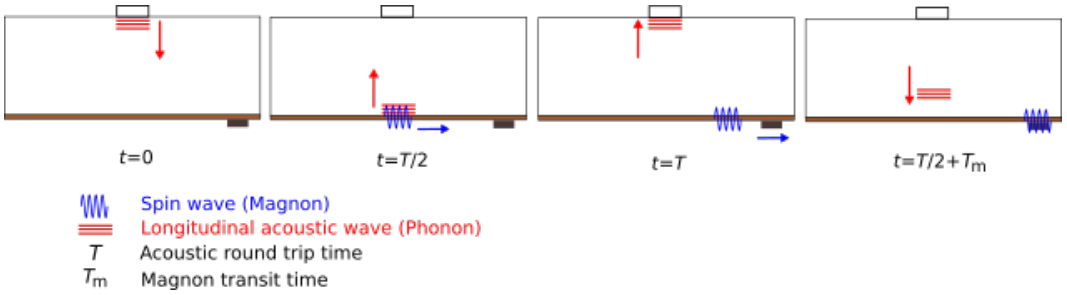

Figure 9.8: The figure shows the sequence of events that occur after the acoustic wave is launched. The notation used here is: T= Acoustic round trip time, T_m= Magnon transit time. At t=0, the acoustic wave is launched, and so at t=$\frac{T}{2}$, the acoustic wave impinges onto the YIG thin film. This generates a laterally propagating spin-wave that takes a time T_m to travel to the output antenna. The signal is therefore measured at t=$\frac{T}{2} + T_m$

phonon interaction. The spin-waves excited are found to be linear with power and the excitation efficiency is close to what has been predicted in section 8.5.

Using configuration 2 as described in section 9.2.1, we measure the output antenna signal as the magnetic field is swept. 3.0 GHz signals are used in these experiments. Figure 9.8 illustrates the sequence of events that happens as the transducer is activated. First, at t=0, the pulse of 3 GHz carrier arrives at the transducer. This in turn produces a longitudinal acoustic wave which travels perpendicular to the waveguide. After time $\frac{T}{2}$, where T is the round trip time of the acoustic wave, the acoustic pulse hits the YIG surface and thereby creates a lateral propagating spin-wave. This wave propagates along the waveguide, and after a time T_m, the wave was picked up by the antenna and is converted into an electromagnetic signal which is subsequently measured. As the acoustic wave returns into the transducer at $t = T$, an acoustic echo signal is detected. This cycle repeats until the acoustic wave fade out due to round-trip attenuation.

9.4.1 Timing information of the signal measured

We first positioned the picoprobe to give a transducer-antenna distance of 0.86 mm (by choosing to contact the transducer that is closest to the antenna) and the

magnetic field was tuned such that a 3 GHz magnon signal can transmit through the YIG waveguide. As we determined from the previous measurement in section 9.3, the velocity of the magnons at 30° is 2.88×10^5 cms^{-1}; the transit time of the magnon signal for a 0.86 mm path is therefore expected to be 29.8 ns. Figure 9.9 shows the 2D plot of the output antenna data at B=90 mT and θ_{ext}=30° at the antenna-transducer distance of 0.86 mm; the echo signals of the phonons are also plotted in the same graph for comparison. It can be clearly seen that for every acoustic echo, there is a corresponding magnon signal. The acoustic wave decays exponentially as expected due to attenuation and the generated magnons also decays proportionally; the power dependence of the magnon signal with respect to the phonon power is discussed in section 9.4.2. Now we experimentally measure the magnon transit time by finding the difference in time between the middle point of two consecutive acoustic echoes (in the time at which the phonons hit the YIG) and the time of arrival of the magnon signal. We find that this measurement gives 27.8 ns which agrees with the predicted result.

To confirm that what we observe is unambiguously the magnon signal is generated by the phonons, we repeat the experiment at various transducer-antenna distances while keeping θ_{ext} fixed at 30°. We have grown the transducers such that the top dots are 0.5 mm apart so that the magnons are excited from fixed and known transducer-antenna distances (0.86 mm+ (n-1)×0.5 mm) where n=1,2... is the number of dots counted from the antenna. The picoprobe is maneuvered to contact to the dot required. As we excite the magnons further and further away from the receive output antenna, we can see that the corresponding magnon peak moves to later time, also shown in figures 9.9, 9.10, 9.11 and 9.12. Using a similar analysis as before, we obtain the experimental result as presented in figure 9.13, which shows the dependence of the magnon transit time with the transducer-antenna distances. It is clear from the figure that the transit time scales linearly with the distance the magnon travels, and the most important observation lies in the fact

that the y-intercept of the plot is -2.5 ns, which suggests that the magnons are indeed generated as the phonons hit the YIG.

Using a similar approach to that described in section 9.3, we obtain a 3D graph with time (ns) along the x axis, applied B-field (mT) along the y axis and the amplitude of the signal displayed as variation of colour. The raw data obtained for θ_{ext}=30° at an antenna-transducer distance of 0.86 mm is shown in figure 9.14a. Due to electromagnetic leakage (the most likely leakage source is from the SPDT switch), we can see a constant voltage offset when the magnetic field matches that of the FMR frequency of the YIG sample (the blue strip presents from around 83 mT to 86 mT). In order to see a cleaner signal, we remove this artifact by changing the signal offset. Figure 9.14b shows the signal after the offset is removed. Notice also that there is a very big spurious signal near t=0 s, the point when the electromagnetic signal is injected initially. This is caused by two effects. Firstly, there is a direct electromagnetic coupling between the picoprobe and the antenna and a signal is measured at almost exactly the instant at which the input acoustic signal is launched. Secondly, the stray electromagnetic field of the probe extends far away spatially, so spin-waves can be excited near the antenna; this accounts for the spin-wave signals that are measured shortly after the activation of the input signal. In order to measure more accurately the magnon signal generated by the acoustic wave, we ignore the time period where those spurious signals occur, i.e., we crop the data from t=1000 ns to t=2000 ns (figure 9.14c). The original data is noisy due to background electromagnetic signals such as pickup from mobile phones, WiFi or radio. In order to improve the signal-to-noise ratio, a Gaussian low pass filter is applied to obtain a sharper image as shown in figure 9.14d. Features of the waveform that have higher Fourier frequencies can be seen more distinctly when a high pass filter is applied (see figure 9.14d). The stray electromagnetic field emerged from the picoprobe extends far away spatially and generates spin-wave near the receiving antenna, which happens every time the

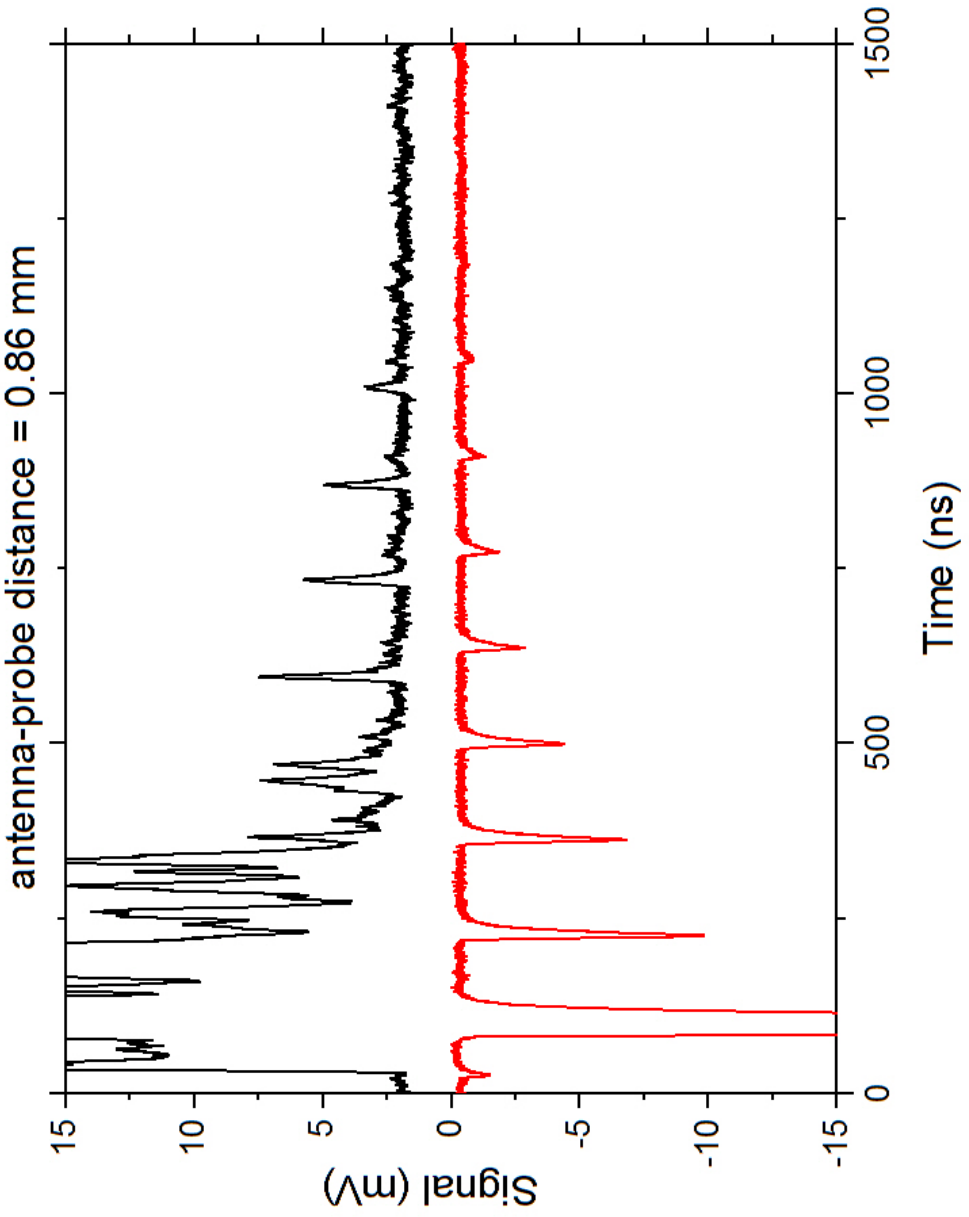

Figure 9.9: The trace of the diode output at θ_{ext}=30° at antenna-to-transducer distances= 0.86 mm. The black trace shows the magnon signal measured using an antenna while the red trace shows the acoustic echoes.

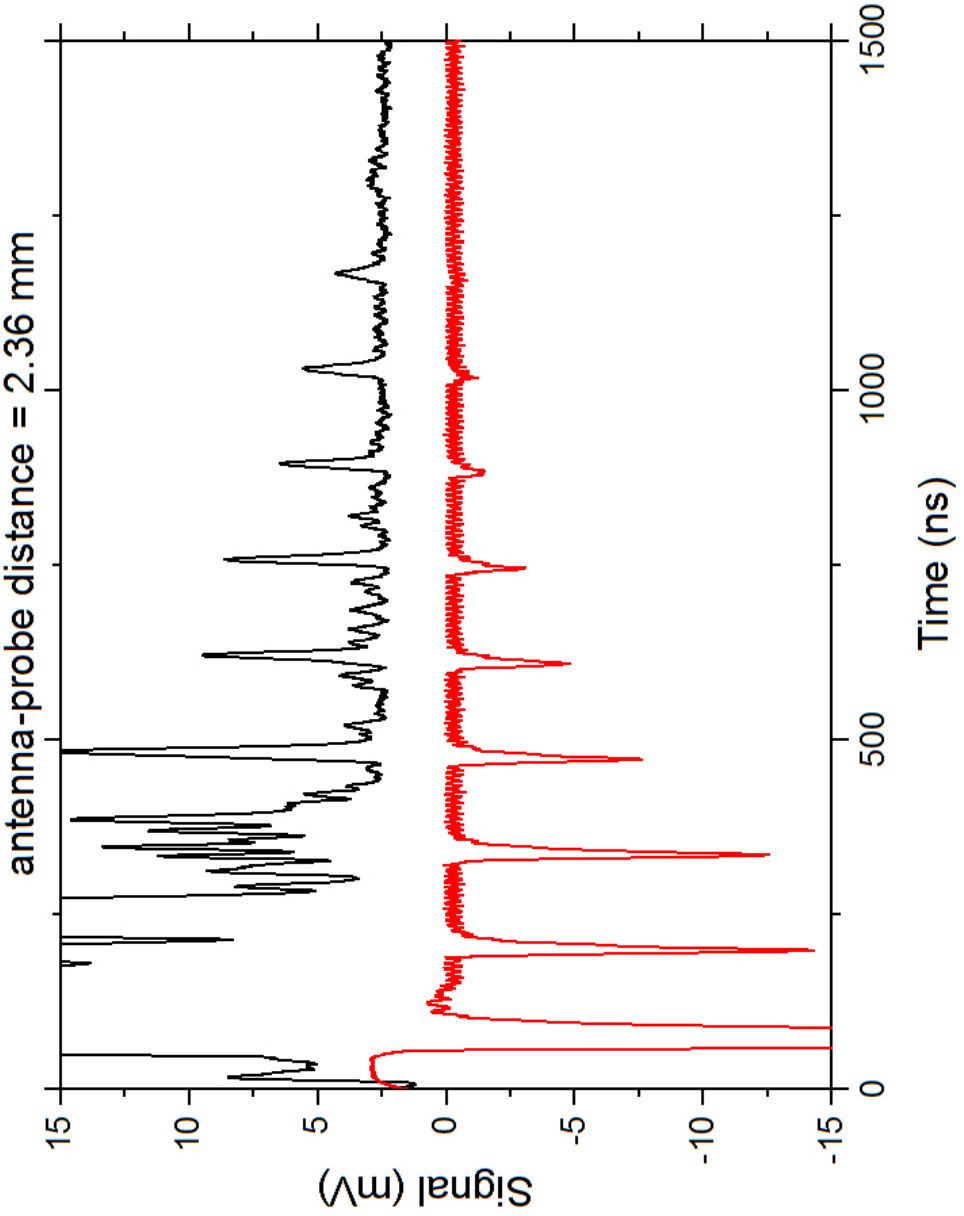

Figure 9.10: The trace of the diode output at θ_{ext}=30° at antenna-to-transducer distances= 2.36 mm. The black trace shows the magnon signal measured using an antenna while the red trace shows the acoustic echoes.

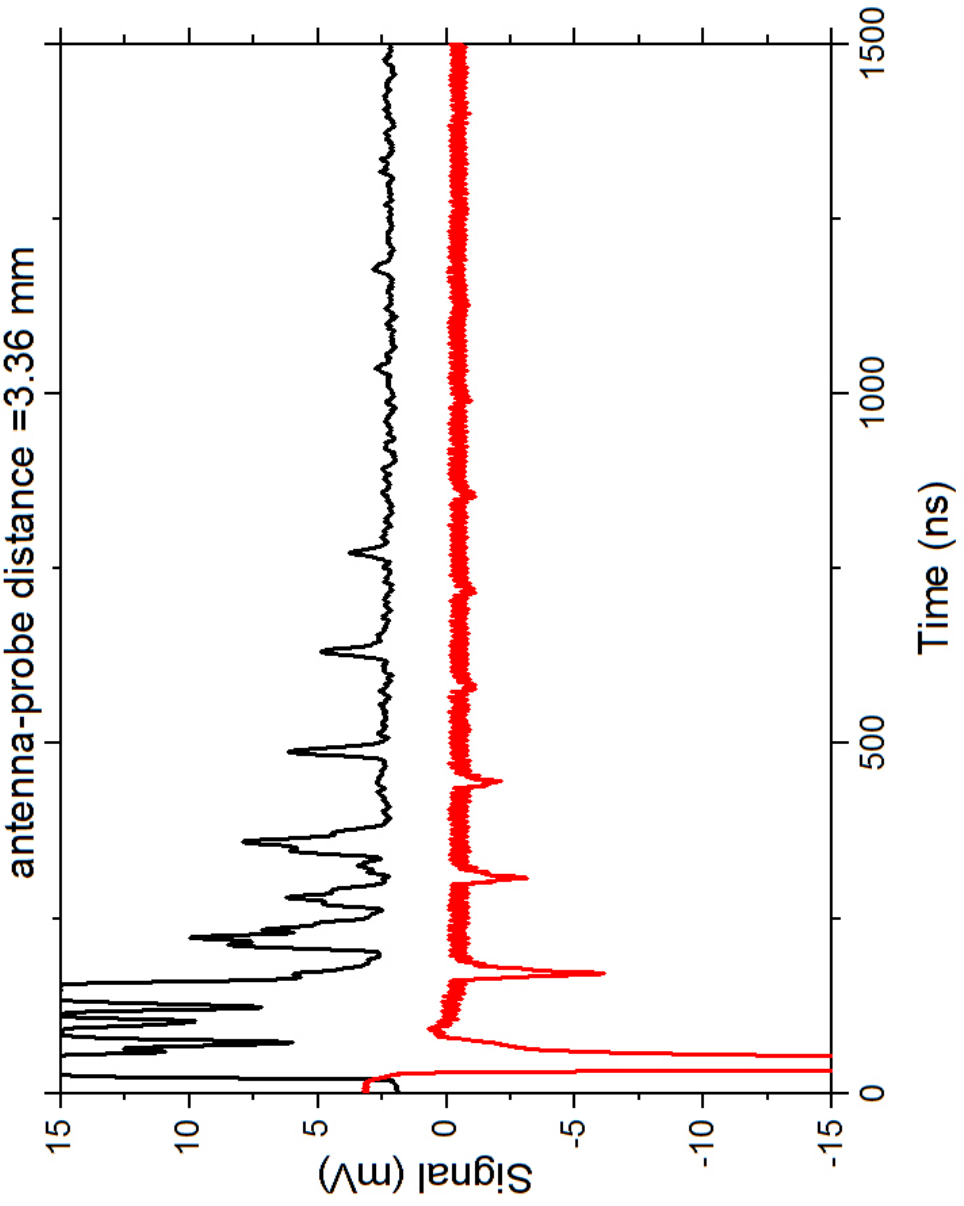

Figure 9.11: The trace of the diode output at θ_{ext}=30° at antenna-to-transducer distances= 3.36 mm. The black trace shows the magnon signal measured using an antenna while the red trace shows the acoustic echoes.

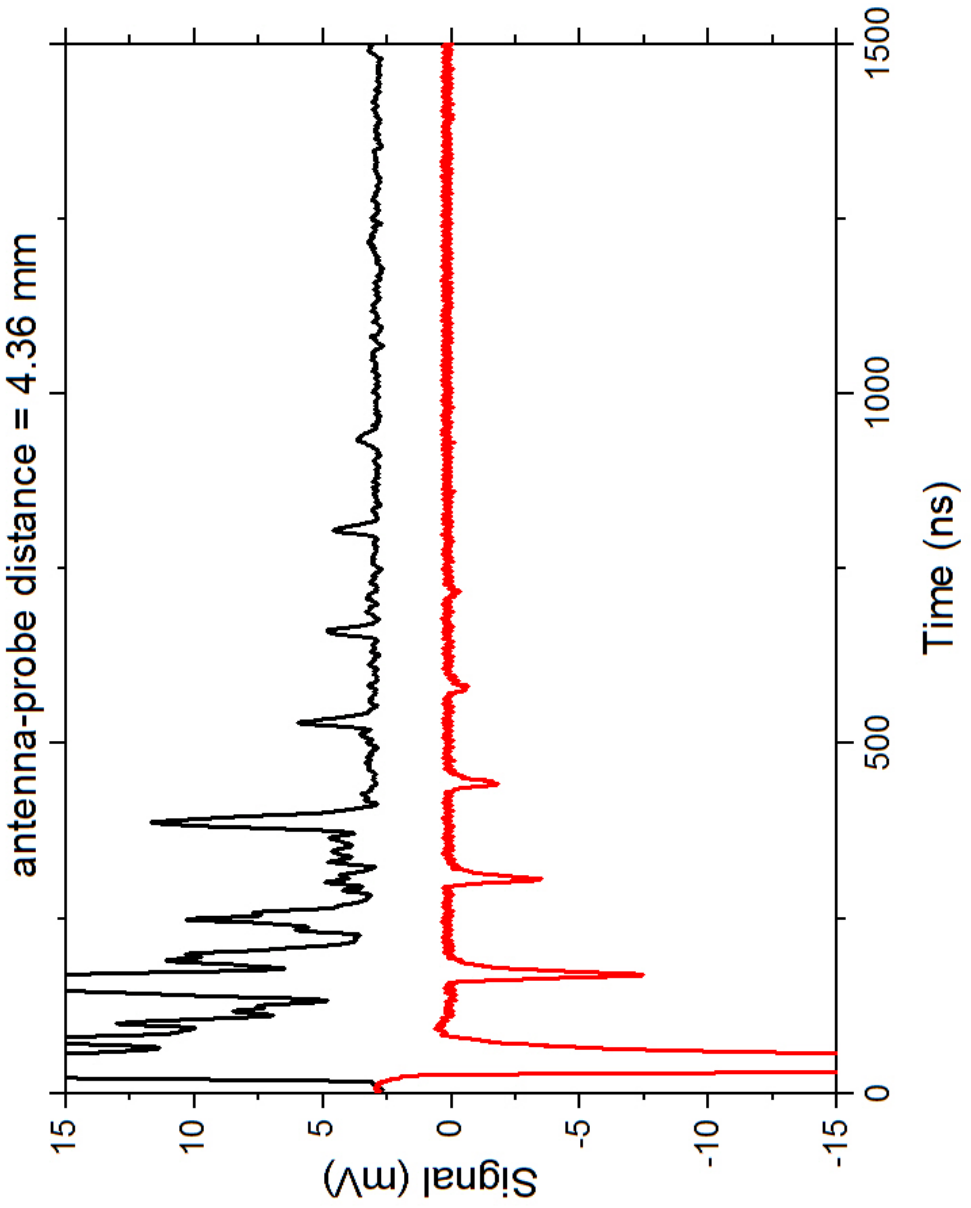

Figure 9.12: The trace of the diode output at θ_{ext}=30° at antenna-to-transducer distances= 4.36 mm. The black trace shows the magnon signal measured using an antenna while the red trace shows the acoustic echoes.

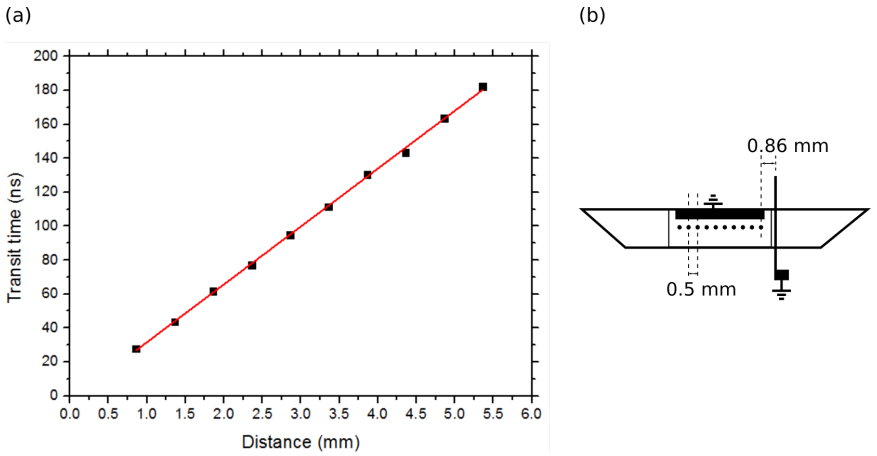

Figure 9.13: (a) The transit time of the magnons generated by the injected phonons versus the distance of transducer from antenna. (b) A schematic featuring the relative positions of the top dots and the output antenna.

acoustic wave returns to the transducer and generates a current. This causes the strip pattern signal that can be seen clearly in figure 9.14e. In the case when the receiving antenna is close to the transducer, the magnon signal generated by the acoustic wave interferes strongly with the spin-wave generated by the stray field and this give rise to a beating pattern.

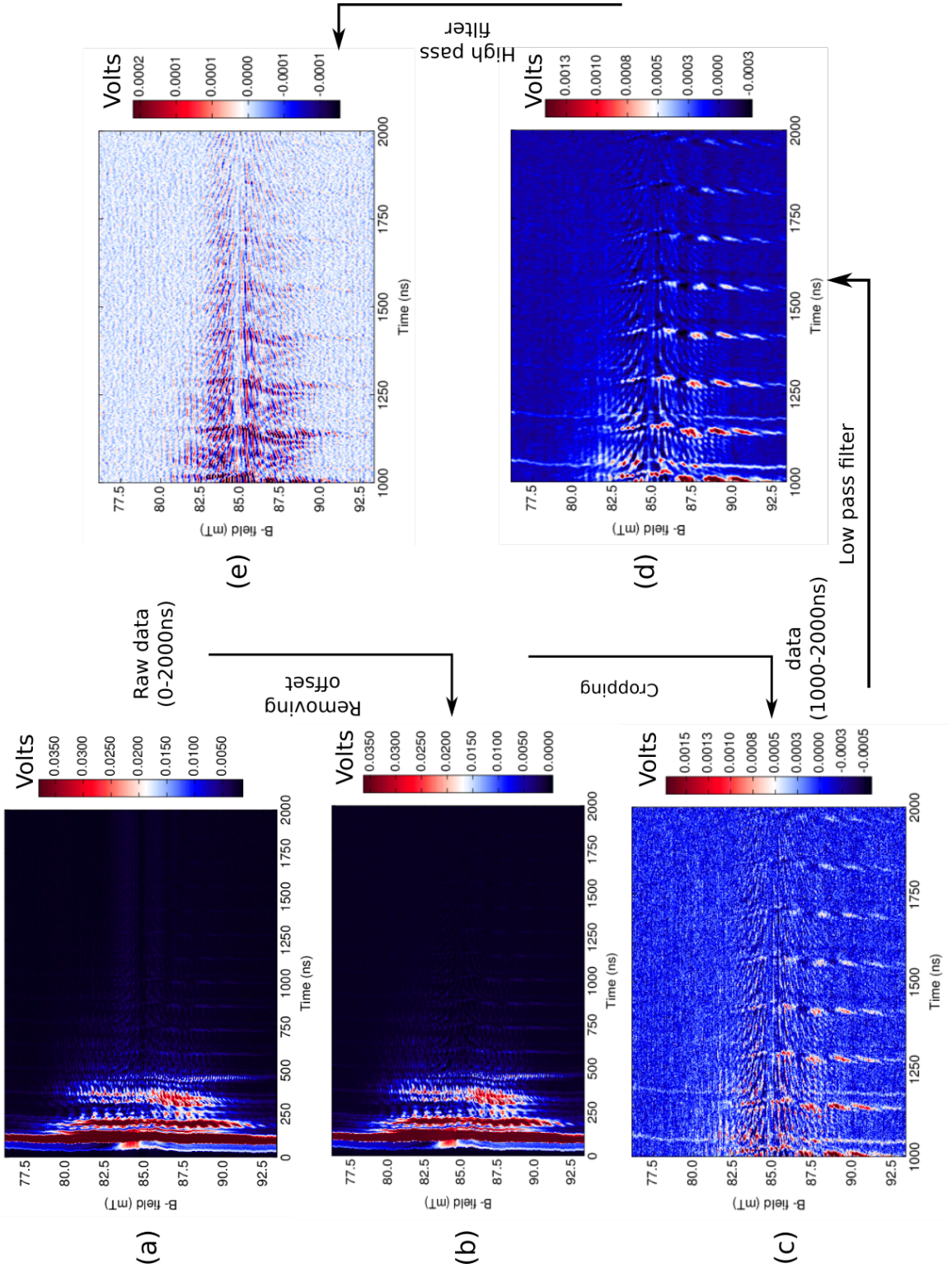

Figure 9.14: 3D data graph obtained when θ_{ext}=30° at an antenna-transducer distance of 0.86 mm. (a) Raw data obtained. (b) Removing the generic offset of the data. (c) Cropping the data from 1000 ns to 2000 ns, so that the initial spurious signals are avoided. (d) Applying a low pass filter to the image to improve the signal to noise ratio, a sharper image is obtained. (e) Applying a high pass filter after the low pass filter, we can see clearly the interference pattern of the spin-waves generated by the stray field of the picoprobe.

9.4.2 Power dependence of the excited MSW signal

YIG thin films are renowned for exhibiting non-linear effects at low power levels; this occurs when the precession angle of the spins is large and the linear relationship between **m** and **h** is no longer valid. Under such circumstances, parametric excitation of spin-waves are possible. Examples include perpendicular pumping - where the uniform precession mode transfers its energy into the propagating modes leading to the amplification of thermally generated travelling magnons: also parallel pumping - the direct generation of spin wave of frequency f by coupling to an alternating magnetic field of frequency $2f$ that is oriented along the magnetization direction. These processes can be observed above a certain threshold power when the excitation energy exceeds the attenuation of the waveguide and the power of the spin-wave generated is a non-linear function of the input driving power.

In order to find out whether the excitation process of the acoustically generated MSW is linear or non-linear, it is instructive to measure the amplitude of the MSW signal as a function of the acoustic power injected. Figure 9.15 illustrates the dependence of the excited MSW signal on acoustic power and it is clear that the relationship is linear and no parametric process was observed.

9.4.3 Lateral MSW at various oblique magnetic field angles

Having convinced ourselves that we can excite magnons by launching longitudinal phonons, we proceed to investigate the characteristic of this magnon signal at various applied magnetic field angles. We carry out this experiment at the transducer-antenna distance of 2.36 mm and again in these experiments a 3 GHz carrier is used. The results are shown in figure 9.16.

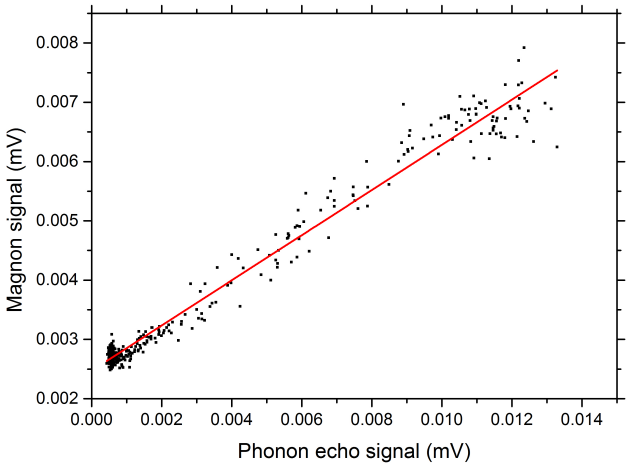

Figure 9.15: The power of the magnon signal generated by the injected phonon versus the injected phonon power

We can predict the type of MSWs (BVMSW or FVMSW) that can be excited at different applied B-field. Consider the intersection of the dotted lie representing the 3 GHz excitation with the dispersion curve of the MSWs (for a given B-field) as illustrated in figure 9.17. At low B-field, the excitation intersects with the FVMSW dispersion; whereas as the B-field moves the whole dispersion up, it starts to intersect the BVMSW branch after going through the FMR point. As we have pointed out in the previous section, the horizontal strip-like signal comes from the excitation of the FMR mode due to leakage signal (figure 9.14a; this gives us a reference as it locates the field where the carrier is FMR-resonant). Using this observation, it is apparent that only BVMSW can be observed from $\theta_{ext} = 15° - 90°$ and only FVMSW can be excited from $\theta_{ext} = 0° - 7.5°$ while both BVMSW and FVMSW can be excited at $\theta_{ext} = 10°$, which is similar to what we have measured in the antenna-antenna configuration (configuration 1). At $\theta_{ext} = 10°$, the FVMSW and BVMSW have quite different speeds and appear particularly nicely resolved in the data.

It was predicted in chapter 8 that the efficiency of acoustic excitation of magnons is proportional to $\sin(2\theta)$, and we shall now attempt to validate this by measuring

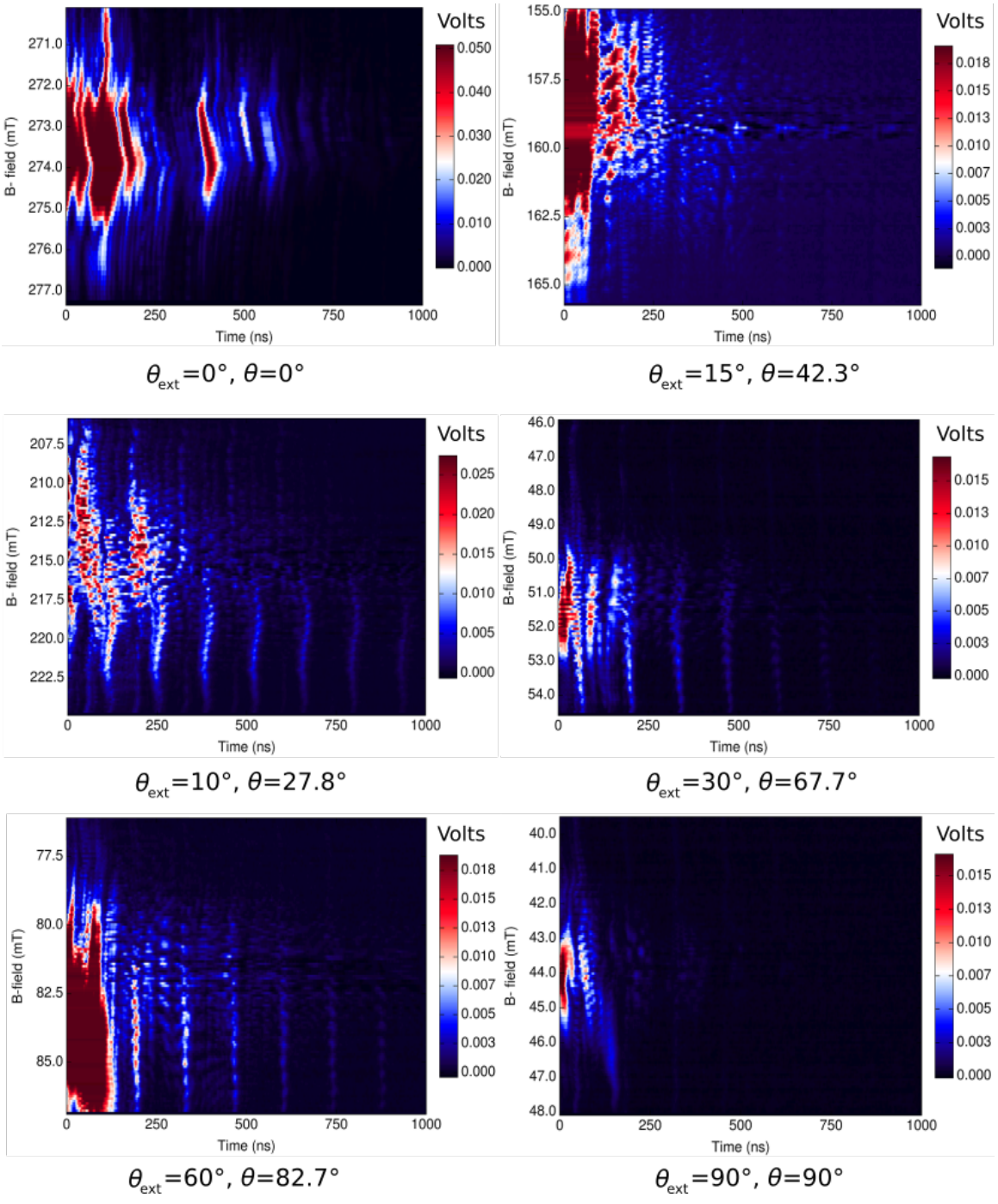

Figure 9.16: Figure showing the spin-wave signal measured by the output antenna for configuration 2 (θ_{ext} ranges from 0-90°) with antenna-to-transducer distance of 2.36 mm.

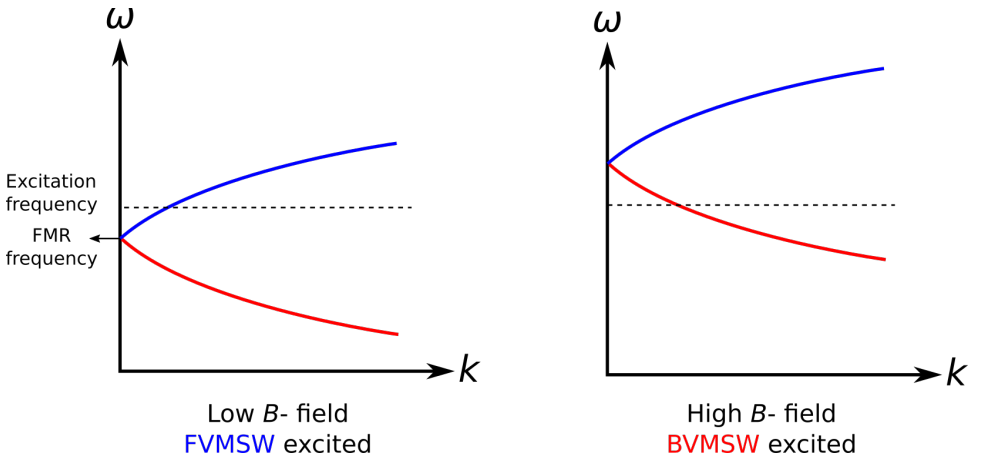

Figure 9.17: A schematic diagram showing the excitation of FVMSW (blue) and BVMSW (red) at low and high B-field respectively at a fixed excitation frequency.

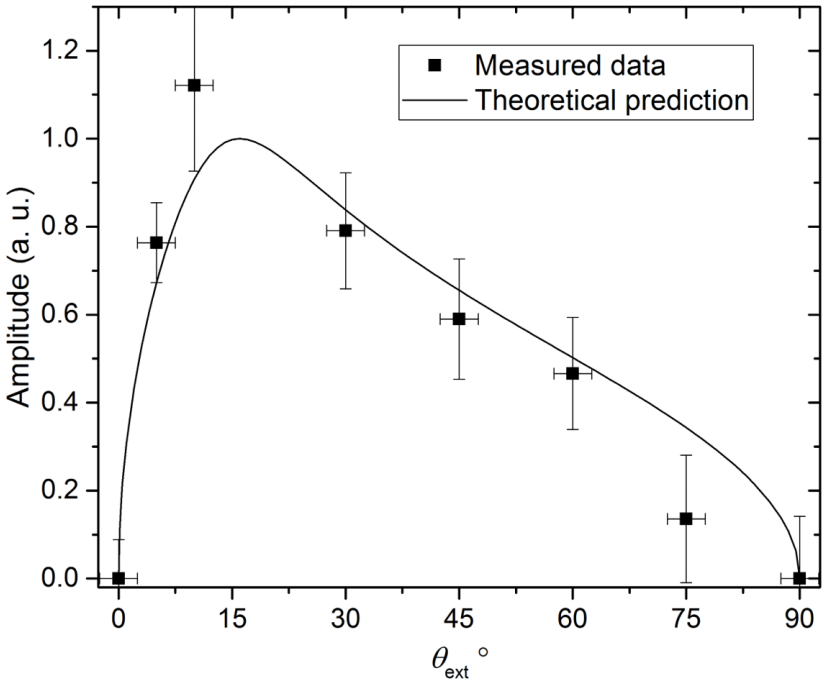

Figure 9.18: Figure showing the relative amplitude spin-wave signal measured by the output antenna for configuration 2 at various θ_{ext} at antenna-to-transducer distance of 2.86 mm

the maximum acoustically generated MSW signal with respect to θ_{ext}.

Plotted in figure 9.18 are the measured and predicted signal amplitudes at various θ_{ext}. Note that $\theta \geq \theta_{ext}$ due to demagnetising effects, this causes the signal amplitudes versus θ_{ext} curve to skew towards the left. A satisfactory match is observed between the measured and predicted values; this confirms our hypothesis of the underlying physical mechanism of phonon-magnon conversion.

There are two sources of experimental errors in this measurement. The main error is caused by the interference of the spin-wave signal caused by the stray pickup which masks the underlying acoustically generated MSW signal. This error is not disastrous. Another error comes from the fact that the picoprobe contact is extremely sensitive to external vibration, so the amplitude of the acoustic wave applied and its attenuation is not entirely stable. We therefore normalise the signal measured to the amplitude of the acoustic wave for the time at which the film gets hit, using the pulse echo data measured.

9.4.4 Frequency dependence of the excited MSW signal

To further consolidate the evidence of the existence of a longitudinal standing magnetoelastic wave, we investigate the acoustically generated magnon signal as a function of frequency ranging from 2.25 GHz to 3.75 GHz. By changing the frequency of the excited signal, we can form standing waves that have different wavelengths in accordance with the dispersion relation of the acoustic wave ($\lambda = v/f$). As discussed in chapter 8, the number of quarter wavelengths of the standing wave λ relative to the YIG film thickness L is essential for determining the coupling strength, i.e., the coupling maximizes when q is an odd integer and minimizes when q is an even integer where $L = q\frac{\lambda}{4}$.

Assuming the thickness of the YIG film is 7.8 μm as determined an earlier section by best fit of the velocity data, we deduce that coupling maxima should occur every 450 MHz. In the range of frequencies in which we can operate, we should expect the 4 peaks to appear at 2.05, 2.5, 2.95 and 3.4 GHz corresponding to L=2.25λ, L=2.75λ, L=3.25λ and L=3.75λ, respectively.

Figure 9.20 shows the acquired normalised magnon signal versus frequency and figure 9.19 illustrates the frequency dependence of the acoustic action of the broadband transducer. One can see immediately a cyclic trend of the signal with increasing frequency, and 4 maxima are observed at 2.25 GHz, 2.78 GHz, 3.05 GHz and 3.55 GHz: this agrees fairly well with theoretically predicted values. The underestimate of the frequency at which the maxima occur might be caused by overestimation of the YIG film thickness or to a change in surface conditions due to magnetoelastic coupling and pinning of the surface spins.

These results suggest that lateral MSW mode coupling onto standing longitudinal elastic waves is indeed the mechanism for acoustical MSW excitation in our experiment.

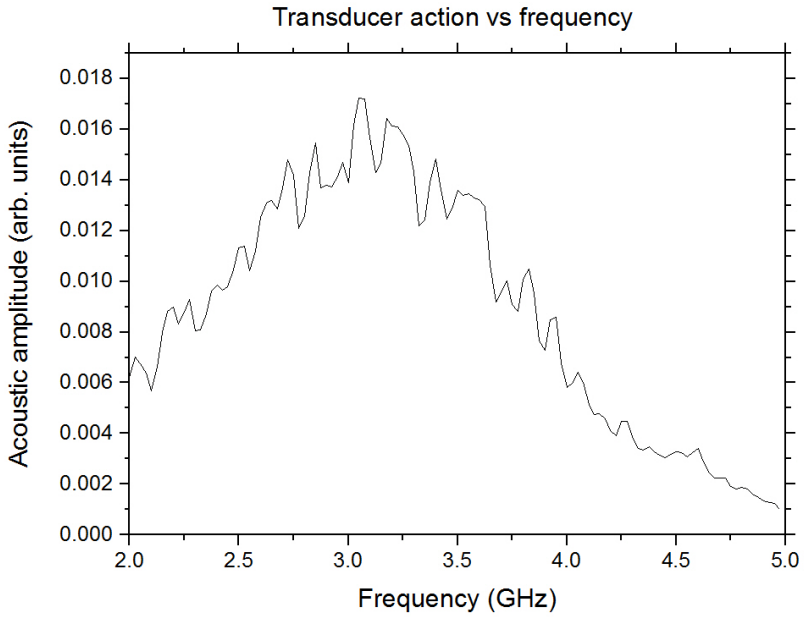

Figure 9.19: The efficiency of the acoustic transducer grown on the YIG waveguide at various frequencies.

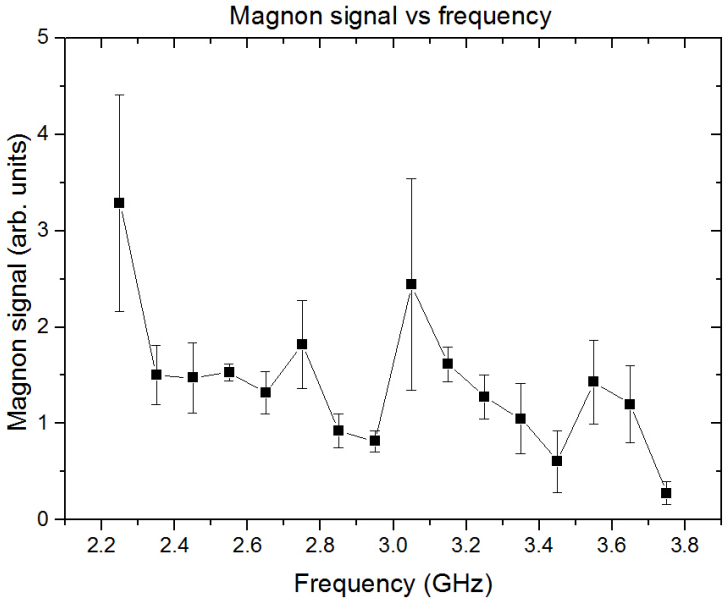

Figure 9.20: Figure showing the relative amplitude of the normalised spin-wave signal measured by the output antenna for configuration 2 at various frequencies at antenna-to-transducer distance of 2.86 mm

Chapter 10

Conclusion and outlook

Over the course of the thesis, we have developed a good understanding of longitudinal ZnO bulk acoustic wave (BAW) transducers. We have successfully grown ZnO thin films that have electromechanical coupling constants up to 81% of the bulk value - and for the first time (to the author's knowledge) - observed a pulse echo at ultra high frequencies near 10 GHz. By integrating this BAW technology into YIG thin film magnonic systems, we have demonstrated experimentally the viability of acoustic magnetostatic spin-wave excitation - an unprecedented approach for magnon generation. In the following, we will summarize the main results obtained and how they fit into the wider scientific context.

In chapter 3, we have used the Mason model to predict the conversion losses of transducers with appropriate geometry, and the predictions were found to agree very well with the experimental results presented in chapter 5. The ability to model the transducer performance allows us to design the transducers appropriately for specific applications.

In chapter 5, we found (by using X-ray and pulse echo characterisation discussed in chapter 4) that both the piezoelectric activities and crystalline qualities of the sputtered ZnO films are critically dependent on the sputtering conditions and

the thicknesses of the ZnO thin films. A strong correlation was found between the piezoelectric properties of the ZnO films and their crystalline quality. In particular, we observed that ZnO films that possess good longitudinal piezoelectric activities tends to be those that have the best c-axis orientation. Conversely, the poor piezoelectric film activity is caused by poor crystalline quality and structural disorder rather than polarization reversal. Moreover, ZnO films that are grown on a gold substrate tend to develop a compressive stress and a layer of disordered (piezoelectrically dead) structure is found adjacent to the gold/substrate interface.

A custom single Langmuir probe device was built (see chapter 6) to investigate the plasma conditions during ZnO deposition. In particular, the energy $e(V_{s,\mathrm{DC}} - V_{f,\mathrm{DC}})$ and flux J of the positive ions that bombard a flat electrically insulating substrate were measured. Combining these results and with knowledge of the deposition rates using the calibrated quartz monitor, we found that ZnO films that are grown in sputtering conditions of high $\Xi = \frac{J \times (V_{s,\mathrm{DC}} - V_{f,\mathrm{DC}})}{\text{Deposition rate}}$ tend to have little c-axis orientation. The implication of this result is that one of the important criteria for producing good c-axis oriented and polarized ZnO thin films is to decrease the energy and flux of the ion bombardment but without decreasing the deposition rate. This criterion can be more readily achieved by using a balanced magnetron design.

So far, all of our fabricated BAW transducers produce longitudinal waves. However, as discussed in section 2.2.2.2, transducers can produce both longitudinal and shear waves if the c-axes of the ZnO grains lie at an angle to the substrate normal. These transducers are suitable for a wider range of applications and are thus highly desirable. Although the fabrication of these transducers is beyond the scope of the thesis, as suggested in our studies of the ZnO growth mechanism in chapter 7, these transducers can potentially be fabricated under high ion bombardment conditions. These condition could be met, for example by using

a very unbalanced magnetron and short substrate-target distance or by directly introducing a RF bias onto the substrate.

After having successfully developed longitudinal ZnO transducers that operate efficiently in the GHz regime, we investigated both theoretically (Chapter 8) and experimentally (Chapter 9) the concept of acoustic excitation of MSWs. This was achieved by directly injecting longitudinal bulk acoustic waves perpendicular to a YIG thin film waveguide. The acoustically generated MSWs were detected using an antenna at a known distance away from the point where the MSWs were excited. By using time-resolved measurements, we observed MSW pulses whose timing corresponds exactly to that expected for acoustically excited MSW (the velocity of the MSWs are known). This confirms our hypothesis that MSWs can indeed be generated acoustically as proposed.

We further investigated the dependence of the excitation efficiency as a function of applied magnetic field angle and carrier frequency. The experimental data obtained from the frequency dependence of the generation efficiency consolidates our belief that the MSWs are mode-coupled to an effective oscillating magnetic field which is generated by the standing elastic wave across the YIG waveguide (via magnetoelastic coupling). However, the results from the field angle dependence of efficiency are a bit more obscure. It was found that the excitation efficiencies approach zero when the field was parallel and perpendicular to the YIG waveguide: this agrees with the predicted angular dependence of the effective magnetoelastic coupling constant ($b_{\text{eff}} \propto \sin(2\theta)$). However, unexpectedly, a dip of excitation efficiency was also found near $\theta \approx 45°$. This effect could be explained if the longitudinal elastic wave is hybridised with the spin waves travelling perpendicular to the YIG waveguide to form a magnetoelastic wave. The impedance changes caused by the significant velocity modulation of magnetoelastic waves near the FMR frequencies prevent the incoming acoustic wave from entering the YIG waveguide and thus less magnon signal is measured at angles with higher b_{eff}.

All in all, we have shown - as a proof of concept - that the BAW transducers can effectively act as point magnon source in YIG thin film waveguides. An even more versatile magnon source could potentially be made by implementing the forementioned transducers that can excite either longitudinal or shear waves. These magnon point sources would be extremely useful in 2D wave computing in the future which is an, as of yet, unseen tool in the magnonicians tool box.

Appendix A

Electric field and sheath thickness estimation using the Child Langmuir's law

[1]Consider an infinite planar geometry as shown in figure A.1, and define the plasma potential to be at zero potential. Define the floating substrate potential to be $\phi = -U$ (U is positive as a floating electrode is always negative to that of the plasma). The potential distribution of the plasma is determined by the 1D Poisson's equation:

$$\epsilon_0 \frac{d^2\phi}{dx^2} = -en(x) \tag{A.1}$$

where n(x) is the net ion density. There are two particle species in the plasma, i.e., ions and electrons. We assume that the ions are cold and that they all have effectively the same speed v_0 in the bulk plasma region. These ions gain energy as they accelerate to the substrate under the action of the electric fields. Conservation of energy means that:

$$\frac{1}{2}m_i v_i^2 = \frac{1}{2}m_i v_0^2 - q_i\phi \tag{A.2}$$

[1]See reference [99] for a more comprehensive analysis of plasma sheath

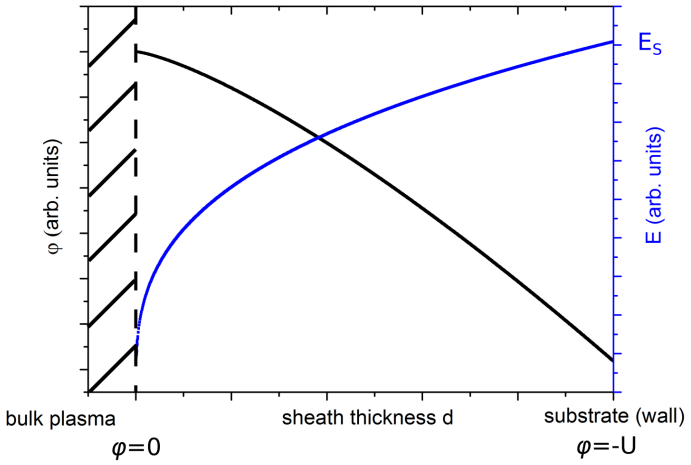

Figure A.1: A schematic diagram showing the geometry of a planar sheath, and the form of the potential and electric field if Child Langmuir's law is assumed.

where m_i, q_i are the mass and charge of the ion respectively, and v_i is the speed of the ion after it has been accelerated by the potential ϕ.

Since the ion flux is constant, $n_i q_i v_i$ is fixed with $n_i(0) = n_0$, so we have:

$$n_i = n_0 \sqrt{\frac{1}{1 - \frac{2q_i\phi}{m_i v_0^2}}}. \tag{A.3}$$

The electrons are assumed to have a Maxwellian distribution of velocities corresponding to a high temperature T, so:

$$n_e = n_0 e^{\frac{e\phi}{k_B T}}. \tag{A.4}$$

The net charge density is therefore:

$$n(x) = n_0 \sqrt{\frac{1}{1 - \frac{2q_i\phi}{m_i v_0^2}}} - n_0 e^{\frac{e\phi}{k_B T}} \tag{A.5}$$

Substituting equation (A.5) into Poisson equation (A.1), and with the change of variables:

$$\eta = -\frac{q_i \phi}{k_B T}, \tag{A.6}$$

$$u = v\sqrt{\frac{m_i}{2k_B T}}, \tag{A.7}$$

and

$$\xi = \frac{x}{\lambda_D}, \tag{A.8}$$

we obtain:

$$\eta'' = \frac{1}{\sqrt{1 + \frac{\eta}{u_0^2}}} - e^{-\eta}. \tag{A.9}$$

Here the prime is the derivative with respect to ξ. This equation encapsulates the heart of the plasma sheath problem; unfortunately it cannot be solved analytically. We now discuss the regime that allows us to derive Bohm's criterion and to reduce this equation to the Child's Langmuir form. We make two basic assumptions, they are:

1. The characteristic length of the system is much larger than the Debye length λ_D, or $\eta'(0) \to 0$ (thin sheath condition)
2. The potential U is large compared to $k_B T$, i.e. $\frac{e\phi}{k_B T} >> 1$

Multiply by η' on both sides of equation (A.9) and integrate from 0 to η to give:

$$\frac{1}{2}\eta'^2 = \left[2u_0^2\left(\sqrt{1 + \frac{\eta}{u_o^2}} - 1\right) + e^{-\eta} - 1\right] + \frac{1}{2}\eta'(0)^2 \tag{A.10}$$

From assumption 1, we neglect $\eta'(0)$ and since the left side of equation (A.10) is positive, we obtain an inequality:

$$2u_0^2\left(\sqrt{1 + \frac{\eta}{u_0^2}} - 1\right) \geqslant 1 - e^{-\eta} \tag{A.11}$$

u_0 is typically of order $10^3\,\mathrm{m}s^{-1}$, so $\frac{\eta}{u_o^2}$ is small and the square root function in equation (A.11) can be approximated using the Taylor expansion. Rearranging equation A.11 yields the Bohm criterion, i.e.,

$$v_0 \geqslant \sqrt{\frac{k_B T}{m_i}} = c_s \tag{A.12}$$

where c_s is the Bohm velocity.

The physical meaning of this equation is that the ions have to enter the sheath with a minimum velocity of $v_0{=}\sqrt{\frac{k_B T}{m_i}}$, so there must exist a region of presheath which accelerates the ions to this speed. With the reduction of ion densities in the presheath, it can be shown that the ion current density of the planar substrate is:

$$j_i = 0.6 q_i n_i c_s, \tag{A.13}$$

which is known as the Bohm ion current density [45, 100].

From assumption 2, $\frac{e\phi}{k_B T} >> 1$, the number of repelling species (i.e., the electrons) is small so it can be neglected. Under this condition, $\frac{2q_i\phi}{m_i v_0^2}$ is also much larger than 1, so the form of the ion density reduces to:

$$n_i = \frac{j_i}{e}\sqrt{\frac{m_i}{-2q_i\phi}} \tag{A.14}$$

We now substitute the change (A.14) back into Poisson's equation:

$$\epsilon_0 \frac{d^2\phi}{dx^2} = -j_i\sqrt{\frac{m_i}{-2q_i\phi}} \tag{A.15}$$

This equation can now be easily integrated analytically, and taking account of the boundary condition that $\phi(0) = 0$, and $\phi'(0) = \eta'(0) = 0$, the potential

distribution $\phi(x)$ is given by:

$$\phi(x) = -\Big(\frac{81}{32}\frac{m_i j_i^2}{q_i \epsilon_0^2}\Big)^{\frac{1}{3}} x^{\frac{4}{3}} \tag{A.16}$$

The electric field E is found by differentiating the potential:

$$E = -\frac{d\phi}{dx} = \Big(\frac{8 m_i j_i^2}{q_i \epsilon_0^2} x\Big)^{\frac{1}{3}} \tag{A.17}$$

The maximum electric field at the substrate surface E_s is:

$$E_s = \Big(\frac{8 m_i j_i^2 U}{q_i \epsilon_0^2}\Big)^{\frac{1}{4}}, \tag{A.18}$$

which is known as the Mackeown equation [101]. The sheath thickness d can be expressed in terms of the potential U, i.e.

$$d^2 = \frac{4}{9}\epsilon_0 \sqrt{\frac{2q_i}{m_i}} \frac{U^{\frac{3}{2}}}{j_i} \tag{A.19}$$

Substituting $j_i = 0.6 q_i n_i c_s$ into equation (A.17) and (A.19), one can eliminate the variable m_i giving the final result:

$$E(x = d) = \Big(\frac{2.88 n^2 q_i k_B T U}{\epsilon_0^2}\Big)^{\frac{1}{4}}, \tag{A.20}$$

$$d = 1.018\Big(\frac{q_i U}{k_B T}\Big)^{\frac{3}{4}} \lambda_D \tag{A.21}$$

where $\lambda_D = \sqrt{\frac{\epsilon_0 k_B T}{e^2 n_i}}$.

Appendix B

The orbital motion limited (OML) theory

[1]Consider the orbital motion of an electron of mass m with an initial energy of eV_0 around a probe of potential V_p with radius r_p. The impact parameter is defined as h. If the speed of the electron is v_p at the probe surface (OP=r_p in the diagram), the conservation of energy gives:

$$\frac{1}{2}mv_p^2 - eV_p = eV_0 \tag{B.1}$$

and the conservation of momentum yields:

$$mvh = mr_p v_p. \tag{B.2}$$

The effective radius for which the electron can be caught by the probe is given by the impact parameter h, which can be rewritten as:

$$h = r_p\left(1 + \frac{V_p}{V_0}\right)^{1/2} \tag{B.3}$$

[1]Much of the derivation described here is based on Allen's work [48].

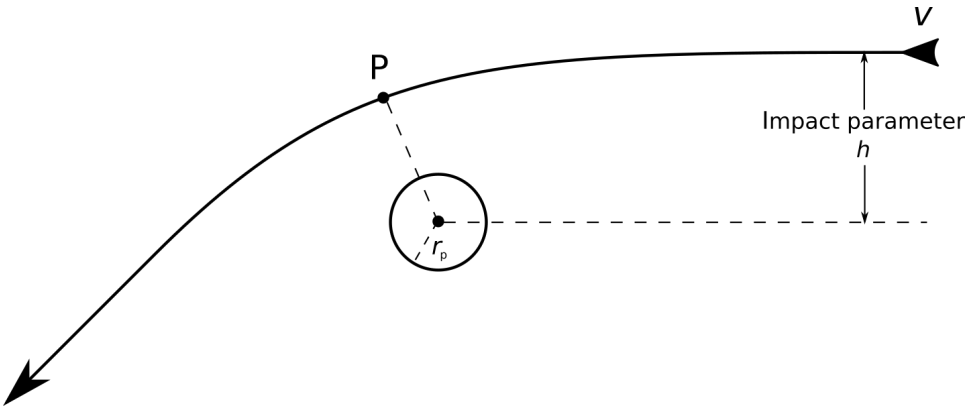

Figure B.1: A schematic diagram showing the orbital motion of an electron with an initial energy eV_0 around a probe of radius r_p with an impact parameter of h

The current due to electrons with a narrow velocity range is therefore:

$$dI = h \cdot e \cdot d\Phi \tag{B.4}$$

where dΦ is the flux of electrons crossing perpendicular to the plane, i.e.:

$$d\Phi = \frac{v}{\pi} dn \tag{B.5}$$

where dn represents the number of electrons that have velocities ranging from v to $v+dv$. Assuming that the electrons follow a Maxwellian distribution, in cylindrical geometry, dn is given by:

$$dn = n_0 \left(\frac{m}{2\pi k_B T} \right) e^{-\frac{mv^2}{2k_B T}} 2\pi v dv. \tag{B.6}$$

Substituting equations (B.5) and (B.6) into equation (B.4) and letting

$$x^2 = \frac{1}{2} \frac{mv^2}{k_B T}, \tag{B.7}$$

$$\eta = a^2 = \frac{eV_p}{k_B T}, \tag{B.8}$$

the total current can be expressed as the integral:

$$I = \int_0^\infty 4n_0 r_p l e \sqrt{\frac{2k_B T}{m}} x e^{-x^2} (x^2 + a^2)^{\frac{1}{2}} dx, \tag{B.9}$$

This integral can be evaluated exactly:

$$I = 2\pi n_0 r_p l e \Big(\frac{k_B T}{2\pi m}\Big)^{\frac{1}{2}} \Big[\frac{2\sqrt{\eta}}{\sqrt{\pi}} + e^{\eta} \mathrm{erfc}(\sqrt{\eta})\Big], \tag{B.10}$$

where the error function is defined as:

$$\mathrm{erfc}(x) = \frac{2}{\sqrt{\pi}} \int_0^x e^{-t^2} dt. \tag{B.11}$$

For $\eta > 2$, we can approximate:

$$\frac{2\sqrt{\eta}}{\sqrt{\pi}} + e^{\eta} \mathrm{erfc}(\sqrt{\eta}) \approx \frac{2(1+\eta)^{\frac{1}{2}}}{\sqrt{\pi}}. \tag{B.12}$$

and therefore we have:

$$I = 2\pi n_0 r_p l e \Big(\frac{k_B T}{2\pi m}\Big)^{\frac{1}{2}} \frac{2}{\sqrt{\pi}} \Big(1 + \frac{eV_p}{k_B T}\Big)^{\frac{1}{2}}. \tag{B.13}$$

So for high η, $I \propto V_p^2$ such that:

$$I \approx A_p e \frac{\sqrt{2}}{\pi} \Big(\frac{eV_p}{m}\Big)^{\frac{1}{2}}. \tag{B.14}$$

Bibliography

[1] F. Bloch. Zur Theorie des Ferromagnetismus. *Z. Phys.*, 61:206, 1930.

[2] J. H. E. Griffiths. Anomalous high-frequency resistance of ferromagnetic metals. *Nature*, 158:670–671, 1946.

[3] A. D. Karenowska, A. D. Patterson, M. J. Peterer, E. B. Magusson and P. J. Leek. Excitation and detection of propagating spin wave at single magnon level. *arXiv*, 1502.06263, 2015.

[4] B. A. Kalinikos, N. G. Kovshikov and A. N. Slavin. Dipole- exchange spin-wave solitons in YIG garnet. *J. Phys. Colloq.*, 49(C8):1583–1584, 1988.

[5] A. A. Serga, S.O. Demokritov, B. Hillebrands and A. N. Slavin. Self generation of two dimensional spin-wave bullets. *Phy. Rev. Lett.*, 92:117203, 2004.

[6] M. Wu, B. A. Kalinikos, D. Carr and C. E. Patton. Observation of spin-wave soliton fractals in magnetic film active feedback rings. *Phys. Rev. Lett.*, 96: 187202, 2006.

[7] M. Wu, A. M. Hagerstrom, A.Kondrashov and B. A. Kalinikos. Excitation of chaotic spin-waves through modulational instability. *Phys. Rev. Lett.*, 102 (23):237203, 2009.

[8] Y. V. Gulyaev. Ferromagnetic film with magnon bandgap periodic structures: magnon crystal. *JETP Lett.*, 77(10):567–570, 2003.

[9] M. Kravczyh and D. Grundler. Review and prospects of magnonic crystals and devices with reprogrammable band structure. *J. Phys. Condens. Matter*, 26:123202, 2014.

[10] M. N. Baibich, J. M. Broto, A. Fert, F. Nguyen Van Dau, F. Petroff, P. Etienne, G. Creuzet, A. Friederich, and J. Chazelas. Giant magnetoresistance of (001)Fe/(001)Cr magnetic superlattices. *Phys. Rev. Lett.*, 61(21): 2472–2475, 1988.

[11] J. E. Hirsch. Spin Hall effect. *Phys. Rev. Lett.*, 83(9):1834–1837, 1999.

[12] E. Saitoh, M. Ueda, H. Miyajima and G. Tatara. Conversion of spin current into charge current at room temperature: inverse spin- Hall effect. *Appl. Phys. Lett.*, 80:182509, 2006.

[13] D. C. Ralph and M.D. Stiles. Spin transfer torques. *J. Magn. Magn. Mater.*, 320(7):1190–1216, 2008.

[14] B. Heinrich, C. Burrowes, E. Montoya, B. Kardasz, E. Girt, Y-Y Song, Y. Sun and M. Wu. Spin pumping at the magnetic insulator (YIG)/Normal metal (Au) interface. *Phys. Rev. Lett.*, 107:066604, 2011.

[15] K. Uchida, S. Takahashi, K. Harii1, J. Ieda, W. Koshibae, K. Ando, S. Maekawa and E. Saitoh. Observation of the spin Seeback effect. *Nature*, 455:778–781, 2008.

[16] Th. Gutjahr-Lokser, D.Sander and J. Kirschner. Magnetoelastic coupling in Co thin films on W (001). *J. Magn. Magn. Mater.*, 220(1):1–7, 2000.

[17] H. Huabl, R. Gross, M. S. Brundt M. Weiler, L. Dreher, C. Herg and S. T. B. Goennenwein. Elastically driven ferromagnetic resonance in Nickel thin films. *Phys. Rev. Lett.*, 106:117601, 2011.

[18] W. P. Wolf and C. H. A. Huan. Magnetoelastic properties of dysprosium aluminum garnet: Theory. *Phys. Rev. B*, 37(4):2033–2049, 1988.

[19] T. Yukawa and M. Tsutsumi. Magnetoelastic waves in yttrium iron garnet film. *Electron Comm Jpn 2*, 77(3):20–27, 1994.

[20] J. R. Eshbach. Spin wave propagation and the magnetoelastic interaction in yttrium iron garnet. *J. Appl. Phys.*, 34(4):1298–1304, 1963.

[21] M. F. Lewis. Excitation of longitudinal magnetoelastic waves in axially magnetized YIG rods. *J. Appl. Phys.*, 41(6):2505–2509, 1970.

[22] R. Q. Scott and D. L. Mills. Propagation of surface magnetoelastic waves on ferromagnetic crystal substrates. *Phys. Rev. B*, 15(7):3545–3557, 1977.

[23] A. A. Serga, A. V. Chumak and B. Hillebrands. YIG magnonics. *J. Phys. D: Appl. Phys.*, 43:264002, 2010.

[24] S. B. Hussain. Fabrication of CdS piezoelectric transducers by electron beam evaporation. *J. Sound Vibration*, 12(2):177–180, 1970.

[25] M. T. Wauk and D. K. Winslow. Vacuum deposition of AlN acoustic transducers. *Appl. Phys. Lett.*, 13(8):286–288, 1968.

[26] M. D. Ambersley and C. W. Pitt. Piezoelectric ZnO transducers produced by rf magnetron sputtering. *Thin Solid Films*, 80(1-3):183–195, 1981.

[27] Y. H. Hsu, J. Lin and W. C. Tang. RF sputtered piezoelectric zinc oxide thin film for transducer applications. *J. Mater Sci: Mater Electron*, 19(7): 653–661, 2008.

[28] M. C. Pan, T. H. Wu, T. A. Bui and W. C. Shih. Fabrication of highly c-axis textured ZnO thin films piezoelectric transducers by rf sputtering. *J. Mater Sci: Mater Electron*, 23(2):418–424, 2012.

[29] T. Shiosaki T. Yamamoto and A. Kawabata. Characterization of ZnO piezoelectric films prepared by rf planar magnetron sputtering. *J. Appl. Phys.*, 51(6):3113–3120, 1980.

[30] Y. Liu, Y. Li and H. Zeng. ZnO-based transparent conductive thin films: Doping, performance, and processing. *J. Nanomaterials*, 2013.196521, 2013.

[31] Z.A. Wang, J.B. Chu, H.B. Zhu, Z. Sun, Y.W. Chen and S.M. Huang. Growth of ZnO:Al films by rf sputtering at room temperature for solar cell applications. *Solid State Electron*, 53(11):1149–1153, 2009.

[32] H. Morkoc and U. Ozgur. Zinc oxide: Fundamentals, materials and device technology. *Wiley- VCH*, 2008.

[33] D. Kohl. *The influence of energetic bombardment on the structure formation of sputtered Zinc Oxide films.* PhD thesis, Rwth Aachen University, 2011.

[34] J. P. Wei and X. Y. Su. Wave propagation in a piezoelectric rod of 6mm symmetry. *Int. J. Solids. Struct.*, 42(13):3644–3654, 2005.

[35] N. F. Foster. Cadmium sulphide and zinc oxide thin-film transducers. *IEEE Trans. Sonics Ultrason.*, 15(1):28–40, 1968.

[36] M. P. Mason. Electromechanical transducers and wave filters. *Van Nostrand, Princeton. NJ*, 1948.

[37] M. P. Mason. Physical acoustics and the properties of solids. *Van Nostrand, Princeton. NJ*, 1958.

[38] Q. Chen and Q. Wang. The effective electromechanical coupling coefficient of piezoelectric thin-film resonators. *Appl. Phys. Lett.*, 86:022904, 2005.

[39] E. K. Sittig. Design and technology of piezoelectric transducers for frequencies above 100MHz. *Physical Acoustics, Vol IX, Academic Press, NY*, pages 221–275, 1972.

[40] Y. Zhang, Z. Wang, J. David and N. Cheeke. Resonant spectrum method to characterize piezoelectric films in composite resonators. *IEEE Trans. Ultrason., Ferroelect., Freq. Control.*, 50(3):321–333, 2003.

[41] C. Li, D. Wang, Z. Li, X. Li, T. Kawaharamura and M. Furuta. Stoichiometry control of ZnO thin film by adjusting working gas ratio during radio frequency magnetron sputtering. *J. Materials*, 2013.547271, 2013.

[42] J. W. Jeon, M. Kim, L. W. Jang, J. L. Hoffman, N. S. Kim and I. H. Lee. Effect of substrate temperature on residual stress of ZnO thin films prepared by ion beam deposition. *Electron Mater. Lett.*, 8(1):27–32, 2012.

[43] J. G. E. Gardeniers, Z. M. Rittersma and G.J. Burger. Preferred orientation and piezoelectricity in sputtered ZnO films. *J. Appl. Phys.*, 83(12):7844–7854, 1998.

[44] S. Takayanagi, Y. Yanagitani and M. Matsukawa. Wideband multimode transducer consisting of c-axis tilted ZnO/ C axis normal ZnO multilayer. *Jpn. J. Appl. Phys.*, 51(7):07GC08, 2012.

[45] D. Bohm. Characteristics of electrical discharges in magnetic fields. *McGraw-Hill, NY*, 1949.

[46] I. Langmuir. The effect of space charge and residual gases on thermionic current in vacuum. *Phys. Rev.*, 2(6):450–486, 1913.

[47] J. E. Allen, R. L. F. Boyd and P. Reynolds. The collection of positive ions by a probe immersed in a plasma. *Proc. Phys. Soc Lond (B)*, 70(3):297–304, 1957.

[48] J. E. Allen. Probe theory - the orbital motion approach. *Phys. Scr*, 45(5): 497–503, 1992.

[49] J. G. Laframboise. *Theory of spherical and cylindrical Langmuir probes in a collisionless Maxwellian plasma at rest.* PhD thesis, University of Toronto, Institute of Aerospace Studies Report, 1966.

[50] F. F. Chen. Langmuir probe analysis for high density plasmas. *Phys.Plasma.*, 8(6):3029–3041, 2001.

[51] J. G. Laframboise and J. Rubinstein. Theory of a cylindrical probe in a collisionless magnetoplasma. *Phys. Fluids*, 19(12):1900–1908, 1976.

[52] M. Mausbach. Parametrization of the Laframboise theory for cylindrical Langmuir probe analysis. *J. Vac. Sci. Technol. A*, 15(6):2923–2929, 2003.

[53] Y. Kajikawa. Texture development of non-epitaxial polycrystalline ZnO films. *J. Cryst. Growth.*, 289(1):387–394, 2006.

[54] Y. Kajikawa, S. Noda and H. Komiyama. Comprehensive perspective on the mechanism of preferred orientation in reactive sputter deposited nitrides. *J. Vac. Sci. Technol., A*, 21(6):1943–1954, 2003.

[55] A. van der Drift. Evolutionary selection, a principle governing growth orientation in vapour-deposited layers. *Philips Res. Rep.*, 22:267–288, 1967.

[56] X. Yang, N. Chen, Z. Yin, X. Zhang, Y. Li, J. You, Y. Wang, J. Dong, M. Cui, Y. Gao, T. Huang, X. Chen, Y. Wang. Epitaxial growth of ZnO on GaN/sapphire substrate by radio-frequency magnetron sputtering. *J. Semiconductor.*, 31:093001, 2010.

[57] S. Rahmane, B. Abdallah, A. Soussou, E. Gautron,P. Y. Jouan, L. Le Brizoual, N. Barreau, A. Soltani and M. A. Djouadi. Epitaxial growth of ZnO thin films on AlN substrates deposited at low temperature by magnetron sputtering. *Phys. Status Solidi A*, 207(7):1604–1608, 2010.

[58] R. Wagers, G. Kino,P. Galle and D. Winslow. ZnO acoustic transducers ultilizing crystalline gold substrata. *IEEE IUS*, pages 194–197, 1972.

[59] N. Fujimura, T. Nishihara, S. Goto, J. Xu and T. Ito. Control of preferred orientation for ZnO- x films: control of self-texture. *J. Cryst. Growth.*, 130: 269–279, 1993.

[60] C. Tang, M. J. S. Spencer and A. S. Barnard. Activity of ZnO polar surfaces: an insight from surface energies. *Phys. Chem. Chem Phys.*, 16(40):22139–22144, 2014.

[61] Y. Zhang, Z. Guo, X. Gao, D. Cao,Y. Dai and H. Zhao. First-principles of wurtzite ZnO (0001) and (000$\bar{1}$) surface structures. *J. Semiconductor*, 31 (082001), 2010.

[62] S. H. Na and C. H. Park. First-principles study of the surface energy and the atom cohesion of wurtzite ZnO and ZnS - implications for nanostructure formation. *J. Korean. Phys. Soc.*, 56(1):498–502, 2010.

[63] F. S. Hickernell. Zinc oxide films for acoustoelectric device applications. *IEEE Trans. Sonics Ultrason.*, 32(5):621–629, 1985.

[64] F. S. Hickernell. The microstructural properties of sputtered zinc oxide SAW transducers. *Revue Phys. Appl.*, 20(6):319–324, 1985.

[65] A. Bogaerts. Effects of oxygen addition to argon glow discharges: A hybrid Monte Carlo fluid modelling investigation. *Spectrochim. Acta B*, 64(11-12): 1266–1279, 2009.

[66] R. Ikoma, T. Yanagitani, S. Takayanagi, M. Suzuki, H. Odagawa and M. Matsukawa. Control of Zn- or O-polar c-axis oriented ZnO films by different ion bombardment conditions to the substrate. *Proc. USE.*, 33:15–16, 2012.

[67] T. Yanagitani and M. Kiuchi. Highly oriented ZnO thin films deposited by grazing ion-beam sputtering: Application to acoustic shear wave excitation in the GHz range. *Jpn. J. Appl. Phys.*, 46(12L):L1167–L1169, 2007.

[68] L. D. Landau and E. M. Lifshitz. Theory of the dispersion of magnetic permeability in ferromagnetic bodies. *Phys. Z. Sowietunion*, 8:153–169, 1935.

[69] T. L. Gilbert. A phenomenological theory of damping in ferromagnetic materials. *IEEE Trans. mag.*, 40(6):3443–3449, 2004.

[70] D. Polder. On the theory of ferromagnetic resonance. *Physica*, 15(1-2): 253–255, 1949.

[71] D. D. Stancil. Theory of magnetostatic waves. *Springer-Verlag*, 8, 1993.

[72] A. G. Gurevich and G. A. Melkov. Magnetization oscillations and waves. *CRC Press, Inc*, 1996.

[73] H. Seidel. The character of waveguide modes in gyromagnetic media. *Bell Syst. Tech J*, 36(2):409–426, 1957.

[74] L. R. Walker. Magnetostatic modes in ferromagnetic resonance. *Phys. Rev.*, 105(2):390–399, 1957.

[75] C. Kittel. On the theory of ferromangetic resonance absorption. *Phys. Rev.*, 73(2):155–161, 1948.

[76] J. R. Macdonald. Ferromagnetic resonance and the internal field in ferromagnetic materials. *P. Phys. Soc. Lond. A*, 64(11):968–983, 1951.

[77] S. N. Bajpai, R. W. Weinert and J. D. Adam. Variable magnetostatic wave delay lines. *J. Appl. Phys*, 58(2):990–996, 1985.

[78] S. N. Bajpai and N. C. Srivastava. Magnetostatic bulk waves in arbitrarily magnetized dielectric layered structure. *Phys. Status Solidi. (a)*, 57(1):307–315, 1980.

[79] A. N. Slavin and Y. K. Fetisov. Influence of the orientation of the static magnetic field on the dispersion curves for magnetization waves in yttrium iron garnet films. *Sov. Phys. Tech. Phys.*, 33(11):1343–1347, 1988.

[80] R. C. LeCraw, E. G. Spencer and C. S. Porter. Ferromagnetic resonance line width in yttrium iron garnet single crystals. *Phys. Rev.*, 110(6):1311–1313, 1958.

[81] V. Cherepanov, I. Kolokolov and V. L'Vov. The saga of YIG: Spectra, thermodynamics, interaction and relaxation of magnons in a complex magnet. *Phys. Rep.*, 229(3):81–144, 1993.

[82] E. E. Anderson. Molecular field model and the magnetization of YIG. *Phys. Rev.*, 134(6A):A1581–A1585, 1964.

[83] A. D. Karenowska. *Some Magnetic Reflections on Wave Dynamics*. PhD thesis, University of Oxford, 2011.

[84] B. A. Auld. Nonlinear magnetoelastic interactions. *Proc. IEEE.*, 53(10): 1517–1533, 1965.

[85] C. Kittel. Physical theory of ferromagnetic domains. *Rev. Mod. Phys.*, 21 (4):541–583, 1949.

[86] E. R. Callen, A. E. Clark, B. DeSavage, W. Coleman, and H. B. Callen. Magnetostriction in cubic Neel ferrimagnets, with application to YIG. *Phys. Rev.*, 130(5):1735–1740, 1963.

[87] R. L. Comstock. Magnetoelastic coupling constants of the ferrites and garnets. *Proc. IEEE.*, 53(10):1508–1517, 1965.

[88] S. Geschwind. Paramagnetic resonance of Fe^{3+} in octahedral and tetrahedral sites in yttrium gallium garnet (YGaG) and anisotropy of yttrium iron garnet (YIG). *Phys. Rev.*, 121(2):363–374, 1961.

[89] B. Luthi. Physical acoustics in the solid state. *Springer Ser. Solid-State Sci.*, 2004.

[90] F. Bitter. Introduction to ferromagnetism. *London: McGraw-Hill Publishing Co., Ltd.*, 1937.

[91] B. A. Auld. Magnetostatic and magnetoelastic wave propagation. *Academic Press, NY*, vol. 2, 1971.

[92] H. Matthews and R. C. LeCraw. Acoustic wave rotation by magnon-phonon interaction. *Phys. Rev. Lett.*, 8(10):397–399, 1962.

[93] J. R. Eshbach. Spin-wave propagation and magnetoelastic interaction in yttrium iron garnet. *Phys. Rev. Lett.*, 8(9):357–359, 1963.

[94] R. W. Damon and H. Van de Vaart. Dispersion of spin waves and magnetoelastic waves in YIG. *Proc. IEEE*, 53(4):348–354, 1965.

[95] V.V. Lemanov, A. V. Pavlenko and A. N. Grishmanovskii. Interaction between elastic and spin waves in yttrium iron garnet crystals. *Sov. Phys. - JETP.*, 32(3):389–393, 1970.

[96] A. E. Clark and R. E. Strakna. Elastic constants of single-crystal YIG. *J. Appl. Phys*, 32(6):1172–1173, 1961.

[97] Z. Kleszczewski and J. Bodzenta. Phonon-phonon interaction in gadolinium-gallium garnet crystals. *Phys. stat. sol (b)*, 146(2):467–474, 1988.

[98] B. A. Kalinikos and A. N. Slavin. Theory of dipole-exchange spin wave spectrum for ferromagnetic films with mixed exchange boundary conditions. *J. Phys. C: Solid State Phys.*, 19(35):7013–7033, 1986.

[99] M. A. Lieberman and A. J. Lichtenberg. Principles of plasma discharges and materials processing. *John Wiley and Sons, Inc.*, 2005.

[100] K. U. Riemann. The bohm criterion and sheath formation. *J. Phys D: Appl. Phys.*, 24(4):493–518, 1911.

[101] S. S. Mackeown. The cathode drop in an electric arc. *Phys. Rev.*, 34(4): 611–614, 1929.